AD_____

Award Number: W81XWH-04-C-0084

TITLE: Analytic Simulation of Tissue Damage from Penetrating Wounds to the Heart

PRINCIPAL INVESTIGATOR: Robert D. Eisler
Amiya K. Chatterjee
Steven F. Stone
M.El-Raheb

CONTRACTING ORGANIZATION: ATK Mission Research
Laguna Hills, CA 92653-1327

REPORT DATE: December 2006

TYPE OF REPORT: Final

PREPARED FOR: U.S. Army Medical Research and Materiel Command
Fort Detrick, Maryland 21702-5012

REPORT DOCUMENTATION PAGE

Form Approved
OMB No. 0704-0188

1. REPORT DATE	2. REPORT TYPE	3. DATES COVERED
01-12-2006	Final	1 Mar 2004 – 31 Jul 2006

4. TITLE AND SUBTITLE

Analytic Simulation of Tissue Damage from Penetrating Wounds to the Heart

5a. CONTRACT NUMBER

5b. GRANT NUMBER
W81XWH-04-C-0084

5c. PROGRAM ELEMENT NUMBER

6. AUTHOR(S)
Robert D. Eisler
Amiya K. Chatterjee
Steven F. Stone
M.El-Raheb

5d. PROJECT NUMBER

5e. TASK NUMBER

5f. WORK UNIT NUMBER

7. PERFORMING ORGANIZATION NAME(S) AND ADDRESS(ES)

ATK Mission Research
Laguna Hills, CA 92653-1327

8. PERFORMING ORGANIZATION REPORT NUMBER

9. SPONSORING / MONITORING AGENCY NAME(S) AND ADDRESS(ES)
U.S. Army Medical Research and Materiel Command
Fort Detrick, Maryland 21702-5012

10. SPONSOR/MONITOR'S ACRONYM(S)

11. SPONSOR/MONITOR'S REPORT NUMBER(S)

12. DISTRIBUTION / AVAILABILITY STATEMENT
Approved for Public Release; Distribution Unlimited

13. SUPPLEMENTARY NOTES
Original contains colored plates: ALL DTIC reproductions will be in black and white.

14. ABSTRACT

ATKMissionResearchwassponsoredbyDARPA'sVirtualSoldierprogramtoanalyticallysimulateresidualwoundtractsandtissuedynamicsassociatedwithasurvivablewoundfromanexplosivelydrivenfragmentpenetratingtheleftventricularwallofthehumanheart.TheMissionResearcheffortconsistedofthreerelatedtasks.InthefirsttaskMissionResearchdevelopedalgorithmsthatdescribeinteractionofthefragmentwithhumantissueandresultingprojectilekinematicsthroughdifferenttissuelayersofthehumanleftventricularwall.InthesecondtaskMissionResearchusedtheprojectilevelocityretardationandtrajectorymodelsdevelopedinTask1asinputconditionstoatransienttissueresponsemodeldevelopedinsubtask2.1tosimulatetissuedisplacementlateraltotheprojectiletrajectoryinsubtask2.2.ThepermanenttissuedisplacementwasusedtosimulatetheresidualwoundtractwhichwasthenintegratedintotheVirtualSoldierHumanHolomer.Inthefinaltechnicaltaskballisticimpactexperimentswereconductedoninstrumentedhomogeneousandnon-homogeneoustargets.Thedatafromtheseexperimentswerecorrelatedwithoutputfrom Task1and2models.

15. SUBJECT TERMS
penetratingwound,woundballistics,terminalballistics,battlefieldcasualty

16. SECURITY CLASSIFICATION OF:			17. LIMITATION OF ABSTRACT	18. NUMBER OF PAGES	19a. NAME OF RESPONSIBLE PERSON
a. REPORT	b. ABSTRACT	c. THIS PAGE			USAMRMC
U	U	U	UU	299	19b. TELEPHONE NUMBER *(include area code)*

TABLE OF CONTENTS

TABLE OF CONTENTS CONCLUDED

LIST OF FIGURES

LIST OF FIGURES CONCLUDED

LIST OF TABLES

INTRODUCTION

ATK Mission Research was sponsored by DARPA's *Virtual Soldier* program to analytically simulate residual wound tracts and tissue dynamics associated with a survivable wound from an explosively driven fragment penetrating the left ventricular wall of the human heart. The resulting ATK Mission Research wound description was used in the DARPA/University of Michigan *Virtual Soldier* program as initial conditions for describing blood loss and occurrence of hemorrhagic shock. The DARPA/ATK Mission Research Statement of Work (SOW) is included as Appendix A.

The Mission Research effort consisted of three related tasks. In the first task entitled *Analytical Simulation of Projectile Trajectory*, Mission Research divided up fragments into three geometric categories – platelet, "chunky" fragment, and slender high aspect ratio projectile – with different governing parameters. For each fragment geometry, algorithms were developed that describe interaction of the fragment with human tissue and resulting projectile kinematics through different tissue layers of the human left ventricular wall. Prof. Andrew McCulloch, Ph.D. (University of California, San Diego – UCSD) and his team assisted Mission Research in executing the UCSD *Continuity* code to develop quasistatic constitutive models for the various layers of tissue through the left ventricular wall. From these quasistatic models, high strain rate tissue property data was developed by Mission Research for input into projectile retardation models. The retardation models, which are specific to the various fragment geometry classes, describe projectile deceleration during tissue penetration and were also developed by Mission Research in this first task.

In the second task entitled *Analytical Simulation of Wound Tract*, Mission Research used the projectile velocity retardation and trajectory models developed in Task 1 as input conditions to a transient tissue response model developed in subtask 2.1 to simulate tissue displacement lateral to the projectile trajectory in subtask 2.2. The permanent tissue displacement was used to simulate the residual wound tract which was then integrated into the *Human Holomer* developed by the University of Michigan for DARPA's *Virtual Soldier* project.

In the final technical task entitled *Ballistic Experiments on Tissue and Surrogate Materials*, ballistic impact experiments were conducted with custom designed launchers and projectiles on instrumented homogeneous and non-homogeneous ordnance gelatin targets. The data from these experiments were correlated with output from Task 1 and 2 models.

Two additional tasks, unrelated to the base effort described above, were added to the Mission Research SOW. The first of these tasks included using a modified Nail Gun developed by the US Army Institute of Surgical Research (ISR) on ordnance gelatin targets and comparing residual damage produced in the gelatin by the ISR Nail Gun as compared to the residual damage from ballistic experiments. A separate letter report and a DVD with high-speed digital video of all experiments were sent under separate cover for this task. The second task included conducting hydrocode analysis of body armor SAPI plates subject to non-penetrating projectiles and blast and is discussed in Appendix O.

TASK 1
PROJECTILE RETARDATION AND TRAJECTORY MODELING

The principal activity in this task was to develop a model that describes velocity retardation and trajectory of the projectile center-of-mass as it penetrates human tissue. The model must use independently measured target mechanical properties that is typically available for human tissue as input. This is important since ballistic test data will not be available for human subjects and only limited, quasistatic human tissue mechanical property data is available. We therefore formulated a projectile retardation model where given data relative to penetration depth versus striking velocity derived from ballistic experiments on a known projectile target combination, where the penetration physics are phenomenologically similar to human tissue, a similar relation can be derived for an unknown projectile-target combination (in this case human tissue) provided that projectile properties, striking conditions, and target material properties are known. We successfully validated the methodology by conducting ballistic penetration experiments on different formulations of gelatin and predicting velocity retardation and projectile kinematics where only quasistatic mechanical properties where known for the gelatin formulations.

In this task three categories of fragments were modeled (cf. Figure 1). The first category is a platelet with length to diameter ratio (L/D) $\rightarrow \varepsilon$ (i.e., fragment thickness dimension is very small). The mean amplitude,δ, of the irregular boundary about the platelet is user specified. The second category is a "chunky fragment" that is symmetrical with length to diameter ratio (L/D) $\approx$ 1. In general this projectile can be represented as an "equivalent sphere" in terms of its penetration characteristics. The third category is a non-symmetric fragment with a user specified L/D where $1 < L/D \leq 2$. We have used as a nominal example of this fragment category a cylinder with a leading edge geometry that is a wedge where the angle of the wedge is user specified. An example of this fragment is shown in Figure 2 and is being used in the Task 3 ballistic experiments.

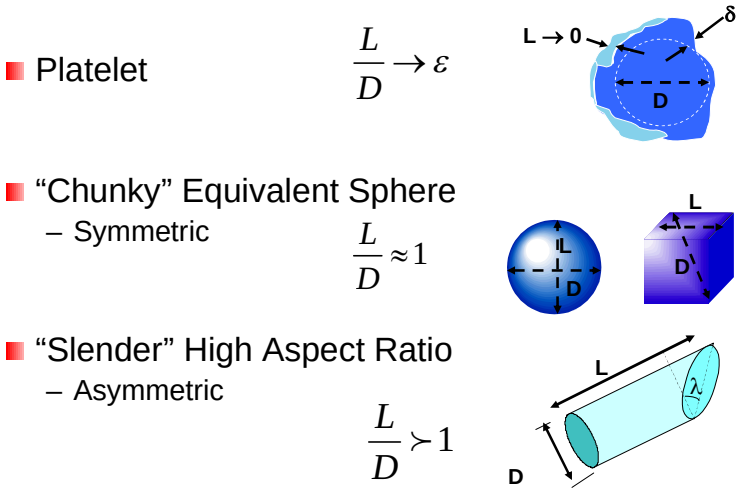

FIGURE 1. Models for three fragment categories

FIGURE 2. 30 Caliber "Wedge Projectile" used in Task 3 Ballistic Experiments

1.1 ESTIMATION OF RETARDATION COEFFICIENTS FROM EXPERIMENTAL DATA AND ITS EXTENSION TO UNKNOWN PROJECTILE-TARGET PAIR

When a projectile enters a target medium at a known velocity, the projectile velocity decreases as penetration depth increases. For analysis, the associated penetration mechanics is idealized as occurring in two phases. The first phase is the initial entry phase when the projectile is not fully embedded in the target. The discussion of this initial phase is deferred until Sections 1.1.2 and 1.1.3. The second phase is the projectile motion after the projectile is fully embedded in the target. Note that for a given projectile-target pair, there is threshold striking velocity below which no penetration takes place and the motion of the pair can be predicted by linear elastic analysis.

Initially, our effort focused on the second phase of the penetration process. To understand the second phase of motion, experimental data from Task 3 relative to penetration of spherical projectiles into 20% gelatin targets was employed. We used three sizes of spherical projectiles; a 0.34 gram, 0.17 inch diameter steel sphere (referred to as a 'BB'), a 1.0 gm, 0.25 inch diameter steel sphere, and there is also some limited 0.375 inch diameter steel sphere data.

Experimental data was collected on the depth of penetration, $\delta(v)$, at different striking velocities, v,. We call this data "experimental $\delta(v)$ versus v" data. This data is presented in the Task 3 discussion. Using the kinematics of a point mass m under a retarding force, $R(v)$, we can relate $R(v)$ and $\delta(v)$ through the following equations.

$$\delta(v) := \int_0^v \frac{v}{R(v)}\,dv \qquad R(v) := \frac{v}{\frac{d}{dv}\delta(v)} \qquad \text{Equation (1-1)}$$

where the mass term have been dropped from the equations. From physical considerations, $R(v) = \alpha + \beta v + \gamma v^2$, then the first term corresponds to very low velocity or a 'static' retarding force, the second term correspond to the Stokes frictional drag while the last term is the fluid drag term with a $\frac{1}{2}\rho v^2$ scaling. Frictional drag is scaled to the viscosity μ of the target medium and the first term is scaled with the elastic modulus of the target.

To develop a retardation force algorithm, Equation (1-1) is used to determine α, β, γ for the projectile target pair used in the experiments. These are called "reference" values. Equation 1-1 can be used to derive the low velocity and high velocity characteristics of the $\delta(v)$ function. It can be shown that $\delta(v) \approx v^2$ as $v \rightarrow 0$ for low velocities and $\delta(v) \approx \ln(v)$ for high velocities. Expanding $\delta(v)$ as

$$\delta(v) = \begin{cases} v^2(a + bv + cv^2), \text{ low v} \\ a'\ln(v) + \frac{b'}{v} + \frac{c'}{v^2}, \text{ high v} \end{cases} \qquad \text{Equation (1-2)}$$

And using the experimental data, we can get the coefficients in Equation 1-2 by curve fitting, and matched asymptotic expansions. Once $\delta(v)$ is known, $R(v)$ and its coefficients can be calculated from Equation 1-1. For 0.25-inch diameter steel balls, experimental data and estimation of the retardation force using Equation 1-1 is shown in Figure 2. In Figure 2, v is in ft/sec, δ is in inches, and R2 is in consistent units.

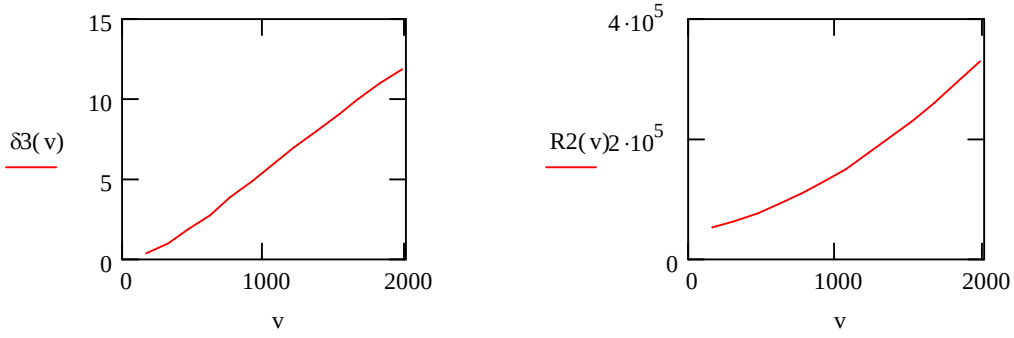

FIGURE 3. Penetration Depth and Retardation forces versus Velocity

To extend these equations to unknown projectile target pairs, we make some fundamental assumptions. We assume that the force of retardation is normal to the projectile surface. That is, the retardation depends only on the normal component of velocity, v_n for a representative point on the projectile surface. If this component is negative, then the force of retardation is zero. Thus,

the normal force is $R = \begin{cases} R(v_n) \text{ if } v_n > 0 \\ 0 \text{ if } v_n \le 0 \end{cases}$.

The projectile is assumed to be rigid as it moves through the target. This is a good approximation if the target is "soft" as is the case for biological tissue and surrogate materials of interest. The scaling laws applied to the various coefficients α, β, γ are done using the physical relations between the respective terms discussed above. Scaling parameters are shown below in Table 1, page 13.

The scaling in the text box was used for the spherical penetration data in the 20% gelatin targets shown in Figure 4. So in this example, the target mechanical properties are unchanged while the projectile properties are different and the scaling for different diameter spherical projectiles is shown. As previously mentioned, a correlation between the theoretical predictions using the method above and experimental data for various spherical projectiles are also shown in Figure 4.

1.1.1 APPLICATION TO NON-SPHERICAL PROJECTILES WITH ASPECT RATIOS $0 < \frac{L}{D} \le 2$

Using the above approximations, we have developed models to predict the motion of two completely different types of projectiles. The first one is a flat fragment with very low L/D while the second one is a cut cylinder with $1 \le$ L/D ≤ 2. These models with the associated theoretical development are briefly discussed below.

1.1.1.1 Flat Fragment (Platelet). A schematic of the fragment and loading is shown in Figure 5.

Equations of Motion

The motion of the center of mass *G* and the motion about *G* are governed by

$$m\dot{\underset{\sim}{V}}_G = -\int_S R(v_n)\hat{\underset{\sim}{n}}\,dS$$
$$\dot{\underset{\sim}{H}}_G = -\int_S \underset{\sim}{r}' \times R(v_n)\hat{\underset{\sim}{n}}\,dS$$

Equation (1-3)

TABLE 1. SCALING METHODOLOGY FOR PENETRATION DEPTH AS FUNCTION OF STRIKING VELOCITY

Use Scaling Laws for Retardation Coefficients

Reference Values: Change when Different Experimental Data is used as Reference Values

Enter Projectile/Target Data

Reference or Experimental Data Values

Target Young's Modulus $E := 4.5 \cdot 10^4$ (psi)

Reference Target Young's Modulus $Er := 4.5 \cdot 10^4$ (psi)

Target Viscosity $\mu := 0.1$ (poise)

Reference Target Viscosity $\mu r := 0.1$ (poise)

Projectile Diameter or
Diameter of Projected Area $D := 0.375$

Reference Projectile Diameter or
Diameter of Projected Area $Dr := 0.25$ (in)

Target Density $\rho := 1.0$ (gm/cc)

Reference Target Density $\rho r := 1.0$ (gm/cc)

Projectile Density $\rho p := 8.0$ (gm/cc)

Reference Projectile Density $\rho pr := 8.0$ (gm/cc)

Projectile Mass $mp := \frac{1}{6} \cdot \pi \cdot (D \cdot 2.54)^3 \cdot \rho p$ (gm)

$mp = 3.62$ (gm)

Reference Projectile Mass $mr := \frac{1}{6} \cdot \pi \cdot (Dr \cdot 2.54)^3 \cdot \rho pr$

$mr = 1.073$ (gm)

Scale Retardation Coefficients

$\alpha n := \alpha r \cdot \frac{mr}{mp} \cdot \left(\frac{D}{Dr}\right)^2 \cdot \frac{E}{Er}$ $\alpha n = 2.7 \times 10^4$ $\alpha = 4.049 \times 10^4$

$\beta n := \beta r \cdot \frac{mr}{mp} \cdot \left(\frac{D}{Dr}\right)^2 \cdot \frac{\mu}{\mu r}$ $\beta n = 34.951$ $\beta = 52.427$

$\gamma n := \gamma r \cdot \frac{mr}{mp} \cdot \left(\frac{D}{Dr}\right)^2 \cdot \frac{\rho}{\rho r}$ $\gamma n = 0.032$ $\gamma = 0.048$

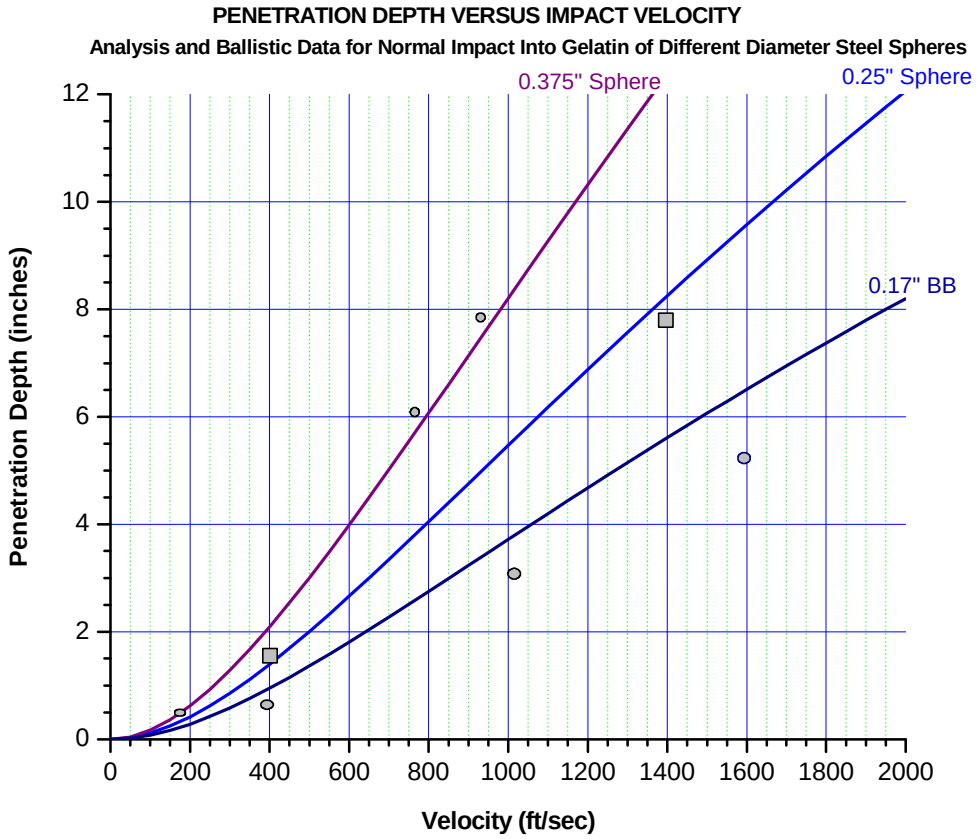

FIGURE 4. Correlation between analytical predictions and ballistic test data for three different diameter spheres shot into 20% ordnance gelatin

In Equation 1-3, $\underset{\sim}{H}_G$ is the angular momentum of the fragment about the center of mass *G* and $\underset{\sim}{r}' = \vec{GP}$. Equation 1-3 represents six nonlinear, second order, coupled differential equations that can be solved using a Runge-Kutta method. Solution to these equations will predict the motion of the center of mass and the rotation of the projectile as it moves about its center of mass. This solves the motion of a flat fragment through the target.

1.1.1.2 FRAGMENT REPRESENTED BY A CUT CYLINDER. The schematic of a "cut-cylinder" and associated loading is shown in Figure 6.

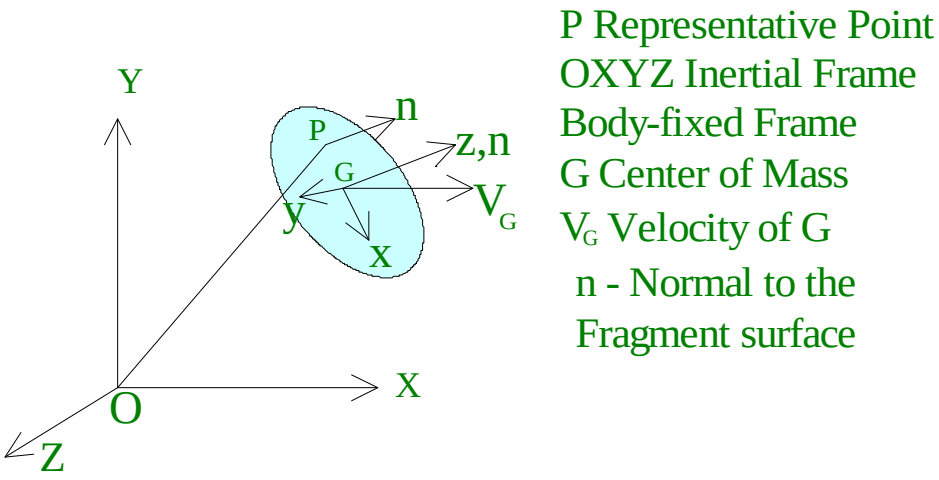

FIGURE 5. Schematic of Loading on a Flat Fragment

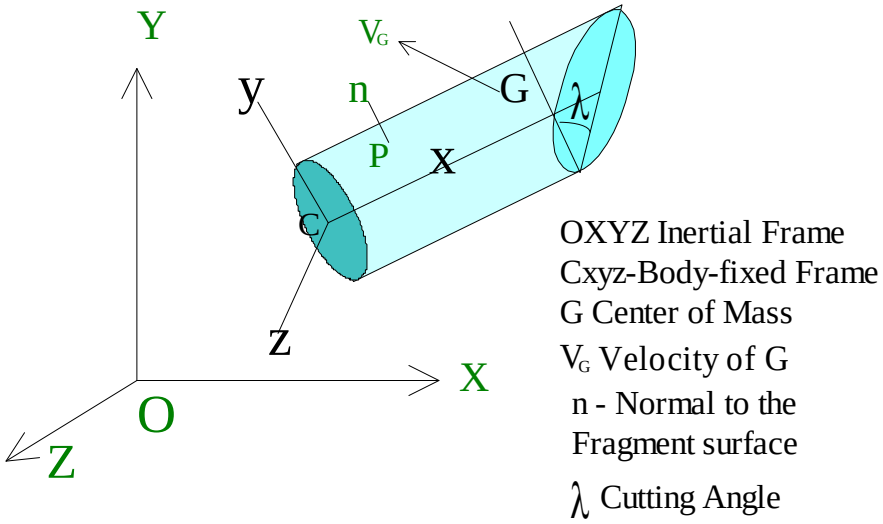

FIGURE 6. Schematic and Loading on a Cut Cylinder

The equations of motions are identical to Equation 1-3 except that the mass moment of inertia matrices are different. The projectile surface has been subdivided into three areas shown by the different colors in Figure 6. Two of these surfaces are flat and have simple normals and representative points while the other one is flat and has more complicated normal orientations at various representative points.

1.1.2 DETERMINING TISSUE THRESHOLD PENETRATION VELOCITY

For a given projectile-target pair, there exists a minimum velocity below which no visible penetration occurs. For elastic targets, this means that the deformation produced during impact is mostly recoverable and virtually no or only a very small indentation is visible. Thus, for a non-penetrating ballistic impact, the input kinetic energy is lost through elastic wave radiation in the target.

While the determination of this characteristic threshold velocity is difficult, some observations are made from experimental data generated in Task 3 for spherical projectiles. For the cases of 0.17 in. and 0.25 in. diameter projectiles, it has been observed that indentation/penetration in the target equivalent to at least one projectile diameter is necessary in order for full penetration to occur. Using this observation, we can use the penetration depth versus incident velocity data for these two cases and determine penetration thresholds. Since penetration threshold data for these two projectile cases is known, we can compare our prediction with experimental results. For the above models, the relation between the penetration depth δ and the incident velocity v is given by $\delta(v) = v^2(a + bv + cv^2)$ where the coefficients *a, b,* and *c* can be obtained by data fitting. For the 0.25 inch diameter spherical projectile, these constants are given above in Table 1. Thus, the theoretical penetration threshold $v_{\min}$ can be calculated from $v_{\min} = \delta^{-1}(d)$ where d is the projectile diameter and δ^{-1} is the inverse function of δ. Since this result depends on the lower end of the velocity field, $v_{\min}$ can be approximated from a simpler equation, $v_{\min} = \sqrt{\frac{d}{a}}$. For a 0.25 inch diameter steel ball, this yields $v_{\min} = 143\frac{ft}{\sec}$ which is very close to what was experimentally observed.

1.1.3 SMALL DEPTH OF PENETRATION MODEL

Models describing the penetration of projectiles of various aspect ratios have been developed earlier using the retardation formula given by a quadratic function in the instantaneous projectile velocity, v. The coefficients used in this formula are determined from the analytical inversion of experimental data for cases where such data is available. Extension of this model to cases where no such experimental data is available has also been developed earlier. The early phase of

penetration, when the incident velocity is at or near the threshold velocity of penetration, has not been explored in detail before, however. Some simple particle kinematics can yield insight relative to the mechanics of penetration during these early phases of penetration prior to the stage when the projectile is fully embedded inside the target and does not rebound elastically. We refer to this analysis as the *small depth of penetration model*. This model can be used for two problems; first to predict the penetration threshold, v_c, as described in Section 1.2,for a given projectile and second, to determine the small depth of penetration for impact velocities near v_c.

The nature of the force of retardation (FR) changes for impact velocities below and above v_c. Such differences in the nature of FR can be obtained from simple one-dimensional motion of a lumped particle mass that represents the projectile. The equation of motion of the projectile of mass m impacting a target with a incident velocity v_i is

$$mv\frac{dv}{dx} = -F(x) \qquad \text{Equation (1-4)}$$

where $F(x)$ is the FR when the surface displacement is x.

If d is the final displacement, then integrating Equation 1-4 above, we have

$$\int_0^d F(x)dx = \frac{1}{2}mv_i^2 \qquad \text{Equation (1-5)}$$

If D is the diameter of the average projected area of the projectile on the target, then $F(x)$ can be written as

$$F(x) = \frac{\pi}{4}D^2\sigma(x) \qquad \text{Equation (1-6a)}$$

If E is the Young's modulus of the target and ℓ is the effective depth, then

$$\sigma(x) = \begin{cases} E\dfrac{x}{\ell} & \text{for elastic displacement} \\ \sigma_c & \text{for penetration} \end{cases} \qquad \text{Equation (1-6b)}$$

In (1-6b), σ_c is the threshold stress for penetration and is a material constant. Substituting (1-6) in (1-5), we have

$$d = \begin{cases} \propto \upsilon \text{ for elastic deformation} \\ \propto \upsilon^2 \text{ for projectile penetration} \end{cases} \qquad \text{Equation (1-7)}$$

Equation (1-7) is consistent with the observed nature of the small depth of penetration for incident velocities near the penetration threshold velocity υ_c.

Using (1-7) and a reference projectile identified by a subscript r, we can write down the formula that gives the functional relation $d = d(\upsilon)$ between the incident velocity υ and the depth of penetration d for a small depth of penetration. The derivation of this result for a spherical or sphere-like projectile of diameter D and density, ρ, is given below. From (1-4) and (1-7), we have, using

$$m = \frac{1}{6}\pi\rho D^3,$$

Writing (1-7) explicitly, we have

$$d(\upsilon) = \left(\frac{\rho\upsilon^2}{3\sigma_c}\right)D \qquad \text{Equation (1-8)}$$

when penetration occurs. The effective spring constant, k, of the target material can be calculated from the following formula.

$$k = \frac{F(x)}{x} = \frac{\pi E D^2}{4\ell} \qquad \text{Equation (1-9)}$$

Thus, the spring stiffness increases as D^2.

Determine Penetration Threshold Velocity, υ_c, Revisited

To determine the penetration threshold velocity, υ_c, we postulate, as in Section 1.1.2, that the penetration depth should be at least the radius (or the effective radius) of the spherical or sphere-like projectile so that υ_c satisfies the condition

$$d(\upsilon_c) = \frac{D}{2} \qquad \text{Equation (1-10)}$$

From (1-8) and (1-10), we have

$$\sigma_c = \frac{2}{3}\rho v_{cr}^2$$

$$v_c = v_{cr}\sqrt{\frac{\rho_r}{\rho}}$$

Equation (1-11)

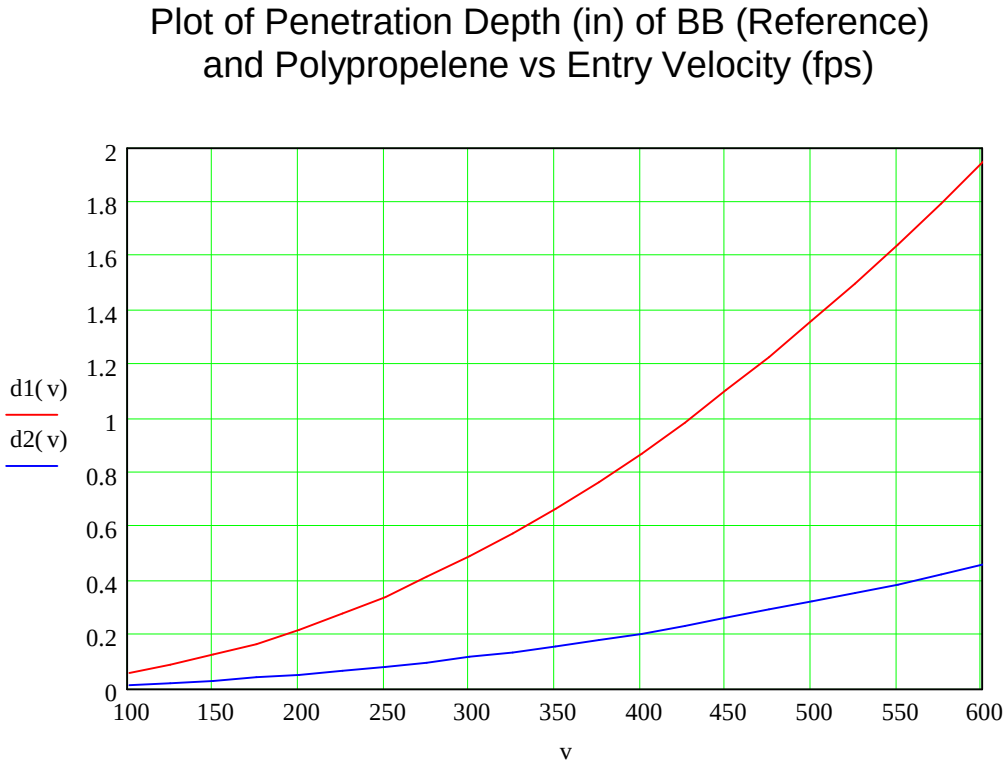

FIGURE 7. Penetration Depth of Steel Spherical Reference Projectile compared with Polypropylene Spherical Projectile

We have experimental data on penetration of small ($D_r = 0.17$ in.) diameter spherical steel ball impacting gelatin blocks. From this data, we derived the penetration threshold velocity $v_{cr} = 175$ fps which is consistent with Equation (1-10). Applying Equation (1-11) to 32 caliber polypropylene spherical ball ($\rho = 1\ \frac{\text{gm}}{\text{cc}}$), we get the predicted threshold velocity $v_c = 495$ fps. This result is very close to the experimentally observed minimum velocity needed for full penetration. In Figure 7, we compare the penetration depth of the reference 'BB' projectile and a polypropylene projectile using the small-depth penetration model. It should be recalled that for a large depth of penetration, penetration depth is proportional to $\ln(v)$ instead of v^2 shown in Equation (1-8) for the small depth of penetration model.

Analysis of New Penetration Data

Using high speed digital video with a frame rate of the order of microseconds, new experimental data on ballistic penetration has been obtained by ATK Mission research as part of the Virtual Soldier effort. Two types of projectiles were used; one is a ¼ in. steel projectile and the other is a ¼ in steel cylinder with an aspect ratio of 2 (See Tables 6, 7, and 8 in Section 3).

Run No. 0506-07
¼ in steel sphere impacting 20% gelatin target at 1,170 fps

Experimental data derived from video images by manual cursor placement is shown in Table 2. The wavy nature of the velocity profile is due to manual data extraction. This data is used to test the analytical models developed earlier from small spherical projectiles penetrating gelatins. This data is used as the reference data labeled as 'BB-data' for extending the capability of analytical prediction of location, velocity and time for penetration of other projectiles in 20% gelatin. The comparison of measured velocity and penetration depth for the ballistic test # 0506-07 shown in Table 2, and analytical prediction (red curve) is shown in Figure 8. For the three other cases shown in Table 6, a cylindrical projectile of ¼ inch base diameter and length to diameter ratio of 2 is used as the projectile.

TABLE 2. Analysis of Digital Video Data for Run No. 0506-07

GBL Test Distance Velocity Direct Read from Phantom 606 at 1170 fps					Target: 20% Gelatin
Case: 0506-07		1/4 in Steel ball	Mass=1.04 gm		Total Depth of Pen = 6.3 in
Start Frame 9					
Elap.Time	Read Dist.(in)	Actual Distance	Speed Read (fps)	Frame	Read from Phantom 606
microsec	inches				
0.0000	0	0	1170		
34.0091	0.404	0.404	989.932	10	d = 0.404 in s = 989.932 ft/s
32.9891	0.425	0.829	1073.588	11	d = 0.425 in s = 1073.588 ft/s
33.0312	0.383	1.212	966.257	12	d = 0.383 in s = 966.257 ft/s
32.9662	0.361	1.573	912.55	13	d = 0.361 in s = 912.550 ft/s
34.0147	0.319	1.892	781.525	14	d = 0.319 in s = 781.525 ft/s
33.0436	0.298	2.19	751.533	15	d = 0.298 in s = 751.533 ft/s
32.9891	0.255	2.445	644.153	16	d = 0.255 in s = 644.153 ft/s
32.9583	0.276	2.721	697.852	17	d = 0.276 in s = 697.852 ft/s
34.0680	0.213	2.934	521.017	18	d = 0.213 in s = 521.017 ft/s
33.0293	0.235	3.169	592.908	19	d = 0.235 in s = 592.908 ft/s
33.0658	0.213	3.382	536.809	20	d = 0.213 in s = 536.809 ft/s
32.9459	0.191	3.573	483.115	21	d = 0.191 in s = 483.115 ft/s
34.0581	0.214	3.787	523.615	22	d = 0.214 in s = 523.615 ft/s
32.9459	0.191	3.978	483.115	23	d = 0.191 in s = 483.115 ft/s
32.9882	0.17	4.148	429.447	24	d = 0.170 in s = 429.447 ft/s
33.1637	0.1709	4.3189	429.435	25	d = 0.170 in s = 429.435 ft/s
34.0451	0.149	4.4679	364.712	26	d = 0.149 in s = 364.712 ft/s

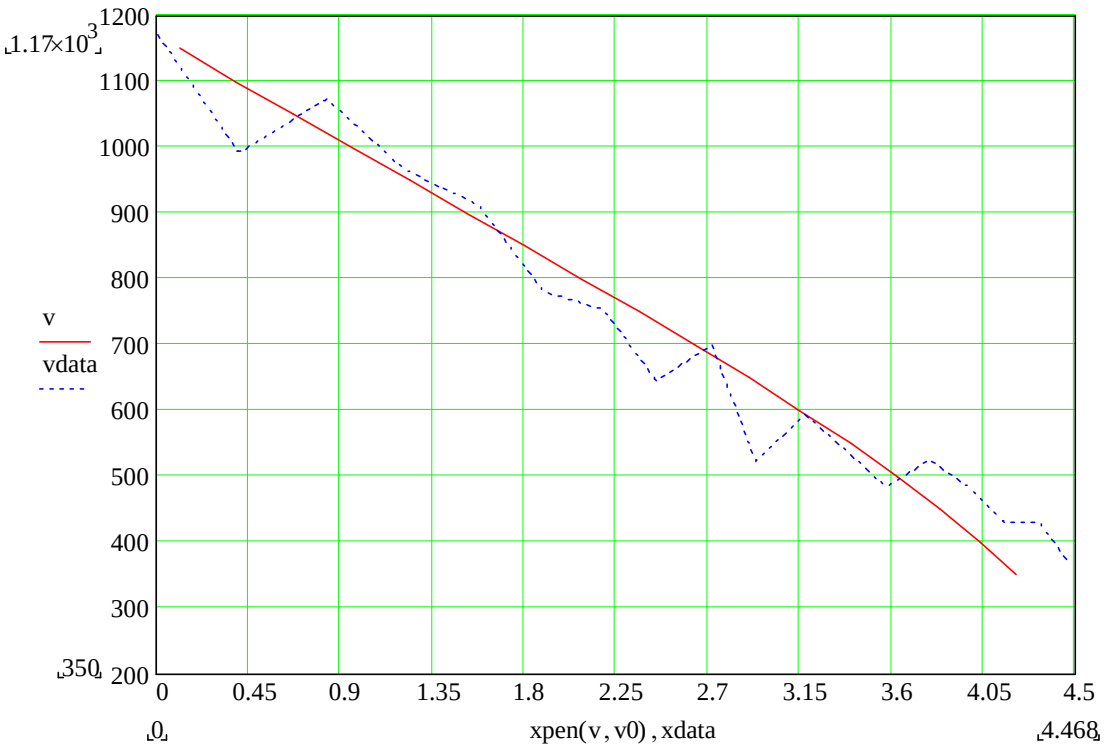

FIGURE 8. Comparison of Recorded Data and Analytical Prediction: Run No. 0506-07

Analysis of other experimental data

- Unlike the spherical projectile (run # 0506-07), cylindrical projectiles tend to rotate as they penetrate the target due to small striking obliquities. For perfectly normal impact in a perfectly homogeneous target, no rotation should be present.
- Since no deviation is observed for spherical projectiles, we postulate that the rotation must occur mainly due to the small obliquity of incident angle.
- For locations where the cylinder is not in contact with the surrounding gelatin target, the velocity normal to the projectile surface is along the inward normal.
- For locations where the cylinder is in contact with the surrounding gelatin target, the velocity normal to the projectile surface is along the outward normal.
- This result conforms to the assumptions made when the analytical model for the projectile penetration was developed.

Similar results are shown for the “cut” cylindrical projectile where the rotational kinematics of the cut-cylinder projectile are simulated in the slides on page 284 (Appendix N) and compared with experimental results.

Captured snap shots for the sphere and cylindrical targets are shown in Figure 9 to support the observations made above.

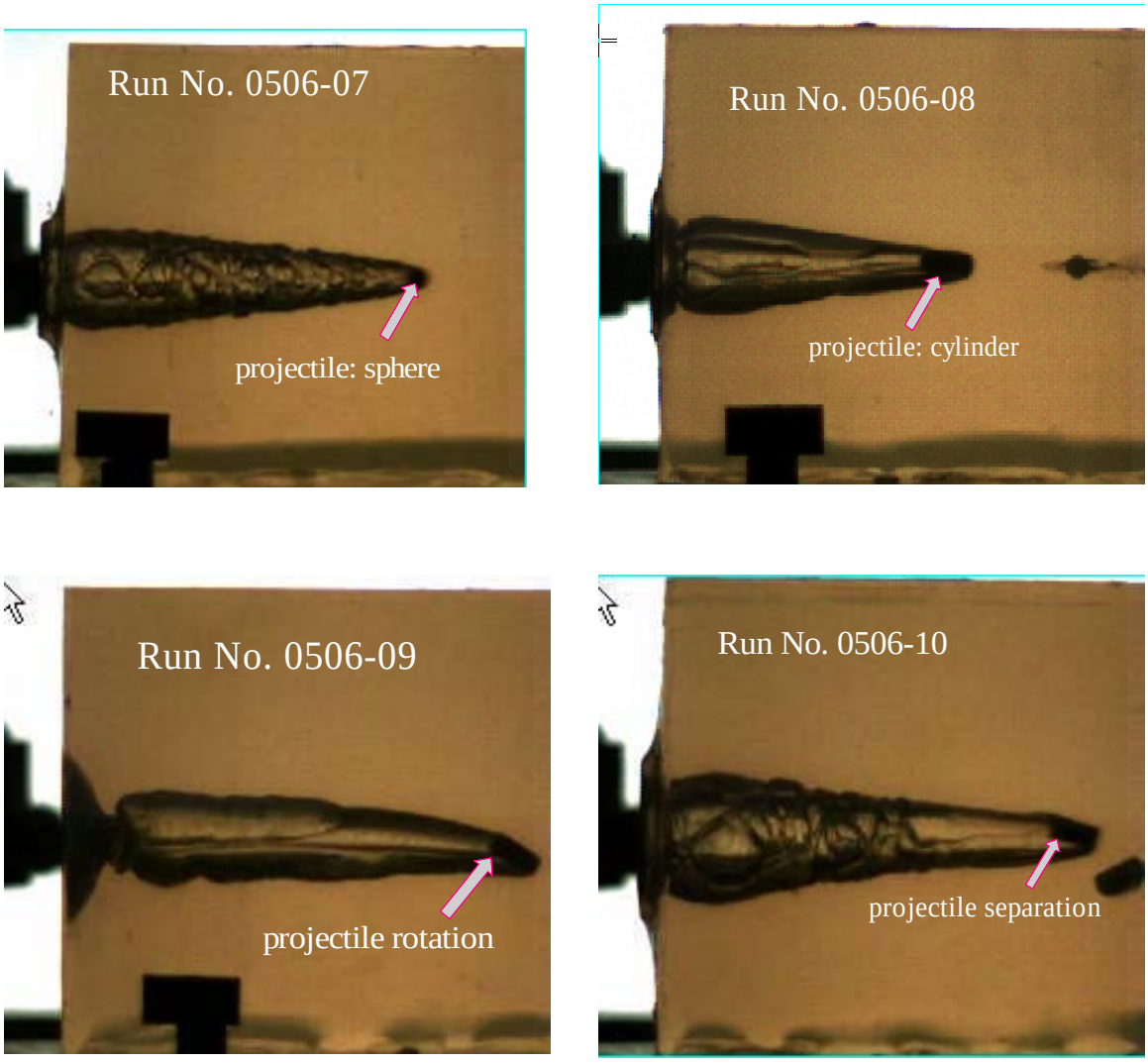

FIGURE 9. Snapshots From Digital Video of Ballistic Experiments

1.1.4 MOTION OF AN ARBITRARY-SHAPED RIGID BODY INSIDE A KNOWN TARGET WITH POSITION DEPENDENT RETARDATION PROPERTIES

Let us consider an arbitrary shaped rigid body penetrating a target where the force of retardation at any point P is dependent on the position of P inside the target. Considering an elementary area dA at P on the surface of the body, we assume that force of resistance is opposite (inward)

to the outward normal, **n** (Figure 10), and its magnitude depends on three position-dependent retardation coefficients α, β, γ, and the normal component $\upsilon_n = \mathbf{v_P}.\mathbf{n}$ of the velocity $\mathbf{v_P}$ of P. From experimental data on penetration of small steel spherical projectiles, we have the depth of penetration $\delta(\upsilon)$ as a function of the incident velocity υ. Using one-dimensional particle kinematics, the force of retardation, $R(\upsilon)$ can be obtained as a function of the instantaneous velocity, υ, from a functional relation between $\delta(\upsilon)$ and $R(\upsilon)$ originally rendered as Equation 1,

$$\delta(\upsilon) = \int_0^{\upsilon} \frac{m\eta}{R(\eta)} d\eta \text{ or } R(\upsilon) = \frac{m\upsilon}{\frac{d\delta}{d\upsilon}} \qquad \text{Equation (1-12)}$$

where m is the mass of the small spherical particle.

In the case of a finite sized rigid body penetrating a given target, we assume that the body surface is composed of an ensemble of small elementary surfaces, and the force of resistance on an elementary area dA depends on the inward velocity at P and three retardation coefficients obtained from Equation (1-12) and experimental data. By using a scaling analysis, we have extended the nature of the retardation force to unknown bodies for which no experimental data is available. It has been established that these coefficients depend on the following material properties at the instantaneous location of dA:

1. Young's Modulus E
2. Target density ρ
3. Target viscosity μ, and
4. Properties of the reference material for which experimental data is available.

The motion of the projectile inside the target is decomposed into: (a) the motion of the center of mass *G*, and (b) the rotational motion of the rigid body about *G*.

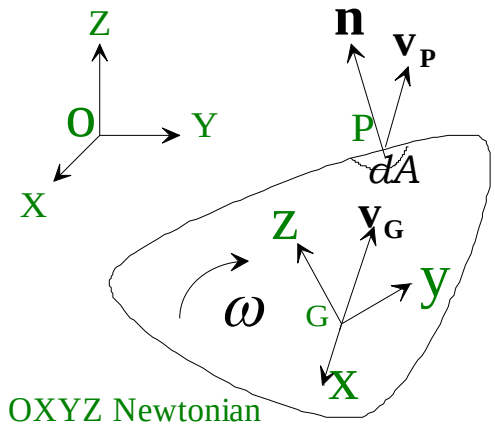

FIGURE 10. Frames of References for Arbitrary Penetrating Body

Writing the force of retardation $R(\upsilon_n)$ per unit area as

$$R(\upsilon_n) = \alpha_P + \beta_P \upsilon_n + \gamma_P \upsilon_n^2 \qquad \text{Equation (1-13)}$$

the equations of motion of the center of mass *G* is given by[1]

1 Overhead dot indicates time derivative

$$m\dot{\mathbf{v}}_{\mathbf{G}} = -\int_A R(\upsilon_n)\mathbf{n}\,dA \qquad \text{Equation (1-14)}$$

and the equation of motion for the rotational motion about *G* is given by

$$\mathbf{M}_{\mathbf{G}} = \dot{\mathbf{H}}_{\mathbf{G}} = -\int_A R(\upsilon_n)\mathbf{n}\times\mathbf{r}_{\mathbf{G/P}}\,dA \qquad \text{Equation (1-15)}$$

In equation (1-15), subscripts P in the retardation coefficients α, β and γ indicate that these coefficients depend on the target material properties at P. In Equation (1-14), $\mathbf{v}_{\mathbf{G}}$ is the velocity of the center of mass G. In Equation (1-15), $\mathbf{M}_{\mathbf{G}}$ is the moment of the retardation forces about *G*, and $\mathbf{H}_{\mathbf{G}}$ is the angular momentum of the rigid body about G, and $\mathbf{r}_{\mathbf{G/P}} = \mathbf{GP}$ (Equation 1-15 and Figure 10).

Using the inertia matrix

$$I = \begin{pmatrix} I_{xx} & -I_{xy} & -I_{xz} \\ -I_{xy} & I_{yy} & -I_{yz} \\ -I_{xz} & -I_{yz} & I_{zz} \end{pmatrix} \qquad \text{Equation (1-16)}$$

about the center of mass *G* with axes along the $Gxyz$ (Figure 10), and the angular velocity ω of the rigid body

$$\omega = \begin{pmatrix} \omega_x \\ \omega_y \\ \omega_z \end{pmatrix} \qquad \text{Equation (1-17)}$$

where the components are along the axes of the rotating frame $F = Gxyz$ attached to the rigid body, the relation between $\mathbf{H}_{\mathbf{G}}$, $\mathbf{I}$ and ω is given by

$$\mathbf{H}_{\mathbf{G}} = \mathbf{I}.\omega \qquad \text{Equation (1-18a)}$$

The relation between the Newtonian derivative operator $\frac{d^N}{dt}$ and frame-related derivative operator $\frac{d^F}{dt}$ is

$$\frac{d^N}{dt} = \frac{d^F}{dt} + \omega \times \qquad \text{Equation (1-18b)}$$

Using (10) Equation (7) can be written as

$$\mathbf{I}\dot{\omega} = \mathbf{M_G} - \omega \times \mathbf{H} \qquad \text{Equation (1-19)}$$

The component equations can now be written from Equation (1-19) in the rotating frame axes *Gxyz* (Figure 10).

In order to track the location of the body at any given time t, the orientation of the body-fixed unit vectors along with the location of the center of mass *G* in the Newtonian frame *OXYZ* should be known. This can be done by solving the differential equations governing the motion of the **i**, **j**, **k** through the target. The details about the motion of **i**, **j**, **k** are described in the next section.

Material Properties Data in a Newtonian Frame and Its Transfer to the Equations of Motion

Two fundamental equations governing the motions of the center of mass *G* and rotation about the center of mass are given in Equations (1-14) and (1-19). The scalar equations arising from these equations can either be written by taking components along body-fixed *Gxyz* (F-frame) or Newtonian *OXYZ* (N-frame) axes. Equation (1-19) is described in F-frame while (1-14) is described in the N-frame. Besides, for visualization of projectile penetration inside the target, all quantities should be translated to the N-frame. The transfer function between these two frames requires the temporal description of the unit vectors along the F-axes to the unit vectors in N-axes. As the rotational angles can only be added incrementally, we also need to include the differential equations describing the change in these unit vectors.

Let

$$\mathbf{i} = \begin{pmatrix} i_X \\ i_Y \\ i_Z \end{pmatrix}, \mathbf{j} = \begin{pmatrix} j_X \\ j_Y \\ j_Z \end{pmatrix}, \mathbf{k} = \begin{pmatrix} k_X \\ k_Y \\ k_Z \end{pmatrix} \qquad \text{Equation (1-20)}$$

be the unit vectors along the Gx, Gy and Gz axes (Figure 10) with components in the N-frame along OX, OY and OZ axes. Then the time derivative of these unit vectors are given by

$$\dot{\mathbf{i}} = \omega \times \mathbf{i}\ ,\ \dot{\mathbf{j}} = \omega \times \mathbf{j}\ ,\ \dot{\mathbf{k}} = \omega \times \mathbf{k} \qquad \text{Equation (1-21)}$$

The transformation matrix $\mathbf{T}$ between the F-axes and N-axes components is given by

$$\mathbf{T} = \begin{pmatrix} i_X & i_Y & i_Z \\ j_x & j_Y & j_Z \\ k_X & k_Y & k_Z \end{pmatrix} \qquad \text{Equation (1-22)}$$

Using the $\mathbf{T}$-matrix, any vector $\mathbf{x}^{\mathbf{F}}$ with components along the F-axes can be converted to same vector $\mathbf{x}^{\mathbf{N}}$ with components along the N-axes through

$$\mathbf{x}^{\mathbf{N}} = \mathbf{T}.\mathbf{x}^{\mathbf{F}} \qquad \text{Equation (1-23)}$$

Using (1-21) and (1-23), the differential equations governing the unit vectors are given by

$$\dot{\mathbf{i}} = (\mathbf{T}.\omega) \times \mathbf{i}\ ,\ \dot{\mathbf{j}} = (\mathbf{T}.\omega) \times \mathbf{j}\ ,\ \dot{\mathbf{k}} = (\mathbf{T}.\omega) \times \mathbf{k} \qquad \text{Equation (1-24)}$$

The integrations shown in (1-14) and (1-15) contain integrands which depend on the location of the point *P* in space and the description of material properties at *P*. Since the integrations are done in F-frame while the material properties are known in N-frame, we need to convert the coordinates of P from the F-frame to the N-frame by using the conversion-formula given by Equation (1-23).

18 Coupled Differential Equations and Their Solution by Runge-Kutta Algorithm

With reference to Figure 10, let us define a 18×1 vector $\mathbf{x}$ whose components are described below:

x_1, x_2, x_3 are the coordinates of G in N-frame Equation (I-25)
x_4, x_5, x_6 are the components of the velocity of the center of mass G in N-frame
x_7, x_8, x_9 are the components of the angular velocity of the body in F-frame
x_{10}, x_{11}, x_{12} are the components or the direction cosines of the unit vector $\mathbf{i}$ in the N-frame
x_{13}, x_{14}, x_{15} are the components or the direction cosines of the unit vector $\mathbf{j}$ in the N-frame
x_{16}, x_{17}, x_{18} are the components or the direction cosines of the unit vector $\mathbf{k}$ in the N-frame

Then the coupled differential equation in $\mathbf{x}$ is given by

$$\dot{\mathbf{x}} = \mathbf{D}(t, \mathbf{x}) \qquad \text{Equation (1-26)}$$

The function $\mathbf{D}(t, \mathbf{x})$ is a vector where each element is the time-derivative of the corresponding element in $\mathbf{x}$. Since these derivatives are completely known in terms of the elements of $\mathbf{x}$ through the equations (1-12)-(1-24), $\mathbf{D}(t, \mathbf{x})$ is a known function. The initial conditions for solving for $\mathbf{x}$ are given by the initial entry scenario where usually the incident velocity and initial angular velocity are known. Using these initial conditions, (1-26) can be solved completely using a Runge-Kutta algorithm. Thus, the kinematics of the rigid body is completely known in the user defined N-frame, and can be displayed for visual simulation of the penetration event.

Numerical Algorithms for Solving the Projectile Trajectory

Equations (1-14), (1-19) and (1-21) describe the differential equations of motion of the center of mass *G* (Figure 10), rotational motion of the body about the center of mass and the orientation of body fixed coordinates. These are (Figure 10):

- $\mathbf{X_G}$, the position vector of the center of mass *G* (Newtonian components),
- $\mathbf{V_G}$, the velocity vector of *G* (Newtonian components),
- ω, angular velocity vector of the projectile (Body-fixed component), and
- $\mathbf{i}$, $\mathbf{j}$, $\mathbf{k}$, unit vectors along the body-fixed axes (Newtonian components).

Since these are all vectors, we have a total of 18 independent time-dependent field quantities that are governed by coupled, nonlinear first order differential equations given in (1-14), (1-19) and (1-21). Using a standard Runge-Kutta algorithm for solving a system of first order, coupled nonlinear differential equations; we can obtain a complete solution of the problem of determining the wound tract due to a projectile motion in a body.

Application of the Runge-Kutta method requires that all derivatives of the variables described can be obtained from analytical, functions of all other variables. For problems involving location-dependent material properties in a user-defined, Newtonian frame, these locations need to be determined analytically from current values of these variables. This makes the problem very complicated since the location of any point on the projectile surface in a Newtonian frame not only depends on the location of the center of mass but also on the orientation of the unit vectors along the body-fixed coordinates. In the absence of location-dependent properties, the dimension of the unknown vector $\mathbf{x}$ in (1-16) can be significantly reduced from 18 to 6.

1.2 SIMULATION OF PROJECTILE TRAJECTORIES

For spheres and sphere-like projectiles with aspect ratio $\frac{L}{D} \approx 1$, the rotational kinematics of the problem is not significant, and hence the problem is simplified to tracking the motion of the center of mass. This is especially true during high velocity penetration except when the material properties vary significantly over the surface of the projectile boundary. This can create a significant moment about the center of mass.

1.2.1 Analytic Simulation of Projectile Trajectory for Platelet, L/D ≈ 0, and Non-Symmetric fragments, L/D ≈ 2.

Two types of projectiles have been considered in the numerical codes written and developed by ATK Mission Research for the determination of projectile motion inside a non-homogeneous target with known properties. For the case of *L/D ≈ 2*, we have used a cut cylinder as an example. The physical dimensions of the cut cylinder are shown in Figure 11. For the case of a platelet with *L/D → 0* we have used a circular plate. The code is correctly predicting the linear motion of a cut cylinder with *L/D ≈ 2* but the rotary motion is under-predicted. Some results are shown in Figure 12.

Due to the complex physics and associated numerical algorithms (described in detail below), we have developed the software in modular forms. Each module has been checked and the complete code has been developed by integrating these modules.

Material: Steel
Short Length L″ : 8 mm
Long Length L: 16 mm
Cutting Angle: 47 degrees
A schematic is shown in Figure 8.

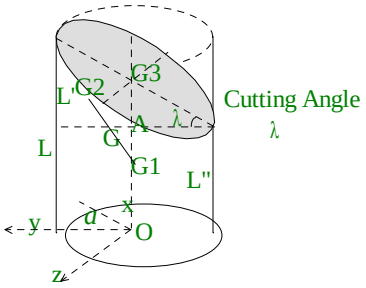

FIGURE 11. Schematic of ATK Mission Research "cut cylinder" projectile

1.2.2 Material Property Modeling

A number of published animal based Strain Energy Functions which have been derived from tissue property experiments were acquired by Mission Research. Stress-Strain relationships

suitable for use in the Mission Research wound Tract analysis and other codes can be derived from these functions. Several resulting stress-strain curves are shown in Figures 13 through 15.

Shown in Figure 13 is a uniaxial stress-strain curve of cardiac muscle from the myocardium of a human left ventricle in the direction of the fibers (*Strength of Biological Materials*, Yamada, 1970). It is noted that 1 gm/mm^2 is about 0.1 bar. Average values of failure strength are reported to be between 0.9 and 1.4 bars depending on age with an average of 1.1 bars. The ultimate strength in the transverse direction is about 1/3 of these values. The failure strains in the fiber direction vary between 63 and 79% with an average of 64%. The failure strain in the transverse direction is about 1.3 times that in the fiber direction.

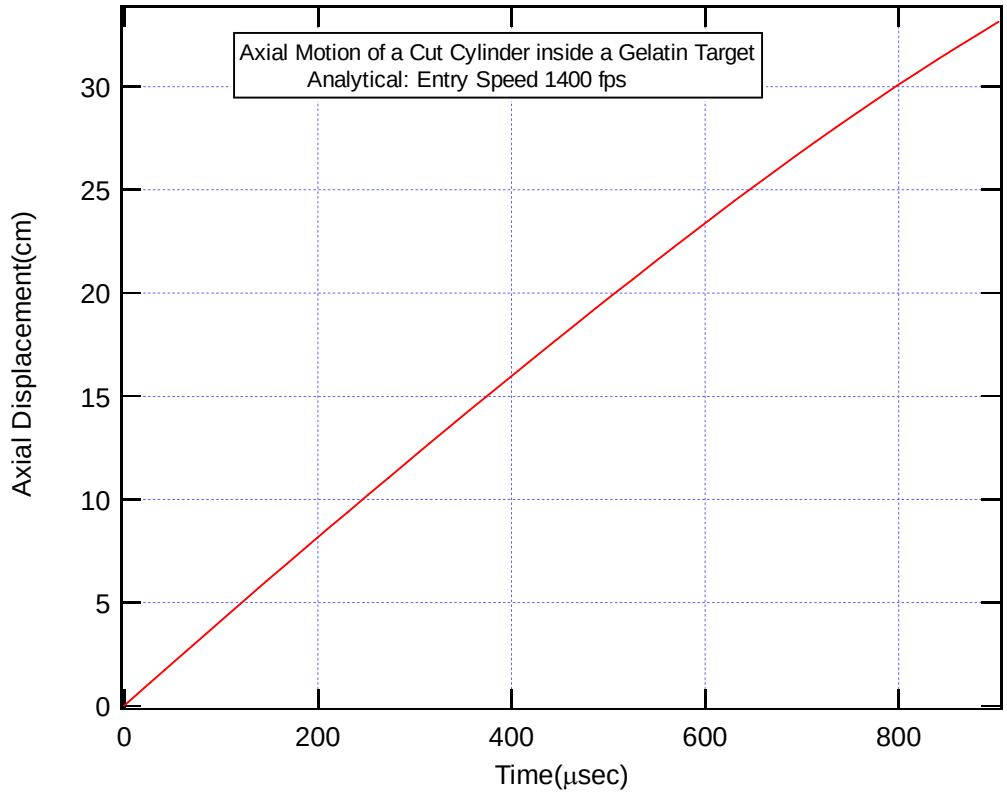

FIGURE 12. Analytical Prediction of Axial Displacement of a Cut Cylinder

Figure 14 is a plot of the stress-stretch ratio in the fiber and transverse directions based upon equal loading biaxial extension data. The fit to the data is based upon an assumed form of the controlling strain energy density function. This information was provided by Prof. McCullouch, Ph.D. from UCSD. It is noted that 10 KPa is 0.1 bars. Stress data in the fiber direction is shown to about 0.8 bars consistent with the values in Figure 13 although the corresponding biaxial strain level is calculated to be about 30%.

A plot of predicted circumferential stress in a human ventricular chamber is shown in Figure 15. The maximum value for the hypertensive case is about 8 KPa. The corresponding strain is about 64%. (*Mechanical Properties of Diseased Hearts During Adaptation*, Chaudhry, 2002).

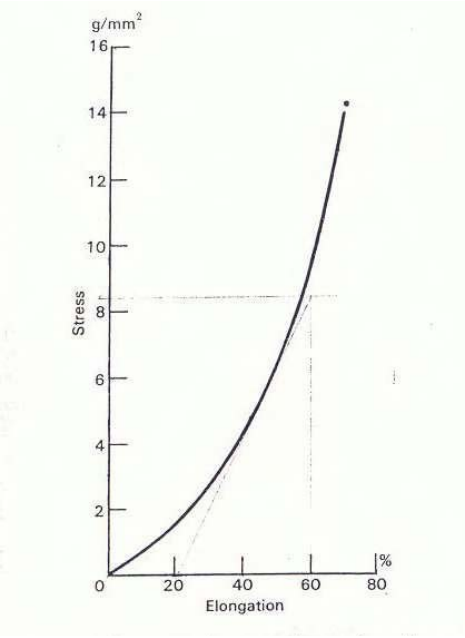

FIGURE 13. Tensile Stress-Stain of Cardiac Muscle on people 20 to 29 years old [Figure 82 from Yamata].

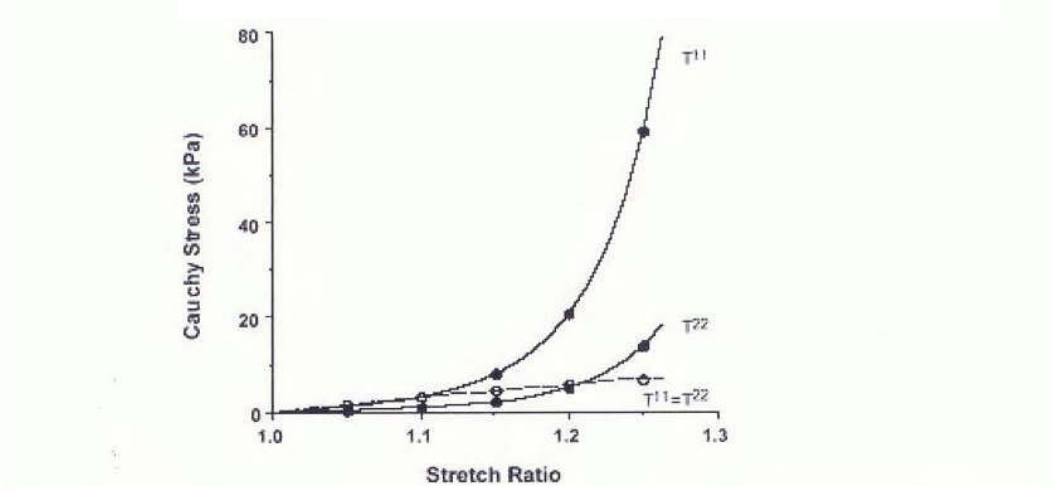

FIGURE 14. Analytic fiber stress and cross fiber stress versus stretch ratio for equibiaxial extension of thin rectangular sheet applicable to cardiac myocardium [original data from Costa et al. 1996 and application based on personal discussion with A. McClulloch/UCSD].

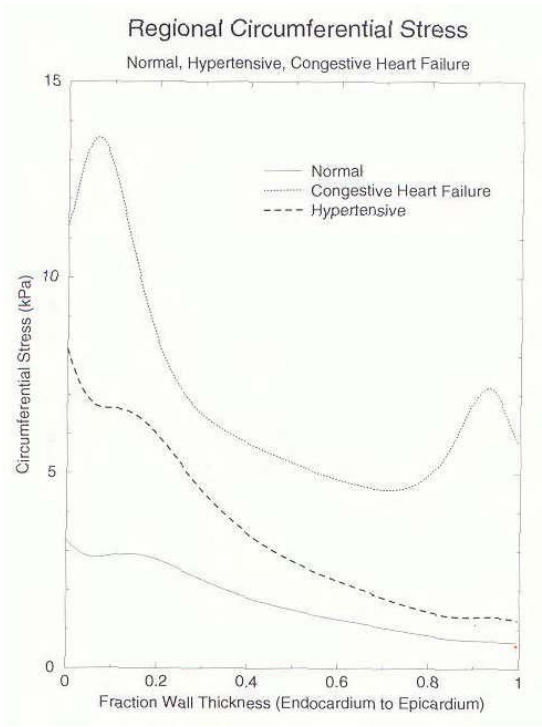

FIGURE 15. Stress versus Ventricular Wall Thickness [from Chaudry]

Human myocardial tissue can be described as a hyperelastic, anisotropic material with principal properties varying in the 'fiber' and 'cross fiber' directions. UCSD has been involved in a number of efforts associated with modeling heart component response and has assembled a library of Strain Energy based constitutive models which have been implemented in the UCSD *Continuity* code. The majority of the existing data is based upon uniaxial and biaxial tension tests which is appropriate for normal expansion. It must be noted that the principal early time stress generated during impact and penetration are compressive and thus compressive data is ultimately needed to verify predictions.

For the purposes of the current effort, UCSD recommended that a Canine based Transversely Isotropic Exponential Strain Energy function be used to derive the required Stress-Strain relations which are currently used as input to the ATK-Mission Research hydrocode models. The orientation of the fiber/cross fiber 'sheets' are known as a function of thickness through the ventricle and can be implemented as required. The properties are known to depend on a number of parameters including moisture content and loading rate but the data base focuses on static loading derived properties.

A typical derived stress-strain relation is plotted in Figure 16. It is seen that failure strengths are very low, on the order a bar. The forms of the constitutive models are given in Table 3.

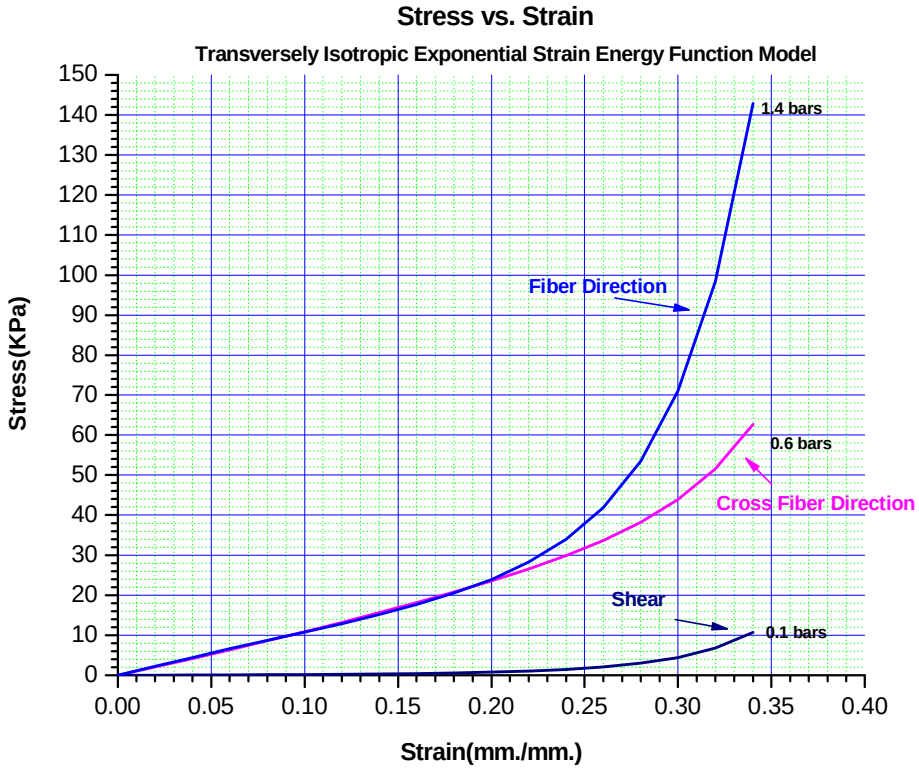

FIGURE 16. Myocardium Stress-Strain Relation

TABLE 3. Simplified Material Models

Structure	Constitutive Model	Strength Model	Failure Model	Anisotropy
Pericardium	Linear	Yield	Strength	NA
Myocardium	Puff	Yield	Strength	Yes
Heart External	Puff	Elastic	Strength	Future
Blood	Shock	None	None	NA

Parameter Sensitivity Studies

A series of 2D hydrocode parameter sensitivity studies were performed modeling gelatin impacts. The shear modulus and material strength were varied. Typical results of penetration depth versus time are shown in Figure 17. A more detailed discussion of the results from this study is included in Appendices H and I. The 2D hydrocode analysis supporting the material parameter sensitivity

studies was performed using (i) a linear elastic heart tissue model, (ii) a half scale MRC wedge fragment, and (iii) a series of thin platelet fragments impacting normal to the target surface.

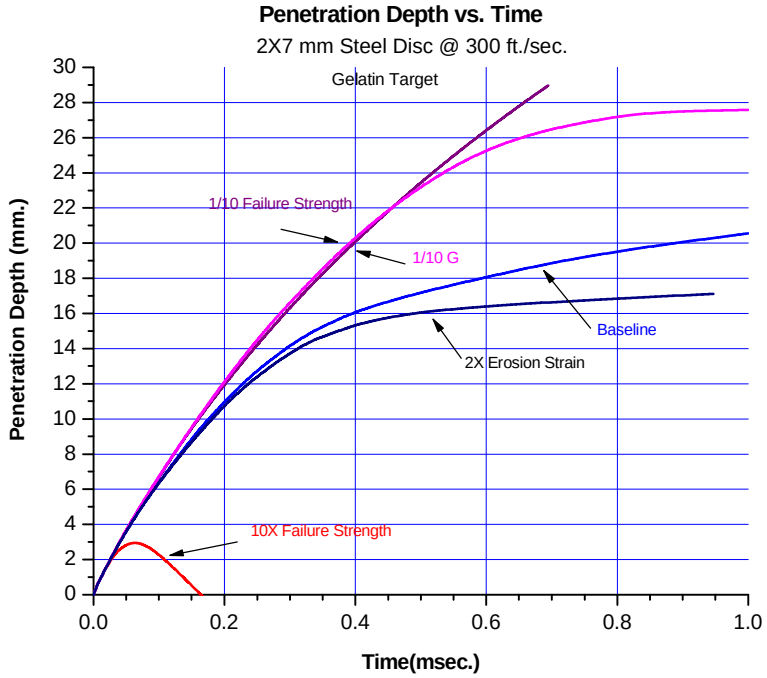

FIGURE 17. Penetration Depth of Platelet Fragment versus Time

As mentioned in Section 1.1.3,the slides on page 284 from the presentation reproduced in Appendix N show a very favorable correlation between cut-cylinder rotational kinematics observed experimentally using high speed digital video and the analytical simulation developed as described in this section.

1.3 ANALYTICAL BACKGROUND OF PENETRATION OF A FRAGMENT INSIDE A GIVEN TARGET WITH NONHOMOGENEOUS MATERIAL PROPERTIES

For modeling the complex, dynamic process of fragment penetration in a given target, we need to understand the mechanical properties of both the target and the fragment, that are responsible for the retardation forces exerted on the projectile during penetration. Some simple analysis are done first where the projectile has simple shapes e.g., a sphere in a target with no material inhomogeneities. Ballistic experiments conducted by Mission Research during the last few years provide us an experimental database on small spherical steel balls, spherical balls of other sizes and cut cylinders penetrating a uniform 20% gelatin used as a tissue-simulant. For various incident velocities, the penetration depths were recorded during these experiments. By using the equation of motion of a rigid body assuming that the projectile does not deform during penetration, we inverted the penetration depth versus incident velocity data to yield the penetration coefficients described in previous quarterly reports for this project. The fundamental equations used in the inversion are repeated below.

$$m\upsilon\frac{d\upsilon}{dx} = -R(\upsilon) = -\left(\alpha + \beta\upsilon + \gamma\upsilon^2\right)$$
$$\delta(\upsilon_s) = \int_0^{\upsilon_s} \frac{m\upsilon}{R(\upsilon)}d\upsilon \qquad \text{Equation (1-27)}$$

In (1-27), m is the projectile mass, υ is the instantaneous velocity of the projectile at a depth x during penetration; α, β, γ are the retardation coefficients, and $\delta(\upsilon_s)$ is the penetration depth for incident velocity υ_s. For the experimental data, penetration depth vs. velocity is shown in Figure 18, and the calculated retardation coefficients per unit mass are

$$\alpha := 4.049\,10^4 \qquad \beta := 52.47 \qquad \gamma := 0.048$$

Thus the equation of motion, first Equation in(1-27), is modified as

$$\upsilon\frac{d\upsilon}{dx} = -R(\upsilon) = -\left(\alpha + \beta\upsilon + \gamma\upsilon^2\right) \qquad \text{Equation (1-28)}$$

In (1-28), α, β, γ are the retardation coefficients per unit mass of the reference projectile.

Retardation coefficients derived from experimental data on 20% gelatins, need to be modified for applications to other projectiles of different shapes and masses. For finite size bodies with multiple boundary areas, we assumed that load per unit differential area can be determined from the retardation laws established for the reference spherical projectile by proper scaling of area and mass. Since increasing projectile mass indicates more kinetic energy available for penetration, retardation coefficients are modified by a factor of $\frac{m_r}{m}$ where the subscript r indicates reference projectile mass which is the BB-mass in this case. Note that mass scaling is inversely proportional for modifying the retardation coefficients. For surface scaling, the load on an elementary area dS is calculated by multiplying the retardation coefficients by a factor of $\frac{dS}{S_r}$ where S_r is the projected area of the reference projectile on the target surface.

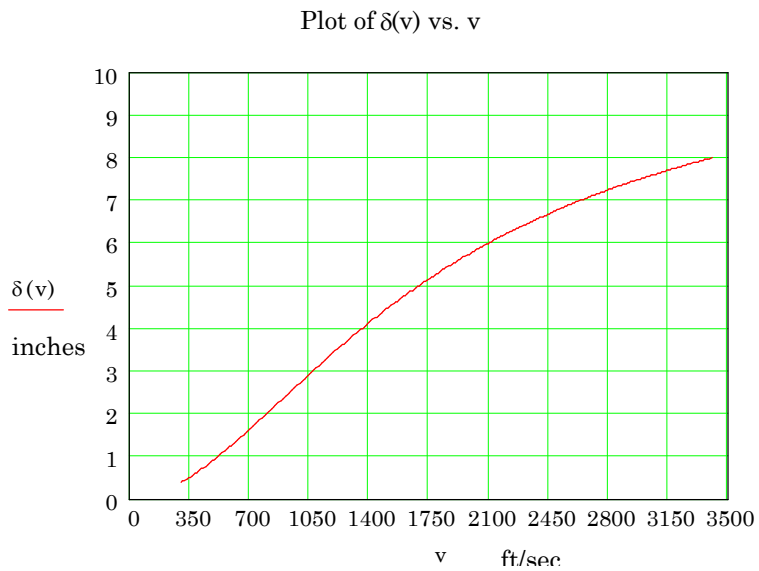

FIGURE 18. Experimental Data: Penetration depth vs. Entry Velocity

For our applications, the problem of the penetration mechanics of a general shaped projectile e.g. a fragment/cylinder/sphere or sphere-like, in a nonhomogeneous human left ventricle is considered. Since the experimental data is obtained for a homogeneous 20% gelatin target, some material scaling is also required. To include the inhomogeneity in material properties on retardation forces, we need to relate the retardation coefficients to the associated physics of the retardation process. For very low impact velocities, static properties of the projectile-target dominate the process. For a rigid projectile, the relevant material property is the Young's modulus of the target. Thus the low-velocity coefficient α is scaled with $\frac{E}{E_r}$ where E is the Young's modulus of the target at the instantaneous contact location of the elemental area dS at time t. The coefficient β is related to the Stoke's friction drag so that it depends linearly on viscosity, and hence on the shear modulus G for harmonic loading. Thus, β is scaled with $\frac{G}{G_r}$. Finally the last term is the fluid drag term related to the density ρ of the target, and hence γ is scaled with $\frac{\rho}{\rho_r}$.

Besides the above scaling laws applied on the retardation coefficients, we also assume that target resistance is always along the inward normal to the surface of the projectile when the projectile velocity is along the outward normal to the projectile surface; otherwise, the retardation force is zero.

TASK 2

WOUND TRACT MODELING AND SIMULATION

This task evolved during the course of the program and bifurcated into two discrete sub-efforts. In the first effort, a nonlinear stress wave propagation model was developed emphasizing ballistic impacts that partially penetrated the human left ventricle. A geometry model of the heart was acquired and discretized into a numerical grid by Stanford University. Material properties were mapped on the numerical grid with the help of the Bioengineering Institute at the University of California in San Diego (UCSD) using the UCSD *Continuity Code*. Stress wave analysis was then conducted by ATK Mission Research using the Autodyn® software package employing various projectiles shown in Figure 1 (page 9). Parameter sensitivity studies were also conducted to understand the appropriate model fidelity for various model features. This effort is discussed in Section 2.1.

The second effort, discussed in Sections 2.2 and 2.3, involves developing a nonlinear spring lattice calibrated to intervening soft tissue properties. The trajectory and velocity retardation models developed in Task 1 are used to cut the springs and impart a velocity vector to the springs as initial conditions. The initial cutting and recoil of the spring lattice plus the subsequent dynamic transient and associated accumulated plastic strain from spring hysteresis establishes the residual diameter of the wound tract. The resulting wound tract is then imported into SCIrun (a scientific visualization tool developed by the University of Utah) for visualization. A SCIrun interface was written for this purpose by ATK Mission Research with the help of the University of Utah *Scientific Visualization Center of Excellence*. This visualization effort is discussed in Section 2.3.3.

2.1 CONSTITUTIVE AND HYDROCODE MODELING

3D models nonlinear dynamic models where developed to allow prediction of the wound tract trajectory, tract dynamics, and stress-strain fields for a human left ventricle penetrated by both a wedge-like and small cylindrical fragment impacting normal to the ventricle surface. In order to perform this analysis, we developed: (1) constitutive models for the pericardium, myocardium and ventricle core, (2) a 3D finite-difference model of the ventricle and projectiles, and (3) a 3D finite-difference model approximating cardiac structures attached to the left ventricle. A range of impact velocities were analyzed in order to ensure that the projectiles slowed to essentially zero velocity in the 'blood' filled central cavity. The output of this effort were animations of the above parameters for a ventricle penetrated by a (1) 7-mm, 45 degree steel wedge impacting at 250 ft/sec. and (2) a 3-mm, steel circular cylinder impacting at 300 ft/sec. both with aspect ratios of 1.

2.1.1 Ventricle Model

In order to perform the desired penetration analysis, a realistic representation of the human left ventricle geometry was required. We obtained a detailed geometry model from Stanford University that was translated by the University of Utah. We went thru a process of 'smoothing' the surfaces and then asked XYZ corporation via its *True Grid*® mesh development program to develop a mesh suitable for input in the Century Dynamics Autodyn™ 3D hydrocode. The pericardium, myocardium and cavity were then filled with approximations to the actual material properties for the Phase I demonstrations.

A procedure similar to that above was used to develop a 'Heart Envelope" so that we could account for the influence of the material surrounding the Ventricle on the Ventricle mechanical response. In order to do this, we relied on a University of Utah supplied porcine heart representation. We were advised that to first order, the size and basic geometry would satisfy our 'Heart Envelope" needs. A picture of the meshed model is shown in Figure 19. Details of the interior mesh are shown in Figure 20.

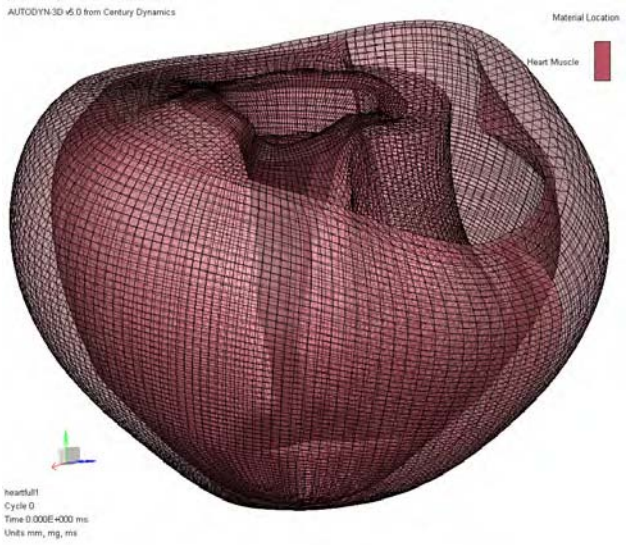

FIGURE 19. Simulate Heart with Embedded Ventricle Finite Difference Mesh

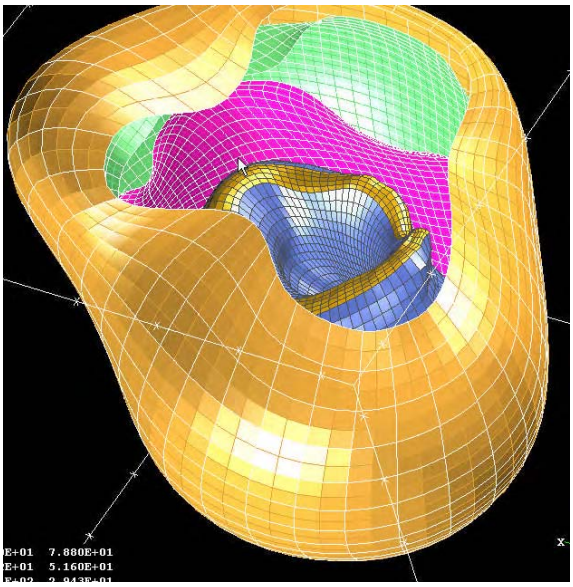

FIGURE 20. Interior Mesh for Embedded Ventricle Model

2.1.2 Wedge Impact Analysis

The first set of analysis was intended to capture behavior of a wedge shaped fragment similar to the one which had been used by ATK-Mission Research both during its gelatin phenomenology ballistic experiments and in several experiments at ISR. Two aspect ratio fragments were used, the first corresponding to that used in the tests and a second with an aspect ratio of 1:1 which was designed to reduce the size of the cavity and the deviation from a linear trajectory. Several impact velocities in the range of 50 to 300 ft/sec were analyzed with the intent of having the projectile stop in the central cavity of the ventricle without penetrating the cardiac septum. The appropriate striking velocity on the ventricle to achieve this was 250 ft/sec. Shown in Figures 21 though 24 are snapshots of the original impact geometry, the external pressure distribution as waves propagate along the surface, the internal pressure distribution and the internal strain. It is worth noting that the pressure generated exceeds 14 bars (over a fairly large volume) which is the level established from previous ATK-Mission Research in vitro testing, necessary to create mechanically induced transient ion gradient upsets.

The results from this analysis were animations which were delivered to the Virtual Soldier team at the University of Michigan as well as the projectile trajectory, cavity dynamics, stress and strain fields.

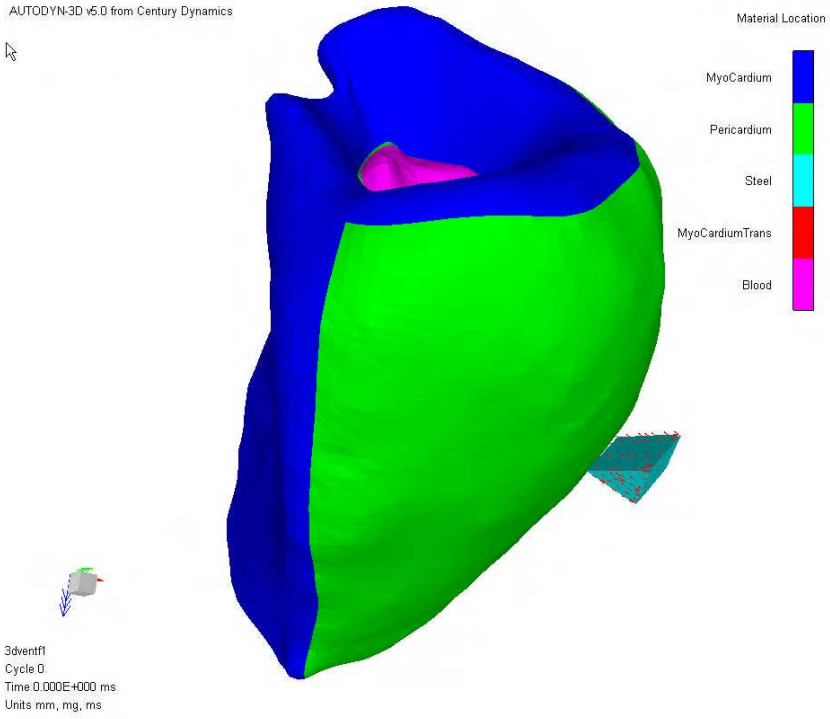

FIGURE 21. Impact Geometry for Wedge Impact of Ventricle

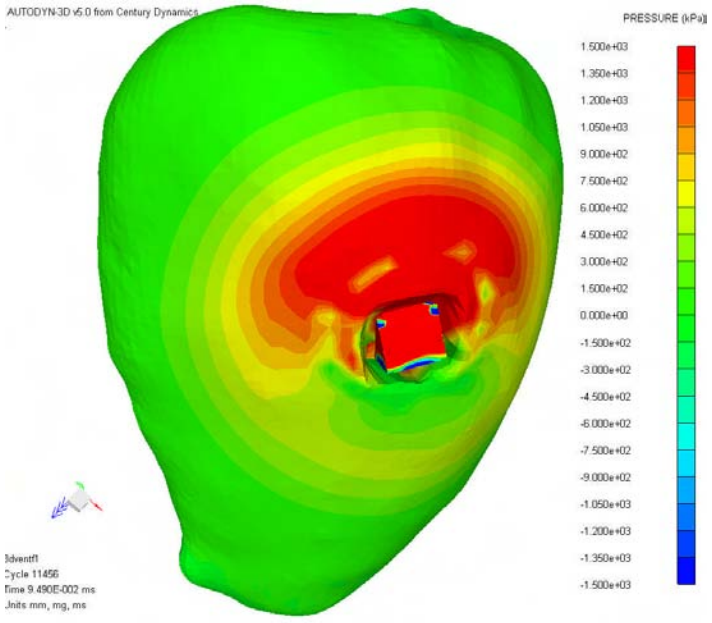

FIGURE 22. Pressure Distribution on Surface of Ventricle from Wedge Impact

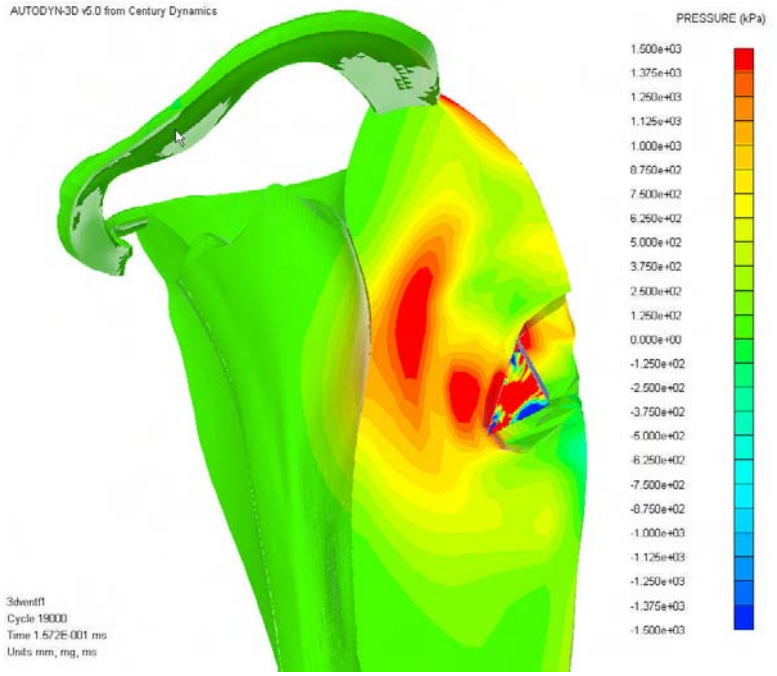

FIGURE 23. Pressure distribution in Interior of Ventricle from Wedge Impact

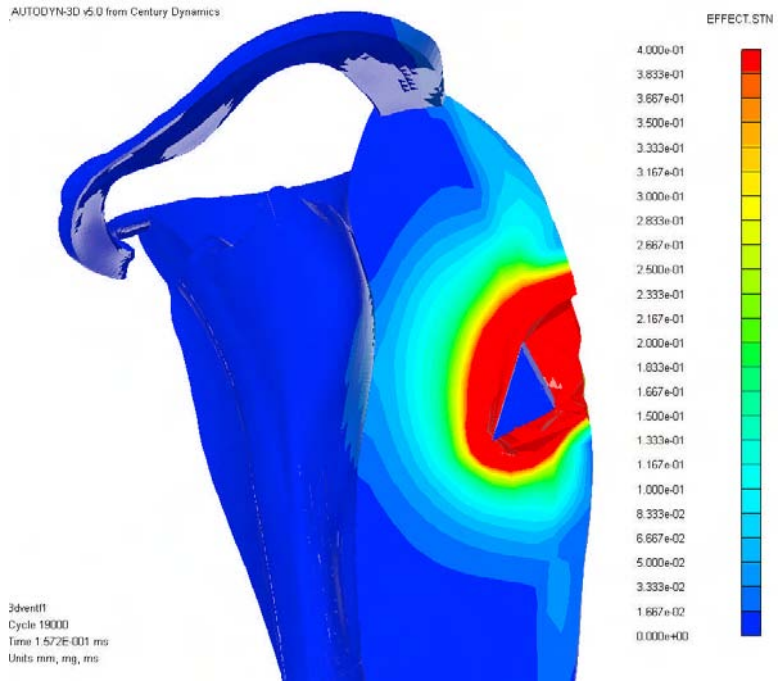

FIGURE 24. Strain Distribution in Interior of Ventricle from Wedge Impact

2.1.3 Cylinder Penetration Model

The final set of analysis was intended to simulate a hypothetical projectile which would: (1) create an approximately 4-mm diameter permanent entrance cavity, (2) a 1 to 2-mm diameter permanent exit cavity on the interior of the ventricle, (3) have the trajectory of the fragment follow a linear path, and (4) have the fragment stop in the blood filled central ventricle cavity without penetrating the septum. In order to accomplish this, we analyzed the response of various diameter circular cylinders all with aspect ratios of 1 traveling at various velocities. The final design was a 3-mm diameter steel cylinder traveling at 300 ft/sec. Shown in Figures 25 though 28 are snapshots of the original impact geometry, the pressure distribution on the ventricle surface, the internal strain distribution and the internal wound tract.

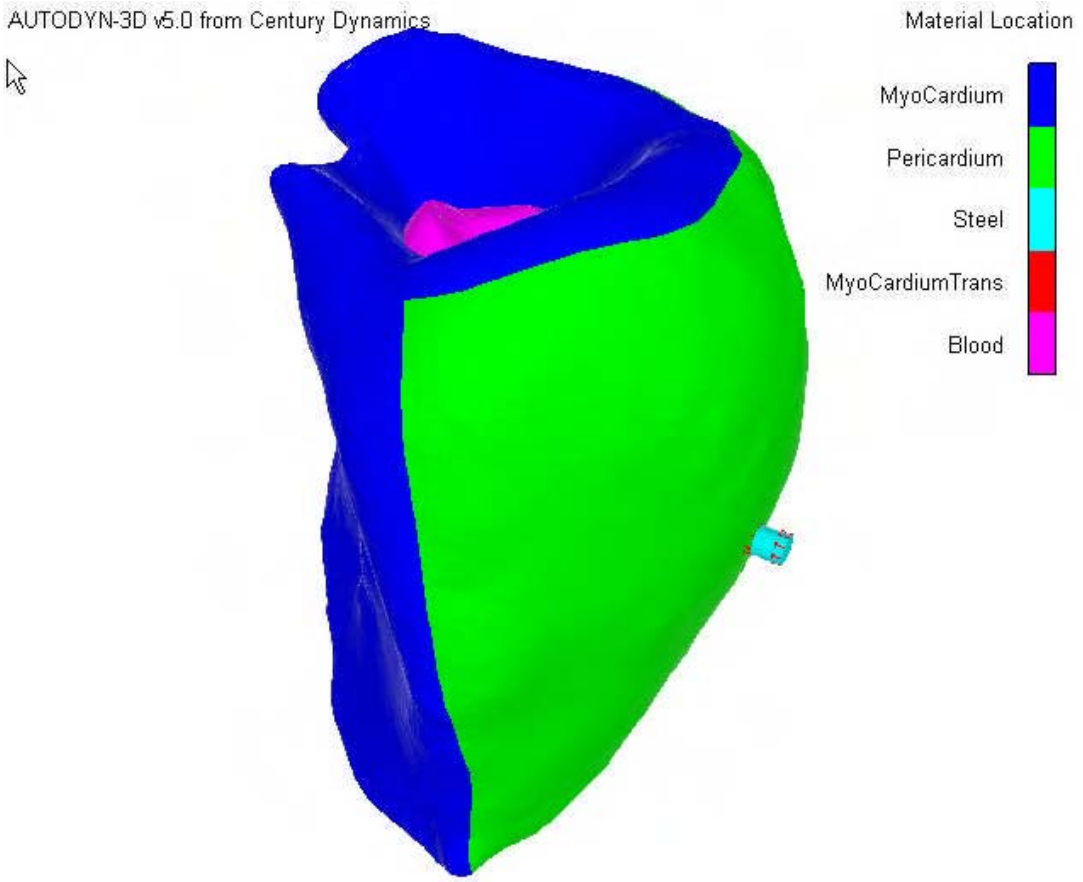

FIGURE 25. Impact Geometry for Cylinder Impact of Ventricle

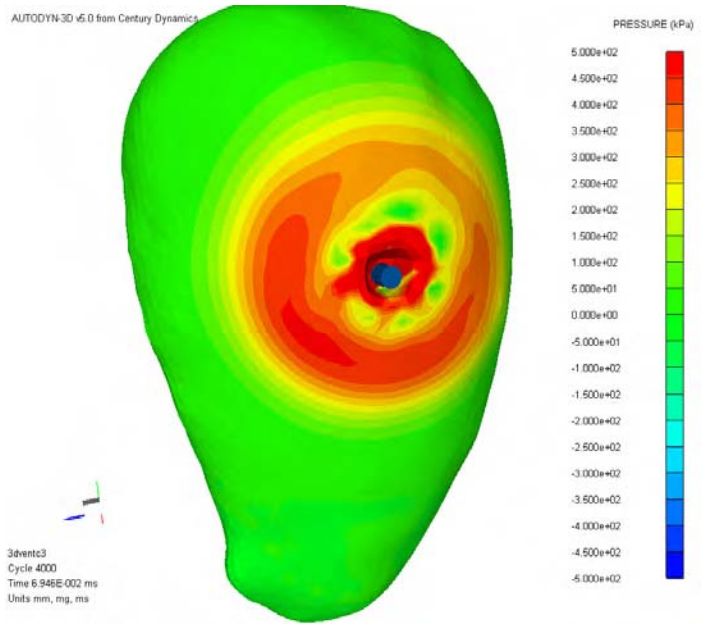

FIGURE 26. Pressure Distribution on Surface of Ventricle- Cylinder Impact

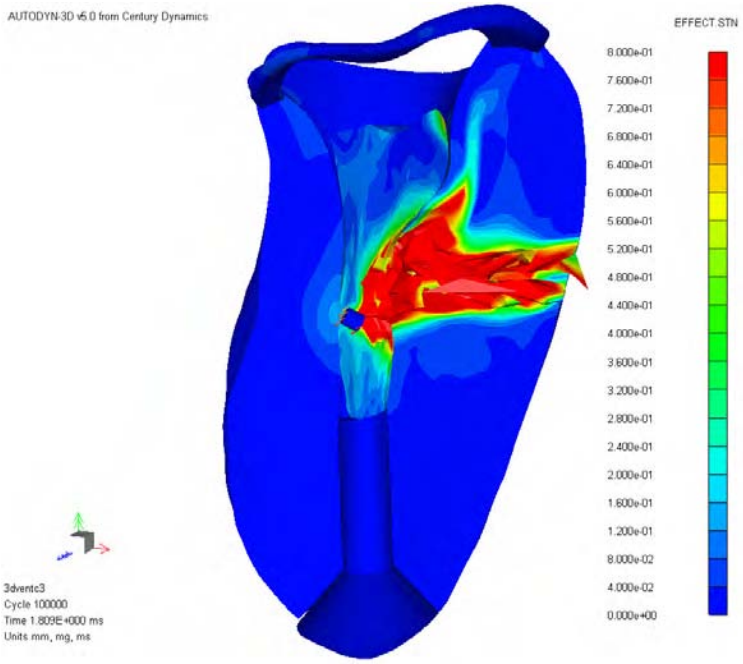

FIGURE 27. Strain Distribution in Interior of Ventricle from Cylindrical Projectile Impact

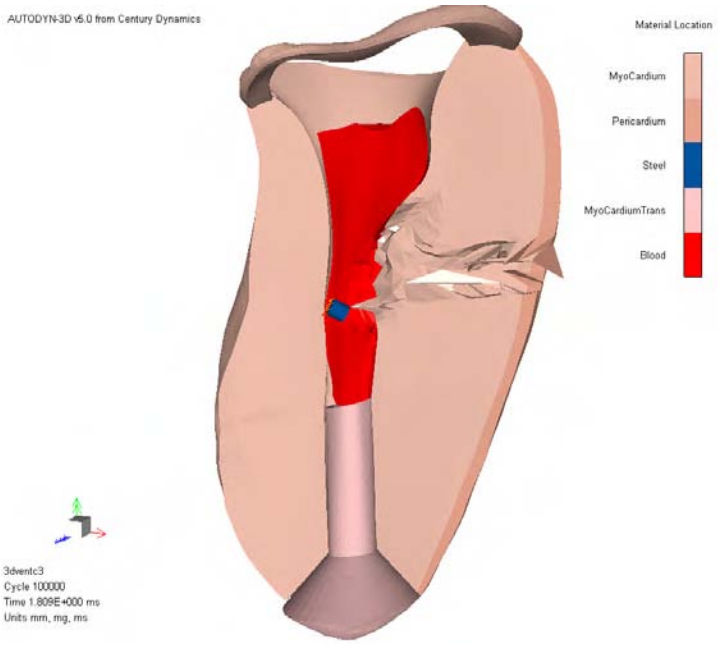

FIGURE 28. Wound Track- Cylinder Impact

2.2 ANALYTICAL DETERMINATION OF WOUND TRACT GEOMETRY

When a projectile penetrates a given target, various parts of the surface of the projectile encounter materials with varying properties. We divide the motion of the projectile inside a target into two parts; we first determine translation by tracking the motion of the center of mass *G* of the projectile and then determine the angular rotation of the projectile due to the associated moments of surface loading about *G*. The relevant equations of motion for both these motions are given by

$$m\frac{d\mathbf{v}}{dt} = \sum_{i=1}^{N}\int_{S_i}\mathbf{F}_{ni}dS \text{ (uniquely determines the motion of G)} \qquad (2\text{-}1a)$$

$$\sum M_x = I_{xx}\dot{\omega}_x - (I_{yy} - I_{zz})\omega_y\omega_z$$
$$\sum M_y = I_{yy}\dot{\omega}_y - (I_{zz} - I_{xx})\omega_z\omega_x \qquad (2\text{-}1b)$$
$$\sum M_z = I_{zz}\dot{\omega}_z - (I_{xx} - I_{yy})\omega_x\omega_y$$

In (2-1a), $\mathbf{v}$ is the velocity vector of G and N is the total number of projectile surfaces with geometric discontinuities, and the subscript n indicates that the force $\mathbf{F}$ is along the inward normal to the projectile surface at the elemental area dS. For example, in the case of a cylinder $N = 3$ which represents three surfaces of geometric discontinuities with two flat surfaces and one curved surface. In the case of a sphere $N = 1$ as we have only one smooth curved surface. In (2-1b), I is the moment-of-inertia matrix about G and $\mathbf{M}$ is the moment vector of all surface loading about G. Overhead dots indicate time derivative.

In a fully three-dimensional problem with material inhomogeneities, equation (2-1) represent a nonlinear, coupled, second order differential equations in 15 unknown variables; six components of displacement and velocity, three components of angular velocity, six independent components of body-fixed unit vectors for Newtonian description of body-fixed coordinate system. Theses equations were solved using the MATHCAD™ code. In the associated MATHCAD code, these are included in a single 15-element vector $\mathbf{x}$ defined as follows. In the following, F-frame indicates body-fixed frame while N-frame is the Newtonian frame.

TABLE 4

Physical Description of x-elements:

x1-x3: Center of Mass G in N-frame (inch)
x4-x6: Velocity of G in N-frame (ft/sec)
x7-x9: Components of Angular Velocity in F-frame (rad/sec)
x10-x12: Components of unit Vector along Gx in N-frame (Nondimensional)
x13-x15: Components of unit Vector along Gy in N-frame

The resulting equations can be solved using built-in Runge-Kutta algorithm in MATHCAD.

2.2.1 Accessing material property from material database

The material property database is known in a Newtonian N-frame. Since the retardation force is a function of material properties at the contact point with the target, coordinates of the contact point are needed during the solution of the nonlinear differential equations. This is done by tracking three orthogonal axes fixed in the projectile, and including six independent differential equations describing the time rate of change of these axes as a function of time. These are the

components x10-x15 described above in Table 4. Only six components are included since the third one can be found from mutual orthogonality conditions of these axes.

2.2.2 Two-Dimensional Version of the Wound Tract Geometry

For some problems when the lateral variation in material inhomogeneities is small or nonexistent, the above problem of determining the wound tract geometry is much simpler. In this case, the resulting problem is two-dimensional, and can be reduced to the determination of only three variables; two for the displacement component of the center of mass *G* and one for the rotation of the body about the z-axis assuming that the motion takes place on the $xy-$plane. The first equation (2-1a) remains unaltered while second equation is simplified to only one equation [by substituting $\omega_x = 0 = \omega_y$ in (2-1b)]

$$\sum M_z = I_{zz}\dot{\omega}_z \qquad (2\text{-}2)$$

These equations can also be solved easily using a Runge-Kutta algorithm.

2.2.3 MATHCAD™ Coding

Both three- and two-dimensional versions of the above nonlinear equations have been coded using the built-in MATHCAD Runge-Kutta algorithm. MATHCAD applicability is somewhat limited since it does not allow access to global variables during the time domain solution once inside the Runge-Kutta module. Thus all functions describing the derivatives of the components x1-x15 are written as stand-alone functions of the x1-x15 with no other dependency on external or global MATHCAD variables. This made the code more complex but if the software is subsequently converted to C, C++ or Fortran languages, these limitations will be eliminated. However, MATHCAD allows us to write and debug the code easily as all equations are written exactly as they are in their respective mathematical forms.

Three types of projectiles are considered for analysis; these are selected on the basis of various aspect ratios, $\frac{L}{D}$ of the projectiles where L is the length and D is the equivalent diameter of the lateral area of the projectile. Cases of very low aspect ratio includes flat projectiles like platelet (Class-I), aspect ratios of approximately one like sphere or spheroid and sphere-like projectiles (Class-II), aspect ratios of more than one like cylinder and cut-cylinder(Class-III). These projectiles are shown in Figure 29.

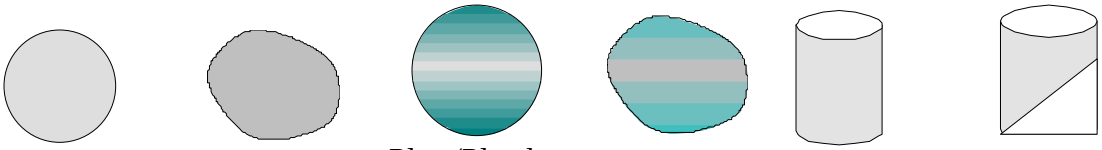

Sphere/Sphere-like Plate/Platelet Cylinder/Cut Cylinder

FIGURE 29. Projectiles of various aspect ratios $\frac{L}{D} \approx 0{,}1$ and >1

The output of the MATHCAD code are the temporal distributions listed below.

- The displacement components of the center of mass G
- The velocity components of G
- The angular rotation components of the projectile about G
- The angular velocity component of the projectile about G
- The orientation of all three body-fixed axes in space

An Example

Out of many cases we analyzed using the MATHCAD developed codes under this program, one example closely related to the demonstration presented in March, 2005 at the University of Michigan during the 5th quarter VSP IPR. The projectile belongs to class III which is a cut cylinder. The geometric dimension and material properties are shown below. Length units are in millimeters (mm), velocity is in ft/sec(fps). The striking Velocity is 200 fps and the input data to the MATCHCAD coded module is shown below.

Wedge Data

Base Diameter $D := 7.0\ mm$ Convert to cm $D := \frac{D}{10}$ Base radius $a := \frac{D}{2}$ $a = 3.5 \times 10^{-1}$

Density $\rho := 8.0\ gm/cc$

Cylinder Length $L := 7.0\ mm$ Convert to cm $L := \frac{L}{10}$ $L = 7 \times 10^{-1}$

Cutting Angle $\lambda := \operatorname{atan}\left(\frac{L}{D}\right)$ $\lambda d := \lambda \cdot \frac{180}{\pi}$ $\lambda d = 4.5 \times 10^{1}$ deg

Wedge Mass mass $m := \pi \cdot \frac{D^2}{4} \cdot \frac{L}{2} \cdot \rho$ gm $m = 1.07757 \times 10^{0}$

The output of the MATHCAD code for this case ate the temporal distribution of the various field quantities, and is shown in Figure 30.

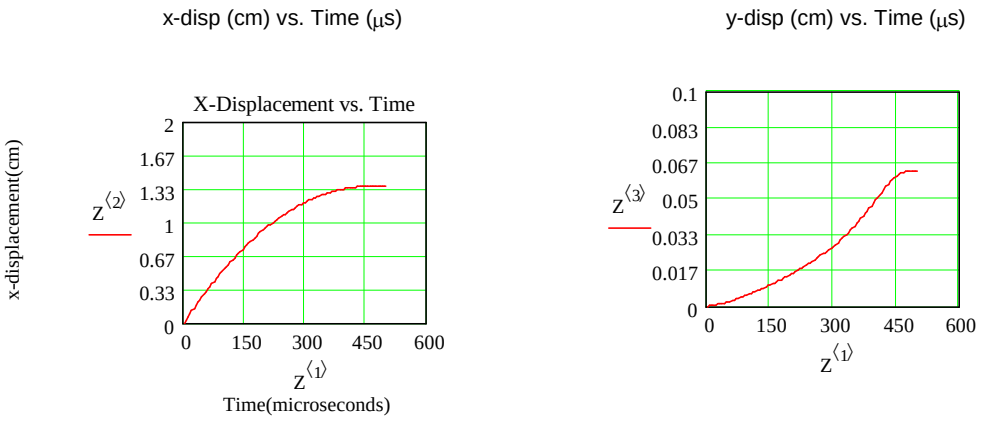

FIGURE 30A. Displacement of the Projectile Center of Mass G

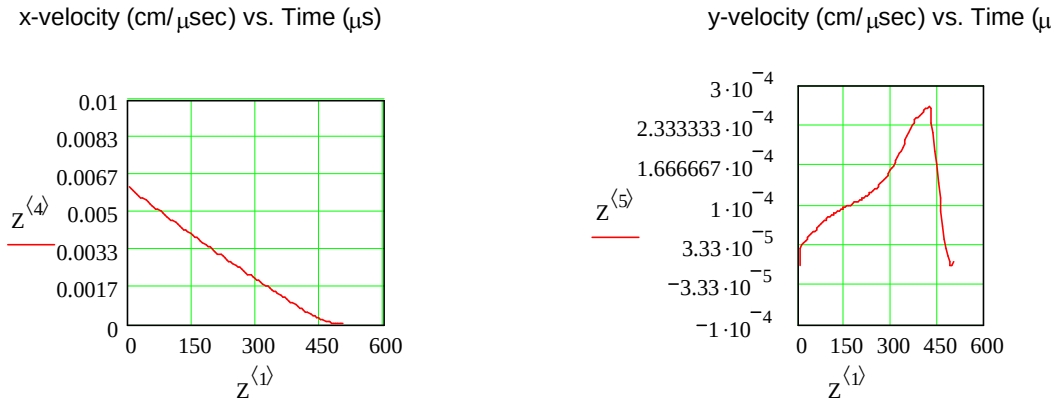

FIGURE 30B. Velocity Components of the Projectile Center of Mass

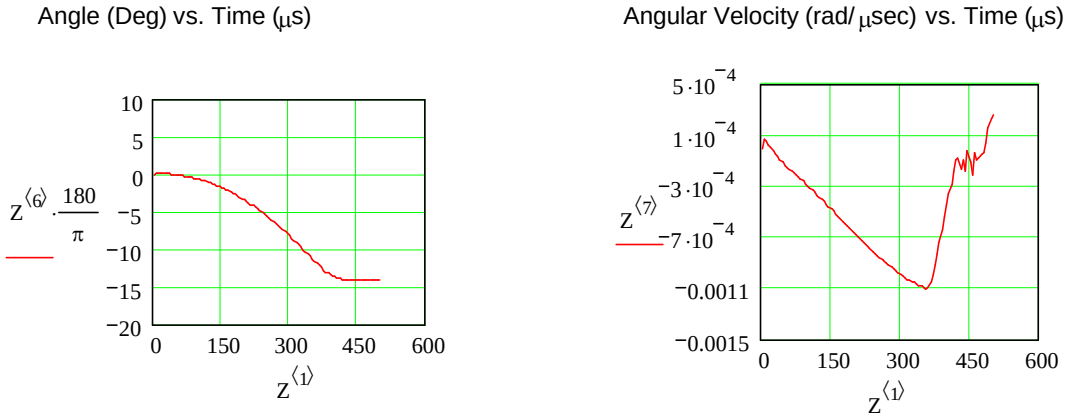

FIGURE 30C. Angular Rotation and Angular Velocity

Initial Cavity formed by Wedge
mm vs. μsec

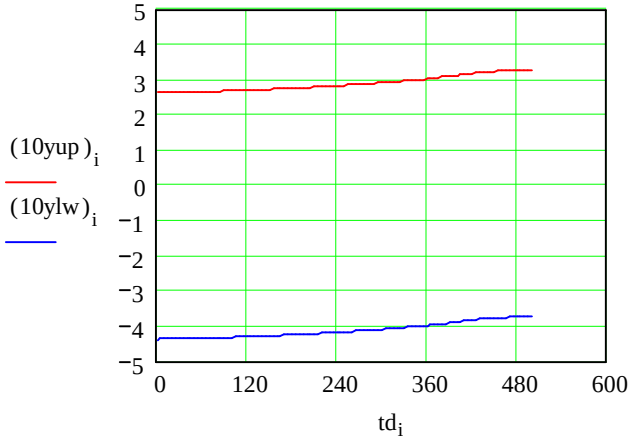

FIGURE 30D. Initial Cavity Formed by Wedge

Comparing these results with experimental data and hydrocode results, we find that the x- and y-components of both displacement and velocity of the center of mass *G* of the cut cylinder are in good agreement. No experimental data is available for the angular velocity of the projectile while the rotation of the projectile as a function of time is in good agreement for about 200-250 microseconds of penetration but the experimental results shows a decrease in angular rotation beyond this time. Our model does not show this decrease. This discrepancy is possibly due to the fact that the target material tends to separate from the projectile surface as it penetrates which is a phenomenon that is not understood completely and hence is not modeled in our analysis. Such separation does not significantly decrease the components of the total retardation force, but their moments about the center of mass of the projectile changes appreciably. This may introduce accumulated error in the predicted rotation of the projectile.

2.2.4 Determination of Initial Cavity Shape from Experimental/Analytical Data

For the case of a cut cylinder or wedge, we may determine the initial cavity shape by tracking four key points on the projectile. These points are shown in Figure 31.

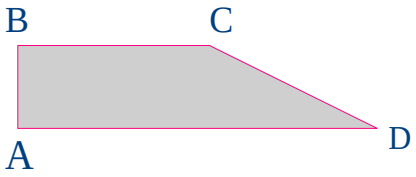

FIGURE 31. Key points of a cut cylinder

For two-dimensional motion, the intial cavity shape can be formed by an upper trace and a lower trace. If the time domain coordinates of these key points are known, the upper and lower trace is given by

$$y_{upper} = Max(y_A, y_B, y_C, y_D)$$
$$y_{low} = Min(y_A, y_B, y_C, y_D)$$

Both analytical and experimental results van be used to find the time domain coordinates of the center of mass and the orientation of the central axis of the projectile. These data can then be mapped to generate the time domain coordinates of these key points.

Properties used for the cut-cylinder penetrating a 20% gelatin block with a speed of 200 fps are shown below, and the intital initial cavity calculated from the above method is shown in Figure 32.

Cylinder Data

Base Diameter $D := 7.4$ mm Convert to cm $D := \frac{D}{10}$ Base radius $a := \frac{D}{2}$ $a = 3.7 \times 10^{-1}$

Density $\rho := 8.0$ gm/cc

Long Lengh $L := 16.0$ mm Convert to cm $L := \frac{L}{10}$ $L = 1.6 \times 10^{0}$

Short Lengh $L2 := 8.0$ mm Convert to cm $Lp2 := \frac{L2}{10}$ $Lp2 = 8 \times 10^{-1}$

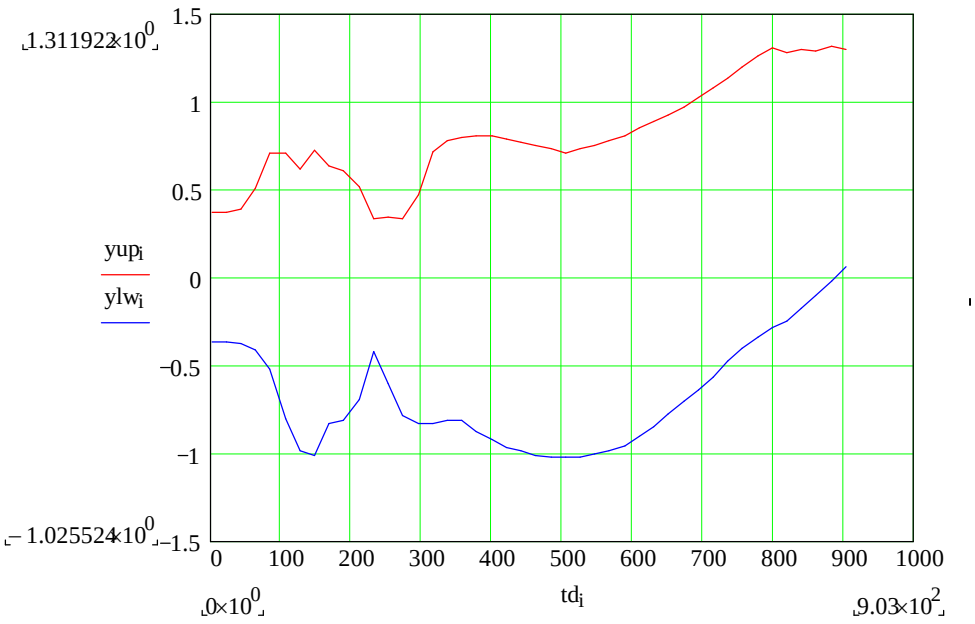

FIGURE 32. Intial Cavity Shape of a Cut Cylinder

2.2.5 Simplified 2D Plane-Strain Axisymmetric Model Parameter Studies

The penetration of a fragment/bullet like projectile thru a human chest and into the heart results in tissue response which is at least non-linear from a constitutive behavior point of view and creates large displacements in the neighborhood of the projectile. In order to explore these effects, a series of analytical continuum models and 2/3D hydrocode models were created where variations on fragment geometry, tissue material properties, property inhomogeneity and impact

conditions were explored. The results from these sensitivity studies are discussed below and in Appendices B and C. These sensitivity studies are being used to guide subsequent development of analytic models which will be the basis for the predictive tools employed at the end of the Phase I portion of the Mission Research Virtual Soldier program.

Three 2D plan-strain axisymmetric models were created using modal analysis. In the first model a cylindrical annulus was created. Two different forcing functions were applied to the inner wall of the annulus. In the first case a pressure was prescribed and in the second an initial velocity corresponding to the pressure employed in the first case. As shown in Appendix C there was minimal difference in applying these two different types of forcing functions. The model was then used with a mixed boundary condition; i.e., an initial velocity was prescribed followed by a pressure release boundary. The results for this simulation are shown in Appendix C.

A second model was developed to explore radial variations in Young's modulus. In one case a series of annuli were used with each annulus having a different modulus. The outermost annulus had a modulus that was a factor of two higher than the inner annulus. In this case, where there was a rather gradual radial variation in moduli, a significant difference in dynamic response was not seen and in general was proportional to changes in the sound speed of the intervening material. However, when the modulus was varied to the same extent but in a discontinuous manner ($\Delta E \approx 60\%$) peak pressures changed by more than 40%. Results for this simulation are also shown in Appendix C.

A third model was developed to examine inhomogeneities that varied in a circumferential manner. This was seen to have the biggest effect due to the development of shear forces at material property interfaces. This is discussed in more detail in Appendix B.

Finally, selected results from the plane-strain analysis above were compared with a 2D axisymmetric model implemented within a hydrocode where the plane-strain assumption was not employed. Surprisingly, these two models yielded similar results as shown in Appendix C.

2.2.6 2D/3D Hydrocode Models

A number of additional hydrocode models were developed with the intent of investigating the sensitivity of penetration depth to the material properties and failure criteria of the gelatin (human soft tissue surrogate). Previous studies have relied on measured bulk modulus, sound speed and static measurements to derive a 1D constitutive model. However, penetration studies have shown that the shear modulus and failure stress/strain of the material have a first order effect on penetration. Ultimately, these properties will have to be either measured or backed out from computer simulations. Currently, we are using known properties and adjusting others by matching hydrocode simulations with penetration data as discussed below.

Our previous model from a 1993 program sponsored by DARPA was based upon using a value for the bulk modulus obtained from flyer plate tests on gelatin and shear modulus obtained from Autodyn™ hydrocode correlation of velocity versus depth predictions developed in Task 1 from a 350 ft/sec BB impact on gelatin. These values are shown in Table 5. The results from these studies suggested that for a reasonable minimum value of shear modulus, say > 100 bars, a value of failure strain of greater than 10 % is required to prevent large penetrations. We used a reasonable value of Poisson ratio, which for nearly incompressible materials such as rubber would be on the order of 0.48. This would necessitate a much larger value of elastic modulus and either a lower value of failure strain or the implementation of a failure stress criteria.

TABLE 5. Potential Variations on Gelatin Material Properties

Correlation Source	Bulk Modulus (Bars)	Shear Modulus (Bars)	Elastic Modulus(Bars)	Poisson Ratio
Charest Flyer	2.32*10^4	2170	6300	0.455
Early GBL BB	2.62*10^4	125	375	~0.498
Estimate	2.62*10^4	940	3000	0.48

The bulk modulus can be derived from a relationship between shear modulus, *G*, and Poisson ratio, *v*. Typical results are shown in Figure 33. The sensitivity of *G* and *v* to an approximately 10% change in bulk modulus is also shown in Figure 33, below.

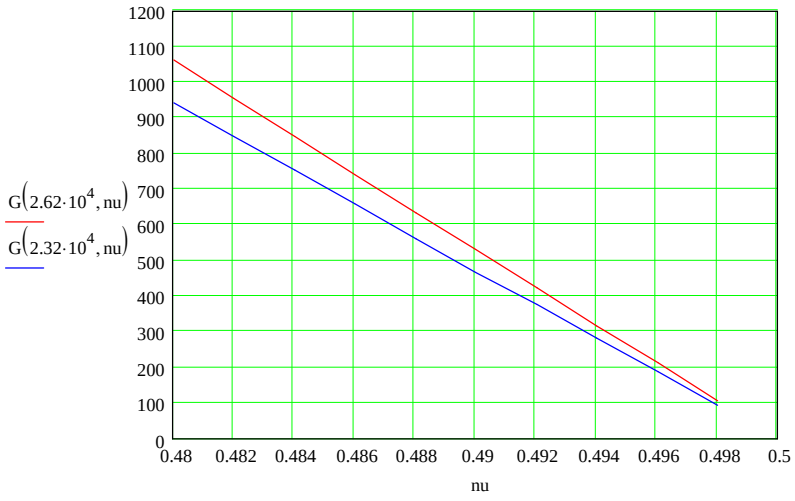

FIGURE 33. Shear Modulus versus Poisson Ratio

The initial hydrocode correlation assumed that the gelatin failed in shear and incorporated a shear strain failure value of 40%. Subsequent thinking suggested that a principal strain criterion might be more appropriate and the hydrocode correlation with experimental data suggested that a value of 10-20% was more appropriate. In order to size reasonable experiments, the model developed in Task 1, which assumes projectile diameter scaling was used to predict penetration depth versus impact velocity. The results have been previously shown in Figure 3 (page 11).

In Figure 4 (page 14), data points from the recent Task 3 ballistic penetration experiments (discussed in Section 3) are plotted along side the predictive curves. It is seen that the model does a good job of fitting the data. Further it can be seen that for a penetration depth of about 6 inches, a dimension typical of the depth of a heart, a velocity in the range of 800-1100 ft/sec for spheres with diameters of interest is appropriate. Thus, steel spheres of diameter 0.25- and 0.375-inches (1-3 grams) at velocities on the order of 1100 ft/sec were used for the numerical simulations.

Normal impacts into gelatin targets consisting in some cases of multiple materials were also considered. The intent was to correlate hydrocode results with the Task 3 impact data and then verify predictions made by the Task 1 modeling for homogenous targets. In this way, we would have a correlation between two different analytical techniques employing different assumptions and experimental data.

A review of selected gelatin samples posttest showed both a residual cavity and radial tears. Based upon this it was speculated that a stress rather than strain failure criteria is appropriate.

A series of 2D hydrocode runs were then conducted where the projectile size, gelatin shear modulus and failure stress were varied. The intent was to come up with an updated set of material properties for gelatin which yielded penetration predictions consistent with current data. The following parameters were varied in the model.

(1) Projectile shape: Sphere and Wedge
(2) Projectile Diameter: Spherical projectiles 0.17-, 0.250-, and 0.375-inch diameter
(3) Projectile Material: Steel and Aluminum
(4) Gelatin Shear Modulus: 100-1000 bars
(5) Gelatin Tensile Stress Failure: 25-100 bars
(6) Erosion strain value used to remove highly distorted elements

A combination of parameters was inferred which allowed the approximate match of penetration velocity versus time and penetration depth. In the case of a 0.375-inch sphere at 1100ft/sec, a snapshot from the analytical simulation is shown in Figure 34. Notice the radial failure pattern which is also observed in the corresponding ballistic experiment. A comparison of the Task 1 model of velocity versus time with the hydrocode prediction is shown in Figure 35. The correlation assumed a nominal bulk modulus, a shear modulus of 125 bars, failure stress of 25 bars and erosion strain of 200%. The corresponding penetration depth versus time is shown in Figure 36. These results compared favorably with those shown in Figure 3 and the ballistic data described in Task 3.

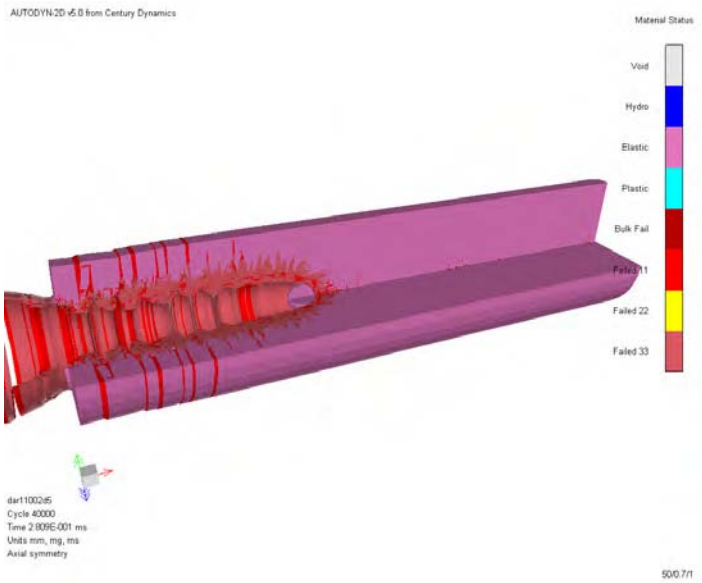

FIGURE 34. Sphere Penetration into Heart Simulant

A series of 3D simulations were also conducted using various spherical projectiles impacting homogenous and layered materials. The trajectory of the projectile in the case where the material was horizontally layered was tracked and seen to deflect away from the stiffer material. A snapshot of this simulation is shown in Figure 37.

A time resolved animated simulation of the solution corresponding to Figure 38 was previously sent to Drs. Rick Satava (DARPA), Gerry Mosses (TATRC), and Brian Athey (University of Michigan).

A response parameter of particular interest is the radial velocity of the cavity wall as a function of time. This parameter will be used in to drive the cavity wall response in the analytical models. Typical results are shown in Figure 39.

The blue line in Figure 39 shows the projectile axial velocity versus time which at zero time is 335 m/sec. The y-velocity curves are cavity wall velocities at various distances from the impact site at locations just outside the radius of the projectile. In general it was found that the wall velocity ***near*** the impact site was on the order of 1/3 of the axial velocity decaying more rapidly than the axial velocity as penetration occurs. The initial duration of the wall response is less than tenths of milliseconds.

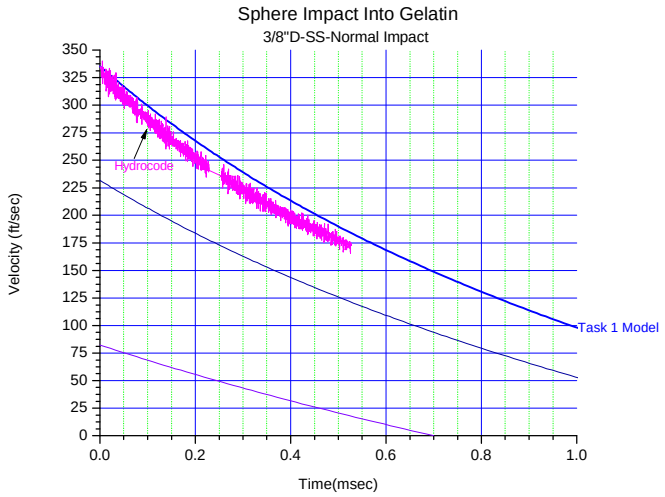

FIGURE 35. Sphere Penetration in Heart Simulant: Velocity vs. Time

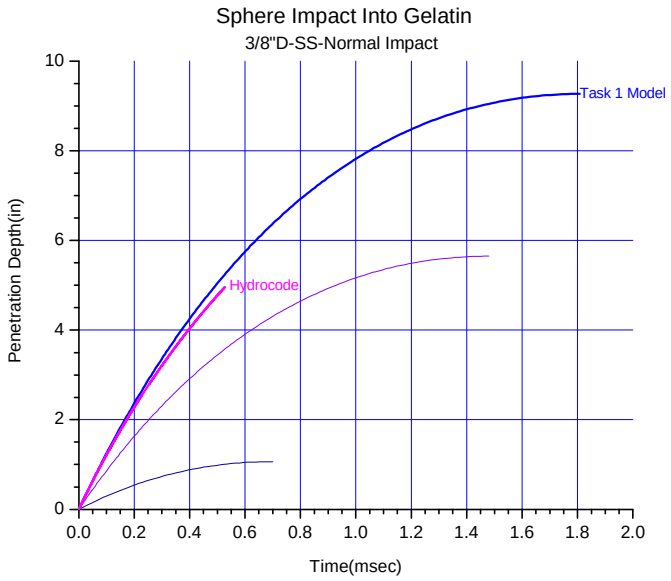

FIGURE 36. Sphere Penetration in Heart Simulant: Depth versus Time

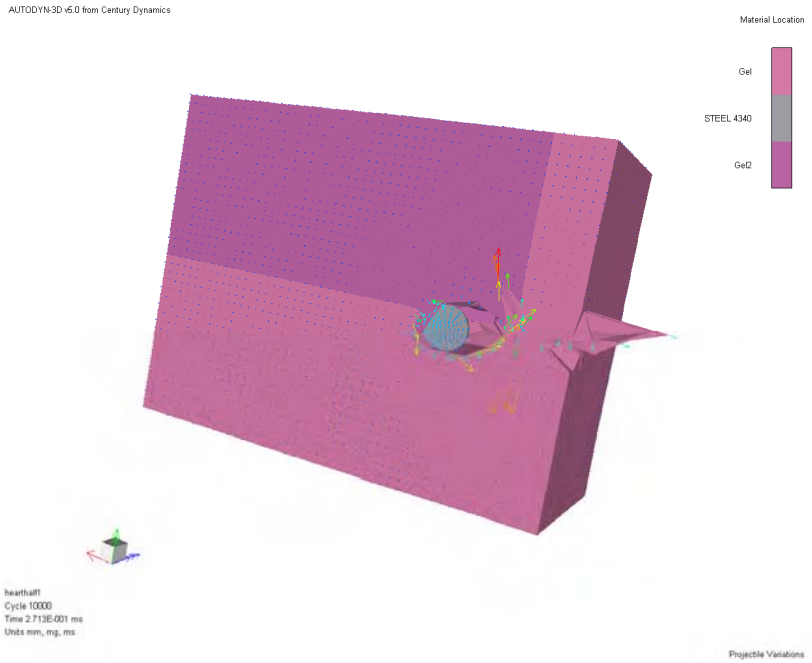

FIGURE 37. Sphere Penetration into Gelatin: Bi-Material, 3D

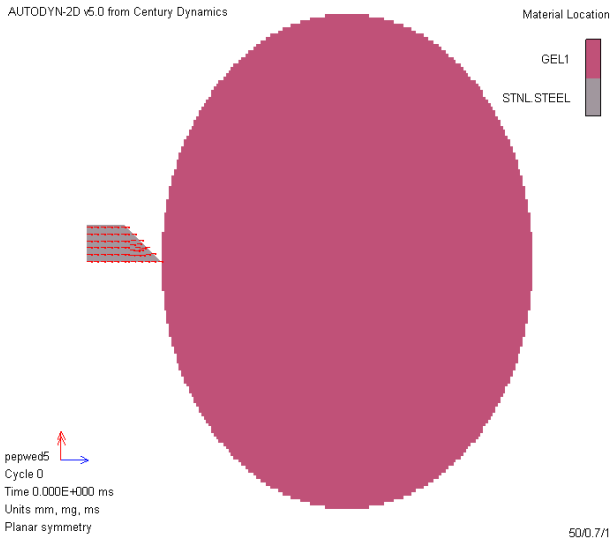

FIGURE 38. Wedge Impact into Heart Simulator

Videos from three ballistic experiments conducted during Task 3 show the projectile trajectory and evolution of the temporary cavity in the wake of the projectile. These videos were also sent previously to DARPA and the University of Michigan and show agreement with pretest analytical predictions. Animated numerical simulations of these experiments were also previously sent to DARPA and the University of Michigan.

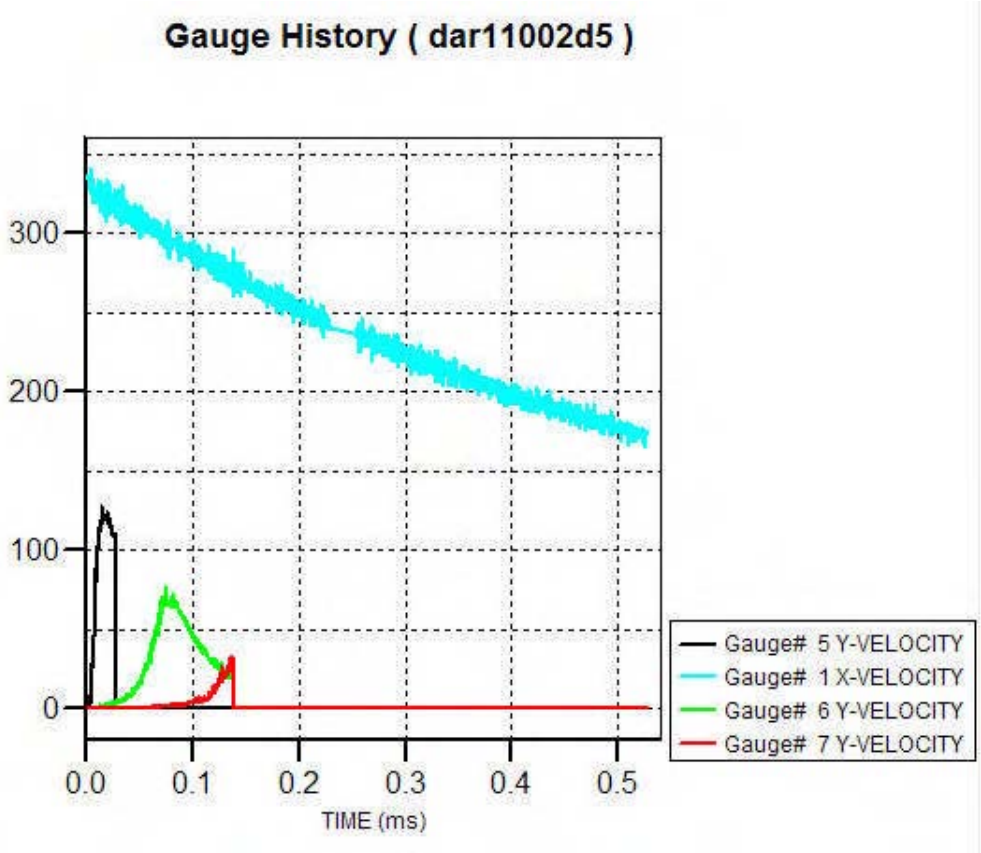

FIGURE 39. Cavity Velocity versus Time

A 3D axisymmetric model is also being developed of the wound tract to determine the initial conditions on the non-linear spring lattice that represent the wound tract boundary and that describe the transient dynamic response of the tissue in the projectile wake. The static analysis prerequisite to the 3-D axisymmetric model of wave propagation in a cylindrical tissue perforated by a concentric cylindrical projectile is discussed in Appendix E.

2.3 WOUND TRACT MODELING AND NONLINEAR SPRING LATTICE

Section 2.3.1 discusses the spring lattice model that describes the transient dynamic response in the projectile wake (SOW 2.3). Section 2.3.2 discusses a modal analysis model that describes radiated stress waves (SOW 2.2). This model is used to determine the initial conditions on the spring lattice model (SOW 2.2.3). Finally, section 2.3.3 describes software that has been developed to interface our wound ballistic codes with the University of Utah SciRUN code. This last effort was done so that the University of Michigan could display our output on the HOLOMER heart so our latest I/O formats that have been updated to work with SciRUN. The output of these models is an MPEG of an analytical simulation of one of our gelatin ballistic experiments. This was also done so that we could easily do reality checks on our code output.

2.3.1 Determination of Temporary and Permanent Cavities in Projectile Wake

A lattice of non-linear springs is used to model the mechanical response of the soft tissue in the wake of projectile motion. A schematic of this model is shown in Figure 40.

The high frequency portion of the power spectrum promotes damage and the energy content in the high frequency band dissipates rapidly due to conversion of energy into mechanical work. The current model is one-dimensional where the force-displacement relation has been derived from experimental data on tissue deflections under various loads. Since these relations are strain rate dependent, we assume average values in the frequency band of interest. Due to residual strain or deflection after each loading and unloading cycle, the loading curves differ from unloading. For both loading and unloading, the force-displacement relations used in our nonlinear spring model are given in Figure 41.

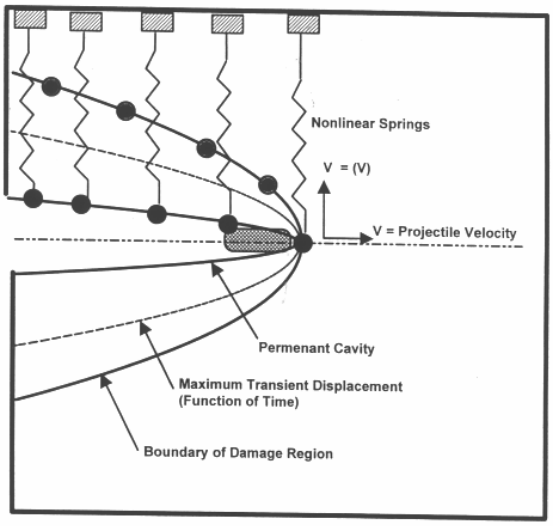

FIGURE 40. Schematics of Nonlinear Spring Model

The input to the nonlinear spring code is the lateral velocity at which the cavity wall is set to motion after the passage of the projectile through that location. For a three dimensional body, it is very difficult to determine the relationship between the lateral cavity velocity and the instantaneous projectile velocity at a given location of the cavity wall. A video tape acquired from Dr. Ronald Bellamy, Col., USAMC shows an AK74 projectile penetrating 10% ordnance gelatin photographed at 20,000 frames a second. From these data, it is estimated that the lateral velocity is about 10% of the projectile velocity. In general, this result depends on the projectile shape and orientation as the projectile is penetrating through a specific location.

For a specific projectile shape with known curvature, if the target is not separated from the projectile and assuming that the projectile is rigid, the velocity of the target material point in contact with the projectile is normal to the projectile surface, and is equal to the normal component of the projectile velocity. For example, in the case of a slant wedge of angle θ, if the projectile velocity is v_0 along the x-direction (Figure 42), the material velocity of the target point is along the normal to the path and is equal to $v_0 \cos\theta$. Then the lateral material velocity along the y-direction is $v_L = v_n \sin\theta = v_0 \cos\theta \sin\theta$. For our cut-cylinder projectile where $\theta \sim 45^o$, $v_L = v_0 / 2$. This result agrees with hydrocode simulation of the projectile penetration process.

Using the three-particle nonlinear spring code where 10% of the projectile is transferred laterally, the nature of permanent and transient cavity for a ¼ inch steel ball moving through a 10% gelatin at 1510 fps is shown in Figure 43. The correlation with some experimental data is also shown in Figure 43.

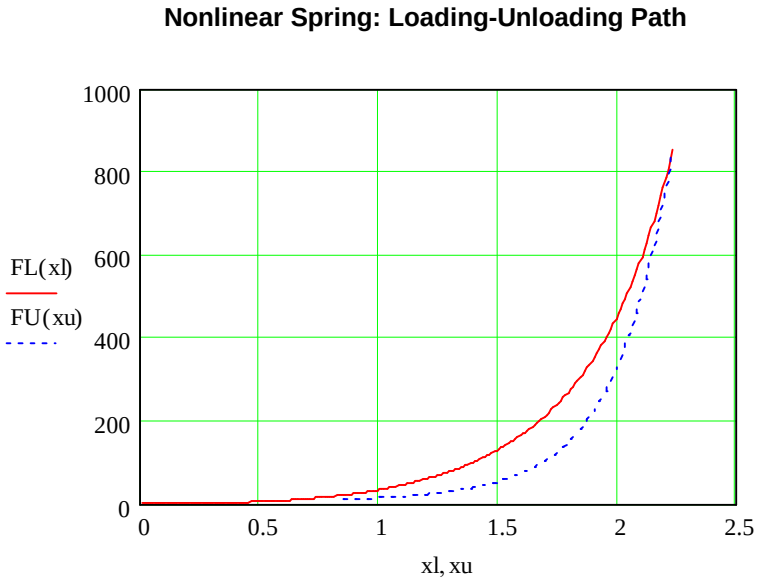

FIGURE 41. Loading-Unloading Paths Used in Nonlinear Spring Code

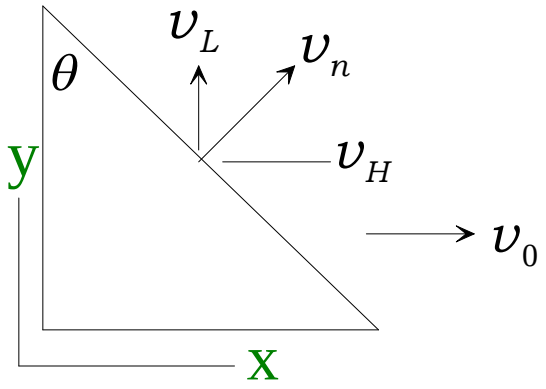

FIGURE 42. Velocity of Material Point in Contact with the Projectile

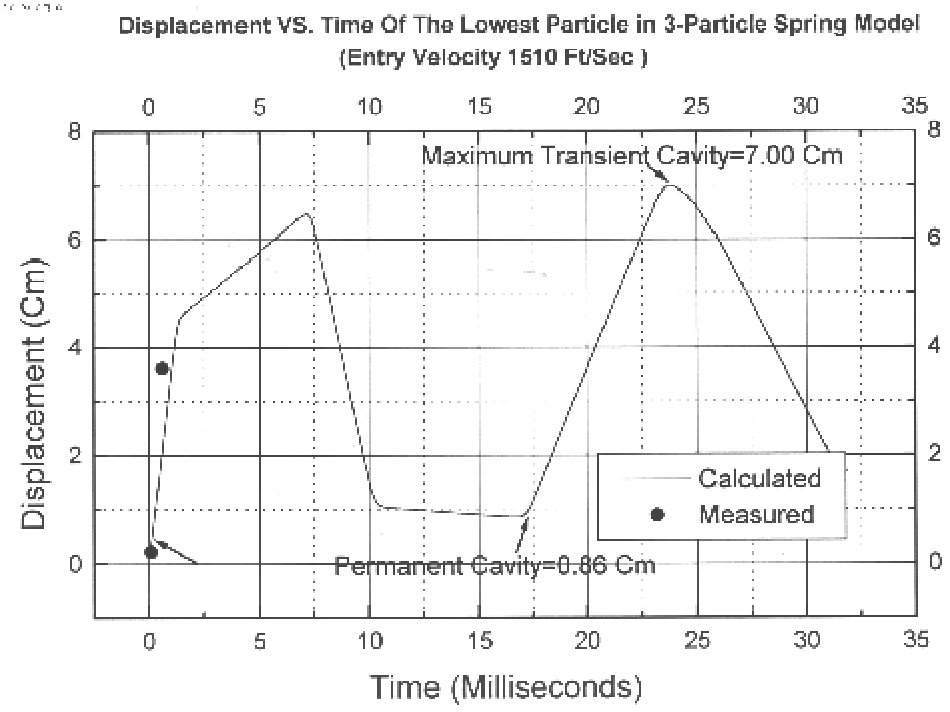

FIGURE 43. Transient and Permanent Cavities from Nonlinear Spring Model

2.3.2 3D Axisymmetric Modal Analysis of Stress Wave Radiation

Penetrating trauma in biological tissue is caused by at least two discrete mechanisms

(1) Tissue damage along projectile path. This interaction is hydrodynamic in nature where inertial and frictional forces dominate projectile motion during deceleration.

(2) Stress waves generated at cylindrical interface between projectile and tissue from radial and axial velocities prescribed by the projectile during penetration. These waves radiate to neighboring tissue causing further damage.

The present analysis concerns mechanism 2 above.

As the projectile penetrates into tissue, it moves material by replacing it with its own volume. When the material fails, it acts more like a fluid, lessening the amount of material being compressed. In the radial direction, material is compressed by an expanding cross-section of the projectile smoothly curved leading edge. As long as the projectile speed is much smaller than the speed of stress waves in the material, the moving projectile can be approximated by radial and axial velocities prescribed along its boundary. For a projectile speed on the order of hundreds of feet per second and a dilatational speed in tissue material of 5600 ft/s, this approximation is valid.

The influenced region is simulated by tissue material in the shape of a hollow cylinder. Let (r,z) be radial and axial coordinates with an origin at one end of the cylinder axis. The inner cylinder radius r_p is that of the penetrating projectile while its outer radius r_o and length l are chosen to include the furthest radial and axial locations affected by penetration. In a coordinate system (r,z) centered at one end of the finite cylinder, the projectile lies in the interval $z_a \le z \le z_b$ such that $z_b - z_a = l_p$ where l_p is projectile length. The tissue material is linear viscous-elastic with a constitutive law that includes first temporal derivatives of stress and strain.

For simplicity and without loss of generality, axial functions satisfying the differential equations and specific boundary conditions at the two ends of the cylinder $z = (0,l)$ are divided into 2 sets. One set satisfying vanishing axial stress σ_{zz} at $z = (0,l)$ which has radial and axial displacements (u,w) proportional to $\left(\sin(m\pi z/l), \cos(m\pi z/l)\right)$ belongs to "problem 1", where m is an integer wave number. The other set satisfying vanishing shear stress τ_{rz} at $z = (0,l)$ which has (u,w) proportional to $\left(\cos(m\pi z/l), \sin(m\pi z/l)\right)$ belongs to "problem 2". The first set applies to radial tractions prescribed at the cylindrical footprint $r = r_o$, $z_a \le z \le z_b$ while the second set applies to prescribed axial tractions along the same footprint. The fact that each set satisfies different boundary conditions

does not affect transient response until waves reflect from the axial boundaries. Consequently, one problem is solved for each type of forcing excitation and results are superimposed if both types of excitation are acting simultaneously.

The form of the forcing function closest to the application is radial and axial velocity prescribed over part of the inner cylindrical boundary, yet this leads to a mixed boundary condition. This difficulty can be overcome by superimposing response from a set of unit radial or axial tractions with time dependent weights prescribed on annular portions of the inner boundary. These weights are updated at each time step using the condition that combined velocity response at the center of each annular portion equals the prescribed instantaneous velocity. In this way, the forcing function is converted to pure radial or axial traction with time varying spatial dependence.

Elastic analysis

In the analysis to follow, all subscript will denote components and not partial derivatives. In cylindrical coordinates, the electrodynamics equations are

$$\mu\nabla^2\mathbf{u}+(\lambda+\mu)\nabla(\nabla\bullet\mathbf{u})=\rho\,\partial_{tt}\mathbf{u} \qquad (2\text{-}3)$$
$$\nabla^2\equiv\partial_{rr}+1/r\;\partial_r+1/r^2\,\partial_{\theta\theta}+\partial_{zz}$$
$$\nabla\equiv\left(1/r\;\partial_r\,r\right)\mathbf{e}_r+(1/r\,\partial_\theta)\mathbf{e}_\theta+(\partial_z)\mathbf{e}_z$$

(r,θ,z) are radial, circumferential and axial independent variables, $\mathbf{u}=\{u,\upsilon,w\}^T$ is displacement vector along these directions, (λ,μ) are Lame constants, ρ is mass density and t is time. Re-write (2-3) as

$$\mu\nabla^2\mathbf{u}+(\lambda+2\mu)\nabla(\nabla\bullet\mathbf{u})-\mu\nabla(\nabla\bullet\mathbf{u})=\rho\,\partial_{tt}\mathbf{u} \qquad (2\text{-}4a)$$

Noting that

$$\mu\nabla^2\mathbf{u}-\mu\nabla(\nabla\bullet\mathbf{u})=-\mu\,\nabla\times\nabla\times\mathbf{u} \qquad (2\text{-}4b)$$

permits casting (2-3) in the form

$$(\lambda+2\mu)\nabla(\nabla\bullet\mathbf{u})\;-\mu\,\nabla\times\nabla\times\mathbf{u}=\rho\,\partial_{tt}\mathbf{u} \qquad (2\text{-}5)$$

Define dilatation Δ and rotation vector $\boldsymbol{\psi}$ as

$$\Delta=\nabla\bullet\mathbf{u}\;,\quad \boldsymbol{\psi}=\nabla\times\mathbf{u} \qquad (2\text{-}6)$$

Substituting (2-6) in (2-5) yields (Love (1944))

$$(\lambda + 2\mu)\nabla\Delta - \mu\,\nabla \times \boldsymbol{\psi} = \rho\,\partial_{tt}\mathbf{u} \tag{2-7}$$

Taking the divergence of (2-7) noting that $\nabla \cdot (\nabla \times \boldsymbol{\psi}) = 0$ yields

$$(\lambda + 2\mu)\nabla^2\Delta = \rho\,\Delta_{tt} \tag{2-8}$$

Taking the rotation of (2-7) noting that $\nabla \times (\nabla\Delta) = \mathbf{0}$ yields

$$\mu\nabla^2\boldsymbol{\psi} = \rho\,\boldsymbol{\psi}_{tt} \tag{2-8}$$

For ax symmetric motions, $\upsilon \equiv \partial_\theta \equiv 0$ and $\psi_r \equiv \psi_z \equiv 0$ reducing (2-8) and (2-9) to

$$\begin{aligned} &(\lambda + 2\mu)\nabla_0^2\,\Delta = \rho\,\Delta_{tt} \\ &\mu\,\nabla_1^2\,\psi_\theta = \rho\,\psi_{\theta,tt} \\ &\nabla_n^2 \equiv \partial_{rr} + 1/r\,\partial_r - n^2/r^2 + \partial_{zz}\ , \quad n = 0,1 \end{aligned} \tag{2-10}$$

Expressing (2-6) in terms of $\mathbf{u}$ yields

$$\begin{aligned} &\Delta = 1/r\,\partial_r\,(r\,u) + \partial_z\,w \\ &\psi_\theta = \partial_z\,u - \partial_r\,w \end{aligned} \tag{2-11}$$

Decoupling u and w in (2-11) produces

$$\begin{aligned} &\nabla_1^2 u = \partial_r\,\Delta + \partial_z\,\psi_\theta \\ &\nabla_0^2 w = \partial_z\,\Delta - 1/r\,\partial_r(r\,\psi_\theta) \end{aligned} \tag{2-12}$$

For the radial "problem 1" satisfying $\sigma_{zz} = 0$ at $z = (0,l)$, harmonic motions in time with radian frequency ω and simply supported boundaries at $z = (0,l)$ yields the separated solution

$$\begin{aligned} &\left\{\Delta(r,z,t),\psi_\theta(r,z,t)\right\}^T = \left\{\overline{\Delta}(r)\cos(k_z z),\overline{\psi}_\theta(r)\sin(k_z z)\right\}^T e^{i\omega t} \\ &\left\{u(r,z,t),w(r,z,t)\right\}^T \ = \left\{\overline{u}(r)\,\sin(k_z z),\overline{w}(r)\,\cos(k_z z)\right\}^T e^{i\omega t} \end{aligned} \tag{2-13}$$

$i = \sqrt{-1}$ and $k_z = m\pi / l$ where m is an integer axial wave number. The z dependence in (2-13) yields $u = \sigma_{zz} = 0$ at the cylinder ends $z = 0, l$. For real k_e and k_s, equation (2-10) admits the solution

$$\begin{aligned} \bar{\Delta}(r) &= C_1 J_0(k_e r) + C_2 Y_0(k_e r) \\ \bar{\psi}_\theta(r) &= C_3 J_1(k_s r) + C_4 Y_1(k_s r) \\ k_e^2 &= \omega^2 / c_d^2 - k_z^2 \ , \quad c_d^2 = (\lambda + 2\mu)/\rho \\ k_s^2 &= \omega^2 / c_s^2 - k_z^2 \ , \quad c_s^2 = \mu / \rho \end{aligned} \tag{2-14}$$

J_n and Y_n are Bessel functions and c_d, c_s are dilatational and shear speeds of sound. If either k_e or k_s is imaginary, J_n and Y_n in (2-14) are replaced by the modified Bessel functions I_n and K_n with appropriate changes in sign. Substituting (2-13) and (2-14) in (2-12) then solving for $\bar{u}(r)$ and $\bar{w}(r)$ yields

$$\begin{aligned} \bar{u}(r) &= -k_e \left(C_1 J_1(k_e r) + C_2 Y_1(k_e r) \right) + k_z \left(C_3 J_1(k_s r) + C_4 Y_1(k_s r) \right) \\ \bar{w}(r) &= k_z \left(C_1 J_0(k_e r) + C_2 Y_0(k_e r) \right) + k_s \left(C_3 J_0(k_s r) + C_4 Y_0(k_s r) \right) \end{aligned} \tag{2-15}$$

In cylindrical coordinates, the constitutive relations are

$$\begin{aligned} &\sigma_{rr} = \lambda \Delta + 2\mu \partial_r u \ , \ \sigma_{\theta\theta} = \lambda \Delta + 2\mu u / r \\ &\sigma_{zz} = \lambda \Delta + 2\mu \partial_z w, \ \ \tau_{rz} = \mu \left(\partial_z u + \partial_r w \right) \\ &\Delta = \partial_r u + u / r + \partial_z w \end{aligned} \tag{2-16}$$

For "problem 1", harmonic motions in time and simply supported boundaries at $(0, l)$ yield the separated relations

$$\begin{Bmatrix} \sigma_{rr} \\ \sigma_{\theta\theta} \\ \sigma_{zz} \\ \tau_{rz} \end{Bmatrix} (r, z, t) = \begin{Bmatrix} \bar{\sigma}_{rr}(r) \sin(k_z z) \\ \bar{\sigma}_{\theta\theta}(r) \sin(k_z z) \\ \bar{\sigma}_{zz}(r) \sin(k_z z) \\ \bar{\tau}_{rz}(r) \cos(k_z z) \end{Bmatrix} e^{i\omega t} \tag{2-17a}$$

Boundary conditions at $r = r_p$ and $r = r_o$ are

$$\begin{aligned}
&\sigma_{rr}(r_p,z,t) = p_r(t)\big[H(z-z_a)-H(z-z_b)\big] \\
&\tau_{rz}(r_p,z,t) \;= 0 \\
&\sigma_{rr}(r_o,z,t) \;\equiv \tau_{rz}(r_o,z,t) \;= 0
\end{aligned} \tag{2-17b}$$

$p_r(t)$ is a time dependent uniform radial traction acting on the inner cylindrical boundary $r = r_p$ in the interval $z_a \le z \le z_b$. The z dependence in (2-17) yields $u = \sigma_{zz} = 0$ at the cylinder ends $z = 0, l$. Substituting (2-13), (2-15) and (2-17) in (2-16) yields

$$\begin{aligned}
\bar{\sigma}_{rr}(r) = &\Big[-\big((\lambda+2\mu)k_e^2+\lambda k_z^2\big)J_0(k_e r)+2\mu\, k_e^2\, J_1(k_e r)\;/(k_e r)\Big]C_1 \\
&+\Big[-\big((\lambda+2\mu)k_e^2+\lambda k_z^2\big)Y_0(k_e r)+2\mu\, k_e^2\, Y_1(k_e r)\;/(k_e r)\Big]C_2 \\
&+2\mu k_s k_z\big[J_0(k_s r)-J_1(k_s r)\;/(k_s r)\big]C_3 \\
&+2\mu k_s k_z\big[Y_0(k_s r)-Y_1(k_s r)\;/(k_s r)\big]C_4
\end{aligned} \tag{2-18a}$$

$$\begin{aligned}
\bar{\sigma}_{\theta\theta}(r) = &-\Big[\lambda(k_z^2+k_e^2)J_0(k_e r)+2\mu\, k_e^2 J_1(k_e r)\;/(k_e r)\Big]C_1 \\
&-\Big[\lambda(k_z^2+k_e^2)Y_0(k_e r)\;+2\mu\, k_e^2 Y_1(k_e r)\;/(k_e r)\Big]C_2 \\
&+2\mu k_s k_z\big[C_3 J_1(k_s r)+C_4 Y_1(k_s r)\;\big]/(k_s r)
\end{aligned} \tag{2-18b}$$

$$\begin{aligned}
\bar{\sigma}_{zz}(r) = &-\big((\lambda+2\mu)k_z^2+\lambda k_e^2\big)\big[C_1 J_0(k_e r)+C_2 Y_0(k_e r)\big] \\
&-2\mu\, k_s k_z\big[C_3 J_0(k_s r)+C_4 Y_0(k_s r)\big]
\end{aligned} \tag{2-18c}$$

$$\begin{aligned}
\bar{\tau}_{rz}(r) = &-2\mu k_e k_z\big[C_1 J_1(k_e r)+C_2 Y_1(k_e r)\big] \\
&-\mu(k_s^2-k_z^2)\big[C_3 J_1(k_s r)+C_4 Y_1(k_s r)\big]
\end{aligned} \tag{2-18d}$$

Since σ_{zz} is proportional to $\sin(k_z z)$ in (2-17), it vanishes at $z = 0,\ l$. This allows a rigid body motion $w(r,z;t) = w_o(t)$ when external traction acts along z. To avoid the rigid body motion, an additional axial functional dependence is considered for "problem 2"

$$\begin{aligned}
&\begin{Bmatrix} u \\ w \end{Bmatrix}(r,z,t) \;= \begin{Bmatrix} \bar{u}(r)\,\cos(k_z z) \\ \bar{w}(r)\,\sin(k_z z) \end{Bmatrix} e^{i\omega t} \\
&\begin{Bmatrix} \sigma_{rr} \\ \sigma_{\theta\theta} \\ \sigma_{zz} \\ \tau_{rz} \end{Bmatrix}(r,z,t) = \begin{Bmatrix} \bar{\sigma}_{rr}(r)\,\cos(k_z z) \\ \bar{\sigma}_{\theta\theta}(r)\,\cos(k_z z) \\ \bar{\sigma}_{zz}(r)\,\cos(k_z z) \\ \bar{\tau}_{rz}(r)\,\sin(k_z z) \end{Bmatrix} e^{i\omega t}
\end{aligned} \tag{2-19a}$$

that satisfies the following boundary conditions at $r = r_p$ and $r = r_o$

$$\begin{aligned} &\sigma_{rr}(r_p, z, t) = 0 \\ &\tau_{rz}(r_p, z, t) = p_z(t)\left[H(z - z_a) - H(z - z_b)\right] \\ &\sigma_{rr}(r_o, z, t) \equiv \tau_{rz}(r_o, z, t) = 0 \end{aligned} \qquad \text{(2-19b)}$$

$p_z(t)$ is a time dependent uniform axial traction acting on the inner cylindrical boundary $r = r_p$ in the interval $z_a \le z \le z_b$. The z dependence in (18a) yields $w = \tau_{rz} = 0$ at the cylinder ends $z = 0, l$. In the analysis to follow, superscripts (1) and (2) will denote radial and axial problems respectively. Derivations for problem (2) follow the same steps as those for problem (1) and are omitted here for shortness. Although conditions at the boundaries $z = 0,\ l$ of each problems are different, they do not affect the transient response at times preceding reflection of waves from these boundaries.

Divide the cylindrical surface $\left\{r = r_p,\ z_a \le z \le z_b\right\}$ into $n+1$ equidistant ring stations with increment Δz_p

$$\begin{aligned} &z_1,\ z_2,\ z_3, ..., z_n \ , \qquad z_l - z_{l-1} = \Delta z_p = const \\ &z_l = z_a + (l-1)\,\Delta z_p \end{aligned} \qquad \text{(2-20)}$$

Assume a uniform pressure of unit intensity to act over each ring segment $z_{l-1} \to z_l$. The elastic-dynamic solution to the k^{th} ring pressure segment is outlined below.

For each pressure segment, expand each dependent variable in terms of eigenfunctions that satisfy homogeneous boundary conditions. Express total displacement $\mathbf{u}_k(r, z; t)$ as a superposition of two terms

$$\mathbf{u}_k^{(1,2)}(r, z; t) = \mathbf{u}_{sk}^{(1,2)}(r, z)\ f_p(t)\ +\ \mathbf{u}_{dk}^{(1,2)}(r, z; t) \qquad \text{(2-21)}$$

$\mathbf{u}_{sk}^{(1,2)}(r, z)$ is static displacement vector satisfying (2-4a) when time derivative vanishes, $\mathbf{u}_{dk}^{(1,2)}(r, z; t)$ is dynamic displacement vector satisfying the dynamic equation of motion (2-4a), and $f_p(t)$ is time dependence of the forcing pressure. For each axial wave number m, express $\mathbf{u}_{dk}^{(1,2)}(r, z, t)$ in the eigenfunctions $\mathbf{\Phi}_{mj}^{(1,2)}(r, z)$ (Appendix F)

$$\mathbf{u}_{dk}^{(1,2)}(r, z, t) = \sum_j \sum_m a_{mjk}^{(1,2)}(t)\ \mathbf{\Phi}_{mj}^{(1,2)}(r, z) \qquad \text{(2-22)}$$

$a_{mjk}^{(1,2)}(t)$ is a generalized coordinate of the j^{th} eigenfunction with m axial half waves from the k^{th} pressure segment. Substituting (2-21) and (2-22) in (2-4a) and enforcing orthogonality of $\mathbf{\Phi}_{mj}^{(1,2)}(r,z)$ yields uncoupled equations in $a_{mjk}^{(1,2)}(t)$. For an undamped elastic cylinder the equation governing $a_{mjk}^{(1,2)}(t)$ is

$$\left(\frac{d^2}{dt^2}+\omega_{mj}^2\right)a_{mjk}^{(1,2)}(t)=\overline{f}_{mjk}^{(1,2)}(t) \qquad \text{(2-23a)}$$

$$\overline{f}_{mjk}^{(1,2)}(t)=N_{amjk}^{(1,2)}\ \ddot{f}_p(t)/N_{mj}$$

$$N_{mj}^{(1,2)}=\int_0^{r_d}\int_0^{h}\mathbf{\Phi}_{mj}^{(1,2)}(r,z)\cdot\mathbf{\Phi}_{mj}^{(1,2)}(r,z)\,dz\ r\ dr \qquad \text{(2-23b)}$$

$$N_{amjk}^{(1,2)}=\int_0^{r_d}\int_0^{h}\mathbf{u}_{sk}^{(1,2)}(r,z)\cdot\mathbf{\Phi}_{mj}^{(1,2)}(r,z)\,dz\ r\ dr$$

ω_{mj} is the resonant frequency. The solution to (2-23a) takes the form

$$a_{mjk}^{(1,2)}(t)=-\frac{1}{\omega_{mj}}\int_0^{t}\sin\omega_{mj}(t-\tau)\ \overline{f}_{mjk}^{(1,2)}(\tau)\,d\tau \qquad \text{(2-24)}$$

Evaluating radial and axial displacements $u_k(r,z;t)$ for problem (1) and $w_k(r,z;t)$ for problem (2) from the k^{th} pressure segment at each central point $z_{cl}=(z_l+z_{l-1})/2$ of a pressure segment yields coefficients of the influence matrices

$$\begin{aligned}U_{lk}(t)&=\sum_j\sum_m a_{mjk}^{(1)}(t)\ \overline{u}_{mjk}^{(1)}(r_p,z_{cl})\ +\ u_{sk}^{(1)}(r_p,z_{cl})\ f_p(t)\\ W_{lk}(t)&=\sum_j\sum_m a_{mjk}^{(2)}(t)\ \overline{w}_{mjk}^{(2)}(r_p,z_{cl})\ +\ w_{sk}^{(2)}(r_p,z_{cl})\ f_p(t)\end{aligned} \qquad \text{(2-25)}$$

$\left\{\overline{u}_{mjk}^{(1)}(r_p,z_{cl})\ ,\ \overline{w}_{mjk}^{(2)}(r_p,z_{cl})\right\}$ and $\left\{u_{sk}^{(1)}(r_p,z_{cl}),w_{sk}^{(2)}(r_p,z_{cl})\right\}$ are modal and static displacement dyads at z_{cl} from the k^{th} pressure segment in problems (1) and (2) respectively. In (2-23) and (2-25) $f_p(t)$ is a first approximation to the time dependence of the applied pressure. One approximation is determined from the plane-strain state when axial length of cylinder and footprint approaches infinity (Appendix G). Enforcing the condition of prescribed displacements $u_p^{(1)}(t)$ and $w_p^{(2)}(t)$ at each time step yields a set of simultaneous equations in the weights $p_k^{(1)}$ and $p_k^{(2)}$

$$\sum_{k=1}^{n} U_{lk}(t)\ p_k^{(1)}(t) = u_p^{(1)}(t) \quad , \qquad l = 1, n$$
$$\sum_{k=1}^{n} W_{lk}(t)\ p_k^{(2)}(t) = w_p^{(2)}(t) \quad , \qquad l = 1, n \tag{2-26}$$

An approximation to $f_p(t)$ is found from the plane-strain problem of the infinite length cylinder with prescribed radial displacement at the inner boundary (Appendix F).

In what follows, superscripts (1,2) are dropped for shortness. For an elastic material, eigenvalues and resonant frequencies are synonymous. In this case, the eigenvalues appear in pairs ω_{mj} and $-\omega_{mj}$. Consequently equation (2-21a) takes the form

$$\left(\frac{d}{dt} - i\omega_{mj}\right)\left(\frac{d}{dt} + i\omega_{mj}\right) a_{mjk}(t) = \bar{f}_{mjk}(t) \tag{2-27a}$$
$$\bar{f}_{mjk}(t) = N_{amjk}\ \ddot{f}_p(t) / N_{mj}$$
$$N_{amjk} = \int_0^l \int_{r_p}^{r_o} \mathbf{u}_{sk}(r,z) \bullet \mathbf{\Phi}_{mj}(x,z)\ r\, dr\, dz \tag{2-27b}$$
$$N_{mj} = \int_0^l \int_{r_p}^{r_o} \mathbf{\Phi}_{mj}(r,z) \bullet \mathbf{\Phi}_{mj}(r,z)\ r\, dr\, dz$$

2.3.3 SciRUN Interface and Visualization of Gelatin Experiments

This effort was to achieve the following objectives:

1. Set up a computer on which to run SCIRun.
2. Model the Projectile.
3. Model the Gelatin Block.

The following was accomplished:

1. Set up a Linux Computer on which to run SCIRun.
2. Provide a method to output the geometry of the projectile from MathCAD for input into SCIRun.
3. Provide a method to output the trajectory of the projectile from MathCAD for input into SCIRun.
4. Program SCIRun to simulate the movement and geometry of the projectile.

5. Generate an MPEG of the projectile simulation.

Step (3) of the planned items will be completed by the end of December II as it more appropriately is handled as the projectile trajectory model is debugged during the V&V phase.

Summary of Deliverables from this task

- DumpProjectile.dll, source code, and related files
- user.xml
- Trajectory Source Code for SCIRun
- extract.sh
- Phase1.net
- PC (Linux Redhat 9 OS) with modified SCIRun code (and all other necessary executables and scripts).
- Phase1.mpg
- movieplayer.exe

Explanation of Deliverables from this task

DumpProjectile.dll

This is a MathCAD specific DLL which is integrated into the Mathcad environment to allow Mathcad to generate a SCIRun compliant "fld" file which defines the geometry of the cut cylinder.

The dll is to be copied to the following directory
Drive Letter:\Program Files\Math Soft\Mathcad 2001i Professional\UserEFI

It should be noted that each projectile shape will require a different interface or dll to write out the file. Ideally, the best solution is to have the Mathcad generate the triangles defining the geometry and input those to a more generic dll/interface which will generate the fld geometry file.

Source code and project configuration files are also included.

user.xml

The xml file user.xml defines the interface to call into the DumpProjectile.dll to create the fld file described above.

This file is to be copied to the following directory (overwriting the existing file):
Drive Letter:\Program Files\Math Soft\Mathcad 2001i Professional\Doc\Funcdoc

The interface to the file is:
was Written := write_projectile(Curve1, Curve2, OutputFile)

where: wasWritten is a real number. If wasWritten = 1, the file was written and if = 0, the file was not written and an error occurred.

Curve1 and Curve2 are both 3xN real matrices which define the closed elliptical (circular) curves on the cut projectile.

OutputFile is a string which gives either a relative or full path of the file to be written.

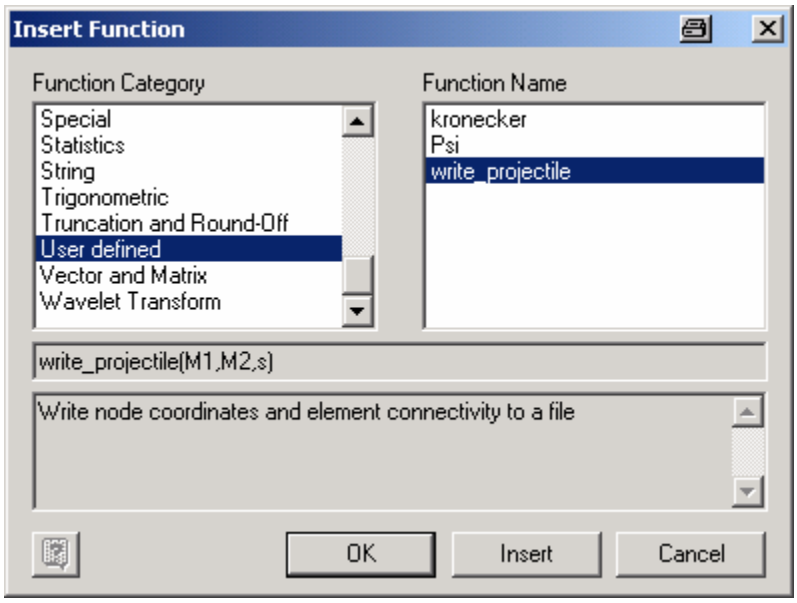

Trajectory Source Code for SCIRun

The most effective way to handle a trajectory path of a rigid body was to create a customized module for outputting transformation matrices as a function of time. This source code was code written to be integrated into SCIRun which reads a specially formatted file which contains the time, position, and I, J, K orientation vectors generated by the Mathcad projectile calculation code (see below). This data is combined for each time step to create a series of time-dependent transformation matrices which are applied to the geometry data in the fld file.

When this code is compiled into SCIRun it creates an MRC specific module called “Trajectory”. This module is then used in the graphical SCIRun net program to apply transformation matrices to the projectile geometry to animate the projectile along the projectile path.

In order to visualize the motion of the projectile it is necessary to slow the simulation down. A partial solution has been built into SCIRun. Through the use of environment variables, the trajectory output can be delayed for a period of time:

- **MRC_TIMESCALE** (Linux command: "export MRC_TIMESCALE=s" where s is a real number greater than 0) – This environment variable sets a scale by which the time steps input in the MRC file are scaled.

- **MRC_TIMEDELTA** (Linux command: "export MRC_TIMEDELTA=s" where s is a real number greater than 0) – This environment variable sets the absolute time between projectile transformations and overrides the effect of MRC_TIMESCALE.

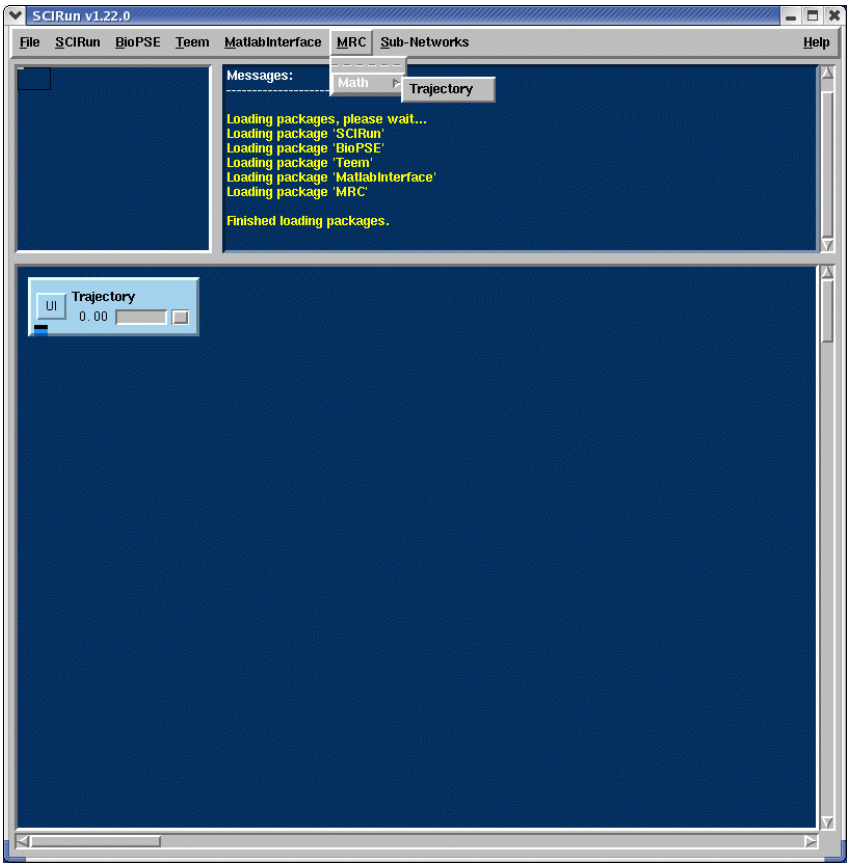

extract.sh

extract.sh is a Bourne shell script to be run on the Linux computer. The time, position, and I, J, K orientation data are output from Mathcad as distinct print files *.prn. These five files along with the fld geometry file are to be zipped up (using PKZIP or WINZIP) and copied onto the Linux computer.

This shell script extracts the files from the zip file and then combines the time, position, I, J, K files into one file called a .mrc file. It is this file which is read by the Trajectory module in SCIRun to process the time-dependent transformation matrices.

Phase1.net

Phase1.net is the SCIRun graphical program which reads in the projectile geometry, animates it using the time-dependent transformation matrices from the Trajectory module, and then displays the projectile.

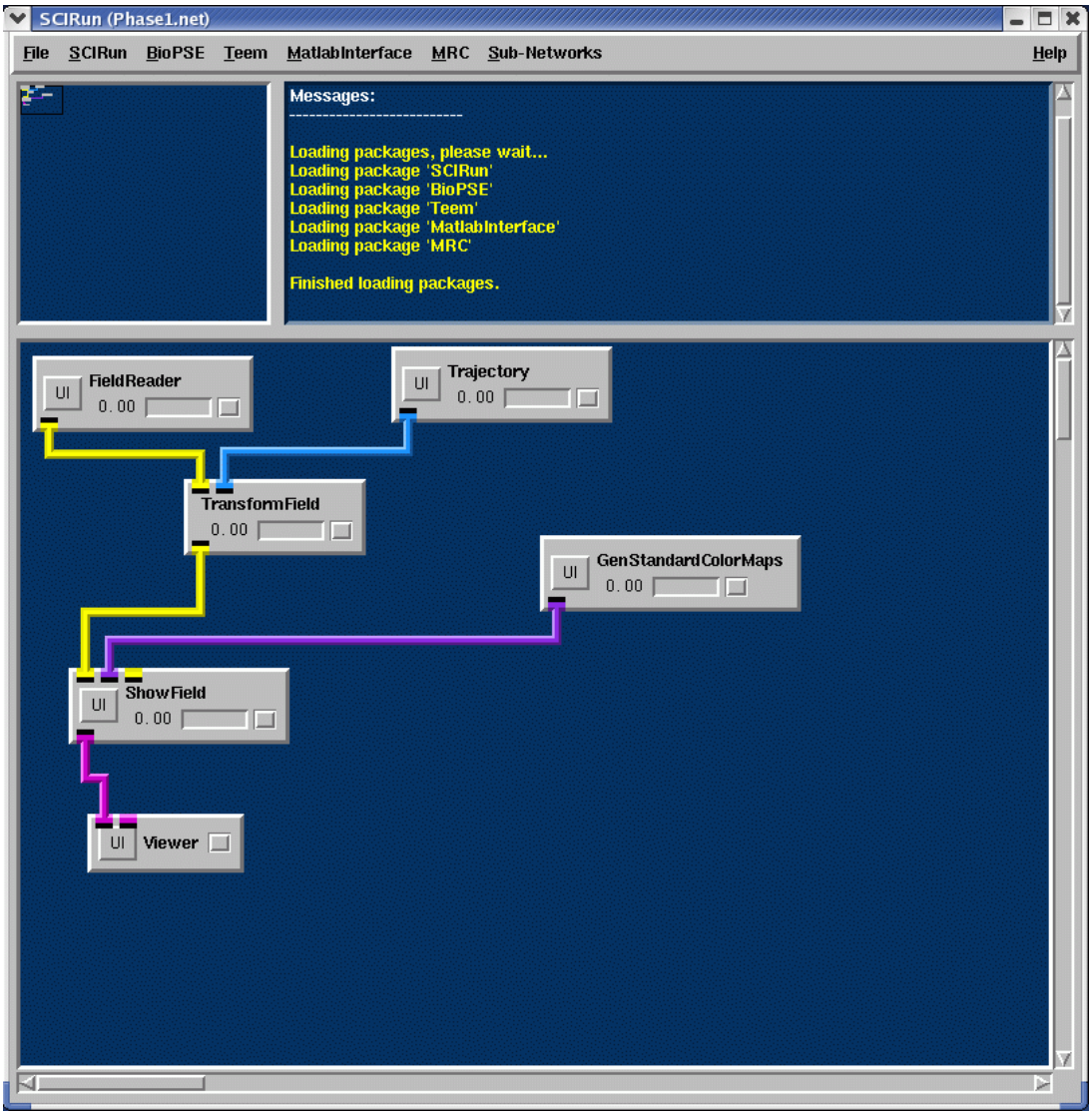

PC (Linux Redhat 9 OS) with Modified SCIRun Code

The University of Utah delivered a PC with Linux OS Redhat 9 installed along with an install of SCIRun.

The Trajectory source code described above has been integrated into SCIRun to support the Trajectory module used to describe the projectile trajectory via a set of time-dependent transformation matrices.

Other executables necessary for creating MPEGs and processing data files are also on the Linux computer.

Phase1*.mpg

These mpegs are generated using SCIRun and the linux utilities to show the projectile animation. Note that there is only one frame per time step.

As mentioned previously, environment variables can be used to slow the graphic output. Varying the speed at which the MPEG is played is also possible, but appears to be reliant on the number of frames available (see below).

SCIRun can output either an MPEG or individual frames. The MPEGs which SCIRun produces tend not to run in even time increments.. However, the frames are of good quality. An MPEG can be created from the frames (which are graphics PPM files) using the Linux "convert" command: "convert –quality 100 *.ppm Phase1.mpg". (It should be noted that the first frame is always the projectile geometry with the last transformation – when creating the MPEG, delete the first PPM file *.0000.ppm.)

Note on MPEG quality and playing: Even with the efforts made so far and a variable-speed MPEG player (see below), it is felt that the MPEG can still be improved. A shell script will be written on Linux which will generate multiple frames from the frame generated by SCIRun for each time step. It is felt that this will remove some of the "jerkiness" from the MPEG as well as make it easier to run the MPEG at a much slower speed.

movieplayer.exe

According to the MPEG-1 standard, a frame is to last 26 milliseconds or about 38 frames per second. We need to find a way to reduce the number of steps per second to a much slower speed.

It was desirable to find an MPEG player which allowed a variable rate of speed to play the frames. movieplayer.exe allows the speed of the MPEG to be anything from 1-300% of normal speed.

Assuming the play rate defined for MPEG-1 above, we should obtain the following behavior at various speeds for the MPEG:

MPEG SPEED	Length of frame	Number of Frames per Second
100%	26 ms	38
50%	52 ms	19
10%	260 ms	4
1%	2600 ms	0.4 or 2.6 seconds per frame

"The Best Movie Player 1.55" may be downloaded from http://www.svenbader.de/e_index.html.

It appears through experimentation that the effectiveness of variable play on the MPEGs we are producing is marginal. It is likely that it is dependent on the number of frames or on how those frames are generated for the MPEG. *However, it does appear that between the time scale and the variable speed MPEG player, we do have control over the speed of the simulation.* Further methods such as repeating frames may be considered for further refinement of the final MPEG.

Data Flow

Consider the following chart:

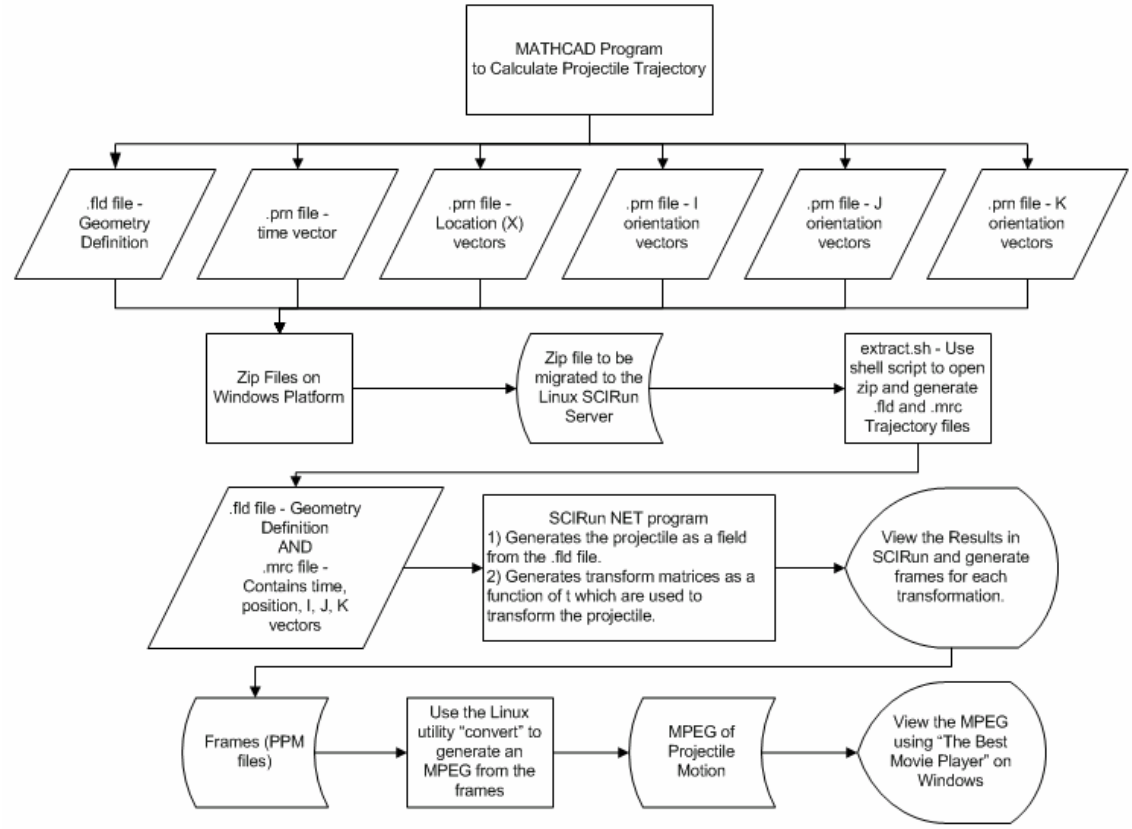

The flow of data is very clearly given here.

Comments on next step in Visualization

The analysis model for the block is axisymmetric. In order to graphically model the block, it will be necessary to write a small preprocessor which will generate a three-dimensional model from the axisymmetric model. The graphical nodes in the axisymmetric model will correspond to the masses in the spring model. The (undeformed) block will correspond to a three-dimensional representation of the axisymmetric spring model (masses) at rest.

At the time of penetration, it will be necessary to gather information from both the spring model (the masses which define the nodes which are now being deformed to define the cavity) and from the hydro code which will provide the strains.

2.3.4 Development of Analytic Model and Permanent Wound Cavity Results

Heart Geometry

The geometry of the heart was provided as a stereo lithography or STL file from Stanford. however, it was necessary to translate the model into a data format which could be used by various engineering analysis software packages. Also, it was necessary to be able to perform a rigid-body transformation (translation and rotation) to place the model in various coordinate frames as required by the analysis software.

Several different operations were performed on the STL model provided by Stanford.

1. Use Paraview 1.8 to decimate the STL file as required for model verification.

2. Use Paraview 1.8 to validate and correct the Zone 12 entry and exit points.

3. Convert the model to an *MSC.Patran Neutral File.* This file is a fairly standard method of passing finite element definitions between different finite element preprocessors. This model was used by a special meshing package to generate a well-conditioned hexagonal mesh for the nonlinear finite element solver; the output being used to create the Mission Research movies.

Modeling Toolkit

In order to perform the data format translations and coordinate frame transformations, a "toolkit" of computer routines was written from which we were able to generate programs as needed to process the geometry as well as generate proper analyses models. The toolkit was a set of C++ classes which were written and tested on both Linux and Win32 platforms. The toolkit has the following capabilities:

- Platform-independent methods for file handling.
- Tensor, Matrix, Vector, Coordinate Frame, and Transformation Matrix support.
- Support for MathCAD objects which allows it to be integrated directly into MathCAD.
- Spline fitting including fitting of n-dimensional splines.
- Other mathematical methods including eigenvalue and eigenvector support.
- Read and Write of STL, SCIRun fld files, and MSC.Patran Neutral Files.

Heart Material Properties

We worked with University of California at San Diego to develop a method for generating material properties for the heart based on the information available. The method included both a first-order approximation and a modeling process by which the Stanford heart model as geometry along with data from other sources to generate the material properties. These properties are derived from an energy function which supports large elastic deformations where the deformations are dependent on the fiber directions in the myocardium. The first-order approximation was used for the Phase 1 model.

Integration of Analyses Results

There were several aspects of the analyses that required integration to generate the final results.

1. The results from the kinematic analysis of the projectile which provide the path of the projectile including location of the center of mass G and rotation about G.

2. The nonlinear spring analysis generated the shape of the cavity from the initial entry till the motion had sufficiently decayed. This data needed to be converted from a time-based representation to a spatial representation in three dimensions.

3. Strain calculations over the time period of interest. The strains calculated included the axial, circumferential and radial strains. From these, we calculated the principal strains and the maximum principal strain at any point.

Using the projectile path as calculated from the kinematic analysis (1) and the shape of the cavity from the spring analysis (2), the cavity shape corresponding to the nonlinear projectile path can be calculated over the time period of interest. Corresponding strain calculations then can be mapped onto the resulting cavity wall as well as into the myocardium of the heart up to a predetermined distance from the cavity wall.

The C++ toolkit was used to create a program which could output the cavity at any point of time along with the strain tensor on the cavity wall. The output was provided as a SCIRun fld file where the geometry was transformed into the Zone 12 coordinates as provided by Stanford. The output was given as to enable downstream applications to easily integrate the analysis results. The following images depict the different strains on the final cavity wall as provided for the demonstration. The images were output directly from SCIRun.

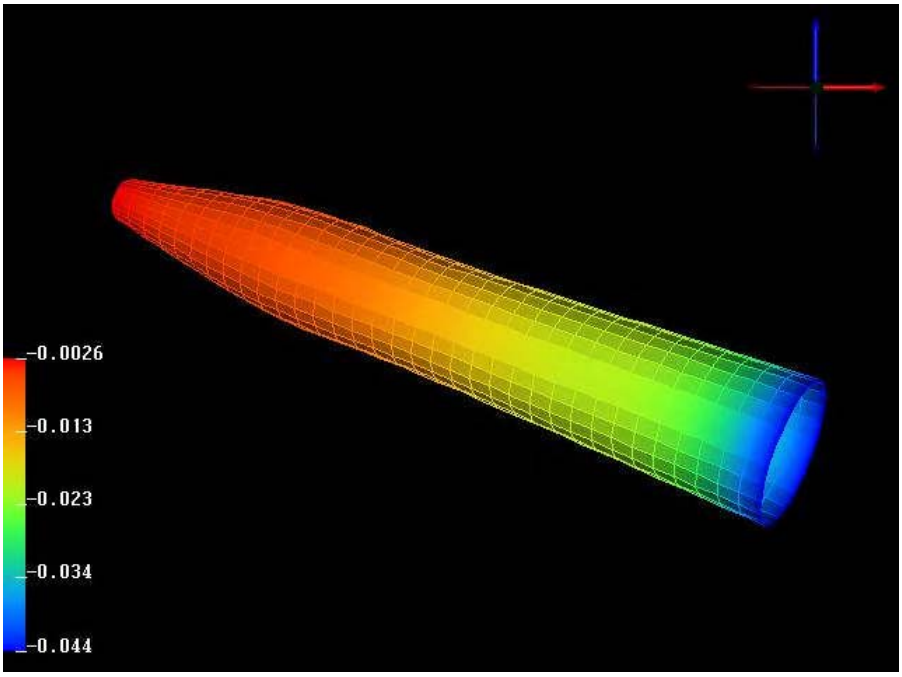

FIGURE 44. Final Cavity Geometry and Final Axial Strain Shown as a Fringe Plot

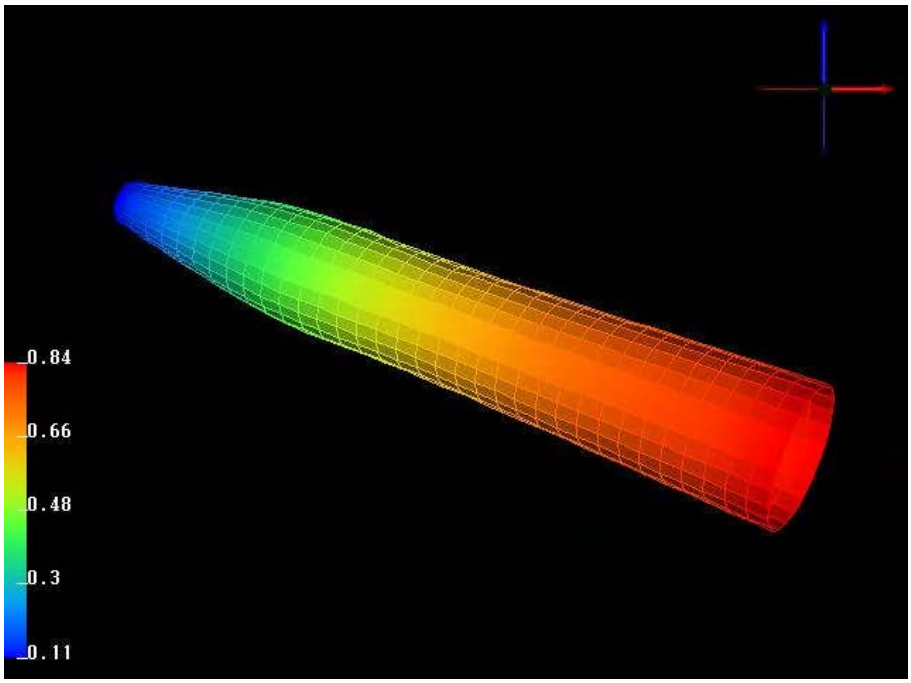

FIGURE 45. Final Cavity Geometry and Final Circumferential Strain Shown as Fringe Plot

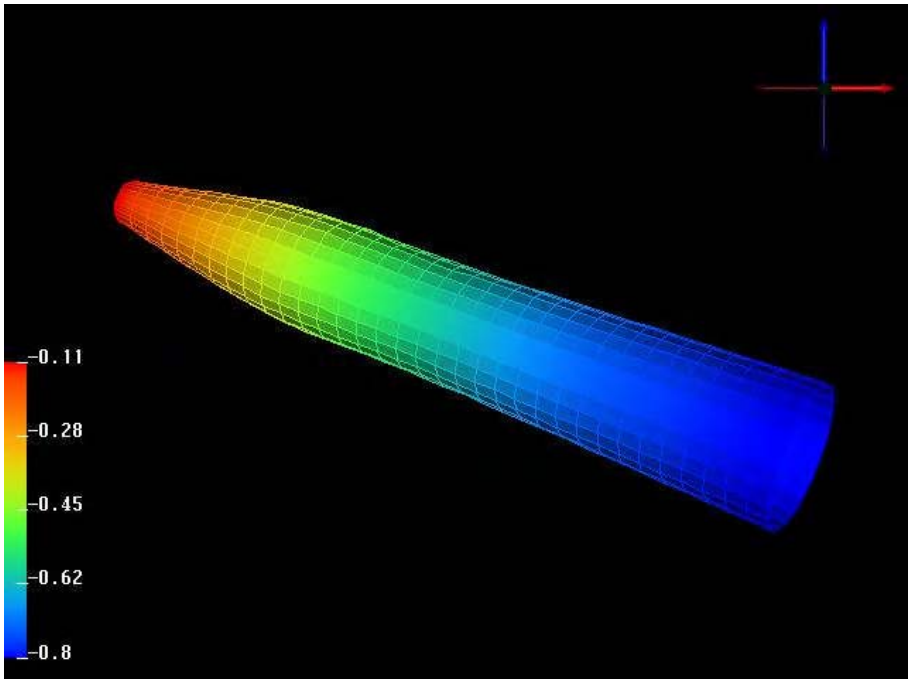

FIGURE 46. Final Cavity Geometry and Final Radial Strain Shown as a Fringe Plot

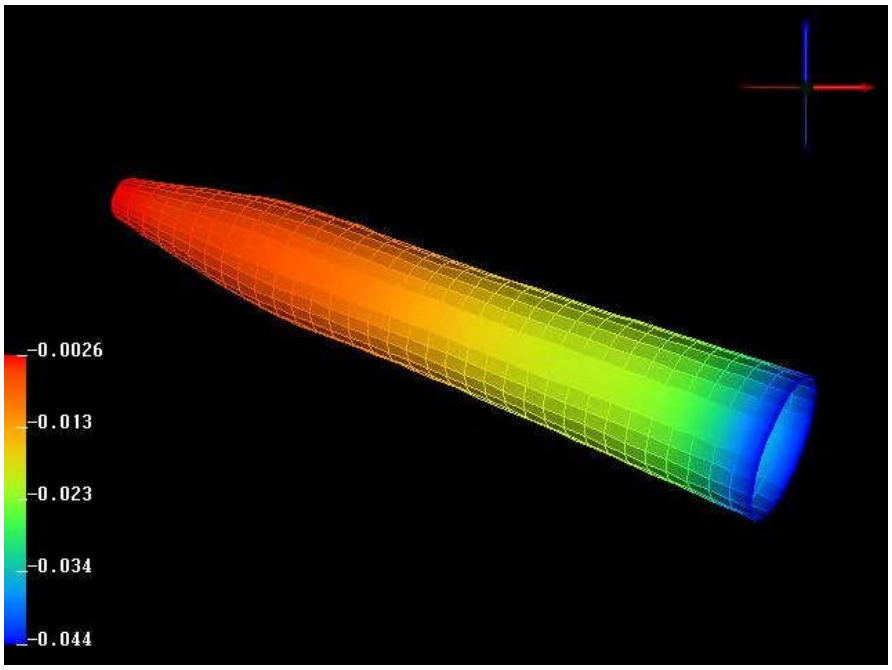

FIGURE 47. Final Cavity Geometry and Final *Principal* Axial Strain Shown as Fringe Plot

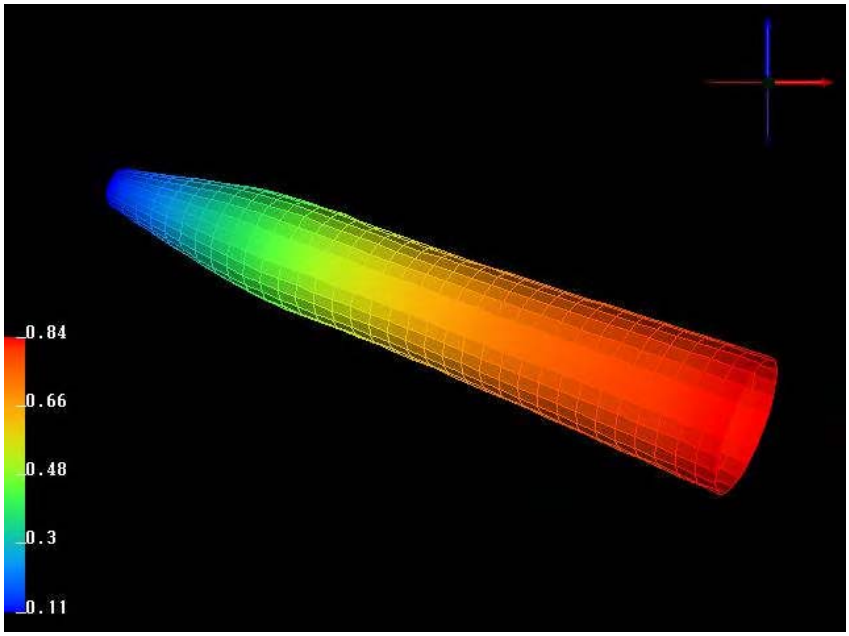

FIGURE 48. Final Cavity Geometry and Final *Principal* Circumferential Strain Shown as a Fringe Plot

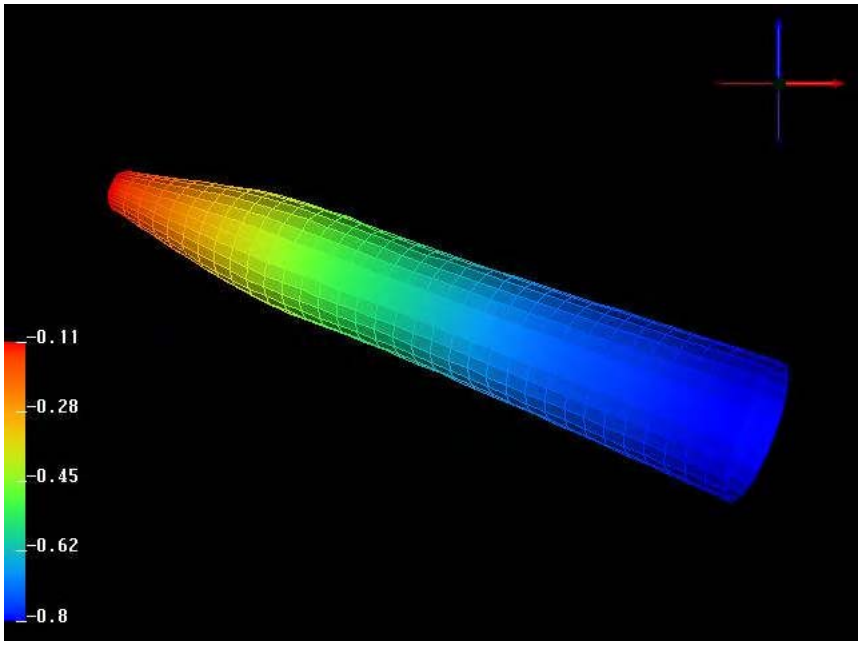

FIGURE 49. Final Cavity Geometry and Final *Principal* Radial Strain Shown as Fringe Plot

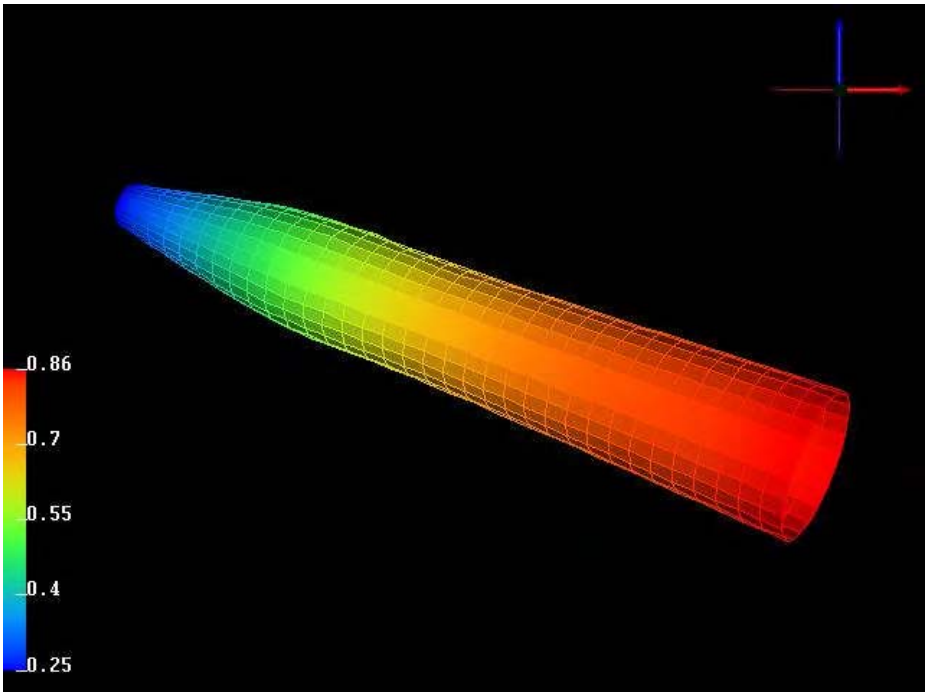

FIGURE 50. Final Cavity Geometry and Largest *Principal* Strain over all Time Steps Shown as a Fringe Plot

Support for Stanford Strain Calculations

Two variations of the code were generated as well to support a request from Stanford University and University of Michigan to provide strain results within the myocardium itself. Stanford University requested that Mission Research generate a series of offset cylinders with strain results. These results were given as SCIRun fld files and represent provide the maximum principal strains at offset distances from the cavity wall into the myocardium. These results were required for Stanford to run their moment calculations.

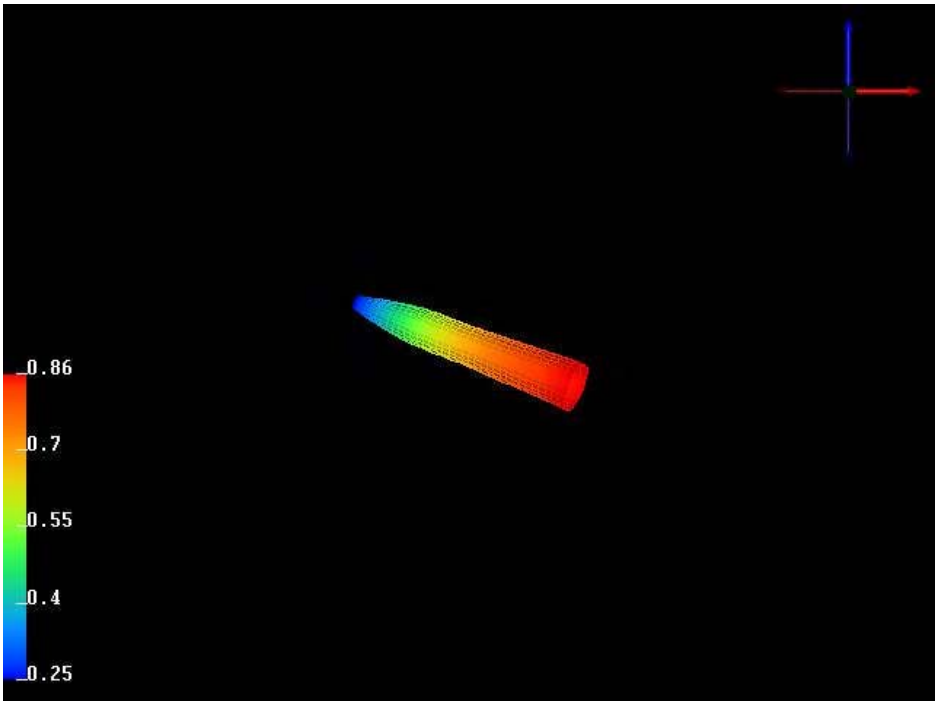

FIGURE 51. Maximum Principal Strain at the Cavity Wall

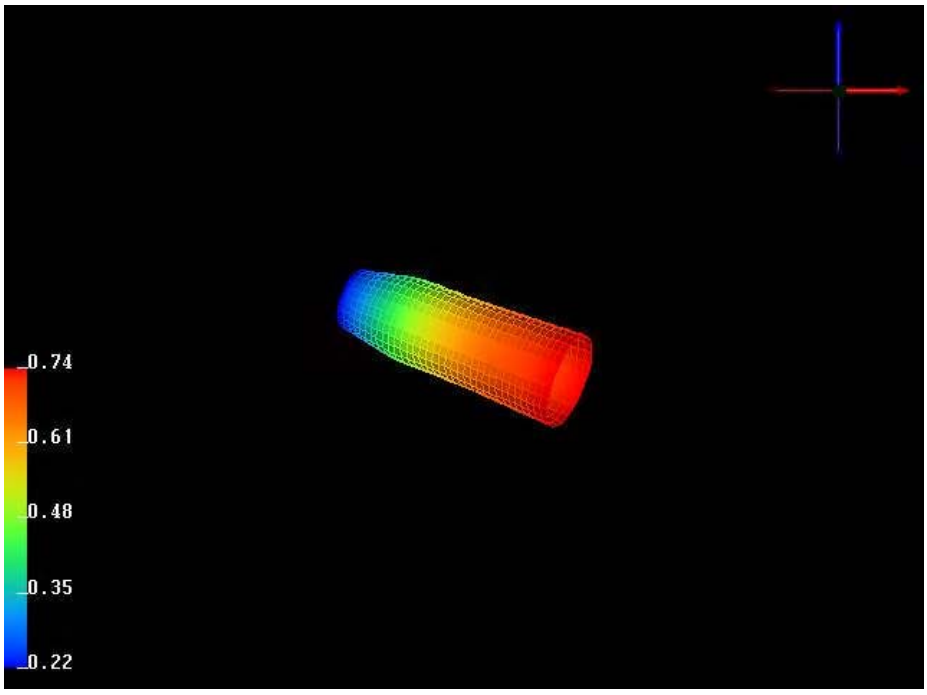

FIGURE 52. Maximum Principal Strain at 2.5 cm from the Cavity Wall

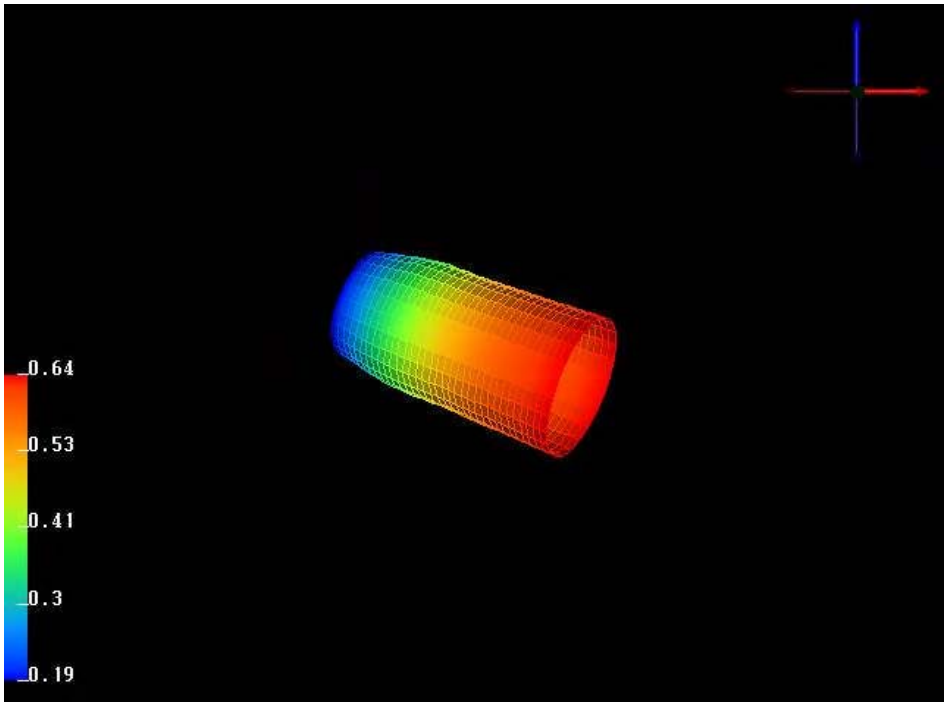

FIGURE 53. Maximum Principal Strain at 5 cm from the Cavity Wall

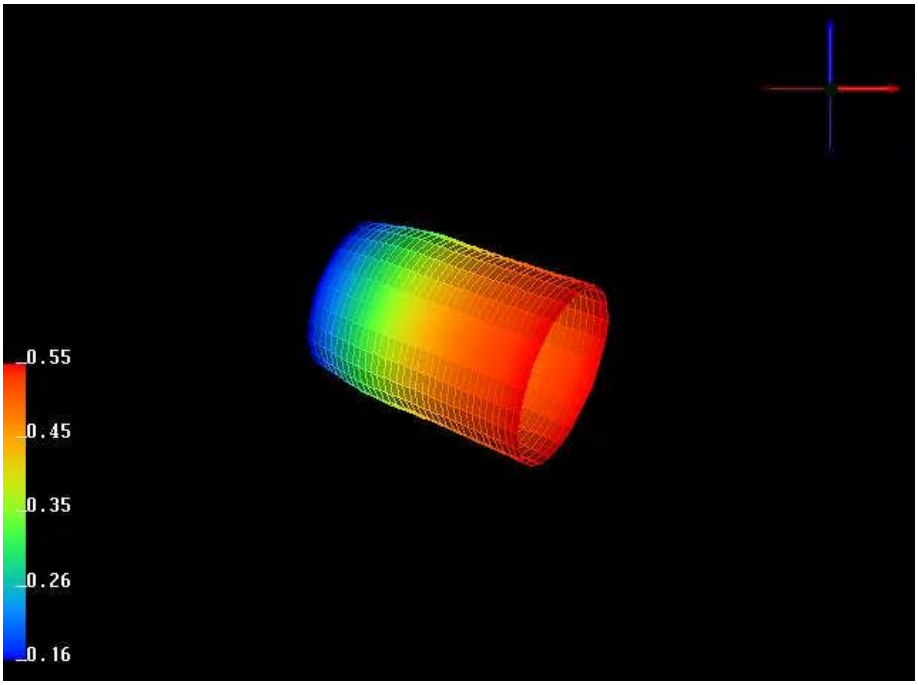

FIGURE 54. Maximum Principal Strain at 7.5 cm from the Cavity Wall

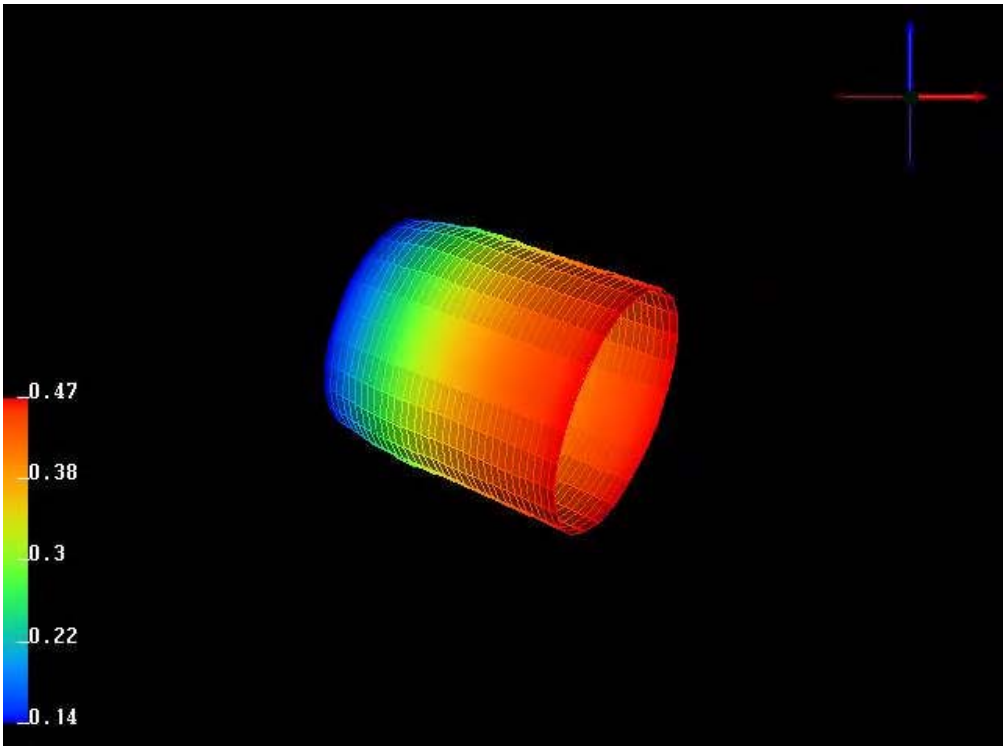

FIGURE 55. Maximum Principal Strain at 10 cm from the Cavity Wall

The University of Michigan desired to obtain strains via a more general API in which points could be input (in Stanford coordinates) via the command line or a file. This is useful for mapping strains into the myocardium. This capability was provided near the end of the preparation time for the demo, so it may not have been used at the demo, but does show the capability to provide such analytical results.

TASK 3
BALLISTIC EXPERIMENTS

Ballistic testing encompassed using different projectiles – various diameter spheres, cylinders, and "cut-cylinders" (cf. Figure 2, page 10) and different target materials – homogenous 10, 15 and 20% ordnance gelatin targets and inhomogeneous hollow 10 and 20% gelatin targets with water inclusions.

3.1 INITIAL BALLISTIC TESTING

Ballistic testing initially focused on implementation of a high-speed digital video system to record the penetration process of two projectiles, namely a 0.250" diameter steel sphere and a steel, right circular cylinder measuring 0.250" diameter and 0.500" length (Length/Diameter, L/D = 2). A monolithic block of 20% ballistic gelatin was impacted at various velocities chosen to produce similar depths of penetration, nominally six inches, or 60% of the target thickness. Finally, the highest velocity which would result in the cylindrical projectile coming to rest within the target material was implemented for better comparison with existing and newly developed data for spherical projectiles. Table 6 presents the shot log for the initial tests which have high-speed digital video records.

TABLE 6. Initial Ballistic Testing

Run #	Projectile	Mass	Target	Velocity (fps)	Depth (in.)
0506-07	1/4" steel sphere	1.04gm	20% gelatin	1170	6.3
0506-08	L/D=2 1/4" steel cylinder	3.12gm	20% gelatin	490	6.3
0506-09	L/D=2 1/4" steel cylinder	3.12gm	20% gelatin	470	5.7
0506-10	L/D=2 1/4" steel cylinder	3.12gm	20% gelatin	740	9.0

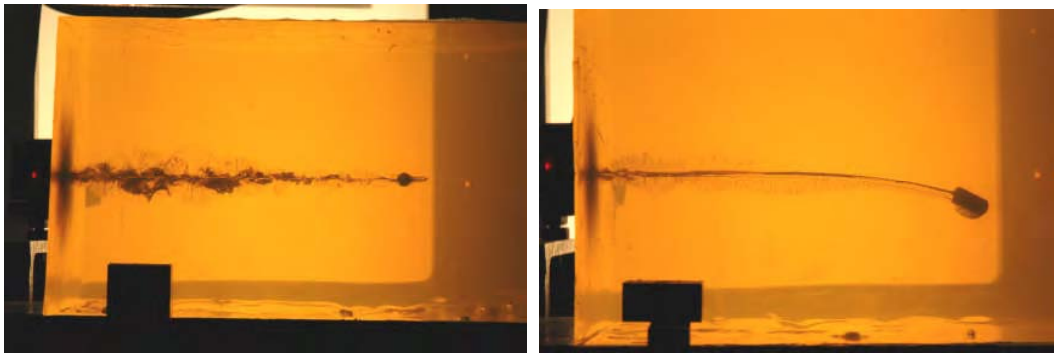

FIGURE 56. Comparison of Typical Wound Track for Sphere and Cylinder

The sphere produced a straight wound track while the cylinder generally produced a wound which deviated from normal as the projectile slowed. Posttest photos of typical wound tracks are presented in Figure 56.

Implementation of the high-speed digital system allowed an accurate record of the penetration history for the two projectiles within the gelatin targets. Posttest processing software facilitated measurement of projectile location throughout the penetration event. Using the framing rate of the camera, an average projectile velocity was calculated between successive frames. Frame-to-frame uncertainties in the precise location of the tip of the projectile resulted in error bands about the actual velocity decay curve. However, since the video data provided a continuous record of the penetration event, uncertainties did not accumulate in the average velocity calculation. Therefore, a curve-fit to the measured data resulted in a reasonable polynomial description of the velocity decay over time for the experiments in Table 6. That data is presented in Figure 57.

In addition to the projectile trajectory information, the high-speed video also reveals a fluid-mechanical, wake-like structure that trails the penetrating projectile (see Figure 58). The origin of this structure contains the projectile. The transverse dimensions first grow and then shrink, ending in a position, which is similar to the permanent wound track created by the projectile.

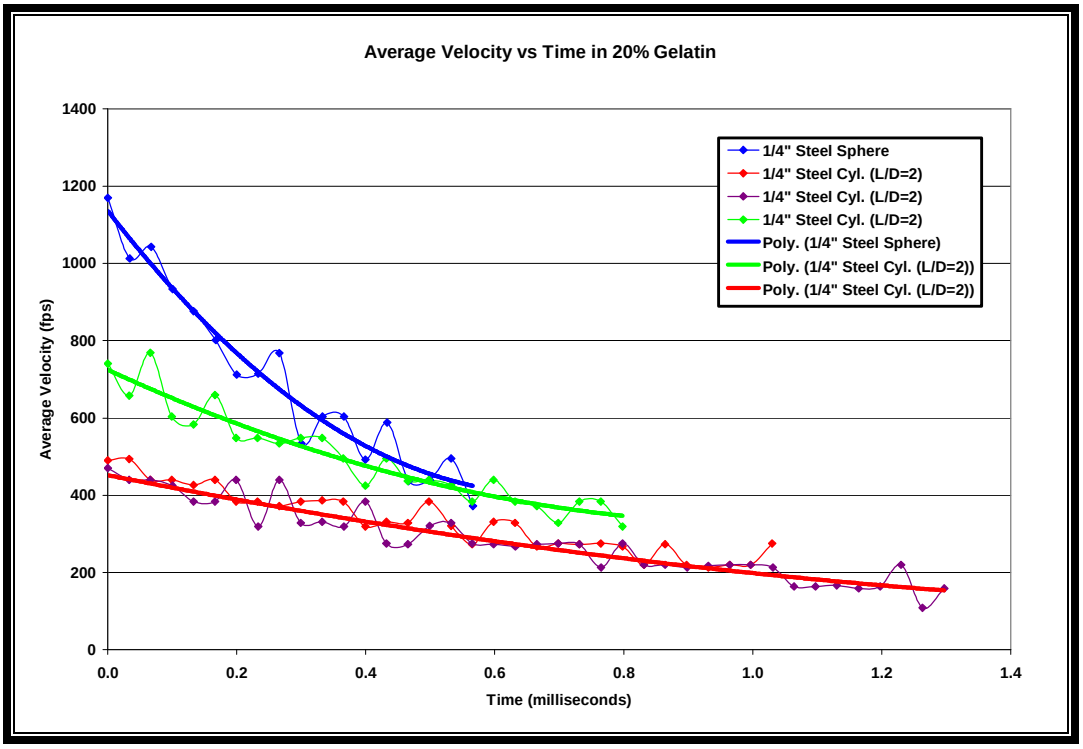

FIGURE 57. Velocity Decay for Cylinder and Sphere in 20% Ballistic Gelatin

The images recorded in the video were generated by imaging the test target against a back-lighted optical diffuser which is basically equivalent to illuminating the target with a point source at infinity. This is the technique used for "Shadow Photography" in fluid mechanics to reveal density gradients (diffraction) in the test volume. It is not clear that the present problem can be treated as a problem in fluid mechanics; however some observations and tentative conclusions can probably be made for a reasonably axisymmetric configuration.

The dark boundaries of the "wake" result from incident light being diffracted, reflected or absorbed by the "altered" property details of the material in these boundaries. The very light region in the center of the "wake" (cf. Figure 58) results from the relative absence of reflective and absorptive changes as well as diffracted light entering the region. A void or a "cavity" will produce these results.

The features discussed above are rather well depicted in the early entry process of a cylinder into the gelatin target as shown in Figure 58. We estimate the local (axisymmetrical) "cavity" to be given by the diameter indicated. A record obtained near the entry site was selected for this presentation because the dimension of the entry hole in the impacted surface can be confirmed by the appearance of a typical crater lip. It must be remembered that we record a two-dimensional image only. A pronounced growth of the "cavity" is very obvious when the cylinder pitches in the imaged plane. This is also consistent with the suggested interpretation of the optical data.

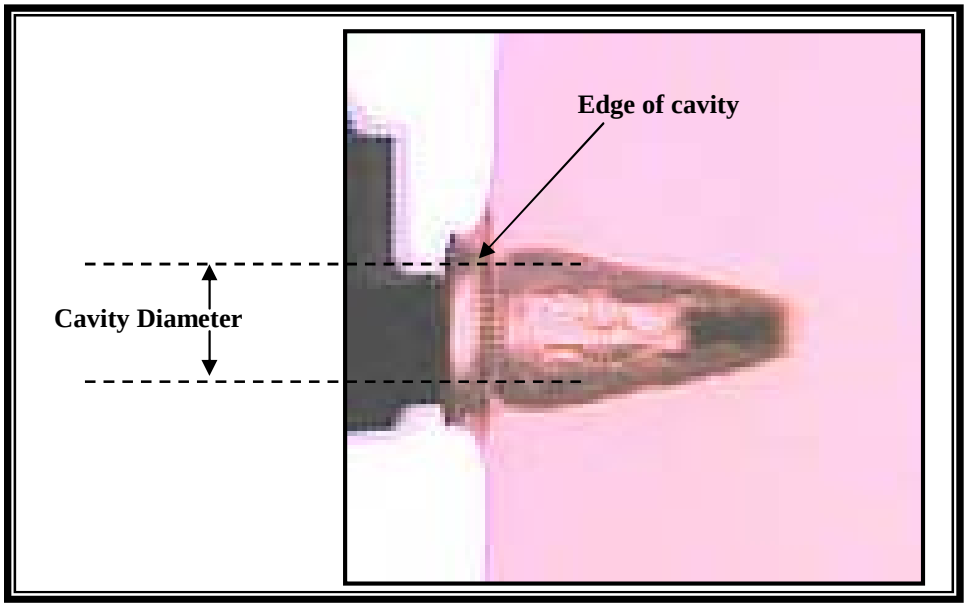

FIGURE 58. Determination of Boundaries of Temporary Cavity (Experiment 0506-10)

3.2 SPHERICAL PROJECTILES

After the initial ballistic tests in Table 6, testing was then dedicated to filling voids in the penetration data space for the primary tissue simulant, namely 20% ordnance gelatin (see Table 8). Previous penetration data obtained by Mission Research and Edgewood Arsenal used small steel spheres (BB's, 0.17" diameter). Limited data for 0.25" steel spheres also existed at Mission Research. It was concluded that the maximum penetration depth could be scaled, over the velocity range of primary interest, by the ballistic coefficient (weight divided by the product of the drag coefficient and the area) of the projectiles. The low velocity range, from zero to some threshold velocity to assure penetration into the target is excluded from this linear dependence, as are the higher velocities, of order 1500 feet per second and above, for small spheres. This is elaborated in the Task 1 discussion.

TABLE 7. Additional Testing using Spherical Projectiles

Projectile	Target	Velocity (fps)	Depth (inches)
BB	20% Gel	280	0.0
BB	20% Gel	340	0.3
BB	20% Gel	400	0.6
BB	20% Gel	530	1.0
BB	20% Gel	675	1.5
BB	20% Gel	700	1.6
BB	20% Gel	1000	2.9
BB	20% Gel	1255	3.6
BB	20% Gel	1600	4.8
BB	20% Gel	1600	4.8
BB	20% Gel	1610	4.9
.25" sphere	20% Gel	245	0.6
.25" sphere	20% Gel	310	1.1
.25" sphere	20% Gel	440	1.6
.25" sphere	20% Gel	1350	6.9
.25" sphere	20% Gel	1455	7.2
.25" sphere	20% Gel	1550	7.5
.25" sphere	20% Gel	1600	8.1
.25" sphere	20% Gel	1630	8.2
.25" sphere	20% Gel	1750	8.1
.375" sphere	20% Gel	810	6.7
.375" sphere	20% Gel	760	6.4
.375" sphere	20% Gel	930	8.0
.375" sphere	20% Gel	185	0.4
.375" sphere	20% Gel	270	2.3
.30" wedge	20% Gel	1120	7.7
.30" wedge	20% Gel	1230	7.8
.30" wedge	20% Gel	710	6.0
.30" wedge	20% Gel	490	4.1
.30" wedge	20% Gel	1360	9.2

With these limitations in mind we were able to correlate old and new spherical projectile penetration data in 20% ordnance gelatin targets. Measured maximum penetration (δ in inches) data using BB's (diameter, $d = 0.17$ Inches) were plotted versus striking velocity for normal impacts (see Figure 59). A linear (hand) fit crosses the velocity axis ($\delta = 0$) at 260 feet per second with a slope of 3.67×10^{-3}, *or* $2.15 \times 10^{-2} d$, with d in inches. The maximum penetration is then:

$$\delta = 2.15 \times 10^{-2} d(V - 260).$$

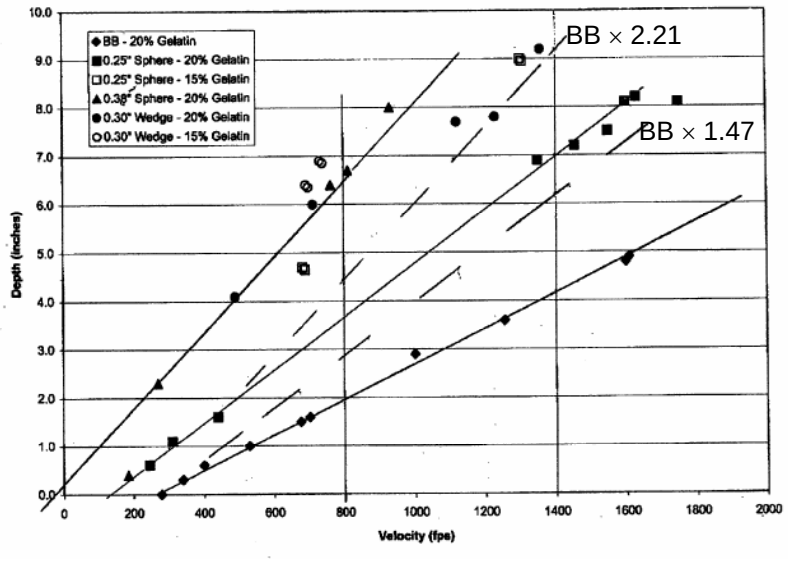

FIGURE 59. Ballistic Data using Spherical Projectiles of Different Sizes

Scaling by ballistic coefficient, that is, scaling by "d" was then applied to existing and the newly generated 0.25" sphere data. The dashed line in the attached figure, labeled "(BB × 1.47)" results from multiplying the fit through the BB-data by 1.47, which is the diameter ratio of the 0.25"-inch spheres and the BB's. This line is seen to fall slightly below the data from 0.25"-sphere impact tests. After parallel translation to cover the new data, shown by triangles, the solid line, labeled 0.25" resulted. It is seen to cross the velocity axis at 130 feet per second, for $\delta = 0$. This line has a slope of 5.40×10^{-3} *or* $2.16 \times 10^{-2} d$, where d is now 0.25". The equation for max penetration is then:

$$\delta = 2.16 \times 10^{-2} d(V - 130)$$

Following the same procedure for the newly generated 0.375-inch steel sphere data yielded a slope of 8.10×10^{-3} *or* $2.16 \times 10^{-2} d$, with a $\delta = 0$ intercept at V = -30 feet per second. The equation for 0.375-inch sphere penetration becomes then:

$$\delta = 2.16 \times 10^{-2} d[V - (-30)]$$

The slopes of the correlation lines through the 3 data sets are proportional to the diameters of the projectiles that generated the data. This suggests that ballistic coefficient scaling holds rather well for the velocity range of primary interest.

An asymmetrical projectile geometry was somewhat arbitrarily selected to explore penetration trajectories of projectile fragments. We elected not to use the complicated geometry identified as the Army Fragment Simulating projectile and opted for a less symmetrical geometry which is readily produced. Our projectile, shown in Figure 2 (page 10), is a .30 caliber modified right circular cylinder, two diameters long with one end ground off at 45 degrees. This configuration is readily launched and will rapidly develop yaw that should lead to early tumbling.

A posttest photograph of an exploratory impact in 20% ordnance gelatin and using the asymmetrical projectile ("Wedge") described above is shown in Figure 60. The large diameter material disruption, early in the penetration (see Figure 61), suggest that the projectile was yawing through 90 degrees. The rapid reduction in the damage diameter, followed by a small cylindrical damage region, suggests that the projectile moved nearly end-on stably for the latter part of its trajectory. The above observations are substantiated by high speed video records, recorded during penetration, and the resting orientation of the projectile. The deviation from a rectilinear trajectory is obvious. Also note that wound tract diameter is highly non-uniform toward the end of its trajectory even when the projectile is traveling without tumbling, base forward. Sometimes the wound tract is much smaller than the projectile diameter and sometimes larger.

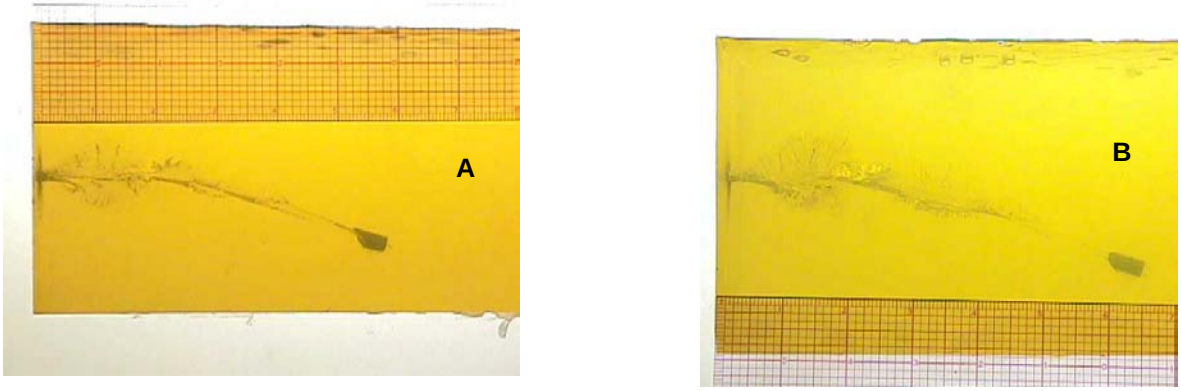

FIGURE 60. Longitudinal Target Cross-Sections showing that projectile has rotated 180 degrees so that it is penetrating base forward. (A) Experiment 040603-02 – Wedge into 20% Gelatin @ 710fps; (B) Experiment 040607-04 – Wedge into 15% Gelatin @ 730fps.

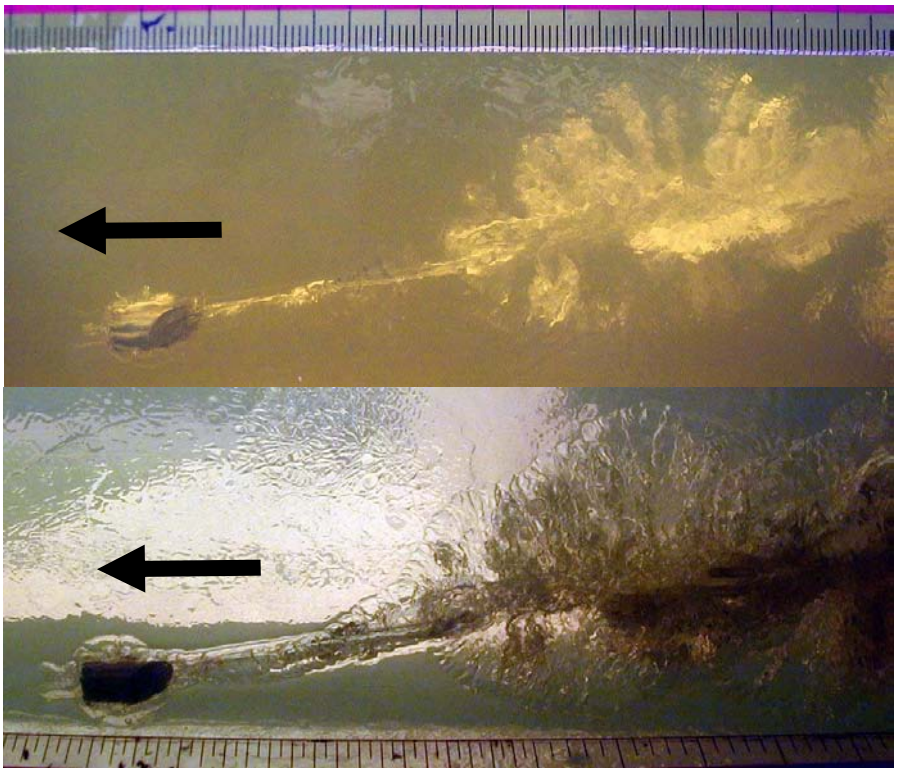

FIGURE 61. Macro Views of Target Damage using different lighting

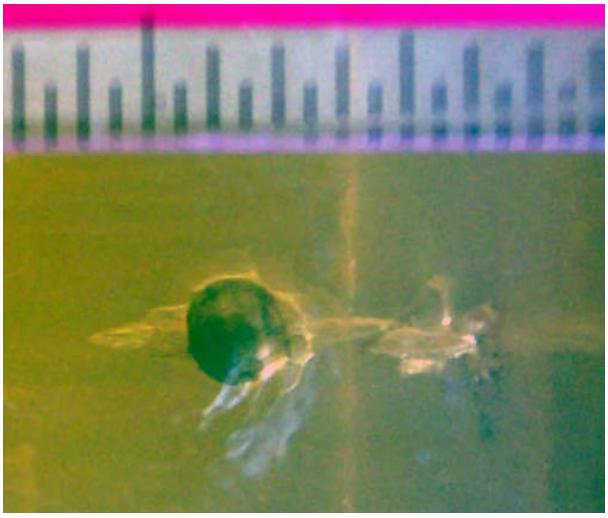

FIGURE 62. Posttest Photograph of Spherical Penetration Ballistic Experiment

Spherical particle impacts, as expected, reveal virtually no deviation from the striking velocity direction. However, here too, a wound tract much smaller than the projected area of the projectile is evident. See Figure 63. Also note that there is material disruption in front of the projectile and the "wound tract" diameter behind the projectile is smaller than the projectile diameter due the recoil of the material in the wake of the projectile.

3.3 VARIATION OF MATERIAL PROPERTIES

Testing of penetration depth, permanent and temporary wound tract, and projectile dynamics in ordnance gelatin targets were also conducted to determine differences in response attributable to differences in material properties in the target material. For this purpose we tested ordnance gelatin of 10% (by weight) and 15% concentrations for comparison to the primary data base generated for 20% ordnance gelatin.

We performed impact tests with spheres and a 30 caliber "wedge-cylinder" projectile with striking velocities ranging from nominally 500 to 1,400 feet per second as seen in the Run Log in Table 8, below. For a qualitative comparison we included a single test using a "standard US Army Fragment Simulator." This small (1.13 grams), asymmetrical projectile produced a penetration depths very similar to those produced by 0.25-inch, spherical projectiles (1.04 grams), in 15% gelatin targets.

TABLE 8. Ballistic Experiments on Homogeneous 10, 15, and 20% Gelatin Targets

Run #	Projectile Diameter (in)	Projectile Shape	Projectile Mass (gms)	Target Material	Velocity (fps)	Projectile Resting Depth (in)	Maximum Visible Penetration (in)
Q2-01	0.250	Sphere	1.04	15% Gelatin	1300	9.0	9.0
Q2-02	0.250	Sphere	1.04	15% Gelatin	680	4.7	4.6
Q2-03	0.300	Wedge	4.10	15% Gelatin	730	6.9	6.8
Q2-04	0.300	Wedge	4.10	15% Gelatin	690	6.4	6.4
Q2-05	0.250	Sphere	1.04	15% Gelatin	900	6.8	6.8
Q2-06	0.250	Sphere	1.04	15% Gelatin	460	3.2	3.2
Q2-07	0.250	Sphere	1.04	15% Gelatin	1390	thru	thru
Q2-08	0.300	Wedge	4.10	15% Gelatin	700	6.7	6.7
Q2-09	0.220	Frag Sim	1.13	15% Gelatin	1060	6.9	6.9
Q2-10	0.300	Wedge	4.10	15% Gelatin	900	7.2	7.6
Q2-11	0.300	Wedge	4.10	15% Gelatin	1000N	7.6	7.9
Q2-12	0.300	Wedge	4.10	20% Gelatin	1050	6.8	7.1
Q2-13	0.300	Wedge	4.10	20% Gelatin	1400	9.2	9.6
Q2-14	0.250	Sphere	1.04	10% Gelatin	600	8.3	8.3
Q2-15	0.250	Sphere	1.04	10% Gelatin	560	8.0	8.0
Q2-16	0.250	Sphere	1.04	15% Gelatin	940	6.0	6.1
Q2-17	0.300	Wedge	4.10	10% Gelatin	470	7.3	7.4

An important objective of this test series was to explore techniques for mapping, in real time, projectile trajectories, especially for the asymmetrical "wedge" projectiles. As expected, high framing rate photography was best suited for this purpose, in transparent targets. These

photographic records reveal projectile location, orientation and velocity, and also formation and collapse of the temporary wound tract.

We have derived projectile pitch data from this record and one example is presented in Figure 63. below. In addition, projectile deceleration as a function of penetration depth was obtained as well as cavity wall dynamics.

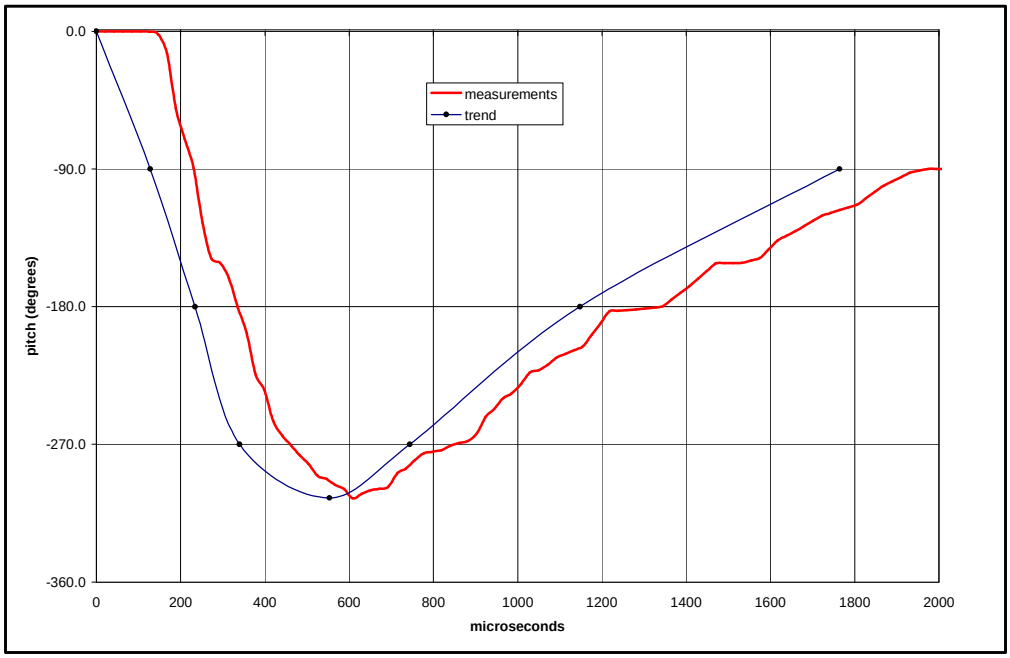

FIGURE 63. Cut-Cylinder Rotation Angle versus Penetration Depth for Experiment Q2-13.

KEY RESEARCH ACCOMPLISHMENTS AND CONCLUSIONS

- A model of tissue response from a survivable penetrating wound to the human left ventricle was developed. The model described the residual wound tract and qualitatively was consistent with anecdotal data from military trauma surgeons regarding these wounds. The predicted wound geometries was also consistent with animal testing.

- The model also described the tissue dynamics of the wound tract from a beating heart, including modulation of the pressure in the wound tract. This was discovered to be an important effect in that for small diameter wounds, the tract periodically opens and closes permitting and obscuring blood loss form the wound. Failure to include his effect results in gross overestimation of blood loss and skewed results for predicted outcomes.

- Stress waves propagating over heart form the ballistic impact are sufficient, based on previous research, to cause transient ion upset in the neighborhood of the wound tract. This upset is sufficient to disrupt the polarization wave causing contraction of the heart. This disruption can cause arrhythmias that can transition into potentially lethal fibrillation. These effects were not further considered in this effort but should be considered in the future.

- A technique was developed to model relevant human tissue dynamic properties based on quasistatic mechanical property data for these tissues. This is important in that dynamic mechanical property data is not available for human tissue and these sets of data are critical input for any subsequent analysis of projectile penetration. The methodology was validated by using various formulations of gelatin where only static mechanical property data was available and correlating with experimental measurements (using high speed digital video) of projectile velocity, projectile rotational kinematics, projectile trajectory, transient target response, and residual cavity (wound tract) in the target as a function of time during and immediately following projectile penetration.

REPORTABLE OUTCOMES

The following five peer-reviewed papers were published from this project. Copies of these papers are included in the indicated appendices for the reader's convenience.

(1) Eisler, R. D., Stone, S. F., and Chatterjee, A, K., *Analytical Simulation of Penetrating Wounds to the Heart*, MMVR 2005. See Appendix N.

(2) El-Raheb, M., *An Acoustic Model for Wave Propagation in a Weak Layer*, JOURNAL OF APPLIED MECHANICS, Vol. 72, September 2005, pages 744-751. See Appendix J.

(3) El-Raheb, M., *Transient Waves in an Inhomogeneous Hollow Infinite Cylinder*, INTERNATIONAL JOURNAL OF SOLIDS AND STRUCTURES, Accepted with Revision, 7 February 2005. See Appendix M.

(4) El-Raheb, M., *Wave Propagation in a Hollow Cylinder Due to Prescribed Velocity at the Boundary*, INTERNATIONAL JOURNAL OF SOLIDS AND STRUCTURES, Accepted with Revision, 8 March 2005. See Appendix K.

(5) El-Raheb, M., *Transient Response in a Finite Hollow Cylinder from Time-Delayed Prescribed Motion at the Boundary*, JOURNAL OF SOUND AND VIBRATION, Accepted with Revision, 11 March 2005. See Appendix L.

CONCLUSIONS

ATK Mission Research was sponsored by DARPA's *Virtual Soldier* program to analytically simulate residual wound tracts and tissue dynamics associated with a survivable wound from an explosively driven fragment penetrating the left ventricular wall of the human heart. The resulting ATK Mission Research wound description was used in the DARPA/University of Michigan *Virtual Soldier* program as initial conditions for describing blood loss and occurrence of hemorrhagic shock. A key finding was that the tissue dynamics of the wound tract from a beating heart, particularly for small diameter wounds that are survivable, are critical in the resulting blood loss calculations. The wound tract periodically opens and collapses due to modulation of pressure within the tract. This intermittent open and closing of the wound intermittently prevents and permits blood loss form the wound. Failure to include the tissue dynamics in the blood loss calculations results in a gross overestimation of blood loss and skewed results for predicted outcomes.

Stress waves propagating over heart form the ballistic impact are sufficient, based on previous research, to cause transient ion upset in the neighborhood of the wound tract. This upset is sufficient to disrupt the polarization wave causing contraction of the heart. This disruption can cause arrhythmias that can transition into potentially lethal fibrillation. These effects were not further considered in this effort but should be considered in the future.

Finally, a technique was developed to model relevant human tissue dynamic properties based on quasistatic mechanical property data for these tissues. This is important in that dynamic mechanical property data is not available for human tissue (although quasistatic mechanical property data is) and dynamic mechanical property data is critical input to any subsequent analysis of projectile penetration into tissue. The ATK Mission Research methodology was validated by using various formulations of gelatin that from previous research were shown to be phenomenologically similar to soft tissue in terms of projectile-tissue interaction. Static mechanical property data was used for these "unknown" formulations of gelatin targets and used to successfully correlate with experimental measurements (using high speed digital video) of projectile velocity, projectile rotational kinematics, projectile trajectory, transient target response, and residual cavity (wound tract) in the target as a function of time during and immediately following projectile penetration.

Two additional tasks, unrelated to the base effort described above, were added to the Mission Research SOW. The first of these tasks included using a modified Nail Gun developed by the US Army Institute of Surgical Research (ISR) on ordnance gelatin targets and comparing residual damage produced in the gelatin by the ISR Nail Gun as compared to the residual damage from ballistic experiments. A separate letter report and a DVD with high-speed digital video of all experiments were sent under separate cover for this task. The second task included conducting hydrocode analysis of body armor SAPI plates subject to non-penetrating projectiles and blast and is discussed in Appendix O.

APPENDIX A

ATK MISSION RESEARCH STATEMENT OF WORK

MISSION RESEARCH CORPORATION (MRC)
STATEMENT OF WORK

MRC will develop analytic models that describe tissue damage from ballistic impact by a fragment with a low striking velocity penetrating the heart. Tissue damage will include descriptions of the projectile trajectory through the heart and tissue damage lateral to the projectile trajectory (the wound tract).

The MRC effort will be divided into two phases. The period of performance for Phase I will be 1 February 2004 though 1 April 2005. The period of performance for the optional second phase will be 1 April 2005 through 1 April 2006. [The period of performance was modified to be consistent with the overall Virtual Soldier Program. Thus, Phase I extends from 1 March 2004 through July 2005 and Phase II is now 2-1/2 years in duration].

TASK DESCRIPTIONS

Phase I will consist of four tasks: (1) analytical simulation of the projectile trajectory, (2) analytic simulation of the wound tract, (3) ballistic experiments on tissue and biosimulant materials, and (4) preparation of deliverables.

PHASE I – PROJECTILE SOFT TISSUE INTERACTION

TASK 1 – ANALYTICAL SIMULATION OF PROJECTILE TRAJECTORY

MRC will develop algorithms and required material properties to describe the trajectory and velocity retardation through biological tissue. This first task will consist of three subtasks: (1) material property measurements; (2) development of projectile retardation algorithms; and (3) Development of algorithms for a user prescribed projectile.

1.1 Tissue Mechanical Properties

MRC will measure relevant properties of biosimulant and tissue materials representative of targets tested in Task 3.

1.2 Projectile Retardation

MRC will develop algorithms in terms of static and dynamic material properties either available in the literature or from Task 1.1 that describe velocity retardation and the path of a prescribed standard projectile through tissue and biosimulant targets.

1.3 Simulation of Arbitrary Projectile

MRC will generalize the algorithms developed in subtask 1.2 for a standard projectile to an arbitrary low velocity projectile.

TASK 2 – ANALYTIC SIMULATION OF WOUND TRACT

Using the projectile velocity retardation and trajectory described in Task 1, MRC will use the transient tissue response model developed in subtask 2.1 to simulate damage lateral to the projectile trajectory in subtask 2.2.

2.1 Analytic Simulation of Tissue Transient Response

MRC will develop transient dynamic response models of the wound tract.

2.1 Analytic Simulation of Wound Tract Geometry

MRC will simulate wound tract geometry using the transient response models developed in subtask 2.1. MRC will also assist in integration of the wound tract model into the human Holomer being developed by the University of Michigan for DARPA's Virtual Soldier project.

TASK 3 – BALLISTIC EXPERIMENTS ON TISSUE AND SURROGATE MATERIALS

MRC will conduct ballistic impact experiments with suitably designed launchers and projectiles on instrumented homogeneous and non-homogeneous ordnance gelatin targets. Hybrid targets will also be developed that include pressurized and un-pressurized porcine hearts in a gelatin matrix. MRC will obtain impact/penetration data and data relative to stress wave formation and propagation in porcine tissue and in the chambers of the heart. The data from these experiments will be correlated to models developed in Tasks 1 and 2.

TASK 4 – PREPARATION OF DELIVERABLES

Deliverables will be threefold and include: (1) quarterly status reports, (2) attendance and presentation at designated quarterly technical interchange meetings, and (3) a Phase I final report.

PHASE II (OPTION) – PROJECTILE TISSUE INTERACTION INCLUDING FLUID, BONE, AND POROUS TISSUE

TASK 5 – PHASE II ANALYTICAL SIMULATION OF PROJECTILE TRAJECTORY

MRC will develop algorithms and required material properties to describe the trajectory and velocity retardation through biological tissue, including bone, fluid interfaces, and porous materials. This task will consist of three subtasks: (1) material property measurements; (2) development of projectile retardation algorithms; and (3) Development of algorithms for user prescribed projectiles.

TASK 6 – PHASE II ANALYTIC SIMULATION OF WOUND TRACT

Using the projectile velocity retardation and trajectory described in Task 5, MRC will use a transient tissue response model developed to simulate fracture and damage lateral to the projectile trajectory.

TASK 7 – PHASE II BALLISTIC EXPERIMENTS ON TISSUE AND SURROGATE MATERIALS

MRC will conduct ballistic impact experiments with suitably designed launchers and projectiles on instrumented homogeneous and non-homogeneous ordnance gelatin targets. Hybrid targets will also be developed that include biological tissue in a gelatin matrix. MRC will obtain impact/penetration data and data relative to stress wave formation and propagation. The data from these experiments will be correlated to models developed in Tasks 5 and 6.

TASK 8 – PHASE II PREPARATION OF DELIVERABLES

Deliverables will be threefold and include: (1) quarterly status reports, (2) attendance and presentation at designated quarterly technical interchange meetings, and (3) a Phase II final report.

APPENDIX B

STATIC SOLUTION OF CYLINDER IN PLANE-STRAIN WITH CIRCUMFERENTIAL INHOMOGENEITIES

Static solution of cylinder in plane-strain with θ-inhomogeneity

The static solution of a hollow cylinder in plane-strain is the first step toward the analysis of transient response. The effect on variables of circumferential or θ-inhomogeneity from an axisymmetric pressure applied at the inner boundary is evaluated.

Static and dynamic solution of the homogeneous hollow cylinder in plane-strain is a straight–forward mathematical task as the problem yields to an exact treatment. Radial inhomogeneity requires a more complicated analysis yet the problem still yields to an exact treatment if a step-wise radial variation in modulus is assumed. In other words, divide the region $r_p \le r \le r_o$ into N_r equidistant annular segments

$$r_j \le r \le r_{j+1} \quad , \quad j = 1,...,N_r$$
$$\Delta r_j = r_{j+1} - r_j \quad , \quad r_j = (r_o - r_p)/N_r$$

r_p and r_o are inner and outer radii, and modulus E_j is constant over each segment yet varies from one segment to the other. r-inhomogeneity is axisymmetric as E varies only along r but remains constant along θ. Consequently, only extensional waves are excited. The solution adopts transfer matrices of annular segments with varying properties.

The θ-inhomogeneity is substantially more complicated since a step-wise discretization along the circumference is not possible. The only way to treat the θ-inhomogeneity analytically is by the Galerkin method. Eigenfunctions of the asymmetric homogeneous dynamic equations are utilized as trial functions in the inhomogeneous dynamic equations. The static solution is attempted first to evaluate the stability and convergence of the Galerkin method.

Fig. 2. plots distribution of variables along r for the homogeneous hollow cylinder made of gelatin with r_p=0.25″ and r_o=3″ with an axisymmetric unit

pressure applied at $r = r_p$. Fig. 2a plots radial displacement u and Fig. 2b plots radial and circumferential stresses $\sigma_{rr}, \sigma_{\theta\theta}$. Note the exponential decay of all variables with r. Also note that magnitudes of σ_{rr} and $\sigma_{\theta\theta}$ are the same at the inner wall and equal the applied unit pressure.

Consider a θ-inhomogeneity in the form

$$E(\theta) = E_0\left[1 + 0.5\cos(2\theta)\right]$$

meaning that modulus is made of an axisymmetric component with magnitude E_o superimposed to a component of magnitude $0.5E_0$ that varies along θ following a $\cos(2\theta)$ distribution. In this way, maximum magnitude is $E_{max} = 1.5E_0$ at $\theta = 0$ and $\theta = \pi$, and minimum magnitude is $E_{min} = 0.5E_0$ at $\theta = \pi/2$, yielding an E_{max}/E_{min} = 3. Fig. 3(a1-d1) plots r distribution of variable with $\theta = 0, \pi/4, \pi/2$ as parameter, while Fig. 3(a2-d2) plots θ distribution with $r = r_p, 2r_p, 4r_p, 8r_p$ as parameter. u and circumferential displacement υ have approximately the same magnitude yet they are almost half the axisymmetric u in Figure 2a. Both u and υ vary periodically along θ as shown in Fig. 3(a2,b2). σ_{rr} achieves its maximum magnitude of unity at the inner boundary consistent with the boundary condition there (see Fig. 3(c1-c2)). An interesting and important finding is the magnitudes of $\sigma_{\theta\theta}$ (Fig. 3(d1-d2)) and axial stress σ_{zz} (Fig. 3(e1-e2)) at the inner boundary. $\sigma_{\theta\theta\,\max}$ is approximately 13 times larger than applied pressure while $\sigma_{zz\,\max}$ is almost 6 times higher than applied pressure. This can be attributed to the θ motion that exists for the inhomogeneous asymmetric case while it vanishes identically for the homogeneous axisymmetric case. Note that remote from the inner boundary $r > r_p$,

magnitudes of $\sigma_{\theta\theta\max}$ and $\sigma_{zz\max}$ are almost twice the applied pressure. Note that for $\theta > \pi/4$ $\sigma_{\theta\theta}$ changes from compression to extension suggesting that circumferential asymmetry produces a magnified tensile $\sigma_{\theta\theta}$ enhancing radial tearing of tissue.

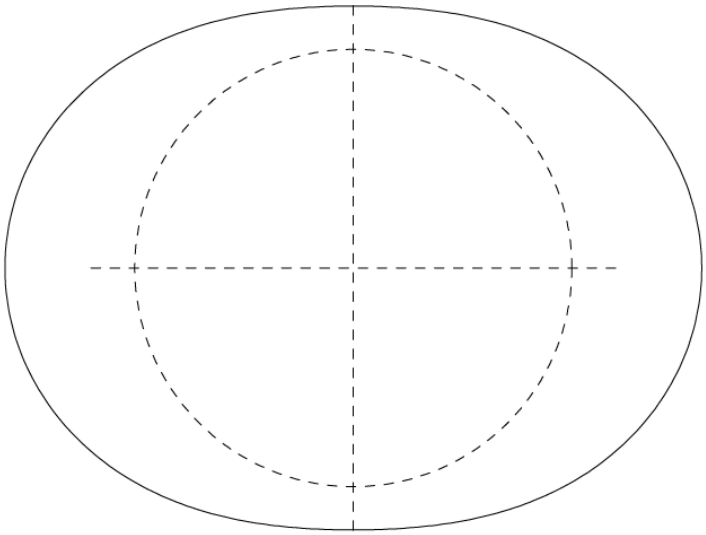

Figure 1. E *circumf. distrib.* E_{min} , E_{max} = $0.50\,E_0$, $1.50\,E_0$

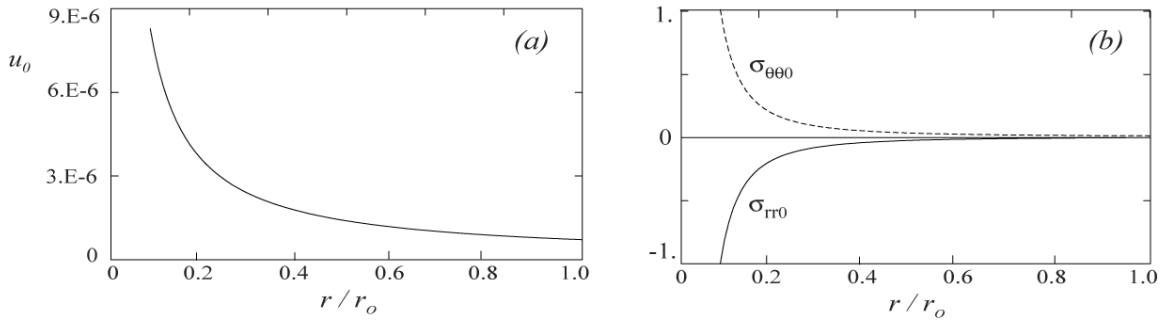

Figure 2. Distribution of axisymmetric static displacement and stresses of homogeneous cylinder in plane strain

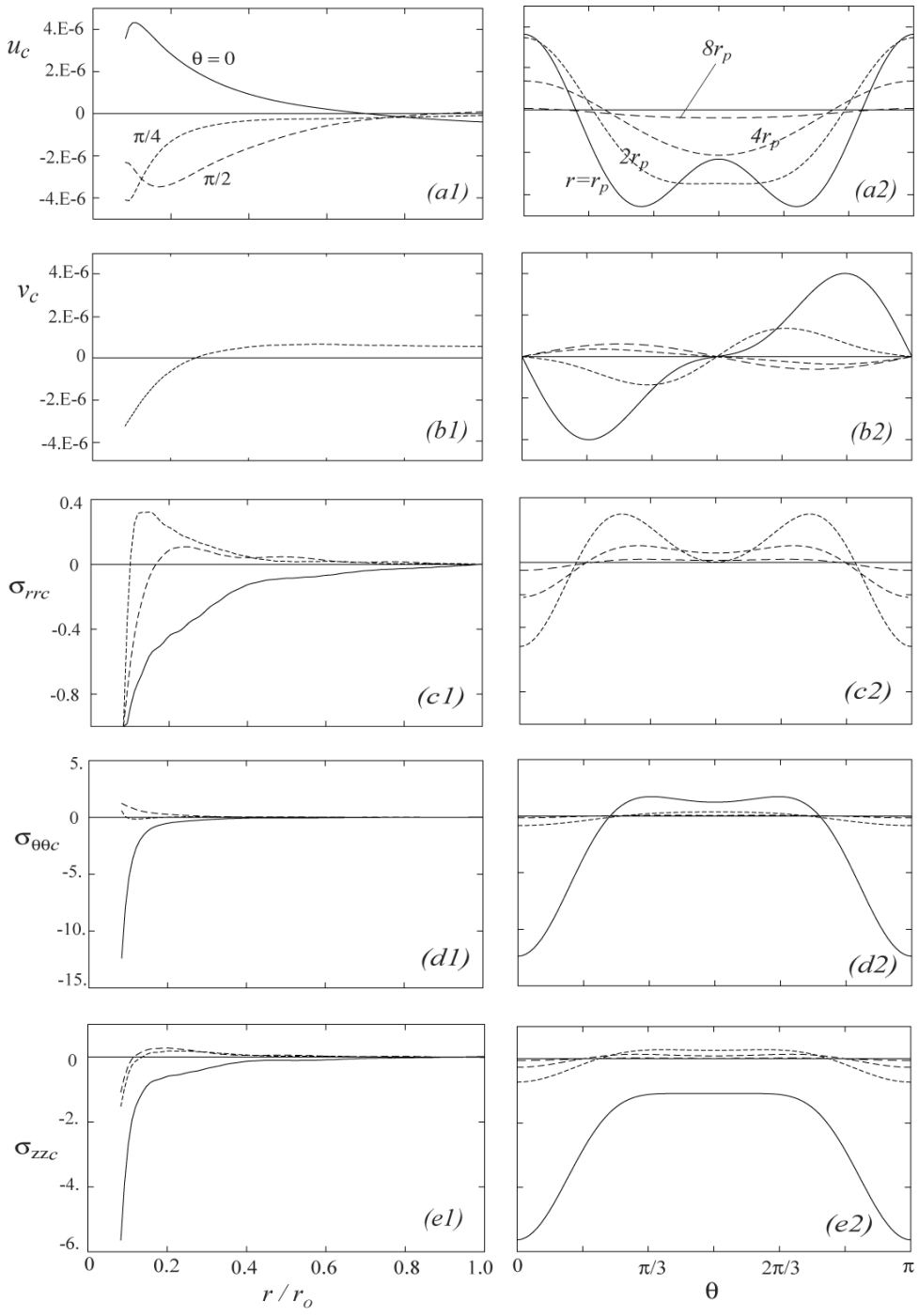

Figure 3. Distribution of static variables of cylinder in plane-strain with θ–inhomogeneity

(a1) - (e1) along r , (a2) - (e2) along θ

APPENDIX C

SIMPLIFIED PLANE-STRAIN ANALYTICAL RESULTS

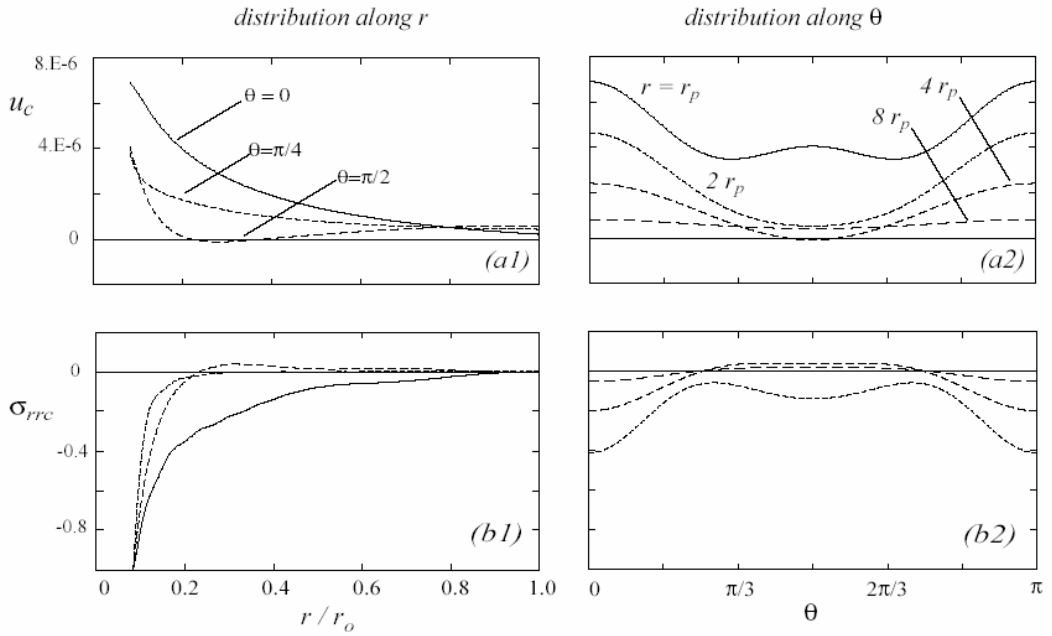

Plane-strain circumferential inhomogeneity in modulus $E = E_o + E_2 \cos(2\theta)$

(a1) ,(b1) distribution along radius with " θ *" as parameter*

(a2), (b2) distribution along circumference with "r" as parameter

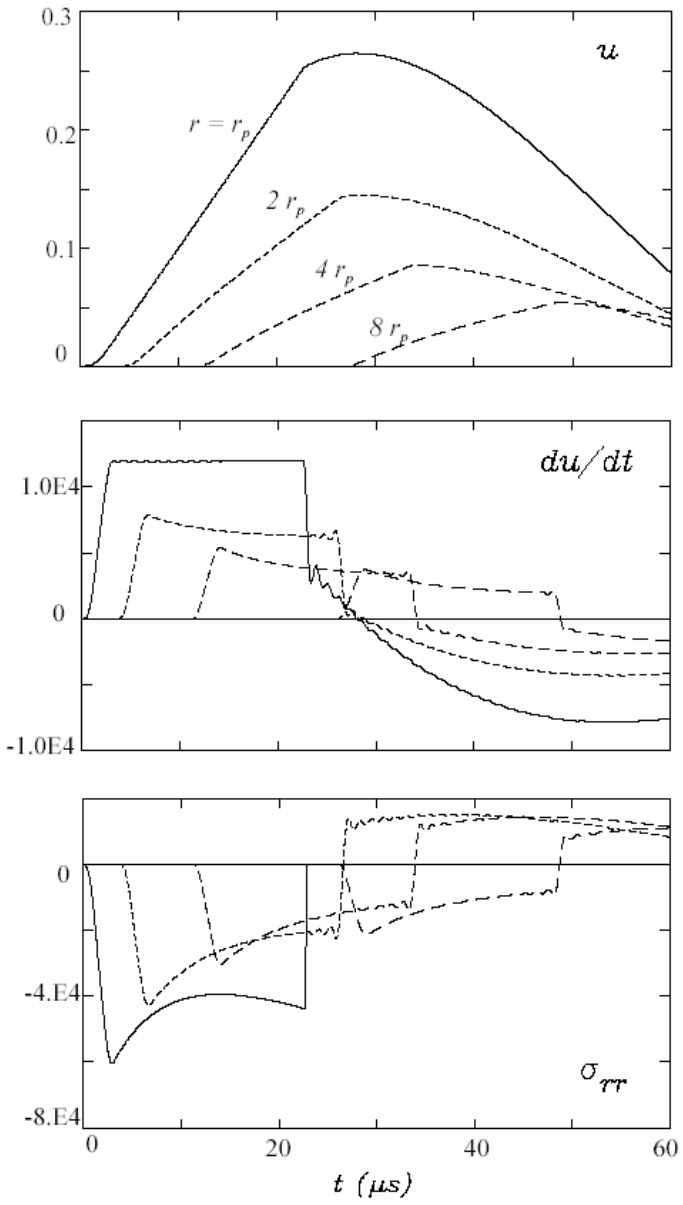

Mixed plane-strain problem :
prescribed motion for $t < 23$ μs
pressure release for $t > 23$ μs

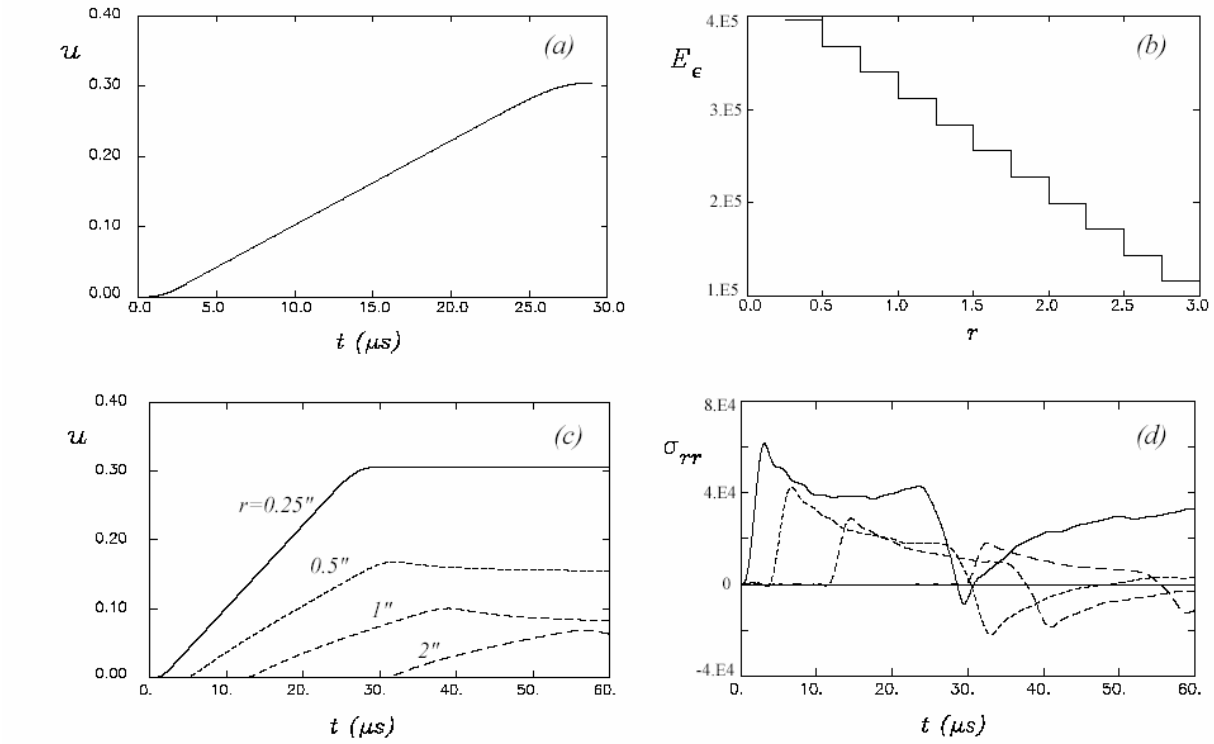

Plane-Strain radial inhomogeneity in modulus E

(a) Prescribed radial displacement, (b) Step-wise radial distribution of E

(c) Radial displacement response (d) Radial stress response

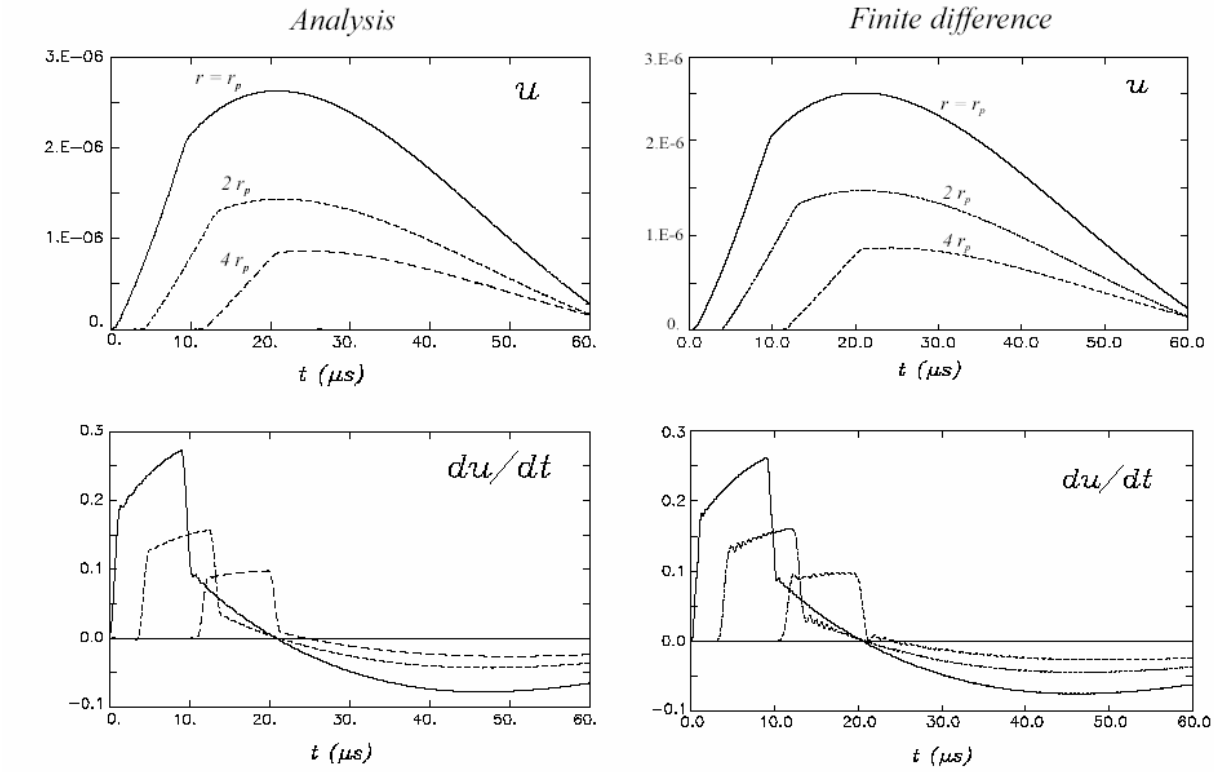

Verification of plane-strain analysis by comparison with finite difference method
Trapezoidal pressure pulse 10 μs duration

APPENDIX D

LISTING OF PROJECTILE TRAJECTORY MATHCAD CODE

MATHCAD CODE

DETERMINATION OF WOUND TRACK

TRANSLATIONAL AND ROTATIONAL MOTION OF

A CUT CYLINDER INSIDE A TARGET
DEVELOPMENT OF GENERAL MODULAR CODE APPLICABLE TO AN ARBITRARY SHAPED PROJECTILE

Moment of Inertia about the Combined Center of Mass G
Geometry of Cut Cylinder

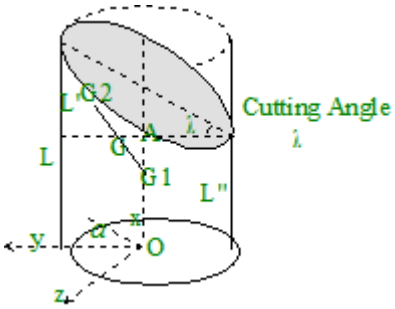

Cylinder Base Radius $a := 1$
Length of Cylinder $L := 4$
Cutting Angle $\lambda d := 30$ **deg**

$\lambda := \lambda d \cdot \frac{\pi}{180}$

$\lambda c := \frac{\pi}{2} - \lambda$

(Complimentary Angle)

$Lp := 2 \cdot a \cdot \tan(\lambda)$

$Lp2 := L - Lp$

$L = 4$

$Lp = 1.155$

$Lp2 = 2.845$

Total Volume: $V := \pi \cdot a^2 \cdot \left(Lp2 + \frac{Lp}{2} \right)$

Cut Volume $V2 := \pi a^2 \cdot \frac{Lp}{2}$

Volume 1 $V1 := V - V2$

$V = 10.753$

$V2 = 1.814$

$V1 = 8.939$

Analysis of Section One: Upper Cut Section

Sectional Functions

$$xn(b) := \left| \begin{array}{l} \phi \leftarrow \operatorname{asin}\left(\frac{b}{a}\right) \\ s \leftarrow \frac{4}{3}\cdot a \cdot \frac{\left[1 - \left(\frac{b}{a}\right)^2\right]^{\frac{3}{2}}}{\pi - 2\cdot\phi - \sin(2\cdot\phi)} \\ s \end{array} \right.$$

$$md(b) := \left| \begin{array}{l} \phi \leftarrow \operatorname{asin}\left(\frac{b}{a}\right) \\ s \leftarrow \frac{a^2}{2}\cdot(\pi - 2\cdot\phi - \sin(2\cdot\phi)) \\ s \end{array} \right.$$

Cut Mass $cutmass(\lambda) := \pi \cdot a^3 \cdot \tan(\lambda)$

$$c(b,\lambda) := a\cdot\tan(\lambda)\cdot\left(\frac{b}{a} + 1\right)$$

x-distance of CM from A, the base center of the cut-section

$$xdis(\lambda) := \frac{\tan(\lambda)\cdot\int_{-1}^{1} c(b,\lambda)\cdot md(b)\,db}{cutmass(\lambda)}$$

y-distance of CM from A, the base center of the cut-section

$$ydis(\lambda) := \frac{\tan(\lambda)\cdot\int_{-1}^{1} xn(b)\cdot md(b)\,db}{cutmass(\lambda)}$$

$xd := xdis(\lambda)$

$yd := ydis(\lambda)$

Ixy of Section One about the base center A

$$IAxy(a,\lambda) := \left| \begin{array}{l} \lambda \leftarrow \frac{\pi}{2} - \lambda \\ \tan\lambda \leftarrow \tan(\lambda) \\ L \leftarrow 2\cdot\frac{a}{\tan(\lambda)} \\ Int \leftarrow \int_0^L x\cdot(L-x)^{\frac{3}{2}}\cdot\left[2\cdot a\cdot\tan\lambda - (L-x)\cdot\tan\lambda^2\right]^{\frac{3}{2}}\,dx \\ ans \leftarrow \frac{2}{3}\cdot Int \\ ans \end{array} \right.$$

Parameter Definitions

$$
\begin{aligned}
&I(G,V,B,A,IA,n) := \\
&\quad GB \leftarrow B - G \\
&\quad GA \leftarrow A - G \\
&\quad \text{if } n \le 3 \\
&\quad\quad fac1 \leftarrow (|GB|)^2 - (GB_n)^2 \\
&\quad\quad fac2 \leftarrow (|GA|)^2 - (GA_n)^2 \\
&\quad\quad ans \leftarrow IA + (fac1 - fac2)\cdot V \\
&\quad \text{otherwise} \\
&\quad\quad k1 \leftarrow n - 3 \\
&\quad\quad k2 \leftarrow k1 + 1 \\
&\quad\quad k2 \leftarrow k2 - 3\cdot \text{floor}\left(\frac{k2-1}{3}\right) \\
&\quad\quad fac1 \leftarrow GB_{k1}\cdot GB_{k2} \\
&\quad\quad fac2 \leftarrow GA_{k1}\cdot GA_{k2} \\
&\quad\quad ans \leftarrow IA + (fac1 - fac2)\cdot V \\
&\quad ans
\end{aligned}
$$

G = Center of Mass of V
B= MI about desired point
A=MI about known point
n=MI index code
n=1 for xx, =2, for yy, 3 for zz
n=4 for xy, =5 for yz and =6 for zx

Check Algorithm

$n := 6$

$k1 := n - 3$

$k2 := k1 + 1$

$$k2 := k2 - 3\cdot \text{floor}\left(\frac{k2-1}{3}\right)$$

$k1 = 3$

$k2 = 1$

Coordinates of Various Key Locations wrt. the uncut base section center O as origin, x-axis along the cylinder axis, y-axis along the cross-sectional axis of symmetry

$$A := \begin{pmatrix} Lp2 \\ 0 \\ 0 \end{pmatrix}$$

$$G1 := \begin{pmatrix} \frac{Lp2}{2} \\ 0 \\ 0 \end{pmatrix}$$

$$G2 := \begin{pmatrix} xd \\ yd \\ 0 \end{pmatrix} + A$$

$$G3 := A + \begin{pmatrix} \frac{Lp}{2} \\ 0 \\ 0 \end{pmatrix}$$

$$A = \begin{pmatrix} 2.845 \\ 0 \\ 0 \end{pmatrix}$$

$$G1 = \begin{pmatrix} 1.423 \\ 0 \\ 0 \end{pmatrix}$$

$$G2 = \begin{pmatrix} 3.206 \\ 0.25 \\ 0 \end{pmatrix}$$

$$G3 = \begin{pmatrix} 3.423 \\ 0 \\ 0 \end{pmatrix}$$

$$g1g2 := G2 - G1$$

$$g1g := \frac{V2}{V} \cdot g1g2$$

$$G := G1 + g1g$$

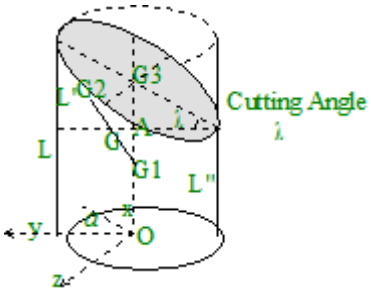

gg3 := G3 – G

g3g := G – G3

ga := G – A

g2g3 := G3 – G2

g2g := G – G2

$$G = \begin{pmatrix} 1.723 \\ 0.042 \\ 0 \end{pmatrix}$$

$$gg3 = \begin{pmatrix} 1.699 \\ -0.042 \\ 0 \end{pmatrix}$$

$$g3g = \begin{pmatrix} -1.699 \\ 0.042 \\ 0 \end{pmatrix}$$

$$g2g = \begin{pmatrix} -1.483 \\ -0.208 \\ 0 \end{pmatrix}$$

$$g2g3 = \begin{pmatrix} 0.217 \\ -0.25 \\ 0 \end{pmatrix}$$

Known Moment of Inertia of Volume 1: V1: About G1, CM of V1

$$IxxV1G1 := \pi \cdot a^4 \cdot \frac{Lp2}{2}$$

$$IyyV1G1 := \pi \cdot a^2 \cdot \frac{Lp2}{4} \cdot \left(\frac{Lp2^2}{3} + a^2 \right)$$

IzzV1G1 := IxxV1G

IxyV1G1 := 0

IyzV1G1 := 0

IzxV1G1 := 0

Known Moment of Inertia of Volume 2: V2: About A, Base Center of Cut Portion

$$IxxV2A := \pi \cdot a^4 \cdot \frac{Lp}{2}$$

$$IyyV2A := \pi \cdot a^2 \cdot \frac{Lp}{8} \cdot \left(\frac{Lp^2}{3} + a^2 \right)$$

$$IzzV2A := IyyV2A$$

$$IxyV2A := IAxy(a, \lambda)$$

$$IyzV2A := 0$$

$$IzxV2A := 0$$

Using the Shift Function $I(G, V, B, A, IA, n)$

Calculate the Moment of Inertia of the cut cylinder about its center of mass G
Volume V1

IxxV1G := I(G1, V1, G, G1, IxxV1G1, 1)

$$G = \begin{pmatrix} 1.723 \\ 0.042 \\ 0 \end{pmatrix}$$

$$G1 = \begin{pmatrix} 1.423 \\ 0 \\ 0 \end{pmatrix}$$

IxxV1G1 = 4.469
IxxV1G = 4.485
V1 = 8.939
IyyV1G := I(G1, V1, G, G1, IyyV1G1, 2)
IyyV1G1 = 8.265
IyyV1G = 9.074
IzzV1G := I(G1, V1, G, G1, IzzV1G1, 3)
IzzV1G1 = 4.469
IzzV1G = 5.294
IxyV1G := I(G1, V1, G, G1, IxyV1G1, 4)
IxyV1G1 = 0
IxyV1G = 0.113
IyzV1G := I(G1, V1, G, G1, IyzV1G1, 5)
IyzV1G1 = 0
IyzV1G = 0
IzxV1G := I(G1, V1, G, G1, IzxV1G1, 6)
IzxV1G1 = 0
IzxV1G = 0

Volume V2
IxxV2G := I(G2, V2, G, A, IxxV2A, 1)

$$G = \begin{pmatrix} 1.723 \\ 0.042 \\ 0 \end{pmatrix}$$

$$G1 = \begin{pmatrix} 1.423 \\ 0 \\ 0 \end{pmatrix}$$

IxxV2A = 1.814
IxxV2G = 1.779
IyyV2G := I(G2, V2, G, A, IyyV2A, 2)
V1 = 8.939

IyyV2A = 0.655
IyyV2G = 4.406

$$G2 = \begin{pmatrix} 3.206 \\ 0.25 \\ 0 \end{pmatrix}$$

$$A = \begin{pmatrix} 2.845 \\ 0 \\ 0 \end{pmatrix}$$

IzzV2G:= I(G2, V2, G, A , IzzV2A, 3)
IzzV2A = 0.655
IzzV2G= 4.371
IxyV2G:= I(G2, V2, G, A , IxyV2A, 4)
IxyV2A = 0.262
IxyV2G= 0.657
IyzV2G:= I(G2, V2, G, A , IyzV2A, 5)
IyzV2A = 0
IyzV2G = 0
IzxV2G:= I(G2, V2, G, A , IzxV2A, 6)
IzxV2A = 0
IzxV2G= 0

Final IG Matrix (Non-Principal)

IxxG:= IxxV1G+ IxxV2(
IyyG := IyyV1G + IyyV2G
IzzG:= IzzV1G+ IzzV2(
IxyG := IxyV1G+ IxyV2(
IyzG := IyzV1G+ IyzV2(
IzxG:= IzxV1G+ IzxV2(

$$IG := \begin{pmatrix} IxxG & IxyG & 0 \\ IxyG & IyyG & 0 \\ 0 & 0 & IzzG \end{pmatrix}$$

$$IG = \begin{pmatrix} 6.264 & 0.77 & 0 \\ 0.77 & 13.48 & 0 \\ 0 & 0 & 9.665 \end{pmatrix}$$

Define Integration point for Various Surfaces for Load Calculation:

1. Flat Surface (base): Labelled S3
2. Slant Plane Surface: labelled S4
3. Curved Surface: Uncut: Labelled S1
4. Curved Surface: Cut: Labelled S2

Body-fixed Axes System for Coordinate Descriptions

Center at the center of the flat base: Origin at G for Body-fixed F-frame used in the analysis
x-axis along the uncut cylinder axis
y-axis is on the plane through the high and low end of the cut surface
z-axis forms the right handed orthogonal system

Check MCAD Runge-Kutta Method: Using External Functions for Derivatives

$\mu := -0.2$

$$\text{row1}(xv) := \left| \begin{array}{l} \text{fac} \leftarrow (xv_1)^2 + (xv_2)^2 \\ s \leftarrow \mu \cdot xv_1 - xv_2 - \text{fac} \cdot xv_1 \\ s \end{array} \right.$$

$$x := \begin{pmatrix} 0 \\ 1 \end{pmatrix}$$

$$D(t, x) := \begin{bmatrix} \mu \cdot x_1 - x_2 - \left[(x_1)^2 + (x_2)^2 \right] \cdot x_1 \\ \mu \cdot x_2 + x_1 - \left[(x_1)^2 + (x_2)^2 \right] \cdot x_2 \end{bmatrix}$$

$$\text{row2}(xv) := \left| \begin{array}{l} \text{fac} \leftarrow (xv_1)^2 + (xv_2)^2 \\ s \leftarrow \mu \cdot xv_2 + xv_1 - \text{fac} \cdot xv_2 \\ s \end{array} \right.$$

$Z := \text{rkfixed}(x, 0, 20, 100, D)$

$n := 0, 1 .. 10($

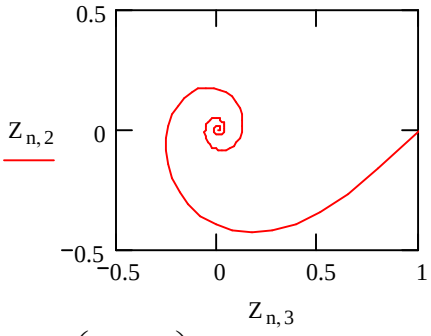

$$D(t, x) := \begin{pmatrix} \text{row1}(x) \\ \text{row2}(x) \end{pmatrix}$$

Using Vector Method

$Zn := \text{rkfixed}(x, 0, 20, 100, D)$

$n := 0, 1 .. 10($

Comparison Between Conventional and Vector Method

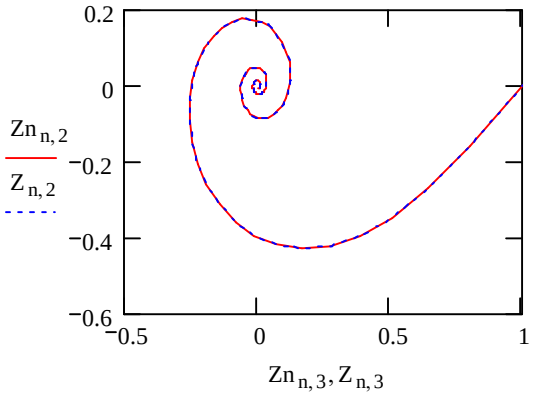

OK

Check the possibility of solving a 18-row vector using MCAD Runge-Kutta Coding

Physical Description of x-elements:

x1-x3: Center of Mass G in N-frame
x4-x6: Velocity of G in N-frame
x7-x9: Components of Angular Velocity in F-frame
x10-x12: Components of unit Vector along Gx in N-frame
x13-x15: Components of unit Vector along Gy in N-frame
x16-x18: Components of unit Vector along Gz in N-frame
N-frame: OXYZ Fixed Newtonian Frame
F-frame: Gxyz Rotating Frame attached to the projectile

Note:
There are two integrands for each of S1-S4 surfaces: These integrands are vectors. First integrand is a force per unit area while second is the moment of this force about G. Components of these vectors are taken along the Newtonian axes for the motion of G while they are taken along the F-frame axes for motion about G.

Initial conditions on x

$x0 := (1\ 0\ 0\ 0\ 1\ 0\ 0\ 0\ 0\ 0\ 0\ 0\ 0\ 0\ 0\ 0\ 0\ 0)$

$x0 := x0^{T}$

Location Dependent Retardation
Coefficients in Newtonian Frame

$\alpha(pn) := pn_1 + pn_2 + pn_3$

$\beta(pn) := 2 \cdot \alpha(pn)$

$\gamma(pn) := 3 \cdot \alpha(pn)$

Motion of the Center of Mass G: Vector-Integrand over S1 surface in Newtonian Frame
Force Integrand for the S1-Surface

$$
\begin{aligned}
&\text{FIGS12}(xv, x, \phi) := \\
&\quad gn \leftarrow \begin{pmatrix} xv_1 \\ xv_2 \\ xv_3 \end{pmatrix} \\
&\quad TFN \leftarrow \begin{pmatrix} xv_{10} & xv_{13} & xv_{16} \\ xv_{11} & xv_{14} & xv_{17} \\ xv_{12} & xv_{15} & xv_{18} \end{pmatrix} \\
&\quad TNF \leftarrow TFN^{-1} \\
&\quad opf \leftarrow \begin{pmatrix} x \\ a \cdot \sin(\phi) \\ a \cdot \cos(\phi) \end{pmatrix} \\
&\quad gpf \leftarrow opf - G \\
&\quad gpn \leftarrow TFN \cdot gpf \\
&\quad pn \leftarrow gn + gpn \\
&\quad \omega \leftarrow \begin{pmatrix} xv_7 \\ xv_8 \\ xv_9 \end{pmatrix} \\
&\quad vpgf \leftarrow \omega \times gpf \\
&\quad pnf \leftarrow \begin{pmatrix} 0 \\ \sin(\phi) \\ \cos(\phi) \end{pmatrix} \\
&\quad vgn \leftarrow \begin{pmatrix} xv_4 \\ xv_5 \\ xv_6 \end{pmatrix} \\
&\quad vgf \leftarrow TNF \cdot vgn \\
&\quad vpf \leftarrow vgf + \omega \times gpf \\
&\quad vn \leftarrow vpf \cdot pnf \\
&\quad sf \leftarrow \begin{pmatrix} 0 \\ 0 \\ 0 \end{pmatrix} \\
&\quad sf \leftarrow -\left(\alpha(pn) + \beta(pn) \cdot vn + \gamma(pn) \cdot vn^2\right) \text{ if } vn > 0 \\
&\quad sf
\end{aligned}
$$

FIGS1(xv, x, ϕ)

Force Integral Over S1 Surface: F-Frame

In F-Frame

$$FS1y(xv) := a \cdot \int_0^{Lp2(\lambda)} \left(\int_0^{2\cdot\pi} FIGS12(xv, x, \phi) \cdot \sin(\phi)\, d\phi \right) dx$$

$$FS1z(xv) := a \cdot \int_0^{Lp2(\lambda)} \left(\int_0^{2\cdot\pi} FIGS12(xv, x, \phi) \cdot \cos(\phi)\, d\phi \right) dx$$

In N-Frame

$$FS1X(xv) := xv_{13} \cdot FS1y(xv) + xv_{16} \cdot FS1z(xv)$$
$$FS1Y(xv) := xv_{14} \cdot FS1y(xv) + xv_{17} \cdot FS1z(xv)$$
$$FS1Z(xv) := xv_{15} \cdot FS1y(xv) + xv_{18} \cdot FS1z(xv)$$

Force Integral Over S2 Surface: F-Frame
Define

$$\phi(x) := \operatorname{asin}\left(\frac{x}{a \cdot \tan(\lambda)} - 1 \right)$$

Components
In F-Frame

$$FS2y(xv) := a \cdot \int_{Lp2(\lambda)}^{L} \left(\int_{\phi(x)}^{\pi - \phi(x)} FIGS12(xv, x, \phi) \cdot \sin(\phi)\, d\phi \right) dx$$

$$FS2z(xv) := a \cdot \int_{Lp2(\lambda)}^{L} \left(\int_{\phi(x)}^{\pi - \phi(x)} FIGS12(xv, x, \phi) \cdot \cos(\phi)\, d\phi \right) dx$$

In N-Frame

$$FS2X(xv) := xv_{13} \cdot FS2y(xv) + xv_{16} \cdot FS2z(xv)$$
$$FS2Y(xv) := xv_{14} \cdot FS2y(xv) + xv_{17} \cdot FS2z(xv)$$
$$FS2Z(xv) := xv_{15} \cdot FS2y(xv) + xv_{18} \cdot FS2z(xv)$$

Define

$$Lp3 := Lp2 + \frac{Lp}{2}$$

Force Integrand Over S4 Angled Flat Surface: F-Frame

Range of Integration for S4 Surface
$0<=r<=1$, $0<=\theta<=2\pi$

$$
\begin{aligned}
\text{FIGS4}(xv, r, \theta) := \;& gn \leftarrow \begin{pmatrix} xv_1 \\ xv_2 \\ xv_3 \end{pmatrix} \\
& TFN \leftarrow \begin{pmatrix} xv_{10} & xv_{13} & xv_{16} \\ xv_{11} & xv_{14} & xv_{17} \\ xv_{12} & xv_{15} & xv_{18} \end{pmatrix} \\
& TNF \leftarrow TFN^{-1} \\
& opf \leftarrow \begin{pmatrix} Lp3 + a \cdot \tan(\lambda) \cdot r \cdot \sin(\theta) \\ a \cdot r \cdot \sin(\theta) \\ a \cdot r \cdot \cos(\theta) \end{pmatrix} \\
& gpf \leftarrow opf - G \\
& gpn \leftarrow TFN \cdot gpf \\
& pn \leftarrow gn + gpn \\
& \omega \leftarrow \begin{pmatrix} xv_7 \\ xv_8 \\ xv_9 \end{pmatrix} \\
& vpgf \leftarrow \omega \times gpf \\
& pnf \leftarrow \begin{pmatrix} \cos(\lambda) \\ -\sin(\lambda) \\ 0 \end{pmatrix} \\
& vgn \leftarrow \begin{pmatrix} xv_4 \\ xv_5 \\ xv_6 \end{pmatrix} \\
& vgf \leftarrow TNF \cdot vgn \\
& vpf \leftarrow vgf + \omega \times gpf \\
& vn \leftarrow vpf \cdot pnf \\
& sf \leftarrow \begin{pmatrix} 0 \\ 0 \\ 0 \end{pmatrix} \\
& sf \leftarrow -\left(\alpha(pn) + \beta(pn) \cdot vn + \gamma(pn) \cdot vn^2\right) \text{ if } vn > 0 \\
& sf
\end{aligned}
$$

Force Integral Over S4 Surface: F-Frame

In F-Frame

$$FS4x(xv) := a\cdot\cos(\lambda)\cdot\int_0^1\left(\int_0^{2\cdot\pi} FIGS4(xv,r,\theta)\,d\theta\right)dr$$

$$FS4y(xv) := -a\cdot\sin(\lambda)\cdot\int_0^1\left(\int_0^{2\cdot\pi} FIGS4(xv,r,\theta)\,d\theta\right)dr$$

In N-Frame

$$FS4X(xv) := xv_{10}\cdot FS4x(xv) + xv_{13}\cdot FS4y(xv)$$

$$FS4Y(xv) := xv_{11}\cdot FS4x(xv) + xv_{14}\cdot FS4y(xv)$$

$$FS4Z(xv) := xv_{12}\cdot FS4x(xv) + xv_{15}\cdot FS4y(xv)$$

Range of Integration for S3 Surface
$0<=r<=1,\ 0<=\theta<=2\pi$

Force Integrand Over S3 Uncut Flat Surface: F-Frame

$$
\begin{aligned}
\text{FIGS3}(xv, r, \theta) := \;& gn \leftarrow \begin{pmatrix} xv_1 \\ xv_2 \\ xv_3 \end{pmatrix} \\
& TFN \leftarrow \begin{pmatrix} xv_{10} & xv_{13} & xv_{16} \\ xv_{11} & xv_{14} & xv_{17} \\ xv_{12} & xv_{15} & xv_{18} \end{pmatrix} \\
& TNF \leftarrow TFN^{-1} \\
& opf \leftarrow \begin{pmatrix} 0 \\ r \cdot \sin(\theta) \\ r \cdot \cos(\theta) \end{pmatrix} \\
& gpf \leftarrow opf - G \\
& gpn \leftarrow TFN \cdot gpf \\
& pn \leftarrow gn + gpn \\
& \omega \leftarrow \begin{pmatrix} xv_7 \\ xv_8 \\ xv_9 \end{pmatrix} \\
& vpgf \leftarrow \omega \times gpf \\
& pnf \leftarrow \begin{pmatrix} -1 \\ 0 \\ 0 \end{pmatrix} \\
& vgn \leftarrow \begin{pmatrix} xv_4 \\ xv_5 \\ xv_6 \end{pmatrix} \\
& vgf \leftarrow TNF \cdot vgn \\
& vpf \leftarrow vgf + \omega \times gpf \\
& vn \leftarrow vpf \cdot pnf \\
& sf \leftarrow \begin{pmatrix} 0 \\ 0 \\ 0 \end{pmatrix} \\
& sf \leftarrow -\left(\alpha(pn) + \beta(pn) \cdot vn + \gamma(pn) \cdot vn^2\right) \text{ if } vn > 0 \\
& sf
\end{aligned}
$$

Force Integral Over S3 Surface: F-Frame

In F-Frame

$$FS3x(xv) := a\cdot\cos(\lambda)\cdot\int_0^1\left(\int_0^{2\cdot\pi} FIGS3(xv,r,\theta)\,d\theta\right)dr$$

$$FS3y(xv) := -a\cdot\sin(\lambda)\cdot\int_0^1\left(\int_0^{2\cdot\pi} FIGS3(xv,r,\theta)\,d\theta\right)dr$$

In N-Frame

$$FS3X(xv) := xv_{10}\cdot FS3x(xv) + xv_{13}\cdot FS3y(xv)$$
$$FS3Y(xv) := xv_{11}\cdot FS3x(xv) + xv_{14}\cdot FS3y(xv)$$
$$FS3Z(xv) := xv_{12}\cdot FS3x(xv) + xv_{15}\cdot FS3y(xv)$$

Evaluating Moment Integrals

$$IGI := IG^{-1}$$

$$\omega vec := \begin{pmatrix} 0.994 \\ -0.4 \\ 0 \end{pmatrix}$$

$$\text{eigenvecs}(IG) = \begin{pmatrix} 0.994 & 0.105 & 0 \\ -0.105 & 0.994 & 0 \\ 0 & 0 & 1 \end{pmatrix}$$

$$test1 := (IG \cdot \omega vec) \times \omega vec$$

$$test1 = \begin{pmatrix} 0 \\ 0 \\ 2.231 \end{pmatrix}$$

$$IGI \cdot test1 = \begin{pmatrix} 0 \\ 0 \\ 0.231 \end{pmatrix}$$

$$IGI \cdot [(IG \cdot \omega vec) \times \omega vec] = \begin{pmatrix} 0 \\ 0 \\ 0.231 \end{pmatrix}$$

APPENDIX E

STATIC ANALYSIS PREREQUISITE TO 3-D AXISYMMETRIC MODEL OF WAVE PROPAGATION IN CYLINDRICAL TISSUE PERFORATED BY CONCENTRIC CYLINDRICAL PROJECTILE

In what follows, all dependent variables pertaining to the static solution will be subscripted by s. The static axisymmetric equations in terms of displacements are

$$\begin{aligned}
&\left((\lambda+2\mu)\hat{\nabla}_1^2+\mu\,\partial_{zz}\right)u_s \;+\; (\lambda+\mu)\partial_{rz}w_s=0\\
&(\lambda+\mu)\partial_z\left(\partial_r+1/r\right)u_s \;+\; \left(\mu\hat{\nabla}_0^2+(\lambda+2\mu)\partial_{zz}\right)w_s=0\\
&\hat{\nabla}_n^2\equiv\partial_{rr}+1/r\,\partial_r-n^2/r^2\;,\qquad n=0,1
\end{aligned}\tag{A1}$$

Equations (A1) decouple to

$$\begin{aligned}
&\mu(\lambda+2\mu)\left(\hat{\nabla}_1^2+\partial_{zz}\right)^2u_s=0\\
&\mu(\lambda+2\mu)\left(\hat{\nabla}_0^2+\partial_{zz}\right)^2w_s=0
\end{aligned}\tag{A2}$$

For the radial traction problem satisfying $\sigma_{zzs}=0$ at $z=(0,l)$, separation of variables is as follows. Summing over all k_z yields

$$u_s(r,z)=\sum_{m=1}^{M}\overline{u}_{ms}(r)\sin(k_{zm}z)\tag{A3a}$$

$$w_s(r,z)=\sum_{m=1}^{M}\overline{w}_{ms}(r)\cos(k_{zm}z)\;,\qquad k_{zm}=m\pi/l\tag{A3b}$$

Substituting (A3) in (A2) produces uncoupled equations in r for each k_{zm}

$$\begin{aligned}
&\left(\hat{\nabla}_1^2-k_{zm}^2\right)^2\overline{u}_{ms}(r)=0\\
&\left(\hat{\nabla}_0^2-k_{zm}^2\right)^2\overline{w}_{ms}(r)=0
\end{aligned}\tag{A4}$$

In what follows, subscript m will be dropped for shortness. Equations (A4) admit the solutions

$$\begin{aligned}
\overline{u}_s(r)&=C_1I_1(k_zr)+C_2K_1(k_zr)\\
&\quad+C_3\left(k_zr\;I_0(k_zr)-I_1(k_zr)\right)-C_4\left(k_zr\;K_0(k_zr)+K_1(k_zr)\right)
\end{aligned}\tag{A5a}$$

$$\begin{aligned}
\overline{w}_s(r)&=C_1I_0(k_zr)-C_2K_0(k_zr)\\
&\quad+C_3\left(\alpha_1I_0(k_zr)+\;k_zr\;I_1(k_zr)\right)+C_4\left(-\alpha_1K_0(k_zr)+k_zr\;K_1(k_zr)\right)
\end{aligned}\tag{A5b}$$

$$\alpha_1=(\lambda+3\mu)/(\lambda+\mu)\;,\quad \alpha_2=\lambda/(\lambda+\mu)$$

Substituting (A5a,b) in the constitutive relations yields

$$\begin{aligned}\bar{\sigma}_{rrs}(r) &= 2\mu k_z\left(C_1\left(I_0(k_z r) - I_1(k_z r)/(k_z r)\right) - C_2\left(K_0(k_z r) + K_1(k_z r)/(k_z r)\right)\right)\\ &+ 2\mu k_z C_3\left(-\alpha_2 I_0(k_z r) + \left(1+(k_z r)^2\right) I_1(k_z r)/(k_z r)\right)\\ &+ 2\mu k_z C_4\left(\ \alpha_2 K_0(k_z r) + \left(1+(k_z r)^2\right) K_1(k_z r)/(k_z r)\right)\end{aligned} \tag{A6a}$$

$$\begin{aligned}\bar{\sigma}_{\theta\theta s}(r) &= 2\mu k_z\left(C_1 I_1(k_z r)/(k_z r) + C_2 K_1(k_z r)/(k_z r)\right)\\ &+ 2\mu k_z C_3\left(\ (1-\alpha_2) I_0(ik_z r) - I_1(k_z r)/(k_z r)\right)\\ &+ 2\mu k_z C_4\left(-(1-\alpha_2) K_0(k_z r) - K_1(k_z r)/(k_z r)\right)\end{aligned} \tag{A6b}$$

$$\begin{aligned}\bar{\sigma}_{zzs}(r) = \ & 2\mu k_z\left(-C_1 I_0(k_z r) + C_2 K_0(k_z r)\right)\\ &+ 2\mu k_z C_3\left(-(\alpha_1+\alpha_2)\ I_0(k_z r)\ - k_z r\, I_1(k_z r)\right)\\ &+ 2\mu k_z C_4\left(\ \ (\alpha_1+\alpha_2) K_0(k_z r) - k_z r\, K_1(k_z r)\right)\end{aligned} \tag{A6c}$$

$$\begin{aligned}\bar{\tau}_{rzs}(r) &= 2\mu k_z\left(C_1 I_1(k_z r) + C_2 K_1(k_z r)\right)\\ &+ 2\mu k_z C_3\left(\ \ k_z r\ I_0(k_z r) + (1-\alpha_2) I_1(k_z r)\right)\\ &+ 2\mu k_z C_4\left(-k_z r\, K_0(k_z r) + (1-\alpha_2) K_1(k_z r)\right)\end{aligned} \tag{A6d}$$

Tractions at the inner and outer surfaces of the tube are expressed as

$$\begin{aligned}&\sigma_{rrs}(r_p, z) = p_r\left(H(z-z_a) - H(z-z_b)\right)\\ &\tau_{rzs}(r_p, z) = 0\end{aligned} \tag{A7a}$$

$$\sigma_{rrs}(r_o, z) \equiv \tau_{rzs}(r_o, z) = 0 \tag{A7b}$$

p_r is a uniform radial traction prescribed at $r = r_p$ in the interval $z_a \le z \le z_b$. Substituting (A6a) and (A6d) in (A7a) and (A7b) and enforcing orthogonality of $\sin(k_z z)$ and $\cos(k_z z)$ produces M (4×4) uncoupled matrix equations in the coefficients C_{km}, $k = 1, 4$

$$\mathbf{M}_{cm}\mathbf{C}_m = \mathbf{f}_m \tag{A8}$$

Coefficients of $\mathbf{M}_{cm}$ are the radial functions multiplying C_{km} in (A6a) and (A6d) evaluated at $r = r_p$ and $r = r_o$, and $\mathbf{f}_m$ is a vector defined by

$$\begin{aligned}&f_{1m} = -2 p_r\left(\cos(k_{zm} z_b) - \cos(k_{zm} z_a)\right)/(k_{zm} l)\\ &f_{2m} \equiv f_{3m} \equiv f_{4m} = 0\end{aligned} \tag{A9}$$

For the axial traction problem satisfying vanishing shear stress $\tau_{rzs} = 0$ at $z = (0, l)$, the expansion in (A3) becomes

$$u_s(r,z) = \sum_{m=1}^{M} \bar{u}_{ms}(r)\cos(k_{zm}z)$$
$$w_s(r,z) = \sum_{m=1}^{M} \bar{w}_{ms}(r)\sin(k_{zm}z) \quad , \qquad k_{zm} = m\pi / l \tag{A10}$$

The boundary conditions are

$$\sigma_{rrs}(r_p, z) = 0$$
$$\tau_{rzs}(r_p, z) = p_z\left(H(z-z_a) - H(z-z_b)\right) \tag{A7a}$$
$$\sigma_{rrs}(r_o, z) \equiv \tau_{rzs}(r_o, z) = 0 \tag{A7b}$$

p_z is a uniform axial traction applied at $r = r_p$ in the interval $z_a \le z \le z_b$. Expressions for displacements and stresses resemble those of the radial problem and are omitted here for shortness.

In all results to follow, geometric and material properties of the cylinder are listed in Table A-1. Figure 1 (a1) plots the static deformed generator from a unit radial displacement prescribed at the footprint

$$u_{so}(r_p, z) = H(z-z_a) - H(z-z_b) \tag{A8a}$$

In (A8) z_a =1.5" and z_b =2.5". The resulting normalized $\sigma_{rrs}(r_p, z)$ distribution plotted in Figure 1 (b1) shows a rise near z_a and z_b of 1.5 times its magnitude at the plateau. Fig. 1(a2,b2) plot static deformed generator and normalized $\sigma_{rrs}(r_p, z)$ distribution for a unit axial displacement prescribed at the footprint

$$w_{so}(r_p, z) = H(z-z_a) - H(z-z_b) \tag{A8b}$$

In this case, σ_{rrs} rises near z_a and z_b to 1.7 times its magnitude at the plateau.

Table A-1. Cylinder properties

$E \quad (lb/in^2)$	4.5×10^4
$\rho \ (lb\,s^2/in^4)$	8.7×10^{-5}
υ	0.48
$l \quad (in)$	*4*
$r_p \quad (in)$	*0.25*
$r_o \quad (in)$	*3*
$c_d \quad (in/s)$	6.74×10^4
$c_s \quad (in/s)$	1.322×10^4

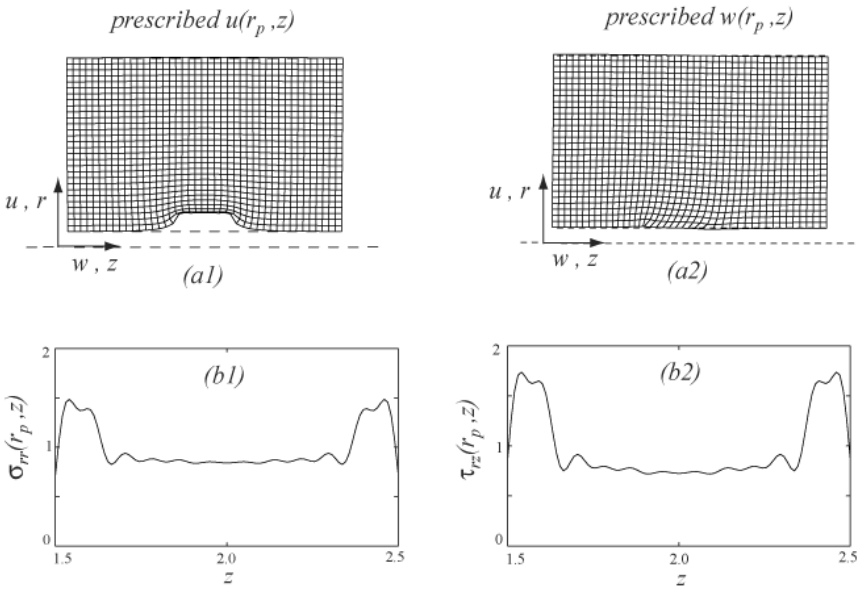

Figure 1. Static deformation and foot-print traction at $r=r_p$, $z_a < z < z_b$
(a1),(b1) prescribed $u(r_p,z)$, *(a2),(b2) prescribed* $w(r_p,z)$

APPENDIX F

MODAL ANALYSIS

The dynamic solution $\mathbf{u}_d(r,z,t)$ satisfies the homogeneous boundary conditions

$$\begin{aligned} &\sigma_{rr}(r_p,z,t)=0\,, \quad \tau_{rz}(r_p,z,t)\;=0 \\ &\sigma_{rr}(r_o,z,t)\;=0\,, \quad \tau_{rz}(r_o,z,t)\;=0 \end{aligned} \tag{B1}$$

Substituting (16a) and (16d) in (B1) yields the matrix equation

$$\mathbf{M}_e\mathbf{C}=\mathbf{0} \tag{B2}$$

$\mathbf{M}_e$ is a 4×4 square matrix, $\mathbf{C}=\{C_1,C_2,C_3,C_4\}^T$ is the vector of unknown coefficients and

$$\begin{aligned} M_{e11} &= -\left((\lambda+2\mu)k_e^2+\lambda k_z^2\right)J_0(k_e r_p)+2\mu\,k_e^2\,J_1(k_e r_p)\;/(k_e r_p) \\ M_{e13} &= 2\mu k_s k_z\left[J_0(k_s r_p)-J_1(k_s r_p)\;/(k_s r_p)\right] \\ M_{e21} &= -2\mu k_e k_z J_1(k_e r_p) \\ M_{e23} &= -\mu(k_s^2-k_z^2)J_1(k_s r) \end{aligned} \tag{B3}$$

M_{e12}, M_{e14}, M_{e22}, M_{e24} have the same form as M_{e11}, M_{e13}, M_{e21}, M_{e23} with J_n replaced by Y_n. Similarly, M_{e3k}, M_{e4k} $k=1,4$ have the same form as M_{e1k}, M_{e2k} $k=1,4$, with r_p replaced by r_o. From the definitions of k_e and k_s in (12), k_e is imaginary when $\omega<k_z c_d$, $c_d=\sqrt{(\lambda+2\mu)/\rho}$, and k_s is imaginary when $\omega<k_z c_s$, $c_s=\sqrt{\mu/\rho}$. Below these cut-off frequencies, J_n and Y_n are replaced by I_n and K_n with appropriate changes in sign. For each m in k_z, a non-trivial solution to (B2) yields the implicit eigenvalue problem

$$det\,|\mathbf{M}_{em}|=0 \quad \Rightarrow \quad \left\{\omega_{mj};\Phi_{mj}(r,z)\right\} \tag{B4}$$

$\left\{\omega_{mj};\Phi_{mj}(r,z)\right\}$ is the Eigen-dyad corresponding to the m^{th} axial wave-number.

APPENDIX G

PLANE-STRAIN PROBLEM

The radial plane-strain problem is that of an infinite hollow cylinder where $\varepsilon_{zz} \equiv w \equiv \partial_z \equiv 0$. The dynamic equation in u then reduces to

$$\begin{aligned} &\hat{\nabla}_1^2 u = 1/c_\varepsilon^2\, \partial_{tt} u \qquad , \quad r_p \le r \le r_o \\ &\hat{\nabla}_1^2 \equiv \partial_{rr} + 1/r\ \partial_r - 1/r^2\ , \quad c_\varepsilon^2 = E_\varepsilon / \rho \\ &E_\varepsilon = E(1-\nu)/\big((1+\nu)(1-2\nu)\big) \end{aligned} \tag{C1}$$

The boundary conditions are

$$u(r_p,t) = f_p(t)\ , \qquad \sigma_{rr}(r_o,t) = 0 \tag{C2}$$

$f_p(t)$ is the time dependent displacement profile prescribed at $r = r_p$. The constitutive law takes the form

$$\begin{aligned} &\sigma_{ii} = \lambda\, \varepsilon_V + 2\mu\, \varepsilon_{ii}\ , \quad ii \to rr,\ \theta\theta,\ zz \\ &\varepsilon_V = \varepsilon_{rr} + \varepsilon_{\theta\theta} \quad , \quad \varepsilon_{zz} \equiv 0 \end{aligned} \tag{C3a}$$

$$\begin{aligned} &\sigma_{rr} = E_\varepsilon \left(\partial_r u + \nu/(1-\nu)\ u/r \right) \\ &\sigma_{\theta\theta} = E_\varepsilon \left(u/r + \nu/(1-\nu)\ \partial_r u \right) \\ &\sigma_{zz} = E_\varepsilon \left(u/r + \partial_r u \right) \nu/(1-\nu) \end{aligned} \tag{C3b}$$

Express $u(r,t)$ as a superposition of a static and a dynamic solution

$$u(r,t) = u_s(r)\ f_p(t) + u_d(r,t) \tag{C4}$$

$u_s(r)$ is the static solution satisfying the inhomogeneous boundary conditions

$$u_s(r_p) = 1\ , \quad \sigma_{rrs}(r_o) = 0 \tag{C5}$$

$u_d(r,t)$ is the dynamic solution satisfying the homogeneous form of boundary conditions (C2). Expand $u_d(r,t)$ in the Eigen functions $\varphi_j(r)$ of (C1)

$$\begin{aligned} &u_d(r,t) = \sum_j a_j(t)\ \varphi_j(r) \\ &\varphi_j(r) = J_1(k_{rj}\, r) + c_2\, Y_1(k_{rj}\, r)\ , \quad c_2 = -J_1(k_{rj}\, r_p)/Y_1(k_{rj}\, r_p) \end{aligned} \tag{C6}$$

Substituting (C6) in the homogeneous form of (C2) yields the dispersion relation

$$
\begin{aligned}
&\alpha_{11}\,\alpha_{22} - \alpha_{12}\,\alpha_{21} = 0 \\
&\alpha_{11} = J_1(k_{r\,j}\,r_p)\,, \qquad \alpha_{12} = Y_1(k_{r\,j}\,r_p) \\
&\alpha_{21} = (\lambda + 2\mu)\,k_{r\,j}\,J_1'(k_{r\,j}\,r_o) + \lambda\,J_1(k_{r\,j}\,r_o)/r_o \\
&\alpha_{22} = (\lambda + 2\mu)\,k_{r\,j}\,Y_1'(k_{r\,j}\,r_o) + \lambda\,Y_1(k_{r\,j}\,r_o)/r_o
\end{aligned}
\tag{C7}
$$

$(\,)'$ stands for derivative with respect to the argument. (C7) determines the wave numbers k_{rj}. The static solution to $\nabla_1^2 u_s = 0$ is

$$
\begin{aligned}
&u_s(r) = Ar + B/r \\
&A = r_p\left(r_p^2 + (\lambda+\mu)\,r_c^2/\mu\right)^{-1}, \quad B = r_p\left(1 - A r_p\right)
\end{aligned}
\tag{C8}
$$

The constitutive law is given by (C3b). Substituting (C6) and (C8) in (C4) and enforcing orthogonality of $\varphi_j(r)$ yields

$$
\begin{aligned}
&\ddot{a}_j(t) + \omega_j^2\,a_j(t) = -\left(N_{a\,j}/N_{j\,j}\right)\ddot{f}_p(t) \\
&N_{j\,j} = \int_{r_p}^{r_o} \varphi_j^2(r)\;r\,dr\;,\;\; N_{a\,j} = \int_{r_p}^{r_o} u_s(r)\;\varphi_j(r)\;r\,dr\;,\quad \omega_j = c_d\,k_{r\,j}
\end{aligned}
\tag{C9}
$$

$(\dot{\,})$ stands for time derivative. The integrals in $N_{j\,j}$ and $N_{a\,j}$ are evaluated analytically in terms of J_n and Y_n for $n = 0,1,2$.

For the radial plane-stress problem, $\sigma_{zz} \equiv w \equiv \partial_z \equiv 0$ yielding the equation

$$
\begin{aligned}
&\hat{\nabla}_1^2 u = 1/c_\sigma^2\;\partial_{tt} u \qquad , \quad \hat{\nabla}_1^2 \equiv \partial_{rr} + 1/r\;\partial_r - 1/r^2 \\
&c_\sigma^2 = E/\left(\rho(1-\nu^2)\right), \quad r_p \le r \le r_c
\end{aligned}
\tag{C10}
$$

(C10) has the same form as (C1) but with a lower speed of propagation since $c_\sigma / c_d = (1-2\nu)^{1/2}/(1-\nu)$ is small when ν is close to 1/2. The constitutive law simplifies to

$$
\begin{aligned}
&\sigma_{rr} = E_\sigma\left(\partial_r u + \nu\,u/r\right) \quad , \;\; \sigma_{\theta\theta} = E_\sigma\left(\,u/r + \nu\;\partial_r u\,\right) \\
&\sigma_{zz} = 0\,, \qquad E_\sigma = E/(1-\nu^2)
\end{aligned}
\tag{C11}
$$

If prescribed displacement at $r = r_p$ is the same for both plane stress and plane strain, then strains are approximately the same. It follows that stresses in (C11) are smaller than those in (C3b) by a factor of $\left(c_\sigma / c_d\right)^2$. In the present

application, if material of the cylinder fails radially within the footprint $z_a \leq z \leq z_b$, then the approximate state of plane-strain changes to that of plane-stress reducing transmitted pressure substantially.

APPENDIX H

EFFECTS OF TARGET PROPERTIES ON FRAGMENT PENETRATION – SENSITIVITY STUDY

SUMMARY

The penetration response of a Gelatin target which is being used as a first order simulant of human heart tissue was studied. The target was subjected to a normal impact at 300 ft./sec. by a steel fragment in the form of a disk with a 4:1 diameter to length ratio. The response was modeled using the Autodyn 2D hydrocode. The failure strength, shear modulus and erosion properties of the target were varied. Of interest was the penetration depth versus time profiles. Also, the left ventricle of the heart was the focus of interest. To first order, this region was assumed to be less than 2 inches deep with the front and rear walls less than 0.5 inches thick. The inner portion is assumed to be filled with blood.

The calculated penetration depths using the baseline Gelatin model was slightly less that 1 inch. Varying the target properties led to penetration depths between 0.1 and greater than 1.2 inches thus potentially putting the fragment somewhere between the inner wall and fluid core. The baseline strength was assumed to be 25 bars. Increasing this level by a factor of 10 had the biggest effect resulting in more than a factor of 10 reduction in penetration depth.

The baseline shear modulus was assumed to be 125 bars. Reducing this level by a factor of 10 resulted in an increase in the penetration depth of about 30%.

The baseline erosion strain was assumed to be 200%. This is the level of strain at which the material is assumed to completely fail and the cells removed from the grid. Doubling this level resulted in a reduction in penetration depth of about 20%.

Based upon these analysis, it is estimated that a factor of 5-10 in shear modulus and/or failure strength will have a significant effect on penetration depth.

BACKGROUND

We are interested in the problem of a small caliber fragment penetrating a human chest cavity, impacting and partially penetrating the heart. The resulting physical damage is manifest in 3 ways:

(1) The projectile generates a wound cavity resulting from the tearing of the material during penetration. This cavity can partially close back on itself but often leaves a residual hole.
(2) The walls of the cavity can be damaged due to both the penetration process and the wall stresses created during the penetration
(3) Tissue remote from the wound cavity can be damaged due to the propagation of stress waves generated by the penetration.

It has been shown by experiment and analysis that the damage and damage trajectory depends to first order on the fragment properties including: projectile velocity, shape, orientation upon impact, and material. The damage also strongly depends upon the tissue material properties and spatial dependence of these properties.

The heart is composed of a number of regions each having its own geometry and material properties. These materials are in general characterized as nonlinear anisotropic with a range of failure strengths. It is not practical or probably required to include the detailed variation of these properties in predicting the critical damage. In order to understand how much uncertainty can be allowed, a series of sensitivity based experiments and numerical predictions are ongoing.

ANALYSIS

A series of 2D axisymmetric hydrocode runs were made using the Autodyn code. In the runs, a steel fragment disc, 7 mm × 1.8 mm, impacts a 3.4 inch thick × 5 inch high elliptical Gelatin heart simulant at 300 ft./sec.

A baseline case is run using the nominal Gelatin material model. Excursions on the Gelatin shear modulus, strength and erosion strain were made with the velocity and penetration depth versus time calculated.

RESULTS

A snapshot of the fragment penetrating the target is shown in Figure D-1. Notice that the 'wound' cavity has a conical like shape expanding behind the penetrating fragment.

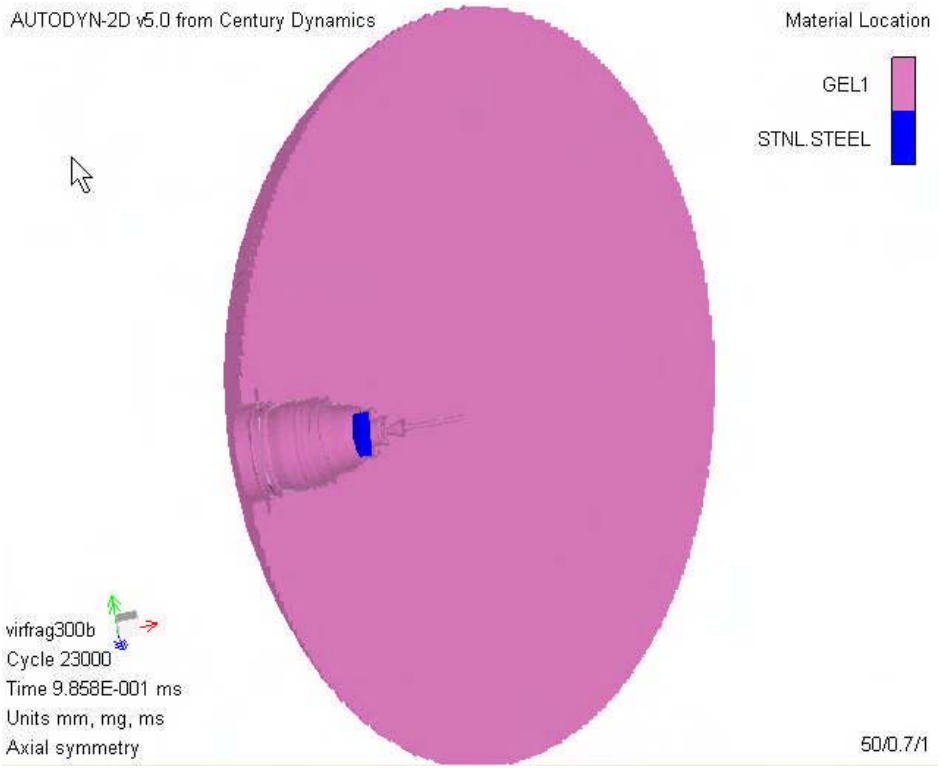

The penetration versus time is shown in Figure D-2. The baseline response is shown as the blue curve. Increasing the failure strength by a factor of 10 results in the lower red curve. Reducing the shear modulus by a factor of 10 results in the upper maroon curve. Reductions in the failure strength and erosion strain result in the intermediate curves. It is seen that a factor of 10 uncertainty in failure strength or shear modulus can have a significant effect on penetration depth.

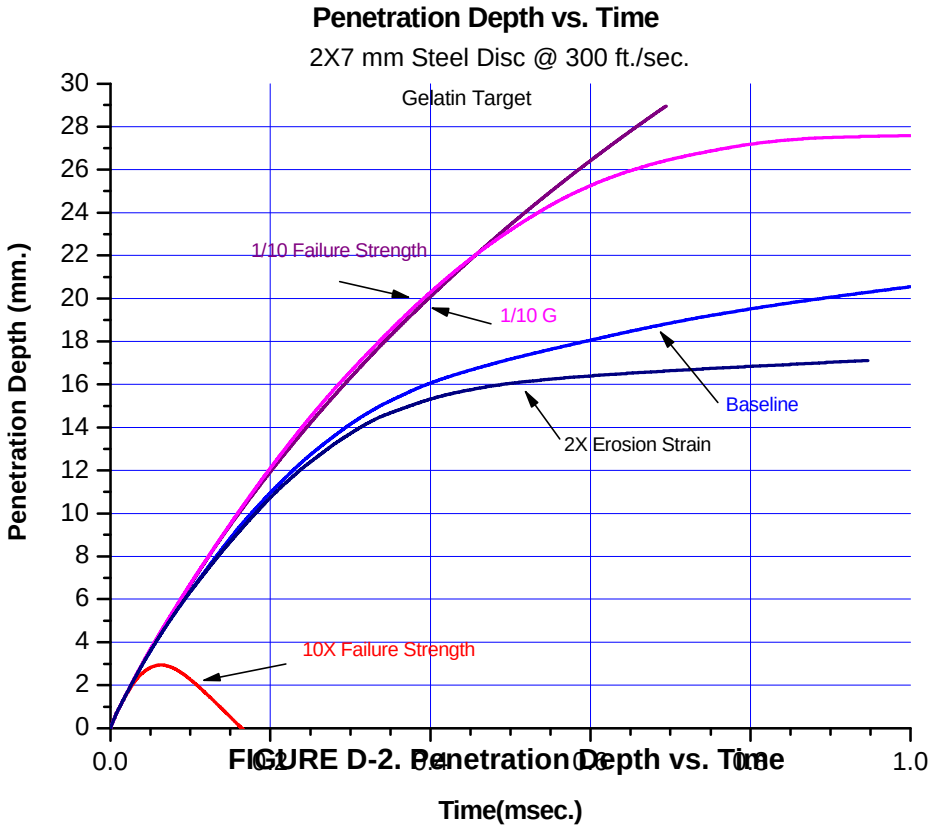

FIGURE D-2. Penetration Depth vs. Time

APPENDIX I

COMPARISON OF LONG ROD VERSUS WEDGE FRAGMENT PENETRATION INTO GELATIN

BACKGROUND

Penetration tests are being performed in support of the Virtual Human program using various 'Nail' like projectiles to investigate certain physical and biological functions. These projectiles are driven into and then stopped at prescribed depths in the targets and thus undergo forced acceleration and then deceleration. The effects of this acceleration vs. time history on target response as compared to what would happen with a projectile which impacts with a known velocity, i.e. launched remains to be explored and is not addressed in this Appendix. Similarly, the details of the target failure which depend upon the failure model and the extend to which Gelatin and biological materials differ also remains to be explored and is not addressed in this Appendix.

The purpose of this study is to explore the similarities and differences one would expect from projectiles with geometries of interest given similar impact conditions and target parameters. To that end, we assumed that the projectiles were given initial velocities and then modeled the penetration into thick gelatin targets.

APPROACH

A series of 2D hydrocode runs were made using various Long Rod and wedge fragments penetrating a gelatin target. Of interest were the (1) deformation patterns, (2) velocity deceleration profiles, and (3) distribution of energy as a function of time.

As a baseline, we explored the effect of a steel wedge fragment. Recall that we had explored this effect earlier wherein we assumed impact velocities on the order of 1000 ft/sec. The early time predicted motion correlated well with that observed in the GBL experiments. However the penetration depths in gelatin were greater that actual heart thicknesses so we decided to re-do the analysis using impact velocities which would result in the projectile remaining in the assumed approximately 4" thick simulated heart.

We then turned the wedge around and contrasted the response with the tip-forward impact. This was done to illustrate the differences in response depending on the orientation of the fragment on impact. The difference in response was not due to differences in kinetic energy (which was the same for both cases).

Finally, we selected a 'long rod' penetrator with what we believed to be a representative 'Nail' projectile geometry which we assumed to be a 4" long by 10 mm diameter circular rod with a hemispherical cap impacting normal to the target. We explored several impact velocities until we came up with one which would cause the 'Nail' to (1) penetrate but stop in the gelatin and (2) penetrate and continue out the back.

SUMMARY

The wound track, energy transfer and resulting damage in gelatin are a strong function of the fragment geometry and fragment striking angle and velocity. Projectiles with irregular geometries will tumble while projectiles with large aspect ratios will penetrate with little relative retardation. The retardation and energy transfer characteristics of 'Wedge' and 'Nail' like projectiles can be very different as demonstrated in this analysis.

RESULTS

(1) Steel Wedge 'Forward' Impacts: Impact Velocities Less 66 m/sec.

The deceleration velocity vs. time profile is shown in Figure E-1. In the case of the higher velocity impact (~220 ft/sec) the penetration process is violent with the projectile causing massive damage ahead of its path. The target material just fails and subsequently provides little penetration resistance thus the projectile velocity reaches a constant state. In the case of the lower velocity impact (~110 ft/sec) The projectile tumbles and moves off the path of its original velocity vector and then is stopped by the target and remains imbedded.

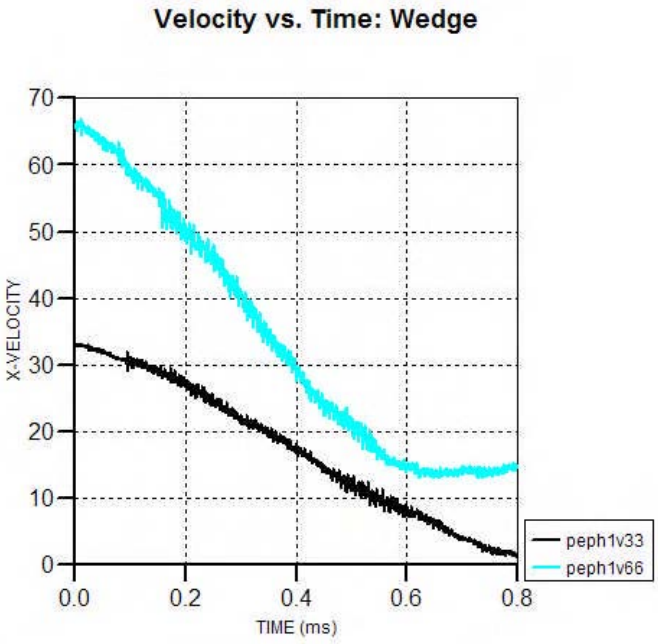

FIGURE E-1. Deceleration Velocity vs. Time for Wedge 'Forward' Impacts

The deformation/pressure fields at 1.2 msec. after impact are shown in Figure E-2.

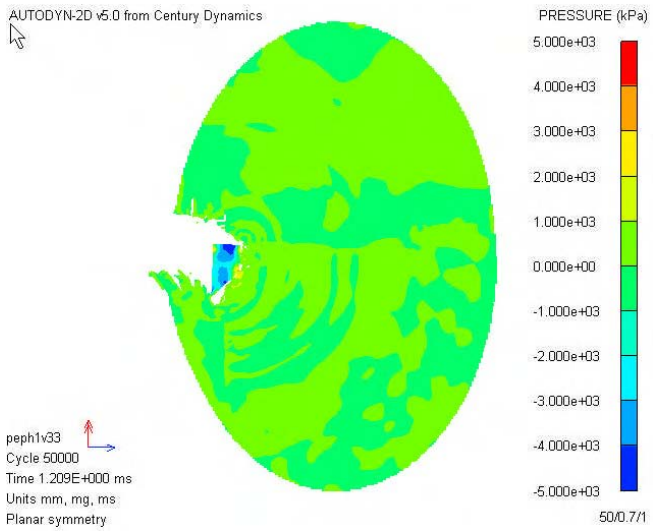

FIGURE E-2. Deformation/Pressure Snapshot for 'Forward' Wedge @ 110 ft/sec.

(2) Steel Wedge 'Backward': Impacts Velocities Less Than 66 m/sec.

In this case, the fragment impacted with cylindrical end first. A comparison of the deceleration velocity for the 'forward' and 'backward' impact orientations is shown in Figure E-3. Notice the very different behavior. The 'forward' first projectile tumbles at early time presenting a much larger projected area and is stopped by the target. The 'backward' first projectile acts like a rod for a long time and then and undergoes only slight rotations and thus decelerates at a much slower rate.

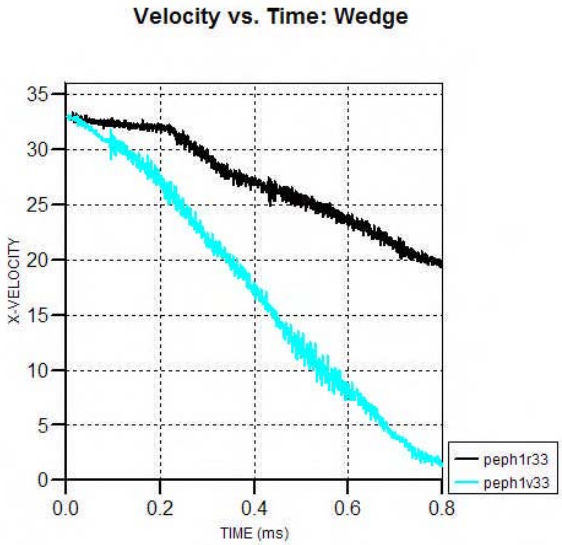

Figure E-3. Deceleration Velocity vs. Time 'Forward','Backward' Wedge @ 110 ft/sec.

A snapshot of the deformation/pressure field is shown in Figure E-4.

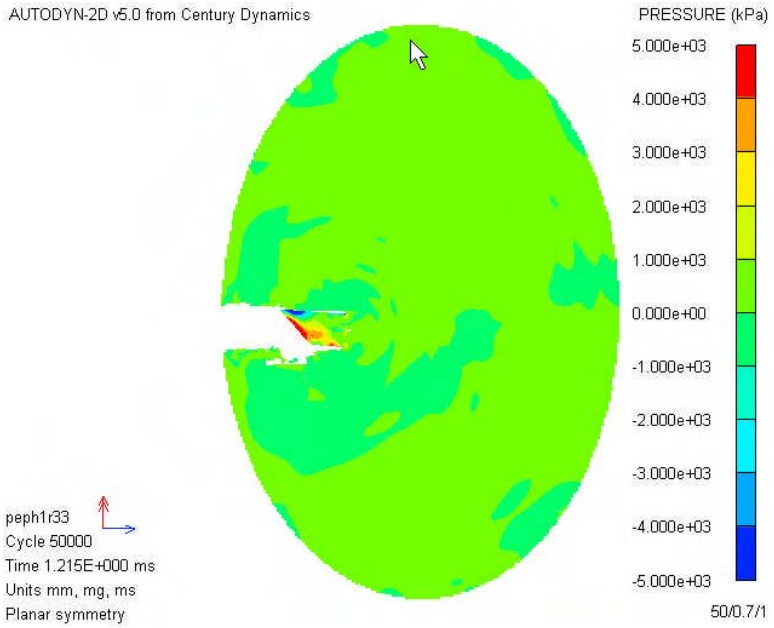

FIGURE E-4. Deformation/Pressure Snapshot for 'Backward' Wedge@110 ft/sec.

(3) Steel 'Long Nail': Impacts at Velocities Less Than 33 m/sec.

A series of runs were made using a 4" long 'Nail' projectile. It was speculated that this type of projectile because of its large aspect ratio and additional momentum/kinetic energy would be fairly penetrating and that was born out in the analysis. Typical velocity deceleration vs. time profiles are shown in Figure E-5. The projectile basically penetrates the target undisturbed at 110 ft/sec. in contrast to the wedge which stopped in the middle of the target. The impact velocity would have to be reduce to less than approximately 50 ft./sec. to prevent penetration.

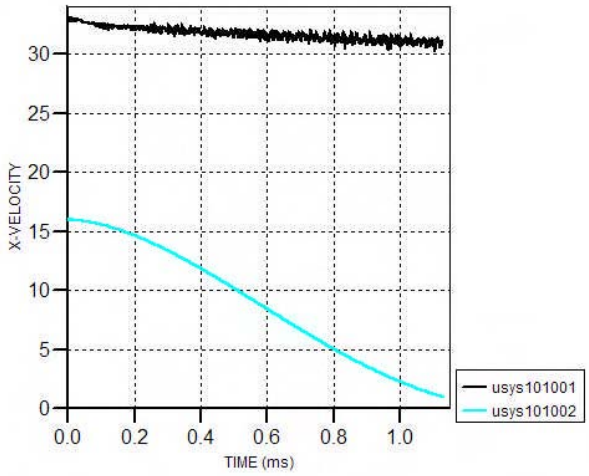

FIGURE E-5. Deceleration Velocity vs. Time 'Long Nail'

A snapshot of the deformation pattern/pressure state is shown in Figure E-6. Notice that the projectile has caused massive 'failure' of the target while continuing to penetrate.

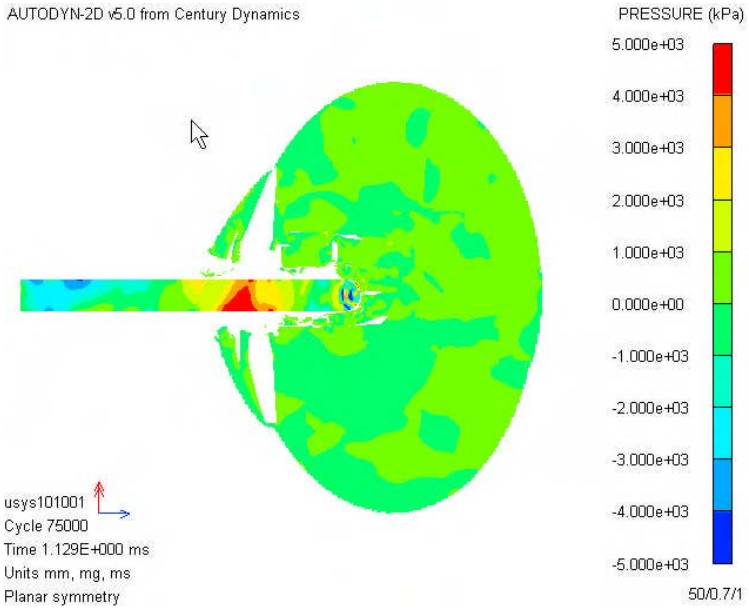

FIGURE E-6. Deformation/Pressure Snapshot for 'Long Nail'@110 ft/sec

(4) Steel 'Short Nail': Impacts at Velocities Less Than 33 m/sec.

A series of runs were made where the length of the 'Nail' was reduced from 4" to about 1.5". This still left an aspect ration of 4:1. The resulting velocity deceleration vs. time results are shown in Figure E-7. It is seen that the projectile actually is decelerating more quickly than the 'long' nail as expected. This will continue as the aspect ratio, and impact momentum is further reduced.

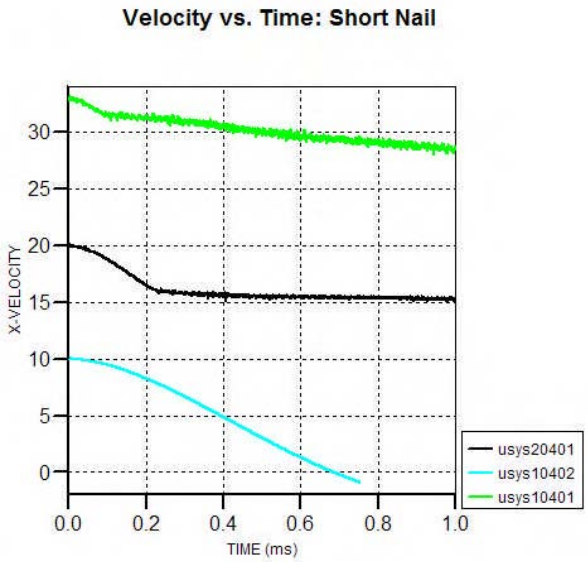

FIGURE E-7. Deceleration Velocity vs. Time 'Short Nail'

The 'Short Nail' still creates substantial target damage behind the projectile at an impact velocity of 110ft./sec. as shown in Figure E-8.

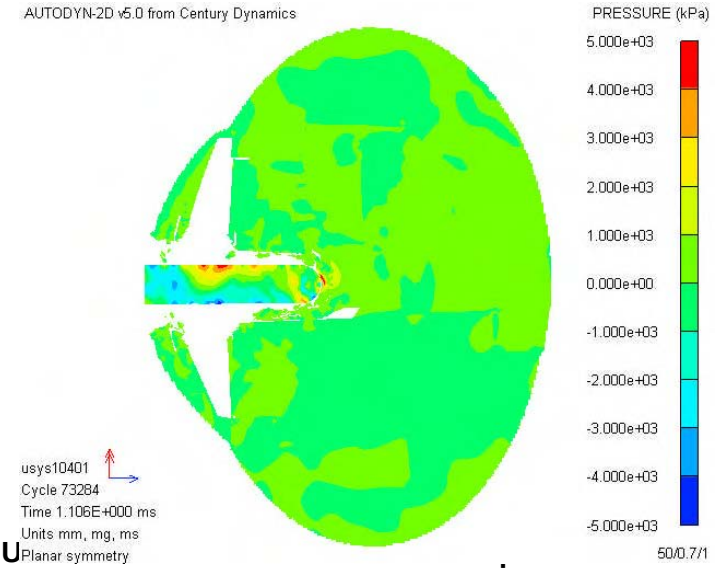

FIGURE E-8. Nail'@110 ft/sec

(5) Energy Partitioning in Targets as a Function of Impacting Fragment Parameters

Upon impact and during subsequent penetration the projectiles transfer energy and momentum to the targets. The energy is partitioned into Kinetic and Strain energy. The fragment and target properties and impact velocity will determine the energy partitioning.

Results for those components of the kinetic and internal portions of the energy in the target are shown in Figures E-9 through E-11. Shown in the plots is total energy in the projectile + projectile as a function of time (minus the energy lost to failed material and numerical error), the total energy transmitted to the target (h130), and the kinetic, internal energy components transmitted to the target.

Results for the 'forward'/'backward' wedge impacts at 110 ft./sec. are shown in Figures E-9 and E-10. First, it is seen that substantial energy is lost to material failure as the projectile tumbles. Second, the kinetic energy in the target is an important portion of the total energy in the target, especially for the 'backward' projectile. Finally, when the energy in the target peaks, it is about 1/3 of the total of the projectile + target energy which is substantial.

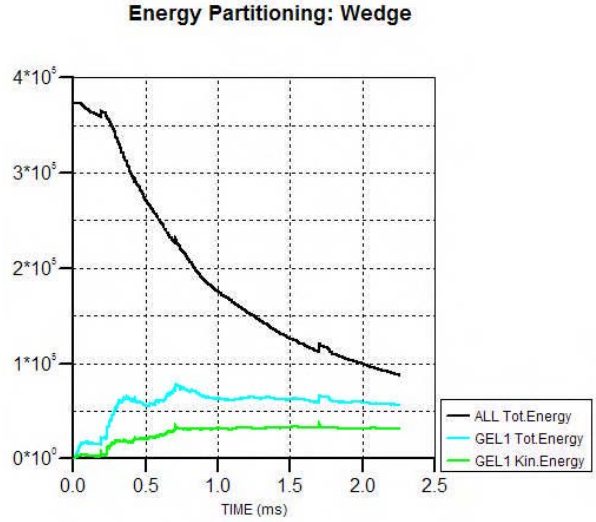

FIGURE E-9. Energy Partitioning during 'Forward' Wedge Impact

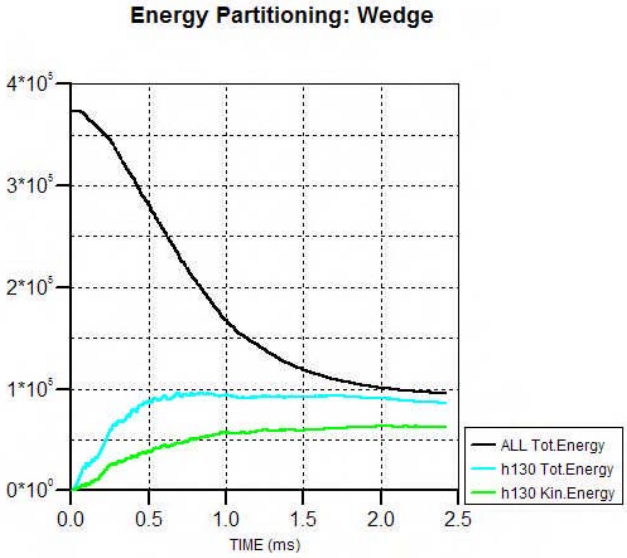

FIGURE E-10. Energy Partitioning during 'Backward' Wedge Impact

In the case of the 'Nail' impacts the results are different as shown in Figure E-11. The solid black and violet lines represent the total energy in the problem for the cases of 110 and 220 ft/sec. striking velocities. Note that these levels do not vary much with time indicating little energy loss due to failure and (numerical error). The cyan line represents the total energy in the target for the 'Long Nail' case. Notice that this is a very small fraction of the incident projectile energy, probably less than 5%. The darker blue line is the total energy in the target for the case on the 'Short Nail' which increases with time as the target slows the projectile down.

If we were to continue to reduce the aspect ratio of the 'Nail' we should approach the result for the 'backward' wedge.

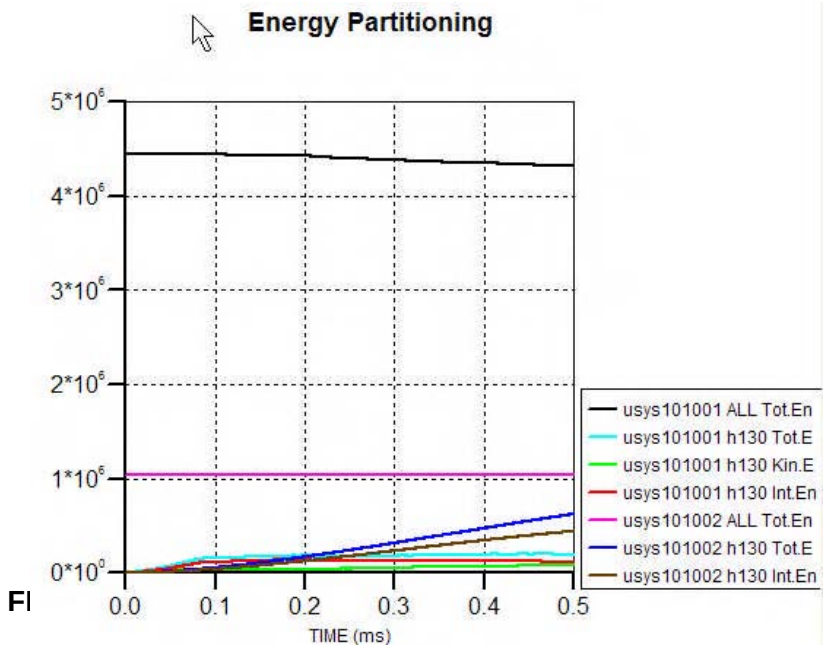

Fl

APPENDIX J

Accepted for Publication in the American Association of Mechanical Engineer's *Journal of Applied Mechanics*

"An acoustic model for wave propagation in a weak layer"

Michael El-Raheb

ATK Mission Research, Laguna Hills, CA

ABSTRACT

An acoustic model is developed for transient wave propagation in a weak layer excited by prescribed pressure or prescribed acceleration at the boundary. The validity of the acoustic model is investigated for the two excitations. A comparison of transient response from the acoustic model and a 3-D axisymmetric elastic model reveals that for prescribed acceleration the acoustic model fails to capture important features of the elastic model even as Poisson ratio ν approaches 1/2. However for prescribed pressure, the two models agree since shear stress is reduced. For prescribed acceleration adopting the modal approach, the mixed boundary-value problem on the excited boundary is converted to a pure traction problem utilizing the influence method. To validate the elaborate modal approach a finite difference model is also developed.

1. Introduction

Laboratory simulation of blunt trauma in living tissue relies on measuring propagation of stress waves from low velocity impact in a weak viscoelastic material such as ordnance gelatin. It has acoustic impedance close to that of water yet living tissue dissipates energy from viscoelasticity and possesses shear rigidity controlling transverse propagation. It has been widely assumed that gelatin is similar to water because it has approximately the same density and bulk speed of sound. In a weak solid like gelatin, effects of the free surface and lateral propagation of a forcing pulse are controlled by shear modulus G and the speed of shear waves respectively. These types of propagation are independent of a loss mechanism like viscoelasticity. Loss produces an attenuation of the pulse over and above that from dispersion. It reduces the participation of high frequency modes by smoothing average response and its gradients.

In a fluid like water, propagation is mostly volumetric, with shear related to dissipation that is proportional to velocity gradient and kinematic viscosity. At the free surface a different kind of wave develops controlled by gravity and depth of the fluid. It can be argued that although water and gelatin have very similar acoustic impedances, shear rigidity of gelatin may control how a stress wave propagates laterally and its character at and close to the free surface. If gelatin is like water then it can be treated as an acoustic fluid governed by the wave equation. In this work the wave equation is derived as a limiting case of the linear elasto-dynamic equations of a homogeneous solid. In fact when Poisson ratio assumes the value of 1/2, the elastic field converts to the acoustic field. One issue addressed in this work is the sensitivity of the solution to Poisson ratio close to 1/2.

To measure transmission of stress waves produced by low velocity impact on gelatin, a layer is bonded onto a metallic substrate instrumented by sensitive carbon gauges. Upon impact, stress waves propagate across the layer reaching the

substrate with substantial reduction in intensity from dispersion and viscous losses. Measuring impact and transmitted pressures are needed to construct the material's constitutive model. Carefully controlled experiments with sufficient accuracy reproducing transient histories for correlation with computed results are very hard to execute. The problem lies in the weakness of the material. Gauges can neither be placed inside the material while gauges at the interface between material and metal substrate suffer from lack of cohesion adding uncertainty to measured data. This difficulty forces investigators to rely on sensitivity studies from analysis and general purpose discretization programs in order to understand phenomena. Moreover, literature in this field addresses quasi-static measurements of elongation omitting important dynamic effects such as strain-rate dependence in the microsecond regime. The simulation of these experiments led to the realization that approximating gelatin as a viscous fluid is valid only for unrealistic impact conditions when pressure over the footprint is uniform.

Acoustic wave propagation governed by the Helmholtz equation has been treated extensively in the literature. Solution techniques range from the analytical for simple geometries to numerical for problems with complicated geometry, medium inhomogeneity and nonlinearity. Theil [1] treats the 1-D viscoelastically damped wave equation analytically. Yserentant [2] shows how a consistent discretization of the acoustic equation can be recovered from the particle model of compressible fluids (see Ref. [3]). Sina and Khashayar [4] solve the 3-D wave equation analytically for arbitrary non-homogeneous media adopting the differential transfer matrix. Sujith et. Al. [5] present an exact solution to 1-D transient waves in curvilinear coordinates adopting transformation of variables suggested by the WKB approximation. Hamdi et. Al. [6] present exact solitary wave solutions of the 1-D wave propagation in nonlinear media with dispersion. Yang [7] solves numerically the wave equation with attenuation from linear friction utilizing grid modification to track wave fronts accurately. Narayan [8] solves the 3-D transient

acoustics in inhomogeneous media by finite difference and Schemann and Bornemann [9] apply the adaptive Rothe integrator. Bailly and Juve [10] present a numerical solution to the 2-D acoustic propagation from transient sources using the dispersion-relation-preserving scheme in space and a fourth-order Runge-Kutta in time. Wagner et. Al. [11] and Gaul and Wenzel [12] use a hybrid boundary element method for frequency and transient acoustic response in bounded and unbounded regions. Mehdizadeh and Paraschivoiu [13] develop a spectral element method to solve the 3-D Helmholtz equation retaining accuracy for large wave numbers. None of the references above addresses 3-D transient propagation from impact analytically.

Acoustic wave propagation in a free disk is developed here adopting a modal analysis validated by a finite difference method. Transient response to prescribed pressure and prescribed acceleration at the boundary is analyzed. Since the primary goal of this work is to investigate the validity of the established belief that tissue can be treated as a fluid, the acoustic equation is derived from the elastic equations of a solid in the limit when Poisson ratio and shear stresses vanish (Appendix A).

Section 2 develops the acoustic model utilizing the modal approach for both prescribed pressure and prescribed acceleration. In the modal approach, the forcing function at the boundary is treated adopting the static-dynamic superposition method (see Berry and Naghdi [14]). The solution is expressed as a superposition of a static term satisfying the inhomogeneous boundary conditions, and a dynamic solution in terms of the eigenfunctions satisfying homogeneous boundary conditions.

Since the projectile’s strength and acoustic impedance are much greater than those of tissue, the excitation transmitted over the boundary at the projectile-tissue interface can be approximated as a given time dependent prescribed motion in contrast to an unknown pressure excitation. However,

this type of excitation would lead to a mixed boundary condition; i.e. pressure gradient prescribed over part of the boundary and zero pressure prescribed over the remaining part. This difficulty can be overcome by the influence method which superimposes response from a set of unit pressures with time-dependent weights prescribed on annular portions of the footprint. These weights are updated at each time step from the condition that combined acceleration at the center of each ring over the footprint equals the prescribed instantaneous acceleration. In this way, the forcing function is converted to pure traction with time-varying spatial dependence.

Section 3 develops the finite difference approach. Radial and axial dependence are discretized by central differences while time dependence is integrated by the Kutta-Runge method.

Section 4 compares acoustic histories from the two approaches validating the modal approach. Histories of the acoustic model are compared to those from a 3-D axisymmetric elastic model demonstrating the inadequacy of the acoustic model when applied to a solid with Poisson ratio near 1/2 and forced by applied acceleration. Sensitivity of the acoustic histories to type of excitation and to parameters of the prescribed acceleration profile is also presented. The effect of Poisson ratio ν on peak elastic stress is evaluated confirming that for prescribed acceleration mismatch of acoustic and elastic results is not caused by small deviations in Poisson ratio ν from 1/2 in the elastic model. Finally, results from the two models are compared for prescribed uniform pressure revealing that the mismatch diminishes when shear stress is reduced.

2. Modal analysis

In the analysis to follow, all variables are independent of circumferential angle due to the assumption of axisymmetry. This condition applies for a cylindrical projectile at normal incidence. Consider a traction-free disk with radius r_d and length h bonded to a rigid sub-strate. Appendix A derives the acoustic equation in the limit when shear stress vanishes in the linear elasto-dynamic equations of a solid. In the analysis to follow, r and z denote radial and axial coordinates. Acoustic propagation in the disk is governed by the acoustic equation

$$\left(\partial_{rr} + 1/r\ \partial_r + \partial_{zz}\right) p_d - 1/c_b^2\ \partial_{tt} p_d = 0 \qquad \text{(1a)}$$

with the following boundary conditions

$$p(r_d, z; t) = 0 \qquad \text{(1b)}$$

$$\begin{aligned} p(r,0;t) &= [H(r) - H(r-r_p)]\ f(t) \quad \textit{prescribed pressure} \\ \partial_z p(r,0;t) &= -\rho\ \ddot{f}_w(t) \quad 0 \le r \le r_p \\ p(r,0;t) &= 0 \quad r_p < r < r_d \end{aligned} \quad \textit{prescribed acceleration} \qquad \text{(1c)}$$

$$\begin{aligned} \partial_z p(r,h;t) &= 0\,, \quad \textit{fixed face, or alternatively} \\ p(r,h;t) &= 0\,, \quad \textit{free face} \end{aligned} \qquad \text{(1d)}$$

where $H(r)$ is the Heaviside function, r_p is footprint radius of the external excitation which is projectile radius, $f(t)$ is time dependence of prescribed pressure and $\ddot{f}_w(t)$ is time dependence of prescribed acceleration. Express $p(r,z;t)$ as a superposition of two terms (see Berry and Naghdi [14])

$$p(r,z;t) = \begin{cases} p_s(r,z)\ f(t) + p_d(r,z;t)\,, & \textit{prescribed pressure} \\ -p_s(r,z)\,\rho\ \ddot{f}_w(t) + p_d(r,z;t)\,, & \textit{prescribed acceleration} \end{cases} \qquad \text{(2)}$$

where $p_s(r,z)$ is the static solution of (1a) with inhomogeneous boundary conditions (1b-d) assuming $f(t) = 1$ or $\ddot{f}_w(t) = 1/\rho$, and $p_d(r,z;t)$ is a dynamic

solution of (1a) satisfying the homogeneous boundary conditions (1b-d) with $f(t)=0$ or $\ddot{f}_w(t)=0$.

The prescribed acceleration boundary condition in (1c) is mixed. In other words, part of the boundary has prescribed pressure gradient and the other part has prescribed pressure. This difficulty can be overcome by dividing the circle bounding the footprint into $n+1$ equidistant radial stations with increment Δr_p

$$0, r_1, r_2, ..., r_{n-1}, r_n \qquad , \qquad r_k - r_{k-1} = \Delta r_p = const$$

where $r_n = r_p$. Assume a uniform pressure of unit intensity acting over each annular segment $r_{k-1} \to r_k$ that is termed source segment. Where subscript z denotes partial derivative with respect to z, evaluating the pressure gradient $P_{z,lk}(r,z;t)$ from the k^{th} source segment at the center of the l^{th} segment $r_{cl} = (r_l + r_{l-1})/2$ that is termed target point and following the expansion in (2) yields

$$P_{z,lk}(r_{cl},0;t) = -p_{zs,lk}(r_{cl},0)\,\rho\,\ddot{f}_w(t) + p_{zd,lk}(r_{cl},0;t) \qquad (3)$$

where $p_{zs,lk}(r_{cl},0;t)$ and $p_{zd,lk}(r_{cl},0)$ are static and dynamic pressure gradients at the l^{th} target point due to the k^{th} source segment. Enforcing the condition of prescribed pressure gradient $p_{zf}(t)$ over the footprint at each time step yields a set of simultaneous equations in the weights $c_k(t)$

$$\sum_{k=1}^{n} P_{z,lk}(r_{cl},0;t)\,c_k(t) = p_{zf}(t) \quad , \quad 1 \le l \le n \qquad (4)$$

The combined pressure from all annular source segments is the superposition of $P_{lk}(r,z;t)$ factored by time dependent weights $c_k(t)$

$$p(r,z;t)=\sum_{k=1}^{n}P_{lk}(r,z;t)\,c_k(t)\quad,\qquad 1\le l\le n$$
$$P_{lk}(r,z;t)=-p_{s,lk}(r,z)\,\rho\,\ddot{f}_w(t)+p_{d,lk}(r,z;t) \tag{5a}$$

Solutions of $p_{s,k}(r,z;t)$ and $p_{d,k}(r,z;t)$ for each unit source segment are outlined in what follows. The static solution for the k^{th} source segment $p_s(r,z)$ takes the form

$$p_{s,k}(r,z)=\sum_{m=1}^{m_r}\psi_{sm,k}(z)\;J_0(k_{rm}\,r)$$
$$\psi_{sm,k}(z)=\alpha_{mk}\sinh(k_{rm}\,z)+\beta_{mk}\cosh(k_{rm}\,z) \tag{5b}$$

where $J_0(k_{rm}\,r)$ is the Bessel function of the first kind and zeroth order. Substituting (5b) in the boundary conditions (1b,c,d) and enforcing orthogonality of $J_0(k_{rm}\,r)$ yields

$$J_0(k_{rm}\,r_d)=0\quad,\quad 1\le m\le m_r \tag{6a}$$

$$\beta_{m,k}=\frac{2\left(r_k J_1(k_{rm}\,r_k)-r_{k-1}J_1(k_{rm}\,r_{k-1})\right)}{r_d^2\,J_1^2(k_{rm}\,r_d)\,k_{rm}} \tag{6b}$$

$$\alpha_{m,k}=\begin{cases}-\beta_{m,k}\tanh(k_{rm}\,h)\;,\;\textit{fixed face, or alternatively}\\ -\beta_{m,k}/\tanh(k_{rm}\,h)\;,\;\textit{free face}\end{cases} \tag{6c}$$

Note that in (3) $p_{zs,lk}\left(r_{cl},0\right)=\partial_z p_{s,k}(r_{cl},0)$.

The dynamic solution $p_{d,k}(r,z;t)$ satisfies

$$\left(\partial_{rr}+1/r\;\partial_r+\partial_{zz}\right)p_{d,k}-1/c_b^2\;\partial_{tt}\;p_{d,k}=0 \tag{7}$$

and the homogeneous boundary conditions in (1b-d). Expand $p_d(r,z;t)$ in terms of its orthogonal eigenfunctions

$$p_{d,k}(r,z;t)=\sum_m\sum_n a_{mn,k}(t)\;\psi_{dn}(z)\;J_0(k_{rm}\,r) \tag{8}$$

Applying the homogeneous boundary conditions in (1b,c,d) to $J_0(k_{rm}\,r)$ and $\psi_{dn}(z)$ produces

$$J_0(k_{rm}\,r_d)=0 \qquad ,\ 1\le m\le m_r \tag{9a}$$

$$\psi_{dn}(z)=\begin{cases}\cos(k_{zn}\,z),\ \cos(k_{zn}\,h)=0\ \rightarrow\ k_{zn}h=\dfrac{1}{2}(2n-1)\pi, & \textit{fixed face}\\ \sin(k_{zn}\,h),\ \sin(k_{zn}\,h)=0\ \rightarrow\ k_{zn}h=n\pi, & \textit{free face}\end{cases},\ 1\le n\le n_z \tag{9b}$$

$$k_{zn}^2+k_{rm}^2=k_{mn}^2 \quad ,\ \ \omega_{mn}=c_b\,k_{mn} \tag{9c}$$

where ω_{mn} is the eigenfrequency corresponding to mode (m,n). Substituting (3) in (1a) with use made of (5),(6),(8) and (9) and enforcing orthogonality of $\psi_{dn}(z)$ and $J_0(k_{rm}\,r)$ yields

$$\begin{aligned}&\ddot{a}_{mn,k}(t)+\omega_{mn}^2 a_{mn,k}(t)=-N_{sd\,mn,k}\ \rho\ f_w^{IV}(t)\ ;\quad f_w^{IV}(t)=\partial^4 f_w(t)/\partial t^4\\ &N_{sd\,mn,k}=\frac{2}{h}\int_0^h \psi_{sm,k}(z)\ \psi_{dn}(z)\,dz\ ,\ \ 1\le m\le m_r\ ,\ 1\le n\le n_z\end{aligned} \tag{10}$$

In deriving Eq. (10) the term $\nabla_0^2\left(-p_s\right)\rho\ \ddot{f}_w(t)$, $(\nabla_0^2\equiv\partial_{rr}+1/r\partial_r)$ vanishes since static pressure $p_s(r,z)$ satisfies the equation $\nabla_0^2 p_s=0$. Acoustic displacements $(w,u)_k$ are determined from (A4)

$$\begin{aligned}&\partial_z p_{d,k}=-\rho\ \partial_{tt}^2\,w_k\\ &\partial_r p_{d,k}=-\rho\ \partial_{tt}^2\,u_k\end{aligned} \tag{11}$$

The solution to (10) is expressed as a Duhamel integral

$$a_{mn,k}(t)=-\frac{\rho N_{sd\,mn,k}}{\omega_{mn}}\int_0^t \sin\omega_{mn}(t-\tau)\ \ f_w^{IV}(\tau)\,d\tau \tag{12}$$

Note that in (11) $\partial_z p_{d,k}(r_{cl},0;t) = p_{zd,lk}(r_{cl},0;t)$ as defined in (3). Once histories of $\partial_z p_{d,k}$ and $\partial_r p_{d,k}$ are determined from solving (10), histories of w_k and u_k are found by integrating (11) numerically.

3. Finite difference

Consider a disk with traction-free boundaries satisfying the conditions

$$\partial_r p(0,z;t) = 0 \qquad (13a)$$

$$p(r_d,z;t) = 0 \qquad (13b)$$

$$\partial_z p(r,0;t) = 0 \qquad (13c)$$

$$\left.\begin{aligned} p(r,h;t) &= \left[H(r)-H(r-r_p)\right] f(t) \quad \textit{prescribed pressure} \\ \partial_z p(r,h;t) &= -\rho \ddot{f}_w(t) \quad , \quad 0 \le r \le r_p \\ p(r,h;t) &= 0 \quad , \quad r_p < r \le r_d \end{aligned}\right\} \textit{prescribed acceleration} \qquad (13d)$$

where $(\dot{})$ denotes time derivative. Unlike the analysis in Section 2 where z has its origin at the excited boundary, in the finite difference scheme z has its origin at the non-excited boundary. Condition (13a) is symmetry about the axis of revolution $r = 0$, (13b) is traction-free boundary at $r = r_d$, (13c) is fixed boundary at $z = 0$, and (13d) is prescribed acceleration for $0 \le r \le r_p$ and traction-free boundary for $r_p \le r \le r_d$ at $z = h$. Form the rectangular grid

$$\begin{aligned} &i = 1 \to n_r \quad , \quad d_r \le r \le r_d - d_r \quad , \quad d_r = r_d/(n_r+1) \\ &j = 1 \to n_z \quad , \quad d_z \le z \le h - d_z \quad , \quad d_z = h/(n_z+1) \end{aligned} \qquad (14)$$

In this grid, nodes do not include points on the boundaries. Expressing Eq. (1a) in central difference to first order yields the following relations depending on position:

a) Internal points $d_r < r < r_d - d_r,\ d_z < z < h - d_z \ \Rightarrow\ 2 \le i \le n_r - 1,\ 2 \le j \le n_z - 1$

$$\alpha_1 p_{i+1,j} + \alpha_2 p_{i-1,j} + \alpha_3 p_{i,j} + \alpha_4 \left(p_{i,j+1} + p_{i,j-1} \right) = 1/c_b^2 \, \ddot{p}_{i,j}$$

$$\alpha_1 = \left(\frac{1}{d_r^{\,2}} + \frac{1}{2 r_i d_r} \right), \;\; \alpha_2 = \left(\frac{1}{d_r^{\,2}} - \frac{1}{2 r_i d_r} \right), \;\; \alpha_3 = -2 \left(\frac{1}{d_r^{\,2}} + \frac{1}{d_z^{\,2}} \right), \;\; \alpha_4 = \frac{1}{d_z^{\,2}} \qquad \text{(15a)}$$

b) Corner point at $r = d_r, \; z = d_z \;\Rightarrow\; i = 1, \; j = 1$

$$\alpha_1 p_{i+1,j} + (\alpha_2 + \alpha_3 + \alpha_4) p_{i,j} + \alpha_4 p_{i,j+1} = 1/c_b^2 \, \ddot{p}_{i,j} \qquad \text{(15b)}$$

c) Points along axis $r = d_r \;, \; d_z < z < h - d_z \;\Rightarrow\; i = 1 \;\; , \;\; 2 \le j \le n_z - 1$

$$\alpha_1 p_{i+1,j} + (\alpha_2 + \alpha_3) p_{i,j} + \alpha_4 (p_{i,j+1} + p_{i,j-1}) = 1/c_b^2 \, \ddot{p}_{i,j} \qquad \text{(15c)}$$

d) Corner point at $r = d_r, \; z = h - d_z \;\Rightarrow\; i = 1, \;\; j = n_z$

For prescribed pressure

$$\alpha_1 p_{i+1,j} + (\alpha_2 + \alpha_3) p_{i,j} + \alpha_4 p_{i,j-1} - 1/c_b^2 \, \ddot{p}_{i,j} = \alpha_4 f(t) \qquad \text{(15d)}$$

For prescribed acceleration

$$\alpha_1 p_{i+1,j} + (\alpha_2 + \alpha_3 + \alpha_4) p_{i,j} + \alpha_4 p_{i,j-1} - 1/c^2 \ddot{p}_{i,j} = -\rho \, \ddot{f}_w(t)/d_z$$

e) Points along boundary $d_r < r < r_d - d_r \;, \; z = d_z \;\; \Rightarrow 2 \le i \le n_r - 1, \;\; j = 1$

$$\alpha_1 p_{i+1,j} + \alpha_2 p_{i-1,j} + (\alpha_3 + \alpha_4) p_{i,j} + \alpha_4 p_{i,j+1} = 1/c_b^2 \, \ddot{p}_{i,j} \qquad \text{(15e)}$$

f) Points along boundary $d_r < r < r_d - d_r \;, \; z = h - d_z \;\; \Rightarrow 2 \le i \le n_r - 1, \;\; j = n_z$

For $0 \le r \le r_p$ and prescribed pressure

$$\alpha_1 p_{i+1,j} + \alpha_2 p_{i-1,j} + \alpha_3 p_{i,j} + \alpha_4 p_{i,j-1} - 1/c_b^2 \, \ddot{p}_{i,j} = \alpha_4 \, f(t) \qquad \text{(15f)}$$

For $0 \le r \le r_p$ and prescribed acceleration

$$\alpha_1 p_{i+1,j} + \alpha_2 p_{i-1,j} + (\alpha_3 + \alpha_4) p_{i,j} + \alpha_4 p_{i,j-1} - 1/c_b^2 \, \ddot{p}_{i,j} = -\rho \, \ddot{f}_w(t)/d_z$$

For $r_p < r \le r_d$

$$\alpha_1 p_{i+1,j} + \alpha_2 p_{i-1,j} + \alpha_3 p_{i,j} + \alpha_4 p_{i,j-1} - 1/c_b^2 \, \ddot{p}_{i,j} = 0$$

g) Corner point at $r = r_d - d_r,\ z = d_z \ \Rightarrow\ i = n_r,\ j = 1$

$$\alpha_2 p_{i-1,j} + (\alpha_3 + \alpha_4) p_{i,j} + \alpha_4 p_{i,j+1} = 1/c^2\, \ddot{p}_{i,j} \qquad (15g)$$

h) Points along boundary $r = r_d - d_r\ ,\ d_z < z < h - d_z \ \Rightarrow\ i = n_r,\ 2 \le j \le n_z - 1$

$$\alpha_2 p_{i-1,j} + \alpha_3 p_{i,j} + \alpha_4 (p_{i,j+1} + p_{i,j-1}) = 1/c_b^2\, \ddot{p}_{i,j} \qquad (15h)$$

i) Corner point at $r = r_d - d_r\ ,\ z = h - d_z \ \Rightarrow\ i = n_r,\ j = n_z$

$$\alpha_2 p_{i-1,j} + \alpha_3 p_{i,j} + \alpha_4 p_{i,j-1} = 1/c_b^2\, \ddot{p}_{i,j} \qquad (15i)$$

In (15a-i), the differential equation is satisfied only at internal points of the grid modified by constraints on the boundaries.

Applying (15a-15i) at all internal points in the grid (14) produces a set of ordinary differential equations in $p_{i,j}(t)$ cast in the form of tri-diagonal blocks as follows

$$\ddot{\mathbf{p}} = c_b^2 \left(\mathbf{M}_p \mathbf{p} - \mathbf{F}(t) \right) \qquad (16)$$

$$\mathbf{M}_p = \begin{bmatrix} \mathbf{A}_1 & \mathbf{C}_1 & & & \\ \mathbf{B}_2 & \mathbf{A}_2 & \mathbf{C}_2 & & \\ & \bullet & \bullet & \bullet & \\ & & \mathbf{B}_{n_r-1} & \mathbf{A}_{n_r-1} & \mathbf{C}_{n_r-1} \\ & & & \mathbf{B}_{n_r} & \mathbf{A}_{n_r} \end{bmatrix}$$

$\mathbf{B}_i$ and $\mathbf{C}_i$ are $(n_z \times n_z)$ diagonal matrices, $\mathbf{A}_i$ is $(n_z \times n_z)$ banded matrix with bandwidth 3, and $\mathbf{F}$ is the global vector of the forcing function in (15d) and (15f). For each point j э $(1 \le j \le n_z)$ along an i line in the grid, coefficients of $p_{i,j}$ in the Laplacian define $\mathbf{A}_i$, coefficients of $p_{i-1,j}$ define $\mathbf{B}_i$, and coefficients of $p_{i+1,j}$ define $\mathbf{C}_i$. The time derivative is expressed in central difference to first order allowing integration in time.

Viscous damping is included following the approximate equation (A12)

$$\left(1+\tilde{\nu}/c_b^2\,\partial_t\right)\left(\partial_{rr}+1/r\,\partial_r+\partial_{zz}\right)p\;-\;1/c_b^2\;\partial_{tt}p\;=0 \qquad \text{(A12)}$$

This modifies (16) to the first order system

$$\begin{aligned}\dot{\mathbf{p}}&=\mathbf{q}\\ \dot{\mathbf{q}}&=c_b^2\,\mathbf{M}_p\,\mathbf{p}+\tilde{\nu}\;\mathbf{M}_p\,\mathbf{q}-c_b^2\,\mathbf{F}(t)\end{aligned} \qquad (17)$$

4. Results

The numerical experiments to follow assume a traction-free gelatin disk $12.7\,mm\;(=0.5\;in)$ thick and $25.4\,mm\;(=1\;in)$ radius with the boundary $z=h$ bonded to a rigid surface. In the elastic model the gelatin properties are (Eisler, R. [16]):

$$\begin{aligned}&E=3.1\times10^9\,dyn/cm^2\;\left(=4.5\times10^4\;lb/in^2\right),\\ &\rho=0.93\;g/cm^3\;\left(=8.7\times10^{-5}\;lb\;s^2/in^4\right),\quad \nu=0.48\end{aligned} \qquad \text{(18a)}$$

The data in (13a) yield a small ratio of $Lame'$ constants $\mu/\lambda=(1-2\nu)/(2\nu)\approx0.0417$ resulting in reduced shear stresses and in turn large displacements. In the acoustic model, bulk modulus E_b, density ρ and speed of sound c_b are then

$$\begin{aligned}&E_b=E/\left(3(1-2\nu)\right)=2.73\times10^{10}\,dyn/cm^2\;\left(=3.95\times10^5\,lb/in^2\right)\\ &\rho=0.93\,g/cm^3\;\left(=0.87\times10^{-4}lb\;s^2/in^4\right)\\ &c_b=\sqrt{E_b/\rho}=1.71\;km/s\left(=6.74\times10^4\;in/s\;\right)\end{aligned} \qquad \text{(18b)}$$

E_b is determined from experimental measurements of c_b.

To confirm the implementation of the complicated analytical approach adopting time dependent influence coefficients, results are first compared to those from the more straight forward numerical finite difference approach derived in Appendix B. Fig. 1 compares acoustic pressure histories from the two approaches

for a layer forced by a prescribed trapezoidal pressure pulse of unit intensity lasting $8\mu s$ with $2\mu s$ rise and fall times and $4\mu s$ plateau applied over a circular footprint with radius $r_p = 6.35mm\ (=0.25\ in)$. Fig. 1(a1,a2) plots histories at $z = 0.5h$ and Fig. 1(b1),(b2)) at $z = h$. For each z, histories at 3 radial stations r/r_p = 0, 0.5 and 0.9 are superimposed. Fig. 1(a1,b1) shows that the prescribed pressure pulse quickly changes profile as the wave travels along z. The flat plateau of the profile acquires a discontinuity in intensity after an interval $\Delta t_1 = 3.5\mu s$ from the wave front equal to travel time of the wave over r_p. Over this interval intensity diminishes smoothly with z, while over the remaining interval $\Delta t_2 = 4.5\mu s$ intensity diminishes steeply with z. At $z = h$, intensity over Δt_1 rises from reflections at the rigid boundary. Histories from the two distinctly different approaches agree confirming the implementation of the analytical model.

The difference in response between the acoustic model and the 3-D axisymmetric elastic model is discussed in what follows. Fig. 2(a,b) plots the eigen-frequency $\Omega\,(kHz)$ versus radial wave number $\lambda_m/\pi = k_{rm}r_d/\pi$ with axial wave number n as parameter for the elastic and acoustic models. For each mode (m,n), Ω of the acoustic model is 5 times higher than that of the elastic model. The reason is that in the acoustic model Ω is proportional to c_b while in the elastic model it is proportional to the flexural phase velocity c_p that is bounded by the shear speed $c_s = \sqrt{E/\left(2(1+\nu)\rho\right)}$. For $\nu = 0.48$, $c_b/c_s = 4.97$ consistent with the ratio observed in Fig. 2. This is the fundamental difference distinguishing the two models. Furthermore, the acoustic model cannot capture transverse wave propagation as no shear is included in the model. Although in the elastic model extensional

modes exist with frequencies proportional to c_b nevertheless flexural modes dominate the response because of their lower frequencies.

Fig. 3 plots prescribed motion $\ddot{f}_w(t)$, $\dot{f}_w(t)$ and $f_w(t)$ when acceleration is prescribed at the footprint. $\ddot{f}_w(t)$ is made of 4 linear segments

1. Linear acceleration: $\ddot{f}_{w1}(t) = \alpha_1 t$, $0 \le t \le t_1$

2. Constant acceleration: $\ddot{f}_{w2}(t) = \alpha_1 t_1$, $t_1 \le t \le t_2$

3. Linear deceleration: $\ddot{f}_{w3}(t) = \ddot{f}_{w2}(t_2) - \alpha_2 (t - t_2)$, $t_2 \le t \le t_3$

4. Constant velocity: $\ddot{f}_{w4}(t) = 0$, $\dot{f}_{w4}(t_3) = U_0$, $t_3 \le t \le t_4$

Assuming that the first three time intervals are equal $(\Delta t_1 = \Delta t_2 = \Delta t_3,\ \Delta t_i = t_i - t_{i-1})$ and $\alpha_2 = \alpha_1$, then α_1 is determined by assigning the constant velocity U_o to $\dot{f}_{w4}(t_3)$. In the analysis to follow

$$\Delta t_{1,3} \equiv \Delta t_1 + \Delta t_2 + \Delta t_3 = 2\mu s\ ,\quad U_0 = 14\ m/s\ (\equiv 46\ ft/s\ ) \tag{19}$$

Fig. 4 compares histories of the elastic and acoustic models from prescribed acceleration. Displacement at $z = 0$ (Fig. 4(a1),(a2)) conforms to the prescribed value in Figure 3(c). At $z = 0$, Fig. 4(b1),(b2) compare histories of axial stress $-\sigma_{zz}$ from the elastic model to pressure p from the acoustic model. Peak stress, pulse duration, distribution of p over the footprint, and shape differ substantially between the two models. At $z = h$, Fig. 4(c1),(c2) compare $-\sigma_{zz}$ to p histories. There, magnitude and pulse width also differ. It is evident from this comparison that the two models differ appreciably in spite of the fact that in the elastic model ν=0.48 is close to the transition value 1/2.

The difference between the two models in response from uniform prescribed pressure and prescribed acceleration is demonstrated in the example to follow. A uniform pressure pulse duplicating that at $r = 0$ in Fig. 4(b2) is applied at $z = 0$ (see Fig. 5(b)). The resulting histories of displacement w and pressure p at $z = h$ are shown in Fig. 5(a) and 5(c). Comparing histories in Fig. 4(a2),(c2) to those in Fig. 5(a),(c) reveals the sensitivity of response to p distribution over the footprint. Further evidence of this sensitivity appears when comparing p and w profiles at $z = 0$ of the two cases. For prescribed acceleration p (Fig. 6(a1)) is not uniform while w (Fig. 6(b1)) is almost constant for $r < r_p$ and discontinuous at $r = r_p$. For prescribed pressure, p (Fig. 6(a2)) duplicates the external pulse while w (Fig. 6(b2)) increases with r reaching a maximum at $r = r_p$ with a discontinuity even stronger than that in Fig. 6(b1).

The parameters characterizing the applied acceleration profile are the final constant velocity U_0, and time interval $\Delta t_{1,3}$ of acceleration and deceleration to reach U_0 smoothly from rest. Fig. 7 plots p_{max} against U_0 with $\Delta t_{1,3}$ as parameter and vice versa. As expected, p_{max} is linear with U_0 (Fig. 7(a1),(a2)). In contrast, p_{max} is non-linear with $\Delta t_{1,3}$ (Fig. 7(b1),(b2)) following a relation $p_{max} \propto U_o \, \Delta t_{13}^{-\alpha}$ where the α depends on z. p_{max} approaches a constant value as $\Delta t_{1,3} \to 0$ when slope of the acceleration profile in Fig. 3(a) becomes infinite. This is the limiting case when U_0 is applied instantaneously. For $\Delta t_{1,3} < 3\,\mu s$, p_{max} goes through a transition when its value at $z = h$ exceeds that at $z = 0$. The transition $\Delta t_{1,3}$ is almost independent of U_0.

Figure 8(a) shows deformed shapes at $t = 8\mu s$ from the elastic model for ν=0.470 and 0.495 keeping bulk modulus E_b the same. This requires expressing the constitutive law in terms of E_b and ν as in Eq. (A2b). Note that bulging of material near the perimeter is more pronounced for ν = 0.495 than for ν=0.470. As ν approaches 1/2, material compressibility diminishes followed by a reduction in phase velocity along r near the free surface which delays propagation of the wave front. In turn, conservation of volume and pressure release beyond the perimeter $r > r_p$ explains the formation and intensification of the bulge. Indeed, the closer ν gets to 1/2 the steeper the displacement gradient $\partial_r w$ along the perimeter reminiscent of the acoustic w profile in Fig. 6(b1). The effect on peak elastic stress $(\sigma_{zz})_{max}$ of ν in the range $0.47 \le \nu \le 0.498$ is shown in Fig. 8(b). Although $(\sigma_{zz})_{max}$ at $z = 0$ is insensitive to ν for $\nu < 0.495$, its value at $z = h$ drops by 76% due to a 6% increase in ν. Unfortunately for attempts to use the acoustic model to capture elastic features, this makes the discrepancy between acoustic and elastic results even larger than that in Fig. 4(c1),(c2).

Convergence of the elastic model with number of modes is paramount in the comparison between elastic and acoustic results. This is especially important since in the elastic model shear drops modal frequencies substantially (see Fig. 2). A larger modal set in the elastic model may be needed for its results to agree with the acoustic model that includes volumetric modes only. To verify convergence of the elastic model, histories from the analysis that produced results in Fig. 4(b1) and Fig. 8(b) are compared to those from the finite volume model employed by El-Raheb [15] that couples projectile and disk with 40,000 nodes. Properties and geometry of the projectile are

$$E_p = 1.21\times10^{11} dyn/cm^2 \left(=1.76\times10^6\ lb/in^2\right),$$
$$\rho_p = 1\ g/cm^3 \left(=9.3\times10^{-5}\ lb\ s^2/in^4\right), \quad \nu_p = 0.3$$
$$r_p = 6.35 mm \left(=0.25\ in\right), \quad h_p = 25.4 mm \left(=1\ in\right), \quad U_p = 20\ m/s \left(=65\ ft/s\right)$$
$$c_{bp} = \left(E_p(1-\nu_p)/\left((1+\nu_p)(1-2\nu_p)\rho_p\right)\right)^{1/2} = 4.1\ km/s \left(=1.6\times10^5\ in/s\right)$$

r_p, h_p are projectile radius and length, U_p is striking velocity and c_{bp} is dilatational speed of sound. Properties of gelatin are given in (13a,b). Based on the acoustic impedances $\left(\rho c_b\right)$ of projectile and gelatin, the velocity of gelatin at the footprint following impact is approximately $U_o = 14\ m/s\ \left(=45\ ft/s\right)$. Histories of axial displacement w at the footprint from the two models coincide (Fig. 9(a1),(a2)) since the asymptotic velocity U_o at the footprint is the same for both models. Fig. 9(b1),(b2) compare histories of axial stress σ_{zz} at the footprint from the two models. In the finite volume model, the drop in σ_{zz} $4\,\mu s$ after impact (Fig 9(b2)) corresponds to $t_{pr} = c_{bp}/2r_p$ the arrival time at $r = 0$ of tensile reflections from the projectile's lateral boundary. This is evidenced by the deviation from linearity of the w histories at t_{pr} in Fig 9(a2). In general, magnitude and shape of the σ_{zz} histories agree suggesting convergence of the analytical elastic model.

For prescribed uniform pressure, w histories from elastic and acoustic models agree (Fig. 10(b1,b2)) except at the footprint $z = 0$ (Fig. 10(a1,a2)). In Fig. 11, the lead pulse in the σ_{zz} histories from the two models is followed by a plateau with lower magnitude. The wave reflected from the constrained face at $z = h$ appears as a peak following the plateau. In the elastic model,

i) Rise time is longer

ii) History is modulated by a periodic oscillation

iii) Magnitude of the reflection dip is reduced.

For prescribed uniform pressure, the two models agree better than for prescribed acceleration implying that mismatch between the two models increases with magnitude of shear stress in the elastic model. Indeed, near the perimeter of the footprint shear stress is lower for prescribed uniform pressure than it is for prescribed acceleration because in the later pressure distribution is not uniform (Ref. [15]).

5. Conclusion

Acoustic wave propagation in a weak layer is treated adopting both a modal and a finite difference approach. The acoustic equation derives from the elasto-dynamic equations when shear stress vanishes. Two types of excitations are considered at the boundary, prescribed pressure and prescribed acceleration. In the modal approach, the external excitation is modeled by the static-dynamic superposition method. Noteworthy results are

1. Acoustic histories from the modal and finite difference approaches coincide.
2. For prescribed acceleration, histories from the acoustic and elastic models disagree both in magnitude and shape because the resulting pressure is not uniform. However the two models show agreement for prescribed uniform pressure because shear stress is reduced.
3. Employing the elastic model reveals that remote from the footprint $(\sigma_{zz})_{max}$ drops sharply as ν approaches 1/2 making the discrepancy between acoustic and elastic results even larger.
4. Convergence of the elastic model with number of modes is verified by comparing its histories with those from a finite volume model coupling projectile and disk.

5. For prescribed acceleration at the boundary, rise time in pressure history is proportional to $\Delta t_{1,3}$ while p_{max} is proportional to $U_o \Delta t_{13}^{-\alpha}$.

6. Histories from prescribed pressure and prescribed acceleration differ because of non-uniform pressure distribution over the footprint.

7. For $\Delta t_{1,3} < (\Delta t_{1,3})_T$, p_{max} goes through a transition when its value at the boundary $z = h$ exceeds that at the footprint $z = 0$. $(\Delta t_{1,3})_T$ is a function of E_b and ρ but is almost independent of U_0.

Appendix A. Acoustic equation in the limit of elasto-dynamic equations

Consider the linear axisymmetric elasto-dynamic equations in cylindrical coordinates

$$\begin{aligned} &\partial_r \sigma_{rr} + (\sigma_{rr} - \sigma_{\theta\theta})/r + \partial_z \tau_{rz} = \rho \partial_{tt} u \\ &\partial_z \sigma_{zz} + \partial_r \tau_{rz} + \tau_{rz}/r = \rho \partial_{tt} w \end{aligned} \qquad \text{(A1)}$$

where $(\sigma_{rr}, \sigma_{\theta\theta}, \sigma_{zz,} \tau_{rz})$ are radial, circumferential, axial and shear stresses, and (u, w) are radial and axial displacements. Bulk modulus E_b relates average normal stress σ_V to volumetric strain ε_V

$$\begin{aligned} &\sigma_V = E_b\, \varepsilon_V \equiv \rho\, c_b^2\, \varepsilon_V, \quad E_b = (3\lambda + 2\mu)/3 \equiv E/\big(3(1-2\nu)\big) \\ &\sigma_V = (\sigma_{rr} + \sigma_{\theta\theta} + \sigma_{zz})/3 \\ &\varepsilon_V = \varepsilon_{rr} + \varepsilon_{\theta\theta} + \varepsilon_{zz} \equiv \nabla \cdot \mathbf{u} = \partial_r u + u/r + \partial_z w \end{aligned} \qquad \text{(A2a)}$$

where (λ, μ) are $Lame'$ constants and c_b is bulk speed of sound. In terms of E_b and ν, the constitutive law takes the form

$$\sigma_{ij} = \frac{3\nu}{(1+\nu)} E_b\, \varepsilon_V\, \delta_{ij} + \frac{3(1-2\nu)}{(1+\nu)} E_b\, \varepsilon_{ij} \qquad \text{(A2b)}$$

As $\nu \to 1/2$, $\sigma_{ij} \to \sigma_V = E_b \varepsilon_V$ recovering the bulk relation in (A2a)

$$\nu \to 1/2 \;\; \Rightarrow \;\; \tau_{rz} = 0, \;\; \sigma_{rr} = \sigma_{\theta\theta} = \sigma_{zz} \equiv -p_d \qquad \text{(A3)}$$

where δ_{ij} is Dirac's delta function. Substituting (A3) in (A1) produces the linear Euler equation

$$\rho\, \partial_{tt}\mathbf{u} = -\nabla p_d \qquad \text{(A4)}$$

where $\mathbf{u}$ is displacement vector. For a homogeneous fluid, conservation of mass takes the form

$$\partial_t \rho + \rho\, \partial_t (\nabla \cdot \mathbf{u}) = 0 \qquad \text{(A5)}$$

The equation of state is

$$\frac{d\, p_d}{d\, \rho} = c_b^2 \qquad \text{(A6)}$$

implying that

$$\partial_t p_d = c_b^2\, \partial_t \rho \qquad \text{(A7)}$$

Unlike the elastic solid where deviatoric or shear stresses contribute to material stiffness and reversible strain energy, in a viscous fluid these stresses are dissipative and irreversible. They are related to acoustic velocity by a constitutive law resembling that of an elastic solid

$$\tau_{ij} = \left(\zeta - 2/3\eta\right)\delta_{ij}\, \partial_t\, \varepsilon_{ll} + \eta\, \partial_t\, \varepsilon_{ij} = \left(\zeta - 2/3\eta\right)\delta_{ij}\, \partial_t\, \partial_{x_l} u_l + \eta\, \partial_t \left(\partial_{x_i} u_j + \partial_{x_j} u_i\right) \qquad \text{(A8)}$$

x_i, x_j are independent variables and $\left(\zeta - 2/3\eta\right)$ and η are coefficients of viscosity for dilatational and deviatoric stains (see Landau and Lifshitz [17] page 48). Eq. (A8) resembles the constitutive relation (A2b) where $3\nu/(1+\nu)E_b$ and $3(1-2\nu)/(1+\nu)E_b$ are replaced by $\left(\zeta - 2/3\eta\right)$ and η. The linearized Navier-Stokes equations simplify to

$$\rho\, \partial_{tt}\mathbf{u} = -\nabla p_d + \partial_t \left[\left(\zeta - 1/6\eta\right)\nabla(\nabla \cdot \mathbf{u}) + \left(\eta/2\right)\nabla^2 \mathbf{u}\right] \qquad \text{(A9)}$$

Conservation of mass and the equation of state are given by (A5) and (A6).

Substituting for $\partial_t \rho$ from (A7) into (A5) yields

$$\partial_t \left[p_d + \rho c_b^2 (\nabla \cdot \mathbf{u}) \right] = 0 \qquad \text{(A10)}$$

Equation (A10) is the time derivative of (A2a) with σ_V replaced by $-p$. For a non-viscous fluid, taking the divergence of (A4), then eliminating $\mathbf{u}$ using (A10) determines the acoustic equation

$$\left(\partial_{rr} + 1/r \, \partial_r + \partial_{zz} \right) p_d - 1/c_b^2 \, \partial_{tt} p_d = 0 \qquad \text{(A11)}$$

Equation (A11) is purely hyperbolic non-dispersive.

For a viscous fluid, adopting the procedure that led to (A11) on (A9) and assuming that $\zeta = 1/6\eta$ yields the approximate viscous acoustic equation

$$\left(1 + \tilde{\nu} / c_b^2 \, \partial_t \right) \left(\partial_{rr} + 1/r \, \partial_r + \partial_{zz} \right) p_d - 1/c_b^2 \, \partial_{tt} p_d = 0 \qquad \text{(A12)}$$

where $\tilde{\nu} = \eta / (2\rho)$ (cm^2/s) is kinematic viscosity.

References

[1] Theil, F., 1998. "Young-measure solutions for a viscoelastically damped wave equation with nonmonotone stress-strain relation", Archive for Rational Mechanics and Analysis 144, 47-78.

[2] Yserentant, H., 2001. "The propagation of sound in particle models of compressible fluids", Numerische Mathematik 88, 581-601.

[3] Yserentant, H., 1997. "A particle model of compressible fluids", Numerische Mathematik 76, 111-142.

[4] Sina, K., Khashayar, M., 2002. "Analytical solution of wave equation for arbitrary non-homogeneous media", Proceedings of SPI, The International Society of Optical Engineering 4772 (2002), 25-36.

[5] Sujith, R., Bala Subrahmanyam, P., T. Lieuwen, P., 2003. “Propagation of sound in inhomogeneous media: Exact solutions in curvilinear geometries”, Journal of Vibrations and Acoustics, Transactions of the ASME 125, 133-136.

[6] Hamdi, S., Enright, W., Schiesser, W., Gottlieb, J., 2003. “Exact solutions of the generalized equal width wave equation”, Lecture Notes in Computer Science 266, 725-734.

[7] Yang, D., 1994. “Grid modification for the wave equation with attenuation”, Numerische Mathematik 67, 391-401.

[8] Narayan, J., 1998. “2.5-D Numerical Simulation of Acoustic Wave Propagation”, Pure and Applied Geophysics 151, 47-61.

[9] Schemann, M., Bornemann, F., 1998. “An adaptive Rothe method for the wave equation”, Computing and Visualization in Science 3, 137-144.

[10] Bailly, C., Juve, D., 2000. “Numerical solution of acoustic propagation problems using linearized Euler equations”, American Institute of Aeronautics and Astronautics Journal 38, 22-29.

[11] Wagner, G., Wenzel, M., Dumont, W., 2001. “Numerical treatment of acoustic problems with the hybrid boundary element method”, International Journal of Solids and Structures 38, 10-13, 1871-1888.

[12] Gaul, L., Wenzel, M., 2001. “Acoustic calculations with the hybrid boundary element method in the time domain”, Engineering Analysis with boundary elements 25, 259-265.

[13] Mehdizadeh, O., Paraschivoiu, M., 2003. “Investigation of a Three-Dimensional Spectral Element Method for Helmholtz's Equation”, Lecture Notes in Computer Science 2668, 819–825.

[14] Berry, J., Naghdi, P., 1956. “On the vibration of elastic bodies having time dependent boundary conditions,” Quarterly of Applied Mathematics 14, 43-50.

[15] El-Raheb, M., 2004. “Wave propagation in a weak viscoelastic layer produced by prescribed velocity on the boundary”, Journal of Sound and Vibration, 275(1-2) pp 89-106.

[16] Eisler, R., 2003. Private communication, Mission Research Corporation, Laguna Hills CA.

[17] Landau, L., and Lifshitz, E., 1959. , *Fluid Mechanics*, Pergamon Press, Addison-Wesley Publishing Company, Inc., 1st English Edition.

Acknowlegment:

This work was supported by a grant from DARPA, executed by the U.S. Army Medical Research and Materiel Command/TATRC Contract # W81XWH-04-C-0084.
The views, opinions and/or findings contained in this paper are those of the author and should not be construed as an official Department of the Army position, policy or decision unless so designated by other documentation.

List of Figures

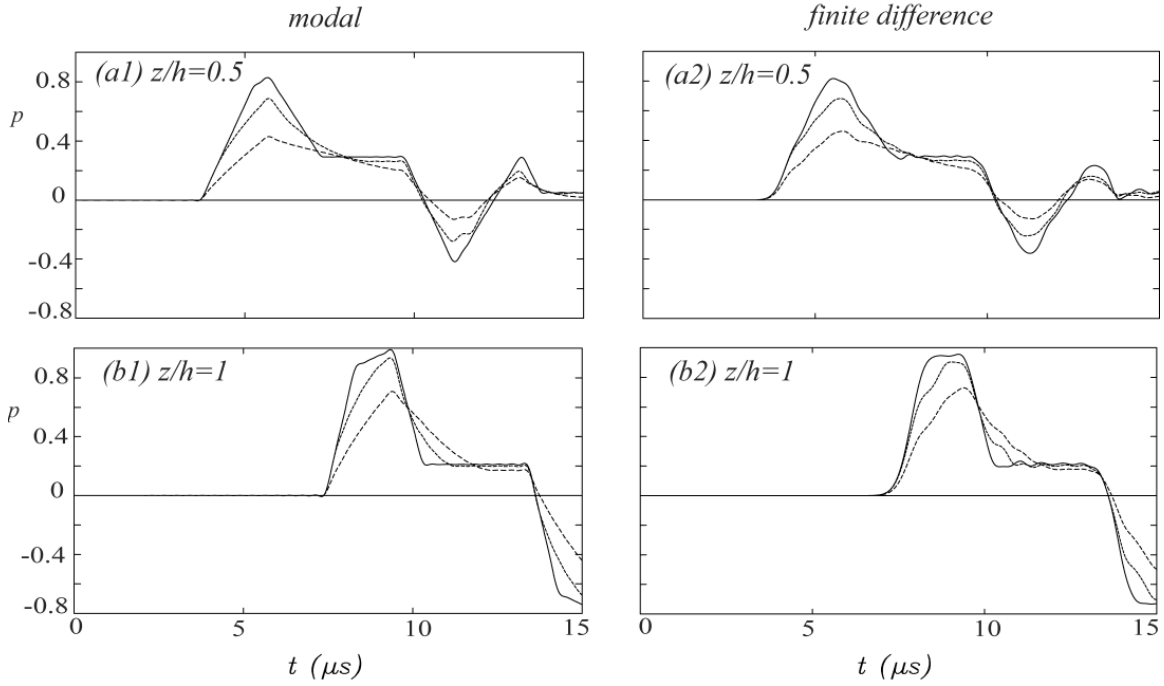

Figure 1. Acoustic histories from prescribed pressure
—— r/r_p=0, ------ 0.5 , - - - - - 0.9
(a1),(b1) modal , (a2),(b2) finite difference

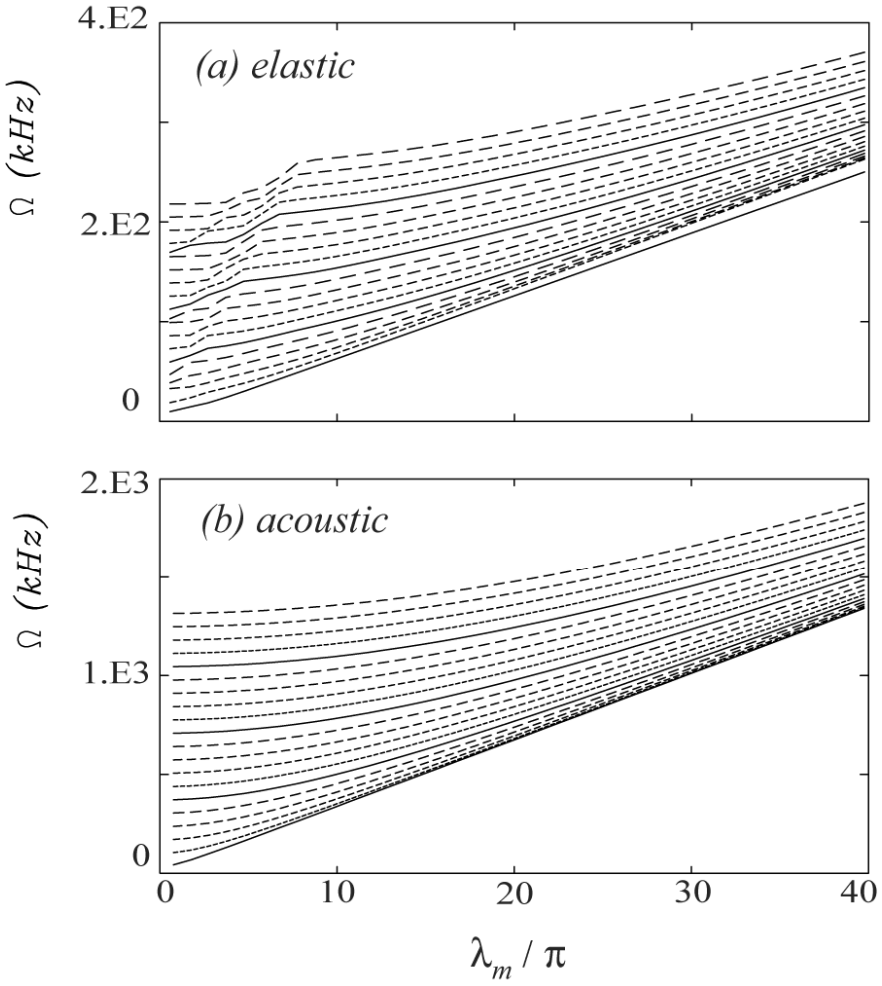

Figure 2. Frequency spectra of elastic and acoustic models (a) elastic model , (b) acoustic model

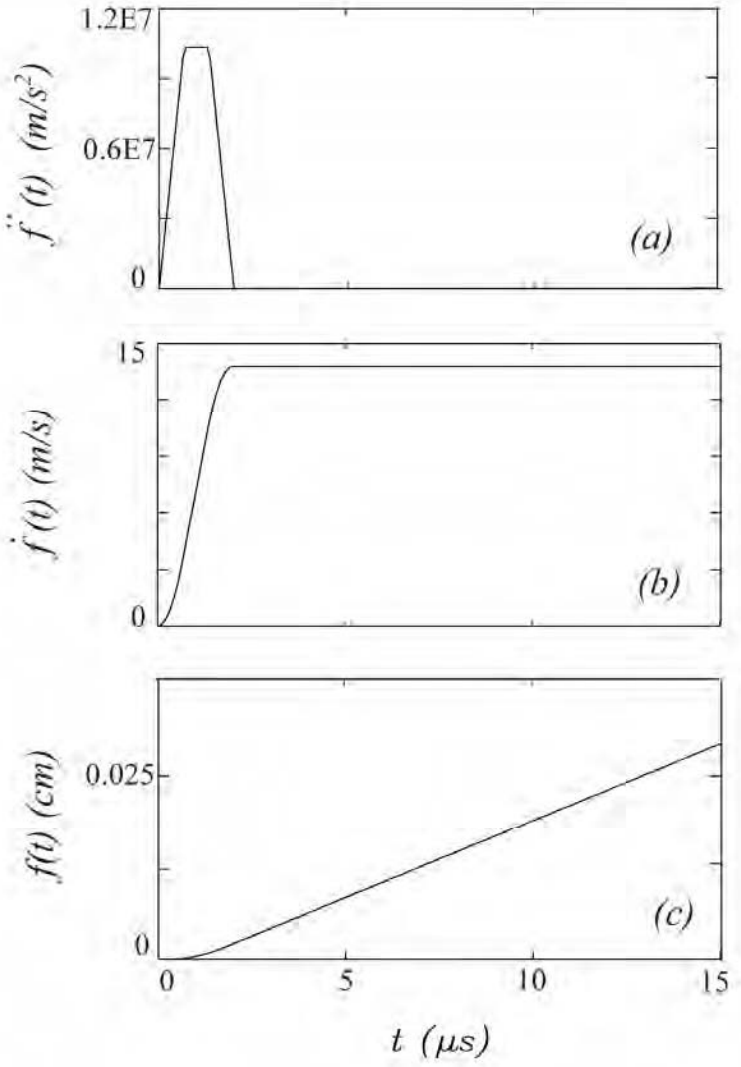

Figure 3. Prescribed motion at footprint
(a) acceleration, (b) velocity, (c) displacement

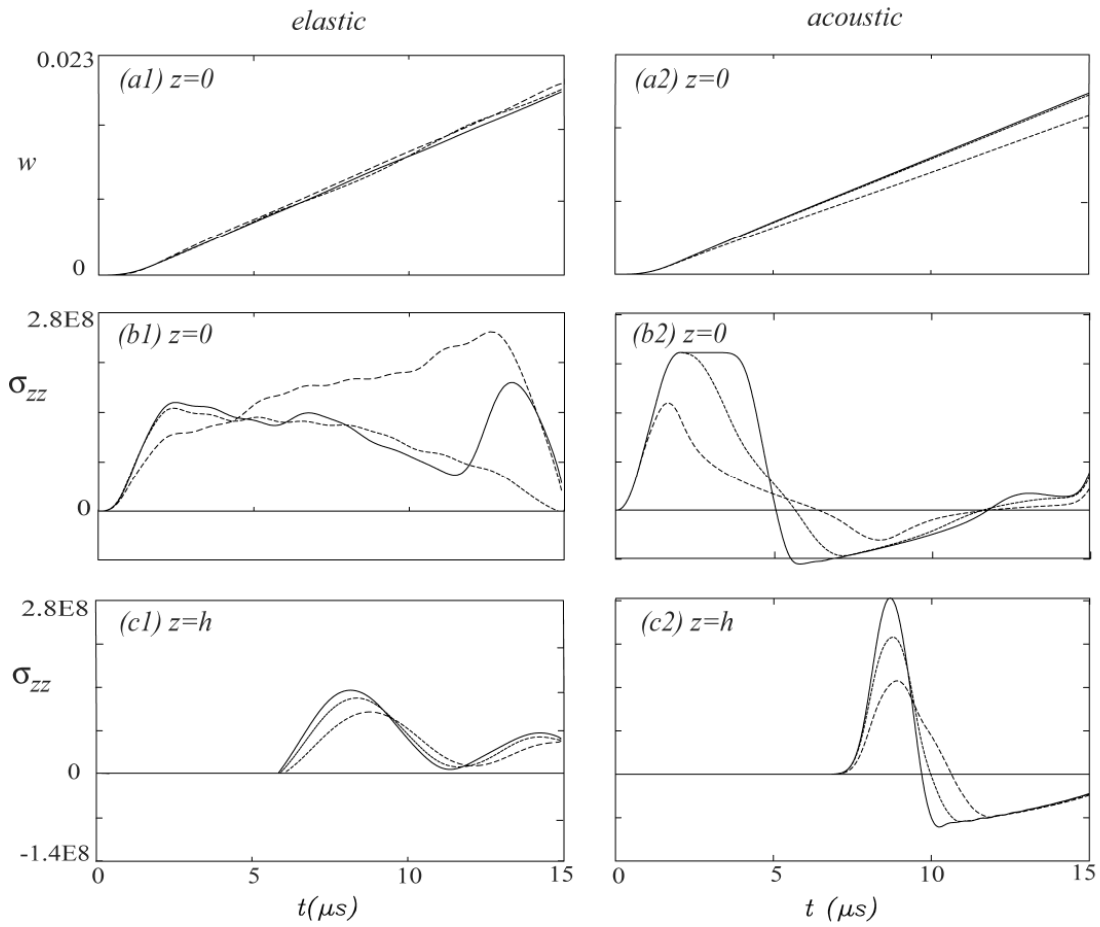

Figure 4. Comparison of elastic and acoustic histories for prescribed acceleration

—— r/r_p=0, ------ 0.5 , - - - - - 0.9

elastic model: (a1) w(r, 0) , (b1) σ_{zz}(r, 0) , (c1) σ_{zz}(r, h)

acoustic model: (a2) w(r, 0) , (b2) σ_{zz}(r, 0) , (c2) σ_{zz}(r, h)

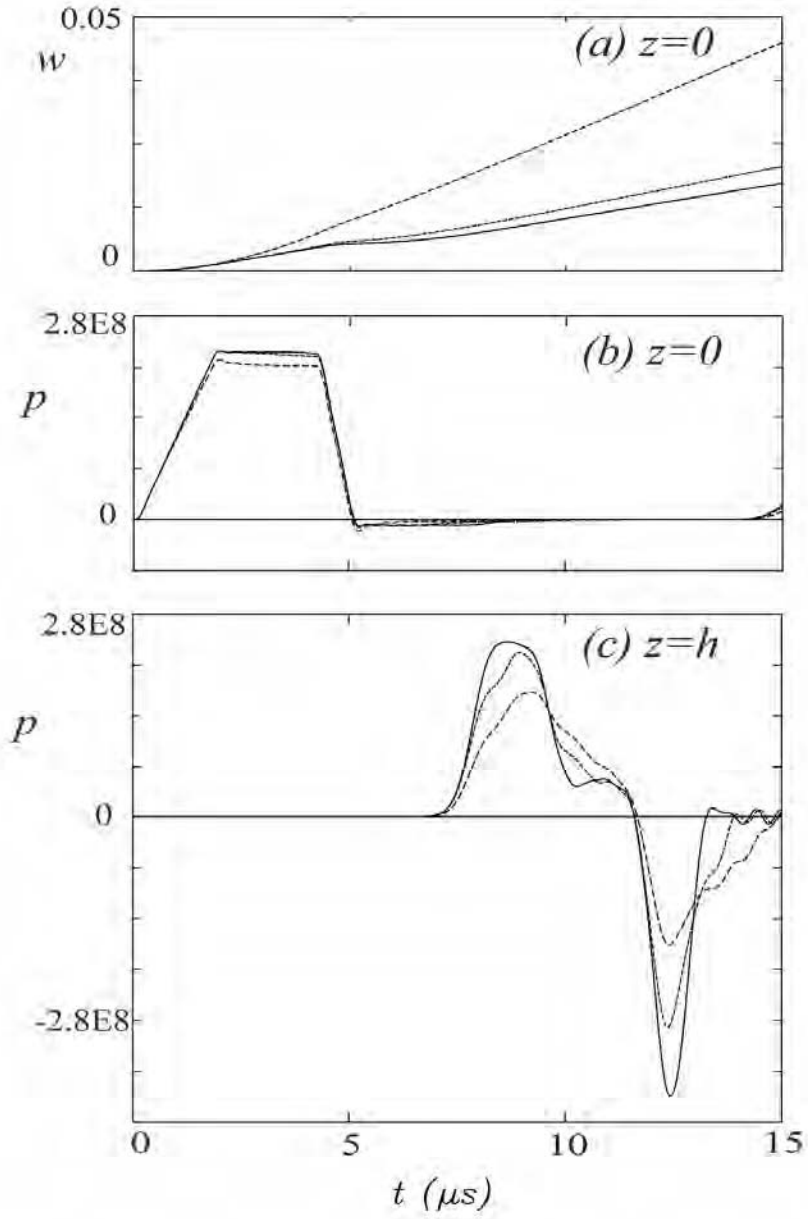

Figure 5. Acoustic histories from prescribed pressure

—— r/r_p =0, ------ 0.5 , - - - - - 0.9

(a) w(r, 0; t) , (b) p(r, 0; t) , (c) p(r, h; t)

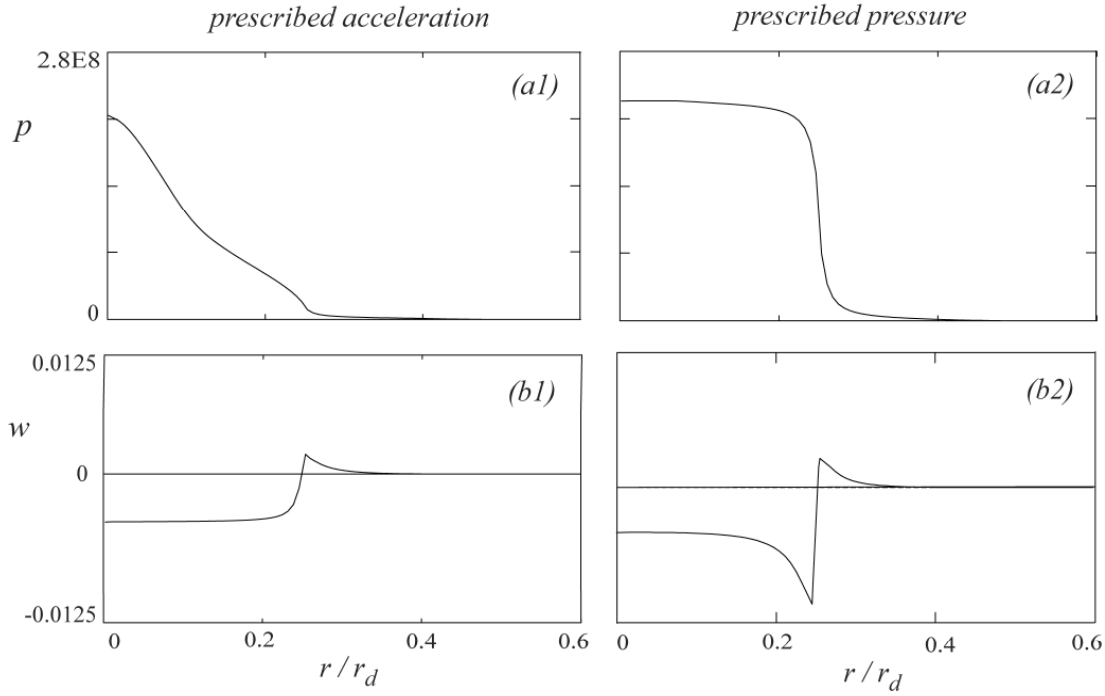

Figure 6. Acoustic pressure and displacement profiles at z=0 and t = 4 μs
(a1),(b1) prescribed acceleration, (a2),(b2) prescribed pressure

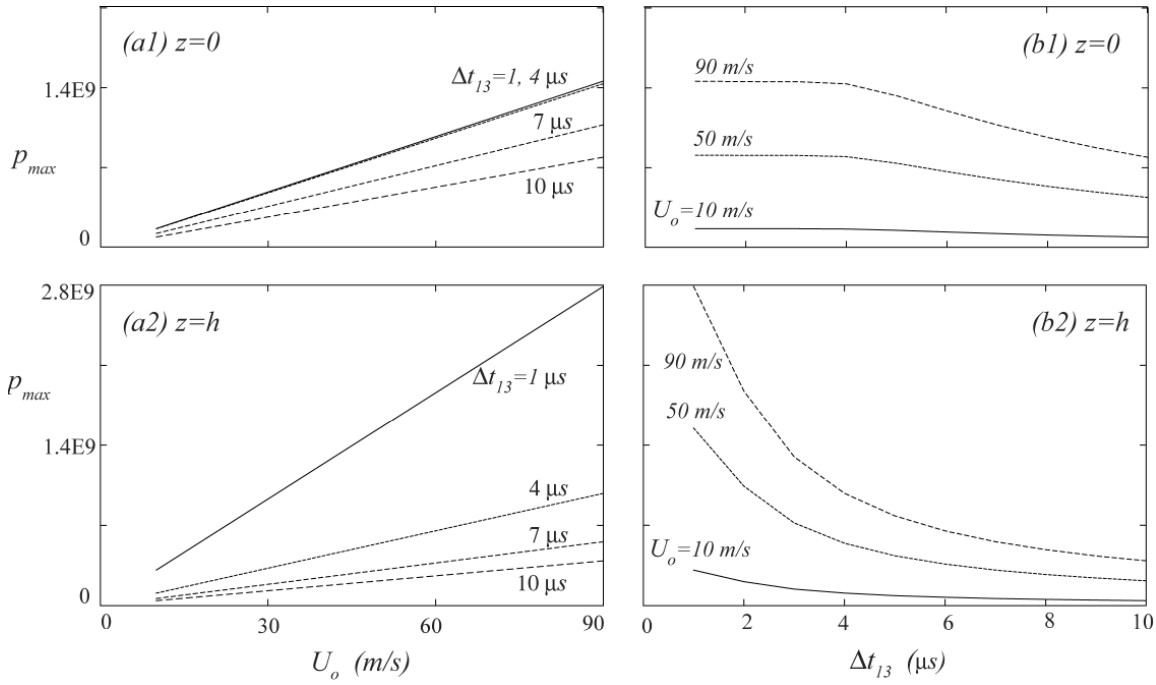

Figure 7. Variation of p_{max} with acceleration parameters U_o and Δt_{13} (a1),(b1) z=0, (a2),(b2) z=h

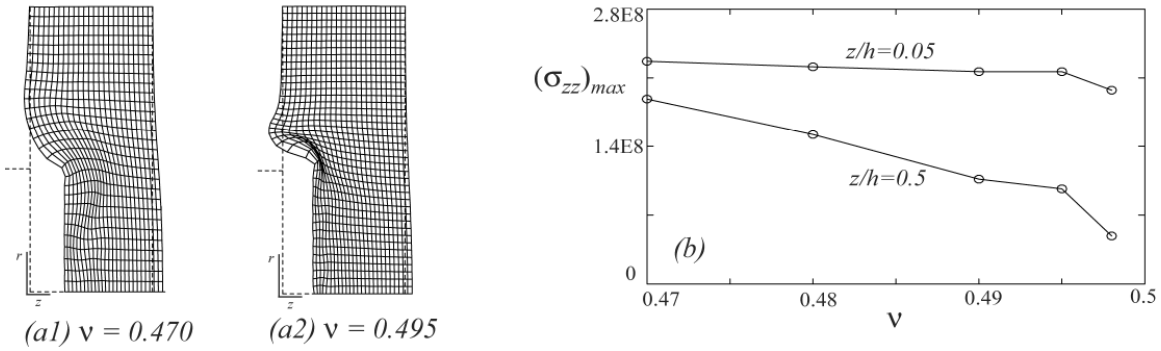

(a1) $\nu = 0.470$ *(a2)* $\nu = 0.495$

Figure 8. Effect of Poisson ratio ν *on :*
(a) deformation snap-shots at $t = 8\ \mu s$ *:*
(a1) $\nu=0.470$ *, (a2)* $\nu=0.495$
(b) variation of peak stress with ν

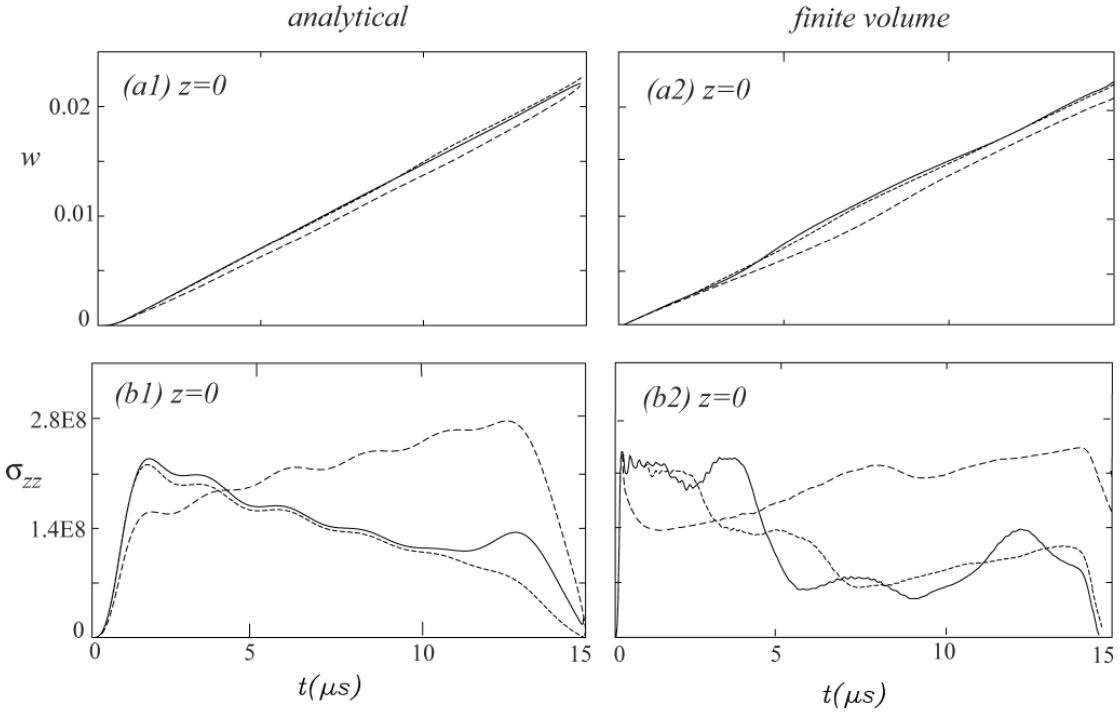

Figure 9. Comparison of analytical and finite volume elastic models

—— r/r_p =0.02 , ----- 0.5 , - - - - 0.96

(a1),(b1) w, σ_{zz} analytical , (a2),(b2) w, σ_{zz} finite volume

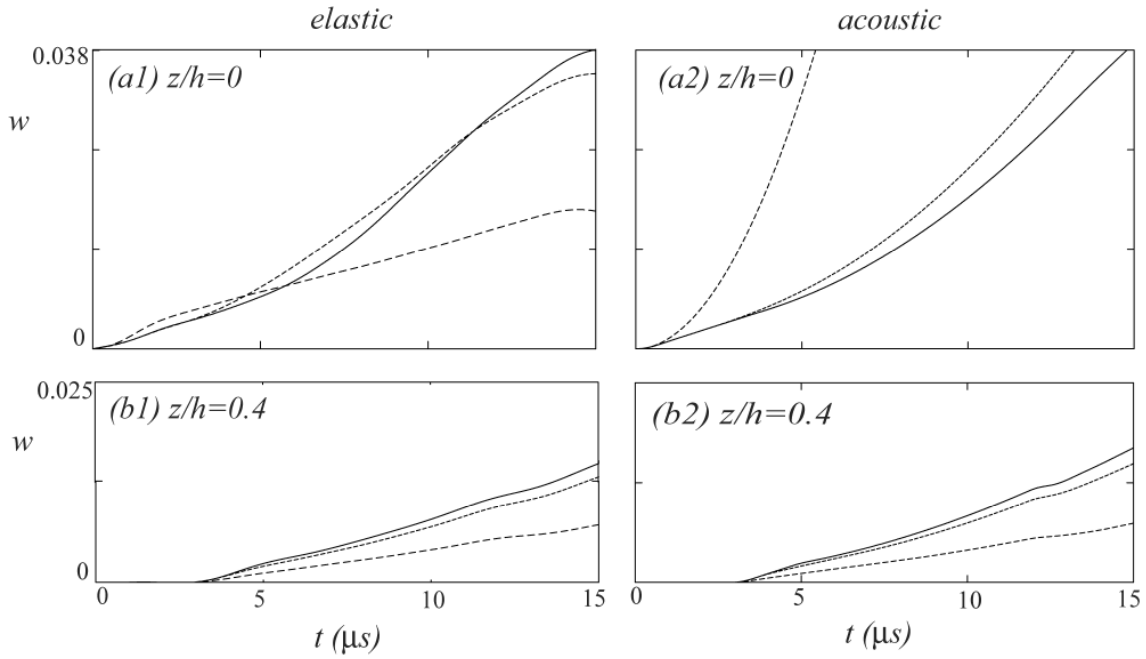

Figure 10. Comparison of w histories from elastic and acoustic models with prescribed pressure; ___ r/r_p =0, ----- 0.5 , - - - - 0.9

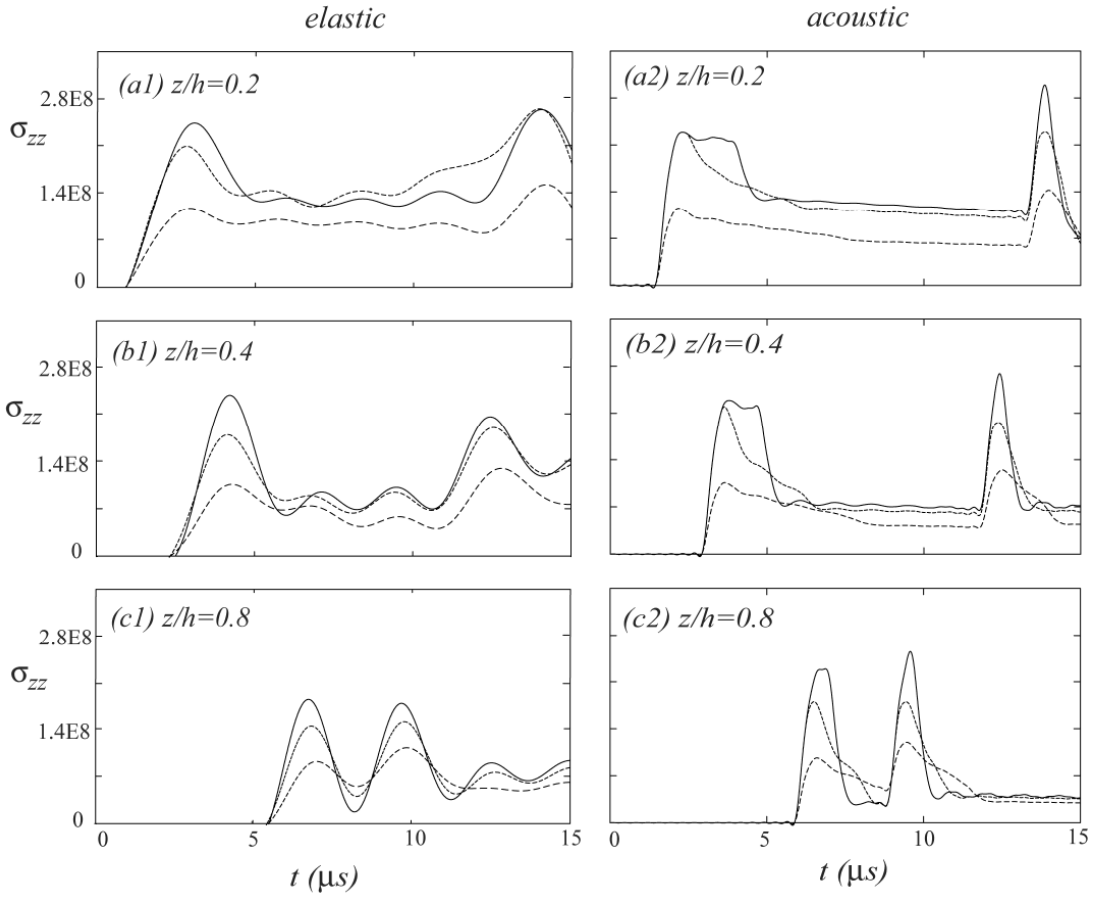

Figure 11. Comparison of σ_{zz} histories from elastic and acoustic models with prescribed pressure; ____ r/r_p =0, ----- 0.5 , - - - - 0.9

APPENDIX K

Accepted for Publication in the *International Journal of Solids and Structures*

"Wave propagation in a hollow cylinder

due to prescribed velocity at the boundary"

Michael El-Raheb

ATK Mission Research, Laguna Hills CA

Summary

Analyzed is transient response of a hollow cylinder to time dependent radial and axial velocities prescribed at the cylinder's inner boundary. Modal and static solutions are superimposed for solving transient response. Axial dependence is expressed by two orthogonal sets of periodic functions; one set satisfies vanishing axial stress at the cylinder ends and applies to the radial traction problem, and the other set satisfies vanishing shear stress at the ends and applies to the axial traction problem. The mixed boundary value problem with velocity prescribed over part of the boundary and vanishing stress prescribed over the remaining part is analyzed by the method of influence coefficients. This method superimposes response from several external annular traction segments of unit intensity with time dependent weights yielding a combined response equal to the prescribed instantaneous velocity.

1. Introduction

Trauma in human organs from projectile penetration is caused by two mechanisms:

i) Tissue damage along projectile path. This interaction is hydrodynamic in nature where inertial and frictional forces dominate the projectile's motion as it decelerates and eventually stops.

ii) Stress waves generated at the cylindrical interface between projectile and tissue from radial and axial velocities prescribed by the projectiles during penetration. These waves radiate to neighboring tissue and organs causing further damage.

The present analysis concerns mechanism ii) above.

As the projectile penetrates into tissue, it moves material by replacing it with its own volume. When the material fails, it acts more like a fluid, lessening the amount of material being compressed. In the radial direction, material is compressed by an expanding cross-section of the projectile's smoothly curved nose. As long as the projectile's speed is much smaller than the speed of stress waves in the material, the moving projectile can be approximated by radial and axial velocities prescribed along its boundary. For a projectile speed of 330 ft/s and a dilatational speed in tissue material of 5600 ft/s, this approximation is valid.

Dynamic response of solid and hollow elastic cylinders has been studied extensively in the literature as it applies to a variety of engineering and science problems. A large body of references concerns sound scattering by elastic cylinders in the frequency domain. Among these are Stanton (1988), Honarvar and Sinclair (1996), Bao et al. (1997), Wang and Ying (2001). Stepanishen and Janus (1990) treat transient radiation and scattering from fluid loaded cylinders. Frequency response of cylinders is analyzed by Grishenko and Meleshko (1978), Batard et al. (1992), and Grinchenko (1999). Soldatos and Ye (1994) treat anisotropic laminated cylinders, and Hussein and Heyliger (1998) consider layered

piezoelectric cylinders. Cheung et al. (2003) analyze the 3-D vibration of solid and hollow cylinders by the Chebyshev-Ritz method. Very few references discuss transient response of elastic cylinders. Paul and Murali (1995) determine the axisymmetric dynamic response of poro-elastic cylinders. Soldatos (1994) presents a compilation of more than 150 references on frequency response of solid and annular elastic cylinders, yet not a single one addresses transient response. Yin and Yue (2002) solve the transient plane-strain response from impulse of infinite length multi-layered cylinders. From the list above, this is the only reference relevant to a special case of the present analysis.

The influenced region is simulated by tissue material in the shape of a hollow cylinder. Let (r,z) be radial and axial coordinates with origin at one end of the cylinder axis. The inner cylinder radius r_p is that of the penetrating projectile while its outer radius r_o and length l are chosen to include the furthest radial and axial locations affected by penetration. In a coordinate system (r,z) centered at one end of the finite cylinder, the projectile lies in the interval $z_a \le z \le z_b$ such that $z_b - z_a = l_p$ where l_p is projectile length. The tissue material is linear visco-elastic with a constitutive law that includes first temporal derivatives of stress and strain.

For simplicity and without loss of generality, axial functions satisfying the differential equations and specific boundary conditions at the two ends of the cylinder $z=(0,l)$ are divided into 2 sets. One set satisfying vanishing axial stress σ_{zz} at $z=(0,l)$ which has radial and axial displacements (u,w) proportional to $\left(\sin(m\pi z/l), \cos(m\pi z/l)\right)$ belongs to "problem 1", where m is an integer wave number. The other set satisfying vanishing shear stress τ_{rz} at $z=(0,l)$ which has (u,w) proportional to $\left(\cos(m\pi z/l), \sin(m\pi z/l)\right)$ belongs to "problem 2". The first set

applies to radial tractions prescribed at the cylindrical footprint $r = r_o$, $z_a \le z \le z_b$ while the second set applies to prescribed axial tractions along the same footprint. The fact that each set satisfies different boundary conditions does not affect transient response until waves reflect from the axial boundaries. Consequently, one problem is solved for each type of forcing excitation and results are superimposed if both types of excitation are acting simultaneously.

The form of the forcing function closest to the application is radial and axial velocity prescribed over part of the inner cylindrical boundary, yet this leads to a mixed boundary condition. This difficulty can be overcome by superimposing response from a set of unit radial or axial tractions with time dependent weights prescribed on annular portions of the inner boundary. These weights are updated at each time step using the condition that combined velocity response at the center of each annular portion equals the prescribed instantaneous velocity. In this way, the forcing function is converted to pure radial or axial traction with time varying spatial dependence.

Section 2 derives frequency and transient response of the hollow cylinder with finite length. Section 3 presents stress histories from prescribed radial and axial pressures and velocities at the inner boundary.

2a. Elastic analysis

In the analysis to follow, all subscript will denote components and not partial derivatives. In cylindrical coordinates, the elastodynamic equations are

$$\mu\nabla^2\mathbf{u} + (\lambda+\mu)\nabla(\nabla\bullet\mathbf{u}) = \rho\,\partial_{tt}\mathbf{u} \qquad (1)$$

$$\nabla^2 \equiv \partial_{rr} + 1/r\;\partial_r + 1/r^2\,\partial_{\theta\theta} + \partial_{zz}$$
$$\nabla \equiv \left(1/r\;\partial_r\, r\right)\mathbf{e}_r + (1/r\,\partial_\theta)\mathbf{e}_\theta + (\partial_z)\mathbf{e}_z$$

(r,θ,z) are radial, circumferential and axial independent variables, $\mathbf{u} = \{u,\upsilon,w\}^T$ is displacement vector along these directions, (λ,μ) are Lame constants, ρ is mass density and t is time. Re-write (1) as

$$\mu\nabla^2\mathbf{u} + (\lambda+2\mu)\nabla(\nabla\bullet\mathbf{u}) - \mu\nabla(\nabla\bullet\mathbf{u}) = \rho\,\partial_{tt}\mathbf{u} \qquad (2a)$$

Noting that

$$\mu\nabla^2\mathbf{u} - \mu\nabla(\nabla\bullet\mathbf{u}) = -\mu\,\nabla\times\nabla\times\mathbf{u} \qquad (2b)$$

permits casting (1) in the form

$$(\lambda+2\mu)\nabla(\nabla\bullet\mathbf{u}) - \mu\,\nabla\times\nabla\times\mathbf{u} = \rho\,\partial_{tt}\mathbf{u} \qquad (3)$$

Define dilatation Δ and rotation vector $\boldsymbol{\psi}$ as

$$\Delta = \nabla\bullet\mathbf{u}\,, \quad \boldsymbol{\psi} = \nabla\times\mathbf{u} \qquad (4)$$

Substituting (4) in (3) yields (Love (1944))

$$(\lambda+2\mu)\nabla\Delta - \mu\,\nabla\times\boldsymbol{\psi} = \rho\,\partial_{tt}\mathbf{u} \qquad (5)$$

Taking the divergence of (5) noting that $\nabla\cdot(\nabla\times\boldsymbol{\psi}) = 0$ yields

$$(\lambda+2\mu)\nabla^2\Delta = \rho\,\Delta_{tt} \qquad (6)$$

Taking the rotation of (5) noting that $\nabla\times(\nabla\Delta) = \mathbf{0}$ yields

$$\mu\nabla^2\boldsymbol{\psi} = \rho\,\boldsymbol{\psi}_{tt} \qquad (7)$$

For axisymmetric motions, $\upsilon \equiv \partial_\theta \equiv 0$ and $\psi_r \equiv \psi_z \equiv 0$ reducing (6) and (7) to

$$\begin{aligned} &(\lambda+2\mu)\nabla_0^2\,\Delta = \rho\,\Delta_{tt} \\ &\mu\,\nabla_1^2\,\psi_\theta = \rho\,\psi_{\theta,tt} \\ &\nabla_n^2 \equiv \partial_{rr} + 1/r\,\partial_r - n^2/r^2 + \partial_{zz}\,, \quad n = 0,1 \end{aligned} \qquad (8)$$

Expressing (4) in terms of $\mathbf{u}$ yields

$$\begin{aligned} &\Delta = 1/r\,\partial_r\,(r\,u) + \partial_z\,w \\ &\psi_\theta = \partial_z\,u - \partial_r\,w \end{aligned} \qquad (9)$$

Decoupling u and w in (9) produces

$$\begin{aligned}\nabla_1^2 u &= \partial_r \Delta + \partial_z \psi_\theta \\ \nabla_0^2 w &= \partial_z \Delta - 1/r \partial_r (r \psi_\theta)\end{aligned} \tag{10}$$

For the radial "problem 1" satisfying $\sigma_{zz} = 0$ at $z = (0, l)$, harmonic motions in time with radian frequency ω and simply supported boundaries at $z = (0, l)$ yields the separated solution

$$\begin{aligned}\left\{\Delta(r,z,t), \psi_\theta(r,z,t)\right\}^T &= \left\{\bar{\Delta}(r)\cos(k_z z), \bar{\psi}_\theta(r)\sin(k_z z)\right\}^T e^{i\omega t} \\ \left\{u(r,z,t), w(r,z,t)\right\}^T &= \left\{\bar{u}(r)\sin(k_z z), \bar{w}(r)\cos(k_z z)\right\}^T e^{i\omega t}\end{aligned} \tag{11}$$

$i = \sqrt{-1}$ and $k_z = m\pi / l$ where m is an integer axial wave number. The z dependence in (11) yields $u = \sigma_{zz} = 0$ at the cylinder ends $z = 0, l$. For real k_e and k_s, equation (8) admits the solution

$$\begin{aligned}\bar{\Delta}(r) &= C_1 J_0(k_e r) + C_2 Y_0(k_e r) \\ \bar{\psi}_\theta(r) &= C_3 J_1(k_s r) + C_4 Y_1(k_s r)\end{aligned} \tag{12}$$

$$\begin{aligned}k_e^2 &= \omega^2 / c_d^2 - k_z^2 \quad , \quad c_d^2 = (\lambda + 2\mu)/\rho \\ k_s^2 &= \omega^2 / c_s^2 - k_z^2 \quad , \quad c_s^2 = \mu / \rho\end{aligned}$$

J_n and Y_n are Bessel functions and c_d, c_s are dilatational and shear speeds of sound. If either k_e or k_s is imaginary, J_n and Y_n in (12) are replaced by the modified Bessel functions I_n and K_n with appropriate changes in sign.

Substituting (11) and (12) in (10) then solving for $\bar{u}(r)$ and $\bar{w}(r)$ yields

$$\begin{aligned}\bar{u}(r) &= -k_e \left(C_1 J_1(k_e r) + C_2 Y_1(k_e r)\right) + k_z \left(C_3 J_1(k_s r) + C_4 Y_1(k_s r)\right) \\ \bar{w}(r) &= k_z \left(C_1 J_0(k_e r) + C_2 Y_0(k_e r)\right) + k_s \left(C_3 J_0(k_s r) + C_4 Y_0(k_s r)\right)\end{aligned} \tag{13}$$

In cylindrical coordinates, the constitutive relations are

$$\sigma_{rr} = \lambda\Delta + 2\mu\,\partial_r u \ , \ \sigma_{\theta\theta} = \lambda\Delta + 2\mu\, u/r$$
$$\sigma_{zz} = \lambda\Delta + 2\mu\,\partial_z w, \ \ \tau_{rz} = \mu\left(\partial_z u + \partial_r w\right) \qquad (14)$$
$$\Delta = \partial_r u + u/r + \partial_z w$$

For "problem 1", harmonic motions in time and simply supported boundaries at $(0,l)$ yield the separated relations

$$\begin{Bmatrix} \sigma_{rr} \\ \sigma_{\theta\theta} \\ \sigma_{zz} \\ \tau_{rz} \end{Bmatrix}(r,z,t) = \begin{Bmatrix} \bar{\sigma}_{rr}(r)\sin(k_z z) \\ \bar{\sigma}_{\theta\theta}(r)\sin(k_z z) \\ \bar{\sigma}_{zz}(r)\sin(k_z z) \\ \bar{\tau}_{rz}(r)\cos(k_z z) \end{Bmatrix} e^{i\omega t} \qquad (15a)$$

Boundary conditions at $r = r_p$ and $r = r_o$ are

$$\sigma_{rr}(r_p,z,t) = p_r(t)\left[H(z-z_a) - H(z-z_b)\right]$$
$$\tau_{rz}(r_p,z,t) = 0 \qquad (15b)$$
$$\sigma_{rr}(r_o,z,t) \equiv \tau_{rz}(r_o,z,t) = 0$$

$p_r(t)$ is a time dependent uniform radial traction acting on the inner cylindrical boundary $r = r_p$ in the interval $z_a \le z \le z_b$. The z dependence in (15a) yields $u = \sigma_{zz} = 0$ at the cylinder ends $z = 0, l$. Substituting (11), (13) and (15a) in (14) yields

$$\begin{aligned} \bar{\sigma}_{rr}(r) = & \left[-\left((\lambda+2\mu)k_e^2 + \lambda k_z^2\right)J_0(k_e r) + 2\mu\, k_e^2\, J_1(k_e r)\,/(k_e r)\right]C_1 \\ & + \left[-\left((\lambda+2\mu)k_e^2 + \lambda k_z^2\right)Y_0(k_e r) + 2\mu\, k_e^2\, Y_1(k_e r)\,/(k_e r)\right]C_2 \\ & + 2\mu k_s k_z\left[J_0(k_s r) - J_1(k_s r)\,/(k_s r)\right]C_3 \\ & + 2\mu k_s k_z\left[Y_0(k_s r) - Y_1(k_s r)\,/(k_s r)\right]C_4 \end{aligned} \qquad (16a)$$

$$\begin{aligned} \bar{\sigma}_{\theta\theta}(r) = & -\left[\lambda(k_z^2 + k_e^2)J_0(k_e r) + 2\mu\, k_e^2 J_1(k_e r)\,/(k_e r)\right]C_1 \\ & -\left[\lambda(k_z^2 + k_e^2)Y_0(k_e r) + 2\mu\, k_e^2 Y_1(k_e r)\,/(k_e r)\right]C_2 \\ & + 2\mu k_s k_z\left[C_3 J_1(k_s r) + C_4 Y_1(k_s r)\right]/(k_s r) \end{aligned} \qquad (16b)$$

$$\bar{\sigma}_{zz}(r) = -\left((\lambda+2\mu)k_z^2+\lambda k_e^2\right)\left[C_1 J_0(k_e r)+C_2 Y_0(k_e r)\right] - 2\mu\, k_s k_z\left[C_3 J_0(k_s r)+C_4 Y_0(k_s r)\right] \tag{16c}$$

$$\bar{\tau}_{rz}(r) = -2\mu k_e k_z\left[C_1 J_1(k_e r)+C_2 Y_1(k_e r)\right] - \mu(k_s^2-k_z^2)\left[C_3 J_1(k_s r)+C_4 Y_1(k_s r)\right] \tag{16d}$$

Since σ_{zz} is proportional to $\sin(k_z z)$ in (15), it vanishes at $z = 0, l$. This allows a rigid body motion $w(r,z;t) = w_o(t)$ when external traction acts along z. To avoid the rigid body motion, an additional axial functional dependence is considered for "problem 2"

$$\begin{Bmatrix} u \\ w \end{Bmatrix}(r,z,t) = \begin{Bmatrix} \bar{u}(r)\cos(k_z z) \\ \bar{w}(r)\sin(k_z z) \end{Bmatrix} e^{i\omega t}$$
$$\begin{Bmatrix} \sigma_{rr} \\ \sigma_{\theta\theta} \\ \sigma_{zz} \\ \tau_{rz} \end{Bmatrix}(r,z,t) = \begin{Bmatrix} \bar{\sigma}_{rr}(r)\cos(k_z z) \\ \bar{\sigma}_{\theta\theta}(r)\cos(k_z z) \\ \bar{\sigma}_{zz}(r)\cos(k_z z) \\ \bar{\tau}_{rz}(r)\sin(k_z z) \end{Bmatrix} e^{i\omega t} \tag{17a}$$

that satisfies the following boundary conditions at $r = r_p$ and $r = r_o$

$$\sigma_{rr}(r_p,z,t) = 0$$
$$\tau_{rz}(r_p,z,t) = p_z(t)\left[H(z-z_a)-H(z-z_b)\right] \tag{17b}$$
$$\sigma_{rr}(r_o,z,t) \equiv \tau_{rz}(r_o,z,t) = 0$$

$p_z(t)$ is a time dependent uniform axial traction acting on the inner cylindrical boundary $r = r_p$ in the interval $z_a \le z \le z_b$. The z dependence in (18a) yields $w = \tau_{rz} = 0$ at the cylinder ends $z = 0, l$. In the analysis to follow, superscripts (1) and (2) will denote radial and axial problems respectively. Derivations for problem (2) follow the same steps as those for problem (1) and are omitted here for shortness. Although conditions at the boundaries $z = 0, l$ of each problems are

different, they do not affect the transient response at times preceding reflection of waves from these boundaries.

Divide the cylindrical surface $\left\{r = r_p,\ z_a \le z \le z_b\right\}$ into $n+1$ equidistant ring stations with increment Δz_p

$$z_1,\ z_2,\ z_3, \ldots\ldots, z_n \ , \qquad z_l - z_{l-1} = \Delta z_p = const$$
$$z_l = z_a + (l-1)\,\Delta z_p \tag{18}$$

Assume a uniform pressure of unit intensity to act over each ring segment $z_{l-1} \to z_l$. The elasto-dynamic solution to the k^{th} ring pressure segment is outlined below.

For each pressure segment, expand each dependent variable in terms of eigenfunctions that satisfy homogeneous boundary conditions. Express total displacement $\mathbf{u}_k(r,z;t)$ as a superposition of two terms

$$\mathbf{u}_k^{(1,2)}(r,z;t) = \mathbf{u}_{sk}^{(1,2)}(r,z)\ f_p(t)\ +\ \mathbf{u}_{dk}^{(1,2)}(r,z;t) \tag{19}$$

$\mathbf{u}_{sk}^{(1,2)}(r,z)$ is static displacement vector satisfying (2a) when time derivative vanishes (Appendix A), $\mathbf{u}_{dk}^{(1,2)}(r,z;t)$ is dynamic displacement vector satisfying the dynamic equation of motion (2a), and $f_p(t)$ is time dependence of the forcing pressure. For each axial wave number m, express $\mathbf{u}_{dk}^{(1,2)}(r,z,t)$ in the eigenfunctions $\mathbf{\Phi}_{mj}^{(1,2)}(r,z)$ (Appendix B)

$$\mathbf{u}_{dk}^{(1,2)}(r,z,t) = \sum_j \sum_m a_{mjk}^{(1,2)}(t)\ \mathbf{\Phi}_{mj}^{(1,2)}(r,z) \tag{20}$$

$a_{mjk}^{(1,2)}(t)$ is a generalized coordinate of the j^{th} eigenfunction with m axial half waves from the k^{th} pressure segment. Substituting (19) and (20) in (2a) and enforcing orthogonality of $\mathbf{\Phi}_{mj}^{(1,2)}(r,z)$ yields uncoupled equations in $a_{mjk}^{(1,2)}(t)$. For an undamped elastic cylinder the equation governing $a_{mjk}^{(1,2)}(t)$ is

$$\left(\frac{d^2}{dt^2}+\omega_{mj}^2\right)a_{mjk}^{(1,2)}(t)=\bar{f}_{mjk}^{(1,2)}(t) \qquad (21a)$$

$$\bar{f}_{mjk}^{(1,2)}(t)=N_{amjk}^{(1,2)}\,\ddot{f}_p(t)/N_{mj}$$

$$N_{mj}^{(1,2)}=\int_0^{r_d}\int_0^{h}\boldsymbol{\Phi}_{mj}^{(1,2)}(r,z)\cdot\boldsymbol{\Phi}_{mj}^{(1,2)}(r,z)\,dz\,r\,dr \qquad (21b)$$

$$N_{amjk}^{(1,2)}=\int_0^{r_d}\int_0^{h}\mathbf{u}_{sk}^{(1,2)}(r,z)\cdot\boldsymbol{\Phi}_{mj}^{(1,2)}(r,z)\,dz\,r\,dr$$

ω_{mj} is the resonant frequency. The solution to (21a) takes the form

$$a_{mjk}^{(1,2)}(t)=-\frac{1}{\omega_{mj}}\int_0^{t}\sin\omega_{mj}(t-\tau)\,\bar{f}_{mjk}^{(1,2)}(\tau)\,d\tau \qquad (22)$$

Evaluating radial and axial displacements $u_k(r,z;t)$ for problem (1) and $w_k(r,z;t)$ for problem (2) from the k^{th} pressure segment at each central point $z_{cl}=(z_l+z_{l-1})/2$ of a pressure segment yields coefficients of the influence matrices

$$\begin{aligned}U_{lk}(t)&=\sum_j\sum_m a_{mjk}^{(1)}(t)\,\bar{u}_{mjk}^{(1)}(r_p,z_{cl})\;+\;u_{sk}^{(1)}(r_p,z_{cl})\;f_p(t)\\ W_{lk}(t)&=\sum_j\sum_m a_{mjk}^{(2)}(t)\,\bar{w}_{mjk}^{(2)}(r_p,z_{cl})\;+\;w_{sk}^{(2)}(r_p,z_{cl})\;f_p(t)\end{aligned} \qquad (23)$$

$\left\{\bar{u}_{mjk}^{(1)}(r_p,z_{cl})\,,\;\bar{w}_{mjk}^{(2)}(r_p,z_{cl})\right\}$ and $\left\{u_{sk}^{(1)}(r_p,z_{cl}),w_{sk}^{(2)}(r_p,z_{cl})\right\}$ are modal and static displacement dyads at z_{cl} from the k^{th} pressure segment in problems (1) and (2) respectively. In (21) and (23) $f_p(t)$ is a first approximation to the time dependence of the applied pressure. One approximation is determined from the plane-strain state when axial length of cylinder and footprint approaches infinity (Appendix C). Enforcing the condition of prescribed displacements $u_p^{(1)}(t)$ and $w_p^{(2)}(t)$ at each time step yields a set of simultaneous equations in the weights $p_k^{(1)}$ and $p_k^{(2)}$

$$\sum_{k=1}^{n} U_{lk}(t)\ p_k^{(1)}(t) = u_p^{(1)}(t) \quad , \qquad l = 1, n$$
$$\sum_{k=1}^{n} W_{lk}(t)\ p_k^{(2)}(t) = w_p^{(2)}(t) \quad , \qquad l = 1, n \tag{24}$$

An approximation to $f_p(t)$ is found from the plane-strain problem of the infinite length cylinder with prescribed radial displacement at the inner boundary (Appendix C).

In what follows, superscripts (1,2) are dropped for shortness. For an elastic material, eigenvalues and resonant frequencies are synonymous. In this case, the eigenvalues appear in pairs ω_{mj} and $-\omega_{mj}$. Consequently equation (22a) takes the form

$$\left(\frac{d}{dt} - i\omega_{mj}\right)\left(\frac{d}{dt} + i\omega_{mj}\right) a_{mjk}(t) = \bar{f}_{mjk}(t) \tag{25a}$$

$$\bar{f}_{mjk}(t) = N_{amjk}\ \ddot{f}_p(t) / N_{mj}$$
$$N_{amjk} = \int_0^l \int_{r_p}^{r_o} \mathbf{u}_{sk}(r,z) \bullet \mathbf{\Phi}_{mj}(x,z)\ r\, dr\, dz \tag{25b}$$
$$N_{mj} = \int_0^l \int_{r_p}^{r_o} \mathbf{\Phi}_{mj}(r,z) \bullet \mathbf{\Phi}_{mj}(r,z)\ r\, dr\, dz$$

2b. Visco-elastic analysis

For a visco-elastic material, ω_{mj} and $\mathbf{\Phi}_{mj}(r,z)$ in (25) are both complex

$$\omega_{mj} = \omega_{mRj} + i\,\omega_{mIj} \tag{26a}$$

$$N_{mj} = \int_0^l \int_{r_p}^{r_o} \mathbf{\Phi}_{mj}(r,z) \bullet \mathbf{\Phi}_{mj}^{*}(r,z)\ r\, dr\, dz \tag{26b}$$

$\Phi^*_{mj}(r,z)$ is the complex conjugate of the eigenfunction. Unlike the elastic case where for each eigenfunction the eigenvalue pair is $+\omega_{mj}$ and $-\omega_{mj}$, in the visco-elastic case the pair is $+\omega_{mj}$ and $-\omega^*_{mj}$ where $(\,)^*$ stands for complex conjugate. This means that $\omega_{1mj} = \omega_{Rmj} + i\,\omega_{Imj}$ and $\omega_{2mj} = -\omega_{Rmj} + i\,\omega_{Imj}$. The reason ω_{Imj} retains the same sign for both solutions is that ω_{Imj} is a measure of damping which reduces amplitude whether the real part is $+\omega_{Rmj}$ or $-\omega_{Rmj}$. Consequently equation (21a) takes the form

$$\left(\frac{d}{dt} - i\omega_{mj}\right)\left(\frac{d}{dt} + i\omega^*_{mj}\right) a_{mjk}(t) = \bar{f}_{mjk}(t)$$
$$\Rightarrow \quad \left[\frac{d^2}{dt^2} + i(\omega^*_{mj} - \omega_{mj})\frac{d}{dt} + \omega_{mj}\omega^*_{mj}\right] a_{mjk}(t) = \bar{f}_{mjk}(t) \tag{27}$$

Noting that $i(\omega^*_{mj} - \omega_{mj}) = 2\omega_{Imj}$ and $\omega_{mj}\omega^*_{mj} = \omega^2_{Rmj} + \omega^2_{Imj}$, (27) simplifies to

$$\left[\frac{d^2}{dt^2} + 2\omega_{Imj}\frac{d}{dt} + \omega^2_{Rmj} + \omega^2_{Imj}\right] a_{mjk}(t) = \bar{f}_{mjk}(t) \tag{28}$$

Clearly, ω_{Imj} acts as a velocity proportional viscous damper. Rewriting (28) in standard form:

$$\left[\frac{d^2}{dt^2} + 2\zeta_{mj}\,\bar{\omega}_{mj}\frac{d}{dt} + \bar{\omega}^2_{mj}\right] a_{mjk}(t) = \bar{f}_{mjk}(t)$$
$$\zeta_{mj} = \frac{\omega_{Imj}}{\bar{\omega}_{mj}} \;;\; \bar{\omega}_{mj} = \sqrt{\omega^2_{Rmj} + \omega^2_{Imj}} \tag{29}$$

yields a solution in terms of a *Duhamel* integral:

$$a_{mjk}(t) = -\frac{1}{\hat{\omega}_{mj}}\int_0^t e^{-\zeta_{mj}\bar{\omega}_{mj}(t-\tau)}\sin\hat{\omega}_{mj}(t-\tau)\;\bar{f}_{mjk}(\tau)\,d\tau \tag{30}$$

$$\hat{\omega}_{mj} = \bar{\omega}_{mj}\sqrt{1-\zeta^2_{mj}}$$

The general constitutive law for a linear viscoelastic material takes the form (see Fung (1965), pp 416-418)

$$\sum_{n=0}^{N_\varepsilon} \tau_{\varepsilon n} \frac{\partial^n \sigma}{\partial t^n} = E_o \sum_{n=0}^{N_\sigma} \tau_{\sigma n} \frac{\partial^n \varepsilon}{\partial t^n} \quad , \quad \tau_{\sigma 0} = \tau_{\varepsilon 0} = 1 \tag{31}$$

$\tau_{\sigma n}, \tau_{\varepsilon n}$ are constants and E_o is a modulus. For a sinusoidal time dependence, (31) assumes the form of a $Pade'$ series

$$\begin{aligned} &\sigma = \beta_\tau(N_\sigma, N_\varepsilon; \omega)\ E_o\, \varepsilon \\ &\beta_\tau(N_\sigma, N_\varepsilon; \omega) = \sum_{n=0}^{N_\sigma} \tau_{\sigma n} (i\omega)^n \ \Big/ \ \sum_{n=0}^{N_\varepsilon} \tau_{\varepsilon n} (i\omega)^n \end{aligned} \tag{32}$$

$\beta_\tau(N_\sigma, N_\varepsilon; \omega)$ is a complex valued function of ω. The simplest linear visco-elastic solid limits N_σ and N_ε to 1 reducing (32) to

$$\sigma = \frac{(1 + \tau_{\sigma 1}\, i\omega)}{(1 + \tau_{\varepsilon 1}\, i\omega)} E_o\, \varepsilon \equiv \beta_\tau(1,1;\omega)\ E_o\, \varepsilon \tag{33}$$

For the constitutive law in (33), approximations to ω_R and ω_I in (26a) are

$$\begin{aligned} &\omega_R \approx \omega_o \left| \beta_\tau^{1/2}(1,1;\omega_{co}) \right|, \quad \omega_I \approx \omega_o\, \mathrm{Im}\left(\beta_\tau^{1/2}(1,1;\omega_{co}) \right) \\ &\omega_{co} = \omega_{Ro} + i\,\omega_{Io} = \omega_o \left[\left| \beta_\tau^{1/2}(1,1;\omega_o) \right| + i\ \mathrm{Im}\left(\beta_\tau^{1/2}(1,1;\omega_o) \right) \right] \end{aligned} \tag{34}$$

ω_o is the eigenfrequency of the linear elastic problem.

3. Results

In all results to follow, geometric and material properties of the cylinder are listed in Table I. Fig. 1(a1) plots the static deformed generator from a unit radial displacement prescribed at the footprint

$$u_{so}(r_p, z) = H(z - z_a) - H(z - z_b) \tag{35a}$$

In (35a) z_a=1.5″ and z_b=2.5″. The resulting normalized $\sigma_{rrs}(r_p,z)$ distribution plotted in Fig. 1(b1) shows a rise near z_a and z_b of 1.5 times its magnitude at the plateau. Fig. 1(a2,b2) plot static deformed generator and normalized $\sigma_{rrs}(r_p,z)$ distribution for a unit axial displacement prescribed at the footprint

$$w_{so}(r_p,z)=H(z-z_a)-H(z-z_b) \qquad (35b)$$

In this case, σ_{rrs} rises near z_a and z_b to 1.7 times its magnitude at the plateau.

Fig. 2(a,b) plots resonant frequency Ω in Hertz versus m with k_r as parameter for the two problems. The two spectra are almost identical for all m and k_r.

In Eq. (23), influence coefficients U_{lk} and W_{lk} require an approximation to the time dependence of the forcing pressure $f_p(t)$. One approximation is determined from the plane-strain state when axial length of cylinder and footprint approaches infinity (Appendix C). Fig. 3(a-d) plot histories of the plane-strain problem when a constant velocity U_o=330 m/s is prescribed at $r=r_p$. There, u history shown as solid line in Fig. 3(a) reproduces the prescribed u_o profile. At $r=2r_p$ and $r=4r_p$, u histories exhibit the time-delay in wave front from propagation with finite speed c_ε. The closeness in magnitude of peak σ_{rr}, $\sigma_{\theta\theta}$ and σ_{zz} (Fig. 3(b,c,d)) implies a hydrodynamic state of stress. Geometric stress attenuation along r is proportional to $r^{-1/2}$.

The $\sigma_{rr}(r_p)$ plane-strain history in Fig. 3(b) serves as the approximation to $f_p(t)$ in the 3-D axisymmetric model as it is the limit when projectile and cylinder lengths are the same. Fig. 4(a1-d1) plots histories from the prescribed uniform pressure profile $f_p(t)$ at the center of the footprint $z=2"$. The u

history in Fig. 4(a1) does not follow the prescribed u_o profile because applied pressure is uniform over the footprint. Applying the influence method of Section 2 yields the histories in Fig. 4(a2-d2). The $u(r_p)$ history in Fig. 4(a2) matches the prescribed u_o profile. At the footprint, except for the higher stress peaks, results from prescribed velocity agree with those from the prescribed plane-strain pressure profile $f_p(t)$. At $r > r_p$, results from the two forcing methods coincide implying that the plane-strain pressure profile is a good approximation to the actual profile determined by the influence method. Geometric stress attenuation along r is proportional to $r^{-3/4}$. Fig. 5(a-d) plots histories from prescribed velocity remote from the footprint at $z = 2.6"$. There, peak normal stresses are 1/5 those under the footprint (see Fig. 4(b2,c2,d2)). This steep drop in stress across the edges of the footprint is caused by the low shear rigidity of the material consistent with the ratio $c_s / c_d \simeq 1/5$ from Table I.

Fig. 6 plots instantaneous $\sigma_{rr}(r_p, z; t_o)$ distributions for $2\mu s \le t_o \le 12\mu s$ in intervals of $2\mu s$. For $t_o = 2\mu s$, the distribution is parabolic with a maximum at the center of the footprint. As time increases, the distribution becomes flatter then develops peaks near z_a and z_b resembling the static case in Fig. 1(b1). The step-like shape of the distribution is an artifact of the finite number of pressure ring segments dividing the footprint. In Fig. 6, the 8 steps correspond to 8 ring segments. The distribution becomes smoother as number of ring segments increases.

For an axial prescribed velocity at $r = r_p$ along $z_a \le z \le z_b$, the approximation to $f_p(t)$ is determined from the solution of the pure-shear problem of an infinite cylinder with axial velocity prescribed at $r = r_p$ derived in Appendix D. Figure

7(a,b) plots histories of w and τ_{rz} for the case of pure shear. Since c_s/c_d=1/5, the time range in these histories is extended to 40μs to allow for the longer arrival time at stations remote from the footprint. The τ_{rz} profile in Fig. 7(b) is then used as an approximation $f_p(t)$ in computing histories with prescribed velocity.

Fig. 8(a1,b1) plots histories at the center of the footprint $z = 2"$ from a uniform $\tau_{rzo}(r_p, z, t) = f_p(t)$ prescribed over the footprint. Fig. 8(a1) shows that $\partial_t w$ is the same as prescribed velocity U_0 =330 ft/s till $t = 10\mu s$, then diminishes to 200 ft/s near $t = 40\mu s$. On the other hand for prescribed velocity, $\partial_t w$ in Fig. 8(b2) is constant for all times and equals U_o. Magnitude of τ_{rz} in Fig. 8(b2) is higher than that in Fig. 8(b1) by approximately a factor of 1.3.

Remote from the footprint at $z = 2.6"$, histories with prescribed pressure (Fig. 9(a1-d1)) are compared to those with prescribed velocity (Fig. 9(a2-d2)). In Fig. 9(a1-d1) all variables are approximately half the corresponding variables in Fig. 9(a2-d2). Fig. 10 plots τ_{rz} distribution along the footprint. For $t_o < 10\mu s$, τ_{rz}'s distribution is uniform. As time increases, τ_{rz} rises steeply near the edges of the footprint reaching a value double its value at the center at $t_o \approx 40\mu s$.

4 Conclusion

Wave propagation in a hollow cylinder is analyzed for pressure and velocity prescribed at its inner boundary. The difficulty arising from the mixed boundary conditions is overcome by the influence coefficient method. An approximation to the prescribed pressure profile needed in this method is determined from the plane-strain solution. Noteworthy results are

1) The stress state close to impact is almost hydrodynamic.
2) Results from prescribed radial velocity agree with those from prescribed uniform pressure determined from the plane-strain model.
3) In the plane-strain model, stress attenuation along r follows $r^{-1/2}$ while in the 3-D axisymmetric model it follows $r^{-3/4}$.
4) For prescribed radial velocity, the instantaneous σ_{rr} distribution is parabolic soon after impact, and approaches the static distribution for large times.
5) Near the center of the footprint, results from prescribed axial velocity agree with those from prescribed uniform shear stress determined from the pure-shear model. However, near the edges of the footprint, stresses from prescribed pressure are half of those from prescribed velocity because in the later τ_{rz} rises near the edges by the same factor.

Appendix A. Static problem

In what follows, all dependent variables pertaining to the static solution will be subscripted by s. The static axisymmetric equations in terms of displacements are

$$\begin{aligned}
&\left((\lambda+2\mu)\hat{\nabla}_1^2+\mu\,\partial_{zz}\right)u_s \;+\; (\lambda+\mu)\partial_{rz}w_s=0\\
&(\lambda+\mu)\partial_z\left(\partial_r+1/r\right)u_s \;+\; \left(\mu\hat{\nabla}_0^2+(\lambda+2\mu)\partial_{zz}\right)w_s=0\\
&\hat{\nabla}_n^2\equiv\partial_{rr}+1/r\,\partial_r-n^2/r^2\;,\quad n=0,1
\end{aligned}\qquad \text{(A1)}$$

Equations (A1) decouple to

$$\begin{aligned}
&\mu(\lambda+2\mu)\left(\hat{\nabla}_1^2+\partial_{zz}\right)^2u_s=0\\
&\mu(\lambda+2\mu)\left(\hat{\nabla}_0^2+\partial_{zz}\right)^2w_s=0
\end{aligned}\qquad \text{(A2)}$$

For the radial traction problem satisfying $\sigma_{zzs} = 0$ at $z = (0, l)$, separation of variables follows Eq. (11) in the text. Summing over all k_z yields

$$u_s(r,z) = \sum_{m=1}^{M} \bar{u}_{ms}(r) \sin(k_{zm} z) \tag{A3a}$$

$$w_s(r,z) = \sum_{m=1}^{M} \bar{w}_{ms}(r) \cos(k_{zm} z) \ , \quad k_{zm} = m\pi / l \tag{A3b}$$

Substituting (A3) in (A2) produces uncoupled equations in r for each k_{zm}

$$\begin{aligned} \left(\hat{\nabla}_1^2 - k_{zm}^2\right)^2 \bar{u}_{ms}(r) = 0 \\ \left(\hat{\nabla}_0^2 - k_{zm}^2\right)^2 \bar{w}_{ms}(r) = 0 \end{aligned} \tag{A4}$$

In what follows, subscript m will be dropped for shortness. Equations (A4) admit the solutions

$$\begin{aligned} \bar{u}_s(r) = C_1 I_1(k_z r) + C_2 K_1(k_z r) \\ + C_3 \left(k_z r \ I_0(k_z r) - I_1(k_z r)\right) - C_4 \left(k_z r \ K_0(k_z r) + K_1(k_z r)\right) \end{aligned} \tag{A5a}$$

$$\begin{aligned} \bar{w}_s(r) = C_1 I_0(k_z r) - C_2 K_0(k_z r) \\ + C_3 \left(\alpha_1 I_0(k_z r) + k_z r \ I_1(k_z r)\right) + C_4 \left(-\alpha_1 K_0(k_z r) + k_z r \ K_1(k_z r)\right) \end{aligned} \tag{A5b}$$

$$\alpha_1 = (\lambda + 3\mu)/(\lambda + \mu) \ , \quad \alpha_2 = \lambda/(\lambda + \mu)$$

Substituting (A5a,b) in the constitutive relations (14) and (15a) of the text yields

$$\begin{aligned} \bar{\sigma}_{rrs}(r) = 2\mu k_z \left(C_1 \left(I_0(k_z r) - I_1(k_z r)/(k_z r)\right) - C_2 \left(K_0(k_z r) + K_1(k_z r)/(k_z r)\right)\right) \\ + 2\mu k_z C_3 \left(-\alpha_2 I_0(k_z r) + \left(1 + (k_z r)^2\right) I_1(k_z r)/(k_z r)\right) \\ + 2\mu k_z C_4 \left(\ \alpha_2 K_0(k_z r) + \left(1 + (k_z r)^2\right) K_1(k_z r)/(k_z r)\right) \end{aligned} \tag{A6a}$$

$$\begin{aligned} \bar{\sigma}_{\theta\theta s}(r) = 2\mu k_z \left(C_1 I_1(k_z r)/(k_z r) + C_2 K_1(k_z r)/(k_z r)\right) \\ + 2\mu k_z C_3 \left(\ (1 - \alpha_2) I_0(i k_z r) - I_1(k_z r)/(k_z r)\right) \\ + 2\mu k_z C_4 \left(-(1 - \alpha_2) K_0(k_z r) - K_1(k_z r)/(k_z r)\right) \end{aligned} \tag{A6b}$$

$$\begin{aligned}\bar{\sigma}_{zzs}(r) = \;& 2\mu k_z\left(-C_1 I_0(k_z r) + C_2 K_0(k_z r)\right) \\ & + 2\mu k_z C_3\left(-(\alpha_1+\alpha_2)\, I_0(k_z r) - k_z r\, I_1(k_z r)\right) \\ & + 2\mu k_z C_4\left(\;(\alpha_1+\alpha_2) K_0(k_z r) - k_z r\, K_1(k_z r)\right)\end{aligned} \qquad \text{(A6c)}$$

$$\begin{aligned}\bar{\tau}_{rzs}(r) = \;& 2\mu k_z\left(C_1 I_1(k_z r) + C_2 K_1(k_z r)\right) \\ & + 2\mu k_z C_3\left(\;k_z r\, I_0(k_z r) + (1-\alpha_2) I_1(k_z r)\right) \\ & + 2\mu k_z C_4\left(-k_z r\, K_0(k_z r) + (1-\alpha_2) K_1(k_z r)\right)\end{aligned} \qquad \text{(A6d)}$$

Tractions at the inner and outer surfaces of the tube are expressed as

$$\begin{aligned}&\sigma_{rrs}(r_p, z) = p_r\left(H(z-z_a) - H(z-z_b)\right) \\ &\tau_{rzs}(r_p, z) = 0\end{aligned} \qquad \text{(A7a)}$$

$$\sigma_{rrs}(r_o, z) \equiv \tau_{rzs}(r_o, z) = 0 \qquad \text{(A7b)}$$

p_r is a uniform radial traction prescribed at $r = r_p$ in the interval $z_a \le z \le z_b$. Substituting (A6a) and (A6d) in (A7a) and (A7b) and enforcing orthogonality of $\sin(k_z z)$ and $\cos(k_z z)$ produces M (4×4) uncoupled matrix equations in the coefficients C_{km}, $k = 1,4$

$$\mathbf{M}_{cm}\mathbf{C}_m = \mathbf{f}_m \qquad \text{(A8)}$$

Coefficients of $\mathbf{M}_{cm}$ are the radial functions multiplying C_{km} in (A6a) and (A6d) evaluated at $r = r_p$ and $r = r_o$, and $\mathbf{f}_m$ is a vector defined by

$$\begin{aligned}&f_{1m} = -2 p_r\left(\cos(k_{zm} z_b) - \cos(k_{zm} z_a)\right)/(k_{zm} l) \\ &f_{2m} \equiv f_{3m} \equiv f_{4m} = 0\end{aligned} \qquad \text{(A9)}$$

For the axial traction problem satisfying vanishing shear stress $\tau_{rzs} = 0$ at $z = (0, l)$, the expansion in (A3) becomes

$$u_s(r,z) = \sum_{m=1}^{M} \bar{u}_{ms}(r)\cos(k_{zm}z)$$
$$w_s(r,z) = \sum_{m=1}^{M} \bar{w}_{ms}(r)\sin(k_{zm}z)\ , \qquad k_{zm} = m\pi / l \tag{A10}$$

The boundary conditions are

$$\sigma_{rrs}(r_p,z) = 0$$
$$\tau_{rzs}(r_p,z) = p_z\left(H(z-z_a) - H(z-z_b)\right) \tag{A7a}$$

$$\sigma_{rrs}(r_o,z) \equiv \tau_{rzs}(r_o,z) = 0 \tag{A7b}$$

p_z is a uniform axial traction applied at $r = r_p$ in the interval $z_a \le z \le z_b$. Expressions for displacements and stresses resemble those of the radial problem and are omitted here for shortness.

Appendix B. Modal analysis

The dynamic solution $\mathbf{u}_d(r,z,t)$ satisfies the homogeneous boundary conditions

$$\sigma_{rr}(r_p,z,t) = 0\ , \quad \tau_{rz}(r_p,z,t) = 0$$
$$\sigma_{rr}(r_o,z,t) = 0\ , \quad \tau_{rz}(r_o,z,t) = 0 \tag{B1}$$

Substituting (16a) and (16d) in (B1) yields the matrix equation

$$\mathbf{M}_e\mathbf{C} = \mathbf{0} \tag{B2}$$

$\mathbf{M}_e$ is a 4×4 square matrix, $\mathbf{C} = \{C_1, C_2, C_3, C_4\}^T$ is the vector of unknown coefficients and

$$M_{e11} = -\left((\lambda+2\mu)k_e^2 + \lambda k_z^2\right)J_0(k_e r_p) + 2\mu k_e^2\, J_1(k_e r_p)\ /(k_e r_p)$$
$$M_{e13} = 2\mu k_s k_z\left[J_0(k_s r_p) - J_1(k_s r_p)\ /(k_s r_p)\right]$$
$$M_{e21} = -2\mu k_e k_z J_1(k_e r_p) \tag{B3}$$
$$M_{e23} = -\mu(k_s^2 - k_z^2)J_1(k_s r)$$

$M_{e12}, M_{e14}, M_{e22}, M_{e24}$ have the same form as $M_{e11}, M_{e13}, M_{e21}, M_{e23}$ with J_n replaced by Y_n. Similarly, M_{e3k}, M_{e4k} $k=1,4$ have the same form as M_{e1k}, M_{e2k} $k=1,4$, with r_p replaced by r_o. From the definitions of k_e and k_s in (12), k_e is imaginary when $\omega < k_z c_d$, $c_d = \sqrt{(\lambda+2\mu)/\rho}$, and k_s is imaginary when $\omega < k_z c_s$, $c_s = \sqrt{\mu/\rho}$. Below these cut-off frequencies, J_n and Y_n are replaced by I_n and K_n with appropriate changes in sign. For each m in k_z, a non-trivial solution to (B2) yields the implicit eigenvalue problem

$$det\,|\mathbf{M}_{em}| = 0 \quad \Rightarrow \quad \left\{\omega_{mj}; \Phi_{mj}(r,z)\right\} \tag{B4}$$

$\left\{\omega_{mj}; \Phi_{mj}(r,z)\right\}$ is the eigen-dyad corresponding to the m^{th} axial wave-number.

Appendix C. Plane-strain problem

The radial plane-strain problem is that of an infinite hollow cylinder where $\varepsilon_{zz} \equiv w \equiv \partial_z \equiv 0$. The dynamic equation in u then reduces to

$$\begin{aligned} &\hat{\nabla}_1^2 u = 1/c_\varepsilon^2\, \partial_{tt} u \qquad , \quad r_p \le r \le r_o \\ &\hat{\nabla}_1^2 \equiv \partial_{rr} + 1/r\ \partial_r - 1/r^2\ , \quad c_\varepsilon^2 = E_\varepsilon/\rho \\ &E_\varepsilon = E(1-\nu)/\big((1+\nu)(1-2\nu)\big) \end{aligned} \tag{C1}$$

The boundary conditions are

$$u(r_p,t) = f_p(t)\ , \quad \sigma_{rr}(r_o,t) = 0 \tag{C2}$$

$f_p(t)$ is the time dependent displacement profile prescribed at $r = r_p$. The constitutive law takes the form

$$\begin{aligned} &\sigma_{ii} = \lambda\,\varepsilon_V + 2\mu\,\varepsilon_{ii}\ , \quad ii \to rr, \theta\theta, zz \\ &\varepsilon_V = \varepsilon_{rr} + \varepsilon_{\theta\theta} \quad , \ \varepsilon_{zz} \equiv 0 \end{aligned} \tag{C3a}$$

$$\begin{aligned}
\sigma_{rr} &= E_\varepsilon \left(\partial_r u + \nu/(1-\nu)\ u/r \right) \\
\sigma_{\theta\theta} &= E_\varepsilon \left(u/r + \nu/(1-\nu)\ \partial_r u \right) \\
\sigma_{zz} &= E_\varepsilon \left(u/r + \partial_r u \right) \nu/(1-\nu)
\end{aligned} \qquad \text{(C3b)}$$

Express $u(r,t)$ as a superposition of a static and a dynamic solution

$$u(r,t) = u_s(r)\ f_p(t) + u_d(r,t) \qquad \text{(C4)}$$

$u_s(r)$ is the static solution satisfying the inhomogeneous boundary conditions

$$u_s(r_p) = 1\,, \quad \sigma_{rrs}(r_o) = 0 \qquad \text{(C5)}$$

$u_d(r,t)$ is the dynamic solution satisfying the homogeneous form of boundary conditions (C2). Expand $u_d(r,t)$ in the eigenfunctions $\varphi_j(r)$ of (C1)

$$\begin{aligned}
u_d(r,t) &= \sum_j a_j(t)\ \varphi_j(r) \\
\varphi_j(r) &= J_1(k_{rj}\, r) + c_2\, Y_1(k_{rj}\, r)\,, \quad c_2 = -J_1(k_{rj}\, r_p)/Y_1(k_{rj}\, r_p)
\end{aligned} \qquad \text{(C6)}$$

Substituting (C6) in the homogeneous form of (C2) yields the dispersion relation

$$\begin{aligned}
&\alpha_{11}\alpha_{22} - \alpha_{12}\alpha_{21} = 0 \\
&\alpha_{11} = J_1(k_{rj}\, r_p)\,, \quad \alpha_{12} = Y_1(k_{rj}\, r_p) \\
&\alpha_{21} = (\lambda + 2\mu)\, k_{rj}\, J_1'(k_{rj}\, r_o) + \lambda\, J_1(k_{rj}\, r_o)/r_o \\
&\alpha_{22} = (\lambda + 2\mu)\, k_{rj}\, Y_1'(k_{rj}\, r_o) + \lambda\, Y_1(k_{rj}\, r_o)/r_o
\end{aligned} \qquad \text{(C7)}$$

$(\,)'$ stands for derivative with respect to the argument. (C7) determines the wave numbers k_{rj}. The static solution to $\nabla_1^2 u_s = 0$ is

$$\begin{aligned}
u_s(r) &= Ar + B/r \\
A &= r_p \left(r_p^2 + (\lambda + \mu)\, r_c^2/\mu \right)^{-1}, \quad B = r_p \left(1 - A r_p \right)
\end{aligned} \qquad \text{(C8)}$$

The constitutive law is given by (C3b). Substituting (C6) and (C8) in (C4) and enforcing orthogonality of $\varphi_j(r)$ yields

$$\ddot{a}_j(t) + \omega_j^2\, a_j(t) = -\left(N_{aj} / N_{jj}\right) \ddot{f}_p(t)$$
$$N_{jj} = \int_{r_p}^{r_o} \varphi_j^2(r)\; r\, dr\;,\; N_{aj} = \int_{r_p}^{r_o} u_s(r)\; \varphi_j(r)\; r\, dr\;,\quad \omega_j = c_d\, k_{rj} \qquad \text{(C9)}$$

$(\dot{\ })$ stands for time derivative. The integrals in N_{jj} and N_{aj} are evaluated analytically in terms of J_n and Y_n for $n = 0,1,2$.

For the radial plane-stress problem, $\sigma_{zz} \equiv w \equiv \partial_z \equiv 0$ yielding the equation

$$\hat{\nabla}_1^2 u = 1/c_\sigma^2\, \partial_{tt} u \quad,\quad \hat{\nabla}_1^2 \equiv \partial_{rr} + 1/r\; \partial_r - 1/r^2$$
$$c_\sigma^2 = E/\left(\rho(1-\nu^2)\right),\quad r_p \le r \le r_c \qquad \text{(C10)}$$

(C10) has the same form as (C1) but with a lower speed of propagation since $c_\sigma / c_d = (1-2\nu)^{1/2}/(1-\nu)$ is small when ν is close to 1/2. The constitutive law simplifies to

$$\sigma_{rr} = E_\sigma \left(\partial_r u + \nu\, u/r\right) \quad,\quad \sigma_{\theta\theta} = E_\sigma \left(\, u/r + \nu\; \partial_r u\, \right)$$
$$\sigma_{zz} = 0\,, \qquad E_\sigma = E/(1-\nu^2) \qquad \text{(C11)}$$

If prescribed displacement at $r = r_p$ is the same for both plane stress and plane strain, then strains are approximately the same. It follows that stresses in (C11) are smaller than those in (C3b) by a factor of $\left(c_\sigma / c_d\right)^2$. In the present application, if material of the cylinder fails radially within the footprint $z_a \le z \le z_b$, then the approximate state of plane-strain changes to that of plane-stress reducing transmitted pressure substantially.

Pure shear problem

For the pure shear problem, $\sigma_{rr} \equiv \sigma_{\theta\theta} \equiv \sigma_{zz} \equiv u \equiv 0$ yielding the equation

$$\hat{\nabla}_0^2 w = 1/c_s^2\, \partial_{tt}^2 w \quad,\quad \hat{\nabla}_0^2 = \partial_{rr} + 1/r\partial_r$$
$$c_s^2 = E/\left(2\rho(1+\nu)\right),\quad r_p \le r \le r_o \qquad \text{(D1a)}$$

$$w(r_p,t) = f_p(t) \ , \quad \tau_{rz}(r_o,t) = 0 \qquad \text{(D1b)}$$

$$\tau_{rz}(r,t) = E/\left(2(1+\nu)\right)\, \partial_r w(r,t) \qquad \text{(D1c)}$$

Express w as a superposition of a static and a dynamic solution

$$w(r,t) = w_s(r)\ f_p(t) + w_d(r,t) \qquad \text{(D2a)}$$

$$\hat{\nabla}_0^2 w_s = 0 \ , \qquad w_s(r_p) = 1 \ , \ \tau_{rzs}(r_o) = 0 \qquad \text{(D2b)}$$

$$\hat{\nabla}_0^2 w_d = 1/c_s^2\ \partial_{tt} w_d \ , \quad w_d(r_p,t) = 0 \ , \ \tau_{rzd}(r_o,t) = 0 \qquad \text{(D2c)}$$

Since (D2b) admits a rigid body motion, a body-force b_f is subtracted from (D2b) so as to equilibrate the external shear traction and $b_f\, f_p(t)$ is added to (D2c) to cancel its effect. This yields

$$\begin{aligned} \hat{\nabla}_0^2 w_s &= -b_f \\ \hat{\nabla}_0^2 w_d &= 1/c_s^2\ \partial_{tt}^2 w_d \ + b_f\ f_p(t) \end{aligned} \qquad \text{(D3)}$$

The solution to w_s satisfying the boundary conditions (D2b) is

$$\begin{aligned} w_s(r) &= \left(2r_o^2 \ln r - r^2\right)/\left(2r_o^2 \ln r_p - r_p^2\right) \\ \tau_{rzs}(r) &= \frac{E}{(1+\nu)} \frac{\left(r_o^2 - r^2\right)}{\left(2r_o^2 \ln(r_p) - r_p^2\right) r} \\ b_f &= 2/\left(r_o^2 \ln r_p - r_p^2/2\right) \end{aligned} \qquad \text{(D4)}$$

Expand w_d in terms of its eigenfunctions $\varphi_j(r)$

$$\begin{aligned} w_d(r,t) &= \sum_j a_j(t)\varphi_j(r) \\ \varphi_j(r) &= J_0(k_{rj}\, r) - \left(J_0(k_{rj}\, r_p)/Y_0(k_{rj}\, r_p)\right) Y_0(k_{rj}\, r) \end{aligned} \qquad \text{(D5)}$$

Substituting (D2a) in (D1a) using (D3) and (D5) and enforcing the orthogonality of $\varphi_j(r)$ produces uncoupled equations in $a_j(t)$

$$\ddot{a}_j(t) + \omega_j^2 a_j(t) = -\left(N_{aj} / N_{jj}\right)\ \ddot{f}_p(t) - \left(N_{bj} / N_{jj}\right) c_s^2\, b_f\ f_p(t)$$

$$N_{aj} = \int_{r_p}^{r_o} \varphi_j(r)\, w_s(r)\ r\, dr\ ,\quad N_{bj} = \int_{r_p}^{r_o} \varphi_j(r)\ r\, dr\ ,\quad N_{jj} = \int_{r_p}^{r_o} \varphi_j^2(r)\ r\, dr \qquad \text{(D6)}$$

$(\dot{})$ is time derivative and ω_j are roots of the dispersion relation

$$J_0(k_{rj}\, r_p) Y_0'(k_{rj}\, r_o) - J_0'(k_{rj}\, r_o) Y_0(k_{rj}\, r_p) = 0\ ,\quad k_{rj} = \omega_j / c_s \qquad \text{(D7)}$$

$(\,)'$ is derivative with respect to the argument.

References

Bao, X., et al., 1997. The resonances of finite-length elastic cylinders and elastic spheroids excited by sound scattering, Journal of the Acoustical Society of America 102, 49.

Batard, H., Quentin, G., 1992, Acoustical resonances of solid elastic cylinders: Parametric study, Journal of the Acoustical Society of America 91, 581.

Cheung, Z., Lo, Y., Au, S., 2003. 3-D vibration analysis of solid and hollow circular cylinders via Chebyshev-Ritz method, Computer Methods in Applied Mechanics and Engineering 192, 13-14, 1575-1589.

Fung, Y.C., 1965. *Foundations of solid mechanics*, 1st edition, Prentice-Hall International Series in Dynamics, Prentice-Hall, Inc., Englewood Cliffs, New Jersey.

Grinchenko, V., Meleshko, V., 1978. Axisymmetric vibrations of an elastic cylinder of finite length, Soviet Physics Acoustics 24, 488

Grinchenko, V., 1999. Eigenforms and eigenfrequency spectrum of finite elastic cylinder, Journal of the Acoustical Society of America 105, 1392.

Honarvar, F., Sinclair A., 1996. Acoustic wave scattering from transversely isotropic cylinders, Journal of the Acoustical Society of America 100, 57.

Hussein, M., Heyliger, P., 1998. Three-dimensional vibrations of layered piezoelectric cylinders, Journal of Engineering Mechanics 124, 1294.

Love, A. E., 1944. *A treatise on the mathematical theory of elasticity*, 1st American edition, Dover Publications Inc., New York, 287-292.

Paul, H., Murali, V., 1995. Dynamic response of axisymmetric poroelastic cylindrical bone, Journal of the Acoustical Society of America 98, 5, 2978.

Soldatos, K., Ye, J., 1994, Wave propagation in anisotropic laminated hollow cylinders of infinite extent, Journal of the Acoustical Society of America 96, 6, 3744-3752.

Soldatos, K., 1994, Review of three-dimensional dynamic analyses of circular cylinders and cylindrical shells, American Society of Mechanical Engineers, Applied Mechanics Reviews, 47, 10, 501-516.

Stanton, T., 1988. Sound scattering by cylinders of finite length. II. Elastic cylinders, Journal of the Acoustical Society of America 83, 64.

Stepanishen, P., Janus, R., 1990. Transient radiation and scattering from fluid loaded elastic cylinders, Journal of the Acoustical Society of America, Suppl. 1 88, S78.

Wang, X., Ying C., 2001. Scattering of Lamb waves by a circular cylinder, Journal of the Acoustical Society of America 110, 1752.

Yin, X., Yue, Z., 2002. Transient plane-strain response of multilayered elastic cylinders to axisymmetric impulse, Journal of Applied Mechanics 69, 825.

Acknowlegment:

This work was supported by a grant from DARPA, executed by the U.S. Army Medical Research and Materiel Command/TATRC Contract # W81XWH-04-C-0084.
The views, opinions and/or findings contained in this paper are those of the author and should not be construed as an official Department of the Army position, policy or decision unless so designated by other documentation.

$E \quad (lb/in^2)$	4.5×10^4
$\rho \ (lb\ s^2/in^4)$	8.7×10^{-5}
υ	0.48
$l \quad (in)$	*4*
$r_p \quad (in)$	*0.25*
$r_o \quad (in)$	*3*
$c_d \quad (in/s)$	6.74×10^4
$c_s \quad (in/s)$	1.322×10^4

Table I. Cylinder properties

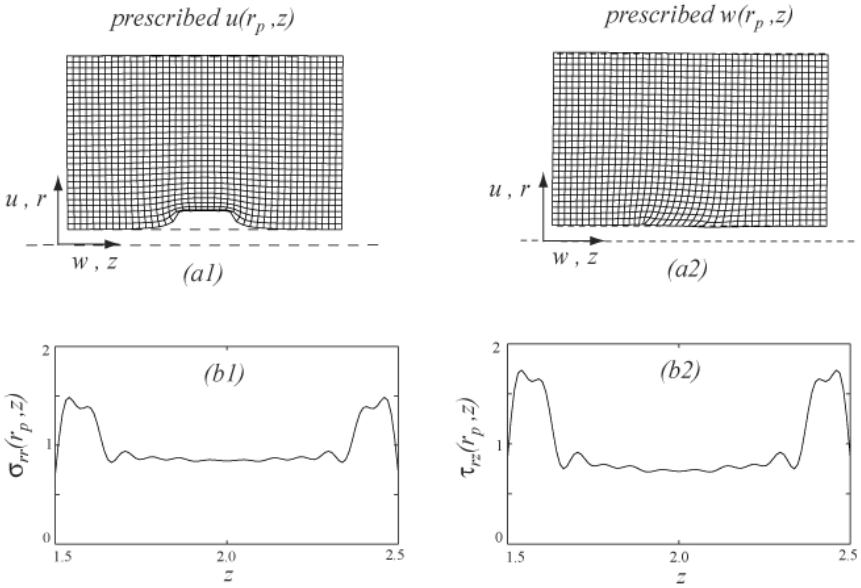

Figure 1. Static deformation and foot-print traction at $r=r_p$, $z_a < z < z_b$
(a1),(b1) prescribed $u(r_p, z)$, (a2),(b2) prescribed $w(r_p, z)$

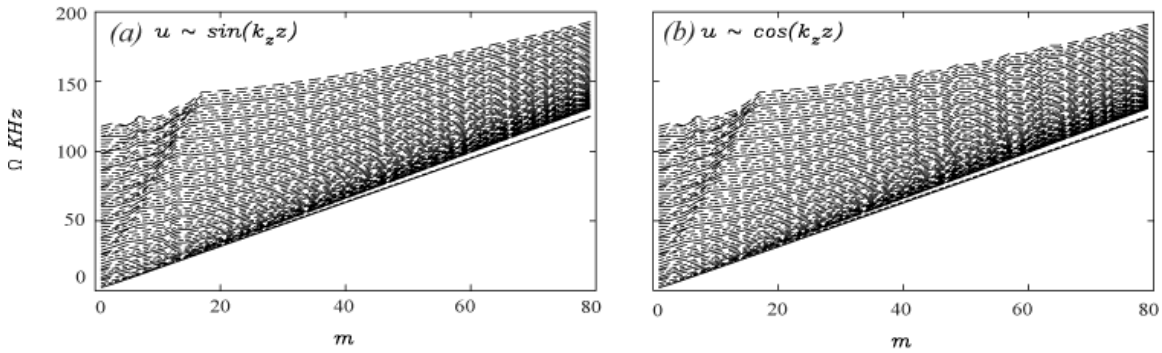

Figure 2. Frequency spectra
(a) radial problem, $u \sim \sin(k_z z)$,
(b) axial problem, $u \sim \cos(k_z z)$

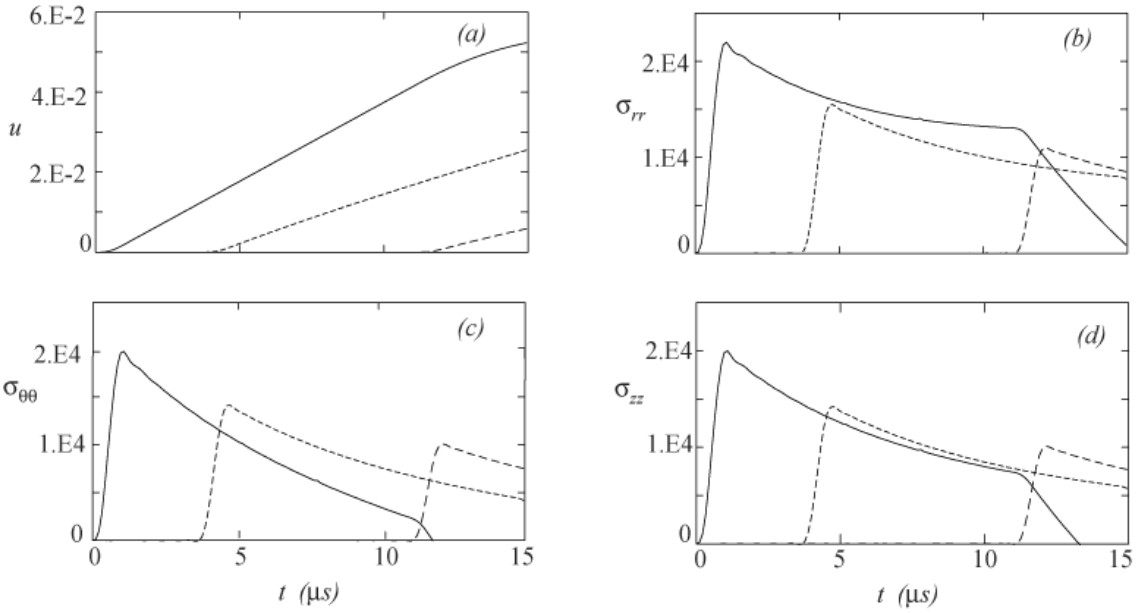

Figure 3. Plane-strain histories from prescribed radial velocity

—— $r = r_p$, ---- $r = 2r_p$, - - - - $r = 4r_p$

(a) u , *(b)* σ_{rr} , *(c)* $\sigma_{\theta\theta}$, *(d)* σ_{zz}

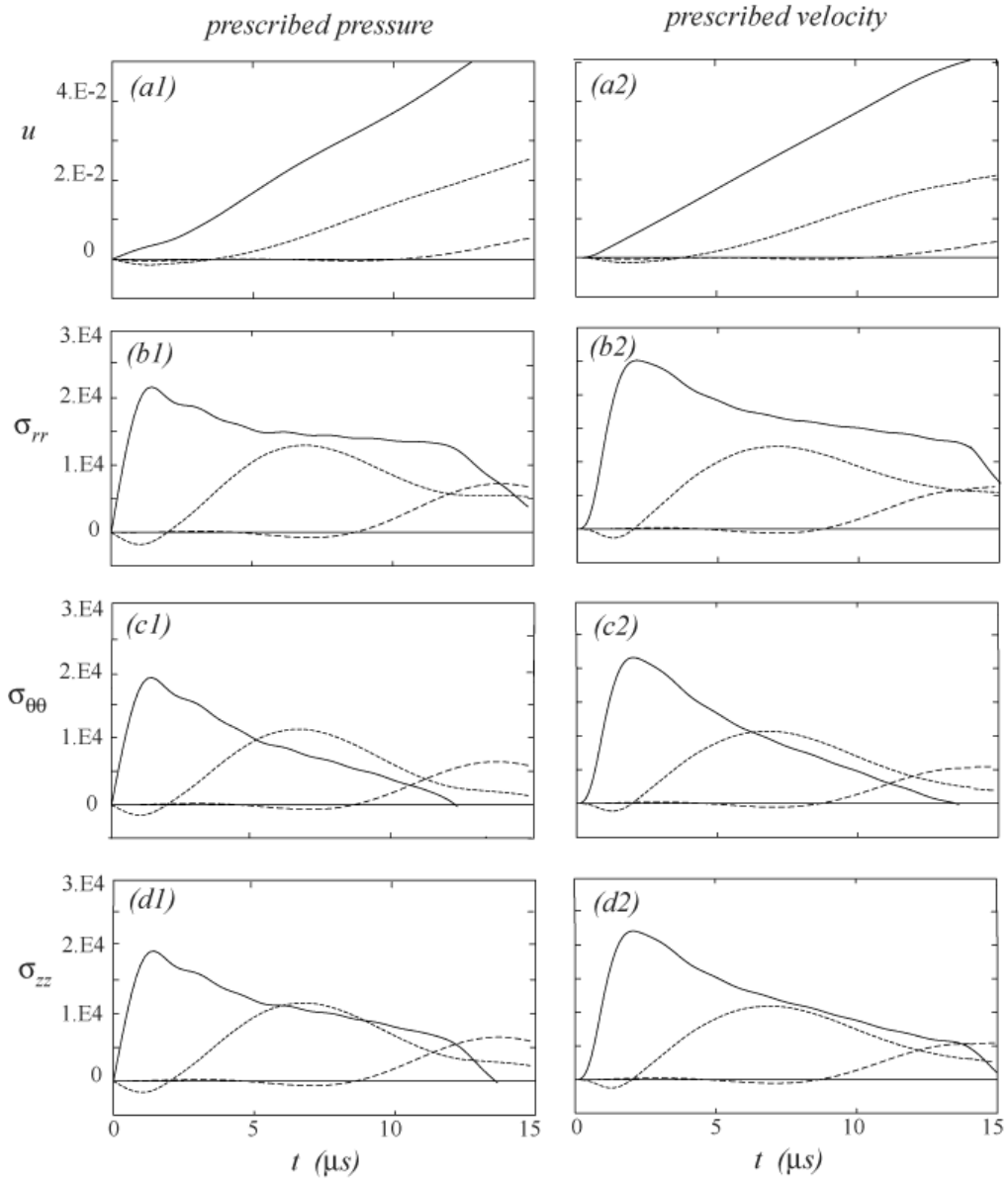

Figure 4. Histories from radial excitation at z=2"

—— $r = r_p$, ---- $r = 2r_p$, - - - - $r = 4r_p$

(a1), (b1), (c1), (d1) prescribed pressure from plane-strain

(a2), (b2), (c2), (d2) prescribed velocity

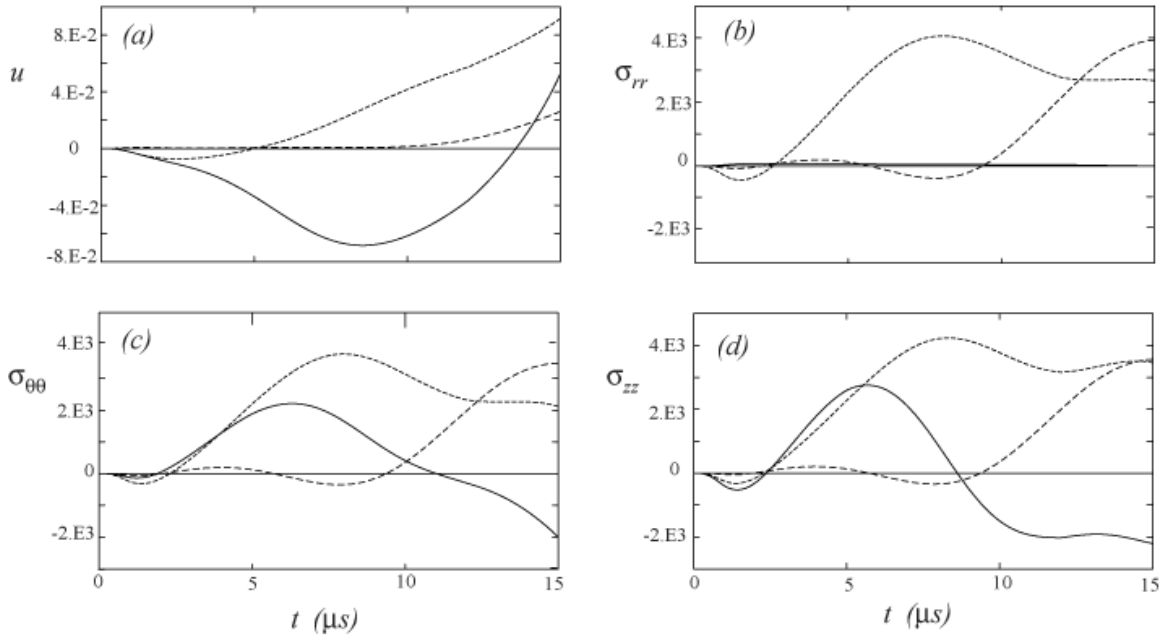

Figure 5. Histories from prescribed radial velocity at z=2.6"

—— $r = r_p$, ---- $r = 2r_p$, - - - - $r = 4r_p$

(a) u , (b) σ_{rr} , (c) $\sigma_{\theta\theta}$, (d) σ_{zz}

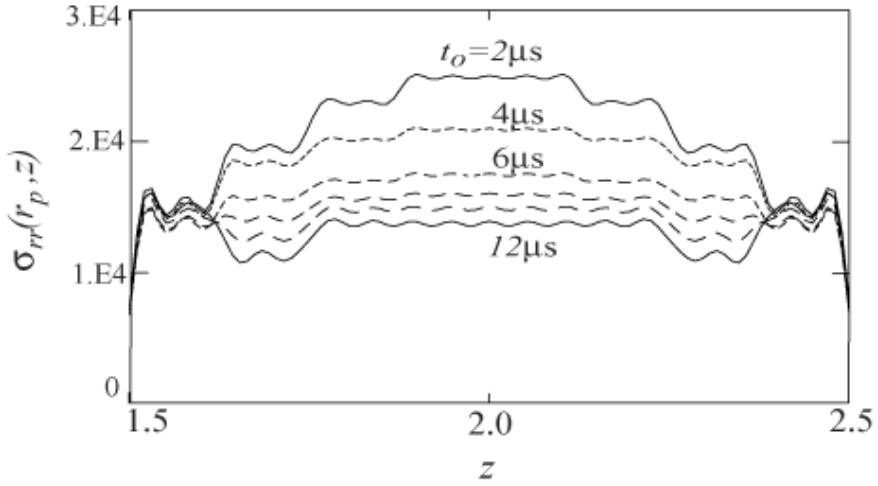

Figure 6. Instantaneous $\sigma_{rr}(r_p, z; t_o)$ distribution over footprint from prescribed radial velocity

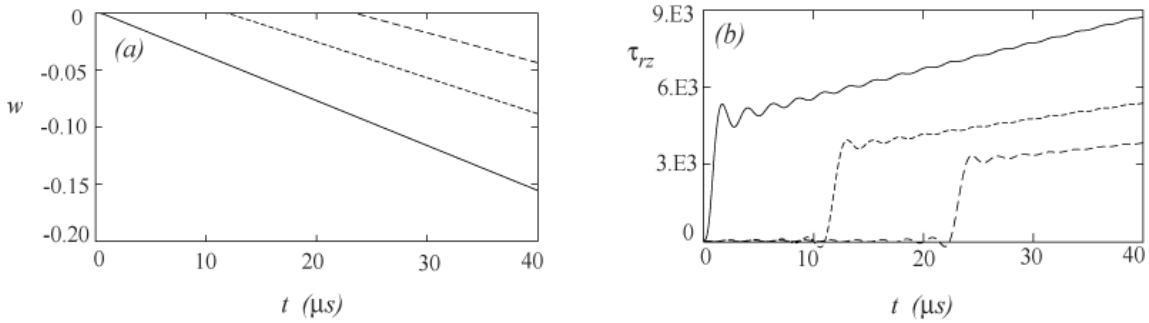

Figure 7. Pure-shear histories from prescribed axial velocity

—— $r = r_p$, ···· $r = 1.6\, r_p$, - - - $r = 2.2\, r_p$; (a) w, (b) τ_{rz}

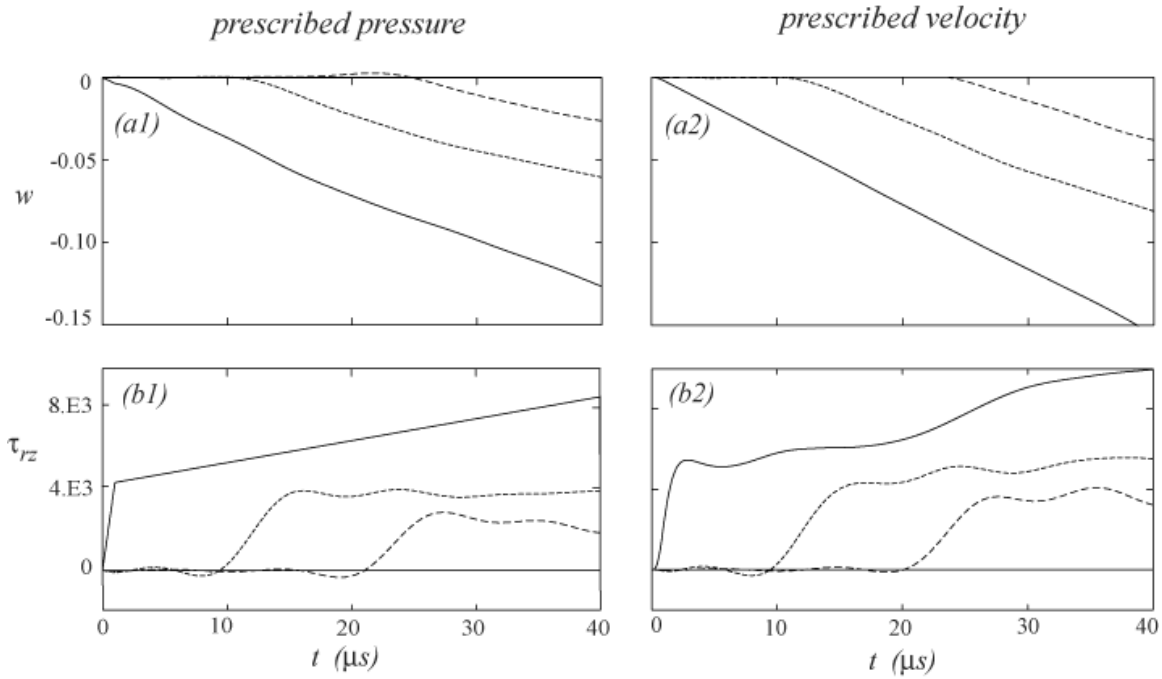

Figure 8. Histories from axial excitation at z=2"

—— $r = r_p$, ---- $r = 1.6\, r_p$, - - - - $r = 2.2\, r_p$

(a1), (b1), prescribed pressure from pure-shear

(a2), (b2), prescribed velocity

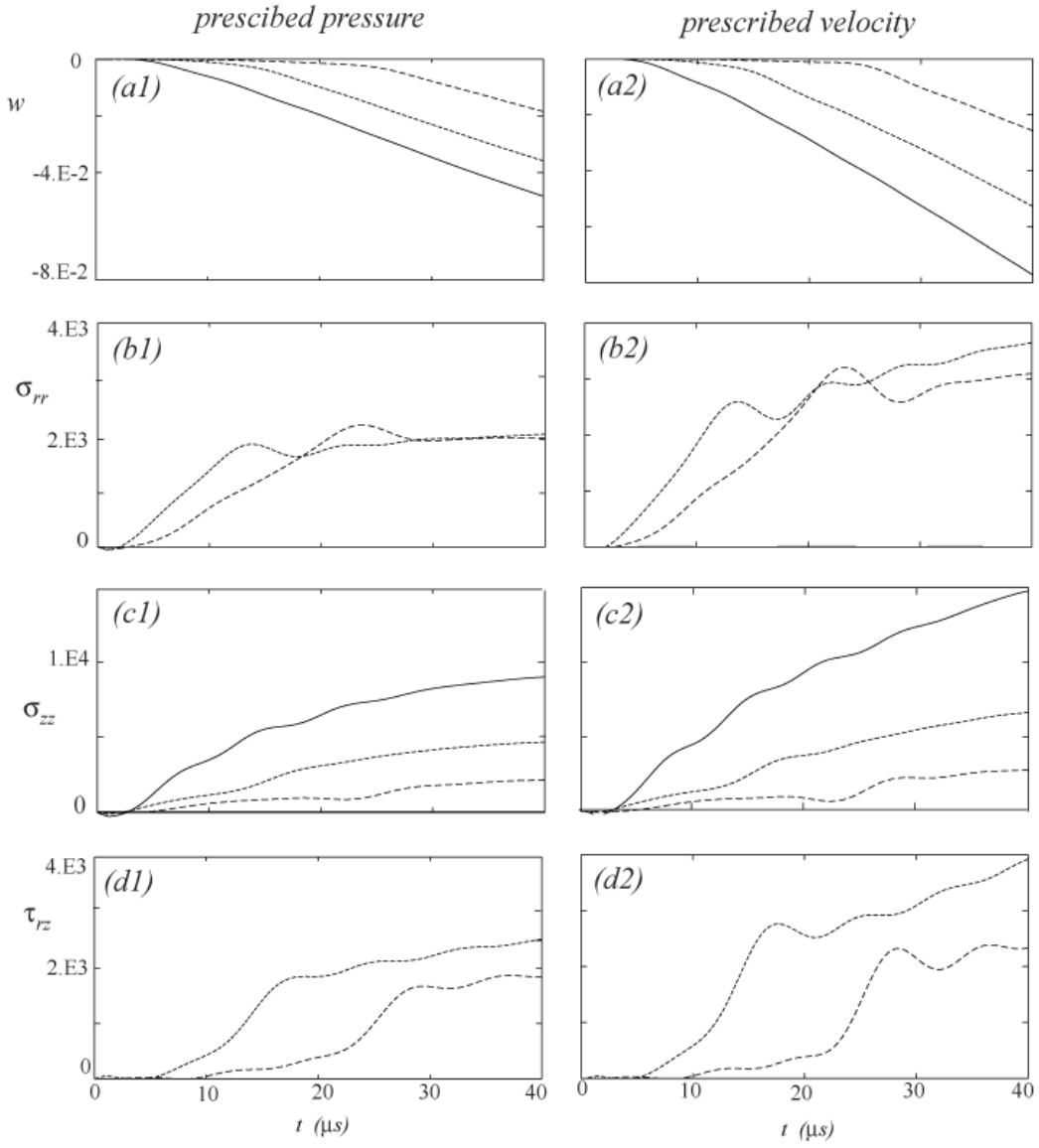

Figure 9. Histories from axial excitation at z=2.6"

—— $r = r_p$, ---- $r = 1.6\, r_p$, - - - - $r = 2.2\, r_p$

(a1) w , (b1) σ_{rr} , (c1) σ_{zz} , (d1) τ_{rz} prescribed pressure from pure-shear

(a2) w , (b2) σ_{rr} , (c2) σ_{zz} , (d2) τ_{rz} prescribed velocity

APPENDIX L

Accepted for publication in the *Journal of Sound and Vibration*

"Transient response in a finite hollow cylinder

from time-delayed prescribed motion at the boundary"

Michael El-Raheb

ATK Mission Research, Laguna Hills CA

Summary

Previous work (to appear in International J. of Solids & Structures, 2005) on transient response of a hollow cylinder to time dependent radial motion is extended to include motion of the excitation along the axis of the cylinder.

1. Introduction

When a projectile penetrates into human tissue, it moves material by replacing it with its own volume. When the material fails, it acts more like a fluid, lessening the amount of material being compressed. In the radial direction, material is compressed by an expanding cross-section of the projectile's smoothly curved nose. As long as the projectile's speed is much smaller than the speed of stress waves in the material, the moving projectile can be approximated by radial and axial velocities prescribed along its boundary [1]. For a projectile speed of 300 ft/s and a dilatational speed in tissue material of 5600 ft/s, this approximation is valid. However, for projectile speed in excess of 1000 ft/s, projectile motion must be considered in the analysis.

The forcing function is a radial motion prescribed over part of the inner cylindrical boundary while the remainder part of the boundary is traction-free. This leads to a mixed boundary value problem whose solution is briefly outlined for completeness while details may be found in Ref. [1]. In order to convert the segment of boundary where motion is prescribed to one where traction is prescribed, response from a set of unit ring tractions with time dependent weights is superimposed. These weights are updated at each time step using the condition that the combined displacement response at the center of each ring equals the prescribed instantaneous displacement. In this way, the forcing function is converted to pure traction with time varying spatial dependence.

2. Analysis

A brief outline of the principal points of the analysis follows in order to clarify how the time-delayed forcing function along the cylinder's axis is included in the algorithm. In cylindrical coordinates, the axisymmetric elastodynamic equations are

$$\mu\nabla^2\mathbf{u}+(\lambda+\mu)\boldsymbol{\nabla}(\boldsymbol{\nabla}\bullet\mathbf{u})=\rho\,\partial_{tt}\mathbf{u} \qquad (1)$$

$$\nabla^2 \equiv \partial_{rr} + 1/r\ \partial_r + \partial_{zz}$$
$$\boldsymbol{\nabla} \equiv \left(1/r\ \partial_r\, r\right)\mathbf{e}_r + (\partial_z)\mathbf{e}_z$$

(r,z) are radial and axial independent variables, $\mathbf{u} = \{u,w\}^T$ is displacement vector along these directions, (λ,μ) are Lame constants, ρ is mass density and t is time. For harmonic motions in time and simply supported boundaries at $(0,l)$ the solution is

$$\begin{aligned}\bar{u}(r,z) &= \left[-k_e\left(C_1 J_1(k_e r) + C_2 Y_1(k_e r)\right) + k_z\left(C_3 J_1(k_s r) + C_4 Y_1(k_s r)\right)\right]\cos(k_z z)\\ \bar{w}(r,z) &= \left[\ k_z\left(C_1 J_0(k_e r) + C_2 Y_0(k_e r)\right) + k_s\left(C_3 J_0(k_s r) + C_4 Y_0(k_s r)\right)\right]\sin(k_z z)\end{aligned} \tag{2}$$

with constitutive relations

$$\begin{aligned}&\sigma_{rr} = \lambda\Delta + 2\mu\,\partial_r u\ ,\ \sigma_{\theta\theta} = \lambda\Delta + 2\mu\, u/r\\ &\sigma_{zz} = \lambda\Delta + 2\mu\,\partial_z w,\ \ \tau_{rz} = \mu\left(\partial_z u + \partial_r w\right)\\ &\Delta = \partial_r u + u/r + \partial_z w\end{aligned} \tag{3}$$

$k_z = m\pi/l$. Boundary conditions at $r = r_p$ and $r = r_o$ are

$$\begin{aligned}&\sigma_{rr}(r_p,z,t) = p_r(t)\left[H(z-z_a) - H(z-z_b)\right]\\ &\tau_{rz}(r_p,z,t) = 0\\ &\sigma_{rr}(r_o,z,t) \equiv \tau_{rz}(r_o,z,t) = 0\end{aligned} \tag{4}$$

$p_r(t)$ is a time dependent uniform radial traction acting on the inner cylindrical boundary $r = r_p$ in the interval $z_a \le z \le z_b$.

Divide the cylindrical surface $\left\{r = r_p,\ z_a \le z \le z_b\right\}$ into $n+1$ equidistant ring stations with constant increment Δz_p

$$z_1,\ z_2, ..., z_l, ..., z_{n+1}\ ,\quad z_l = z_1 + (l-1)\Delta z_p\,,\quad \left(z_n - z_1\right)/n = \Delta z_p \tag{5}$$

Assume a uniform pressure of unit intensity to act over each ring segment $z_{l-1} \to z_l$. The elasto-dynamic solution to the k^{th} ring pressure segment is outlined below.

For each pressure segment, expand each dependent variable in terms of eigenfunctions that satisfy homogeneous boundary conditions. Express total displacement $\mathbf{u}_k(r,z;t)$ as a superposition of two terms

$$\mathbf{u}_k(r,z;t) = \mathbf{u}_{sk}(r,z)\ \hat{f}_p(t)\ +\ \mathbf{u}_{dk}(r,z;t) \qquad (6)$$

$\mathbf{u}_{sk}(r,z)$ is static displacement vector satisfying (1) when time derivative vanishes, $\mathbf{u}_{dk}(r,z;t)$ is dynamic displacement vector satisfying the dynamic equation of motion (1), and $\hat{f}_p(t)$ is time dependence of the forcing pressure. For each axial wave number m, express $\mathbf{u}_{dk}(r,z,t)$ in the eigenfunctions $\mathbf{\Phi}_{mj}(r,z)$

$$\mathbf{u}_{dk}(r,z,t) = \sum_j \sum_m a_{mjk}(t)\ \mathbf{\Phi}_{mj}(r,z) \qquad (7)$$

$a_{mjk}(t)$ is a generalized coordinate of the j^{th} eigenfunction with m axial half waves from the k^{th} pressure segment. Substituting (6) and (7) in (1) and enforcing orthogonality of $\mathbf{\Phi}_{mj}(r,z)$ yields uncoupled equations in $a_{mjk}(t)$. Evaluating radial and axial displacements $u_k(r,z;t)$ and $w_k(r,z;t)$ from the k^{th} pressure segment at each central point $z_{cl} = (z_l + z_{l-1})/2$ of a pressure segment yields coefficients of the influence matrices

$$U_{lk}(t) = \sum_j \sum_m a_{mjk}(t)\ \bar{u}_{mjk}(r_p, z_{cl})\ +\ u_{sk}(r_p, z_{cl})\ \hat{f}_p(t) \qquad (8)$$

$\bar{u}_{mjk}(r_p, z_{cl})$ and $u_{sk}(r_p, z_{cl})$ are modal and static displacement dyads at z_{cl} from the k^{th} pressure segment. Since $\hat{f}_p(t)$ is arbitrary, it was found from numerical experiments that a simple ramp is appropriate

$$\hat{f}_p(t) = (t/\Delta t_1)\left[H(t) - H(t-\Delta t_1)\right] + H(t-\Delta t_1) \qquad (9)$$

where Δt_1 is rise time of the first line segment in the prescribed acceleration profile shown in Fig. 2(c). Enforcing the condition of prescribed displacement $u_p(t)$ at each time step yields a set of simultaneous equations in the weights p_k

$$\sum_{k=1}^{n} U_{lk}(t)\, p_k(t) = u_p(t) \quad , \qquad l = 1, n \tag{10}$$

In the case of time-delayed prescribed displacement where the projectile moves axially varying length of the footprint instantaneously, $\hat{f}_p$ depends not only on time t but also on axial coordinate z in the form

$$\hat{f}_p(\hat{t}) \, , \quad \hat{t} = \left(t - z/V_p\right) H\left(t - z/V_p\right) \tag{11}$$

V_p is projectile speed and $H\left(t - z/V_p\right)$ is the Heaviside function. The significance of (11) is that at some station z, $\hat{f}_p$ acts only when $t \geq z/V_p$ otherwise it vanishes thus the term "time-delayed".

3. Results

In all results to follow, geometric and material properties of the cylinder are listed in Table I. The footprint extends from z_a=0.1″ to z_b=1.6″. The properties in Table I yield extensional and shear wave speeds c_d and c_s 5610 ft/s and 1115 ft/s and the ratio $c_d / c_s \simeq 5$.

Fig. 1 plots prescribed radial motions at the cylinder's inner boundary from a cylindrical projectile with a spherical nose 0.25" in radius and V_p=1000 ft/s. For a moving projectile, prescribed motion starts at one end of the cylinder and moves inward into the cylinder with the speed of the projectile as shown in Fig. 2 for three different projectile axial positions $z = 0, 5\Delta z_p \, , 10\Delta z_p$.

Since the plane-strain cylinder is the simplest example, it is presented first for comparison with the finite length cases. Fig. 3(a-e) plots histories of the plane-strain cylinder for the prescribed motion in Fig. 2 at three radial stations $r = r_p, 2r_p, 4r_p$. At $r = r_p$ (Fig. 3(a)), u follows the prescribed displacement in Fig. 2(a), and du/dt (Fig. 3(b)) follows prescribed velocity in Fig. 2(b). The first reflection from the outer boundary $r = r_o$ happens at $t \approx 80\mu s$ as evidenced by the sudden rise in histories there. At $r = 2r_p$ and $r = 4r_p$, u histories exhibit the time-delay in wave front from propagation with finite speed c_ε. Soon after motion starts, the closeness in magnitude of peak σ_{rr}, $\sigma_{\theta\theta}$ and σ_{zz} (Fig. 3(c,d,e)) implies a hydrodynamic state of stress. Note the sharp rise in stress history at $t \approx 80\mu s$ when the first reflection from $r = r_o$ is felt at the corresponding z.

Fig. 4 plots histories from prescribed motion uniform over the footprint at three different axial stations; z = 0.25", 0.8" and 1.7". The first two stations lie within the length of the footprint l_p=1.5" while the z=1.7" station is outside this interval. In Fig. 4, histories of all dependent variables at each $z-$station lie along a column, while histories of a dependent variable for the three $z-$stations lie along a row. Soon after start of motion, the u histories at z=0.25" and 0.8" in Fig. 4(a1,a2) follow the plane-strain case in Fig. 3(a). However, the first reflection is not accompanied by sharp rises in response as in plane-strain. At z=1.7", u and du/dt response is attenuated as expected since that station is remote from the footprint. Magnitude of the w histories is comparable to those of u at z=0.25". However, w attenuates substantially at the other stations. An explanation is that w motion is controlled by shear waves which for the present material are 5 times weaker than extensional waves controlling u. Soon after start of motion and within the footprint, normal stress

histories (Fig. 4(d1-d3,e1-e3,f1-f3)) resemble those of the plane-strain case in that magnitude of the three stress components is approximately the same implying a hydrostatic state of stress. Agreement of results from plane-strain and finite cylinder with prescribed uniform motion implies that the plane-strain approximation is satisfactory for axial stations within the footprint. Also, magnitude of stress remote from the footprint is comparable to that within the footprint after the initial hydrostatic transient elapses.

Fig. 5 plots histories from time-delayed prescribed motion. The same nomenclature applies as in Fig. 4. Comparing histories of u and du/dt in Fig. 4(a1-a3,b1-b3) and Fig. 5(a1-a3,b1-b3) it is apparent that except for the shifted response at the footprint, magnitude and shape of response are the same. However, magnitude of w histories in Fig. 5(c1-c3) are almost 1/2 those in Fig. 4(c1-c3). This is caused by the reduction in shear in the time-delayed prescribed displacement compared to the uniform case. Comparing stress histories in Fig. 5(d1-d3,e1-e3,f1-f3) and Fig. 4(d1-d3,e1-e3,f1-f3) reveals that soon after start of motion, the time-delayed case looses the initial hydrostatic transient while magnitudes following this transient are comparable. This steep drop in stress across the edges of the footprint is caused by the low shear rigidity of the material consistent with the ratio $c_s/c_d \simeq 1/5$.

Figure 6 plots snap-shots of the deformed cylinder generator for the two types of excitation at 3 times $t = 40\mu s, 80\mu s$ and $110\mu s$. Note the expanding footprint in the case of the time-delayed case (Fig. 6(a2-c2)). Fig. 7 plots instantaneous $\sigma_{rr}(r_p, z; t_o)$ distributions for $10\mu s \le t_o \le 110\mu s$ in intervals of $10\mu s$. In both types of excitation, pressure at the ends of the footprint is higher than that at intermediate stations. For the time delayed excitation, Fig. 7(b) shows the expansion of the footprint with time following prescribed displacement in Fig. 2. The undulation in the $\sigma_{rr}(r_p, z; t_o)$ distribution is an artifact of the finite

number of pressure ring segments dividing the footprint. The distribution becomes smoother as number of ring segments increases.

4 Conclusion

An extension to wave propagation in a hollow cylinder is presented for motion of the excitation along the cylinder's axis. Two types of excitation are considered, a uniform prescribed motion and a time delayed prescribed motion. Noteworthy results are

6) Soon after motion starts, the normal stress state for the plane-strain cylinder and finite cylinder with uniform prescribed displacement is almost hydrostatic. Displacement, velocity and stress responses over the footprint for these two cases are comparable.
7) Response from time-delayed excitation is similar to that from uniform excitation in magnitude and form although the former response does not exhibit the hydrostatic state soon after motion starts.

References

1. M. El-Raheb, Wave propagation in a hollow cylinder due to prescribed velocity at the boundary, to appear in International J. of Solids & Structures, 2005.

Acknowledgement

This work was supported by a grant from DARPA, executed by the U.S. Army Medical Research and Materiel Command/TATRC Contract # W81XWH-04-C-0084.
The views, opinions and/or findings contained in this paper are those of the author and should not be construed as an official Department of the Army position, policy or decision unless so designated by other documentation.

$E \quad (lb/in^2)$	4.5×10^4
$\rho \ (lb\ s^2/in^4)$	8.7×10^{-5}
υ	0.48
$l \quad (in)$	*4*
$r_p \quad (in)$	*0.25*
$r_o \quad (in)$	*3*
$c_d \quad (in/s)$	6.74×10^4
$c_s \quad (in/s)$	1.322×10^4

Table I. Cylinder properties

Figure captions

Figure 1. Prescribed motion
(a) u_p (in) , (b) du_p/dt (ft/s), (c) d^2u_p/dt^2 (ft/s^2)

Figure 2. Delayed prescribed displacement
left line z=0, middle line $z=5\Delta z_p$, right line $z=10\Delta z_p$

Figure 3. Histories of plane-strain cylinder with prescribed displacement
(a) u , (b) du/dt , (c) σ_{rr} , (d) $\sigma_{\theta\theta}$, (e) σ_{zz}

Figure 4. Histories of cylinder with uniform prescribed displacement
(a1) u , (b1) w, (c1) du/dt , (d1) σ_{rr} , (e1) $\sigma_{\theta\theta}$, (f1) σ_{zz} : z=0.25",
(a2) u , (b2) w, (c2) du/dt , (d2) σ_{rr} , (e2) $\sigma_{\theta\theta}$, (f2) σ_{zz} : z=0.8",
(a3) u , (b3) w, (c3) du/dt , (d3) σ_{rr} , (e3) $\sigma_{\theta\theta}$, (f3) σ_{zz} : z=1.7"

Figure 5. Histories of cylinder with delayed prescribed displacement
(a1) u , (b1) w, (c1) du/dt , (d1) σ_{rr} , (e1) $\sigma_{\theta\theta}$, (f1) σ_{zz} : z=0.25",
(a2) u , (b2) w, (c2) du/dt , (d2) σ_{rr} , (e2) $\sigma_{\theta\theta}$, (f2) σ_{zz} : z=0.8",
(a3) u , (b3) w, (c3) du/dt , (d3) σ_{rr} , (e3) $\sigma_{\theta\theta}$, (f3) σ_{zz} : z=1.7"

Figure 6. Time snap-shots of cylinder with prescribed displacement
(a1) t=40 μs , (b1) t=80 μs , (c1) t=110 μs : uniform ,
(a2) t=40 μs , (b2) t=80 μs , (c2) t=110 μs : time-delayed

Figure 7. Snap-shots of $|\sigma_{rr}(r_p, z; t_o)|$ distribution in cylinder with prescribed displacement at $10\mu s \le t_o \le 110\mu s$

(a) uniform : —— top t=10μs, bottom t=110μs
(b) time-delayed : —— far left t=10μs, far right t=110μs

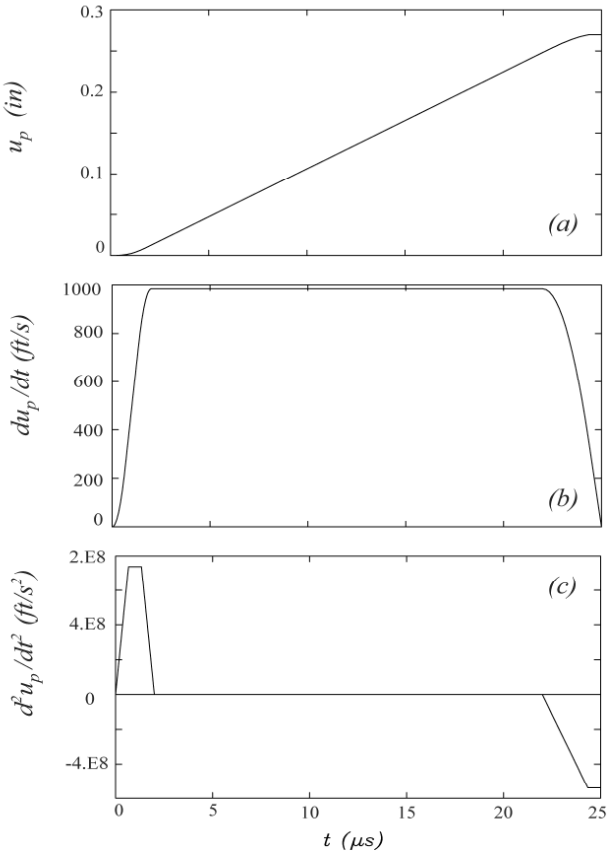

Figure 1. Prescribed motion
(a) u_p (in) , (b) du_p/dt (ft/s), (c) d^2u_p/dt^2 (ft/s^2)

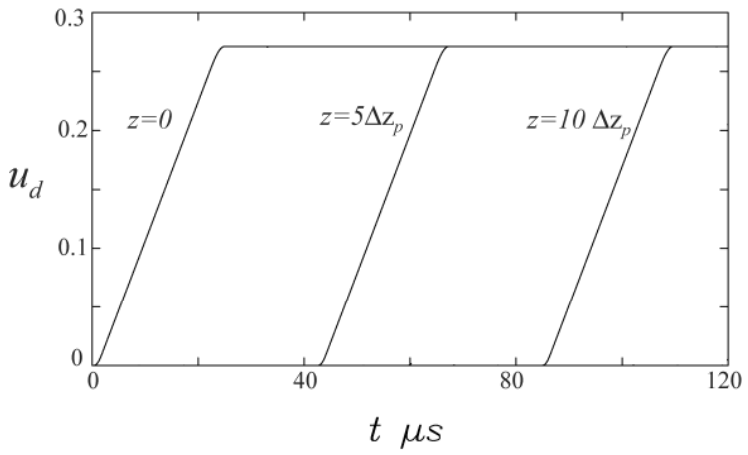

Figure 2. Delayed prescribed displacement
left line z=0, middle line z=5Δz$_p$, right line z=10Δz$_p$

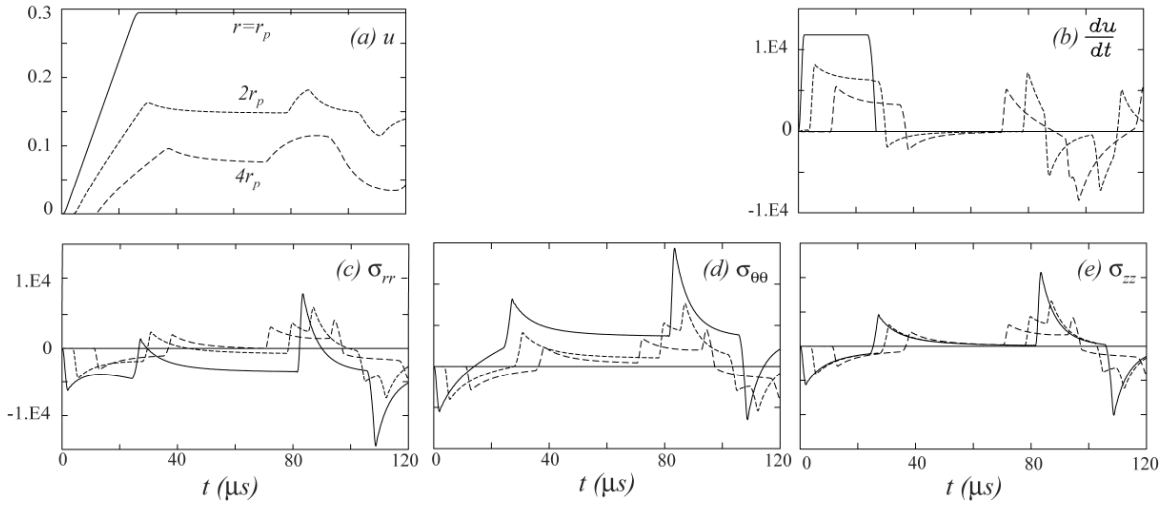

Figure 3. Histories of plane-strain cylinder with prescribed displacement
(a) u , (b) du/dt , (c) σ_{rr} , (d) $\sigma_{\theta\theta}$, (e) σ_{zz}

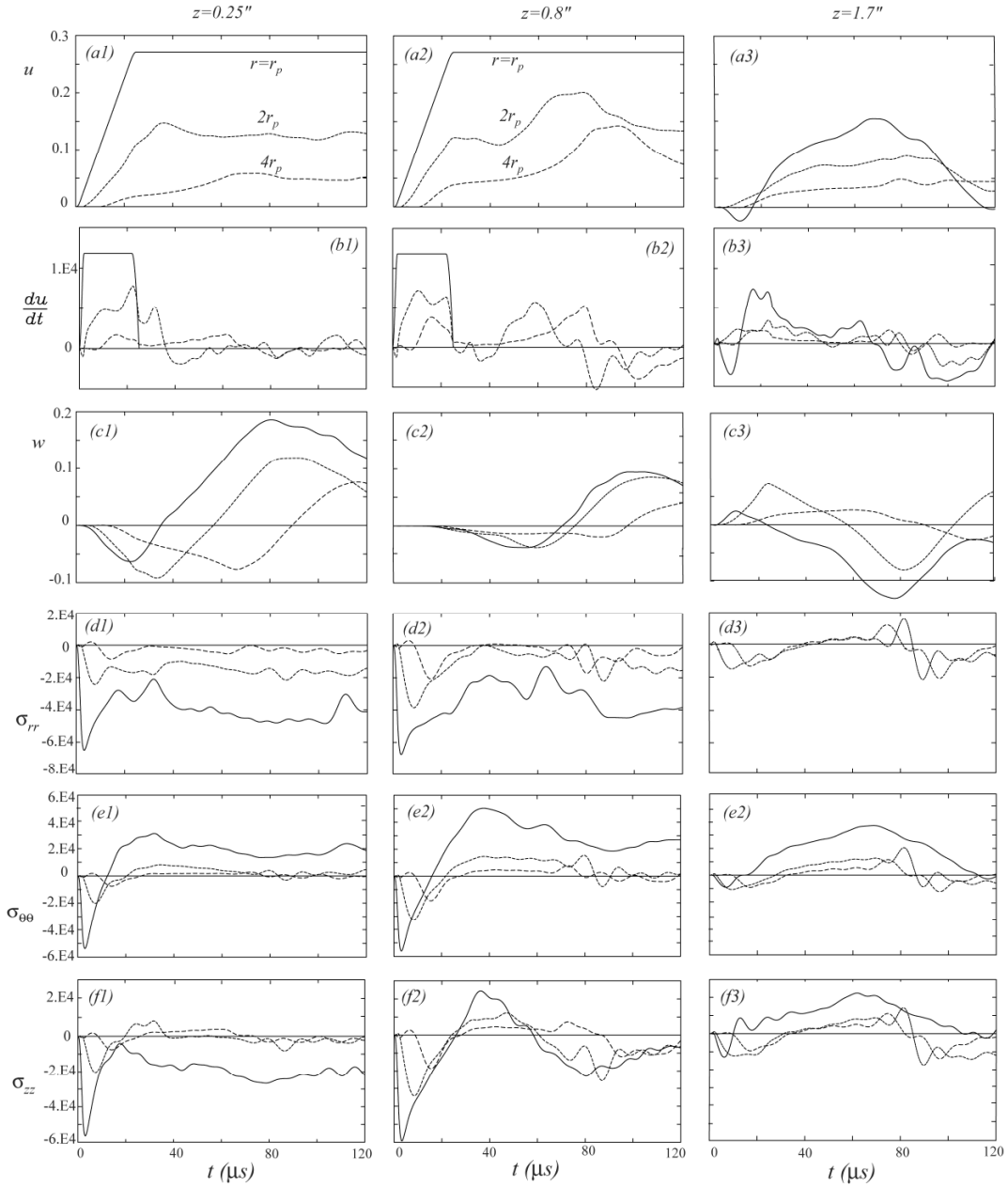

Figure 4. Histories of cylinder with uniform prescribed displacement

(a1) u , (b1) w, (c1) du/dt , (d1) σ_{rr} , (e1) $\sigma_{\theta\theta}$, (f1) σ_{zz} : z=0.25″,

(a2) u , (b2) w, (c2) du/dt , (d2) σ_{rr} , (e2) $\sigma_{\theta\theta}$, (f2) σ_{zz} : z=0.8″,

(a3) u , (b3) w, (c3) du/dt , (d3) σ_{rr} , (e3) $\sigma_{\theta\theta}$, (f3) σ_{zz} : z=1.7″

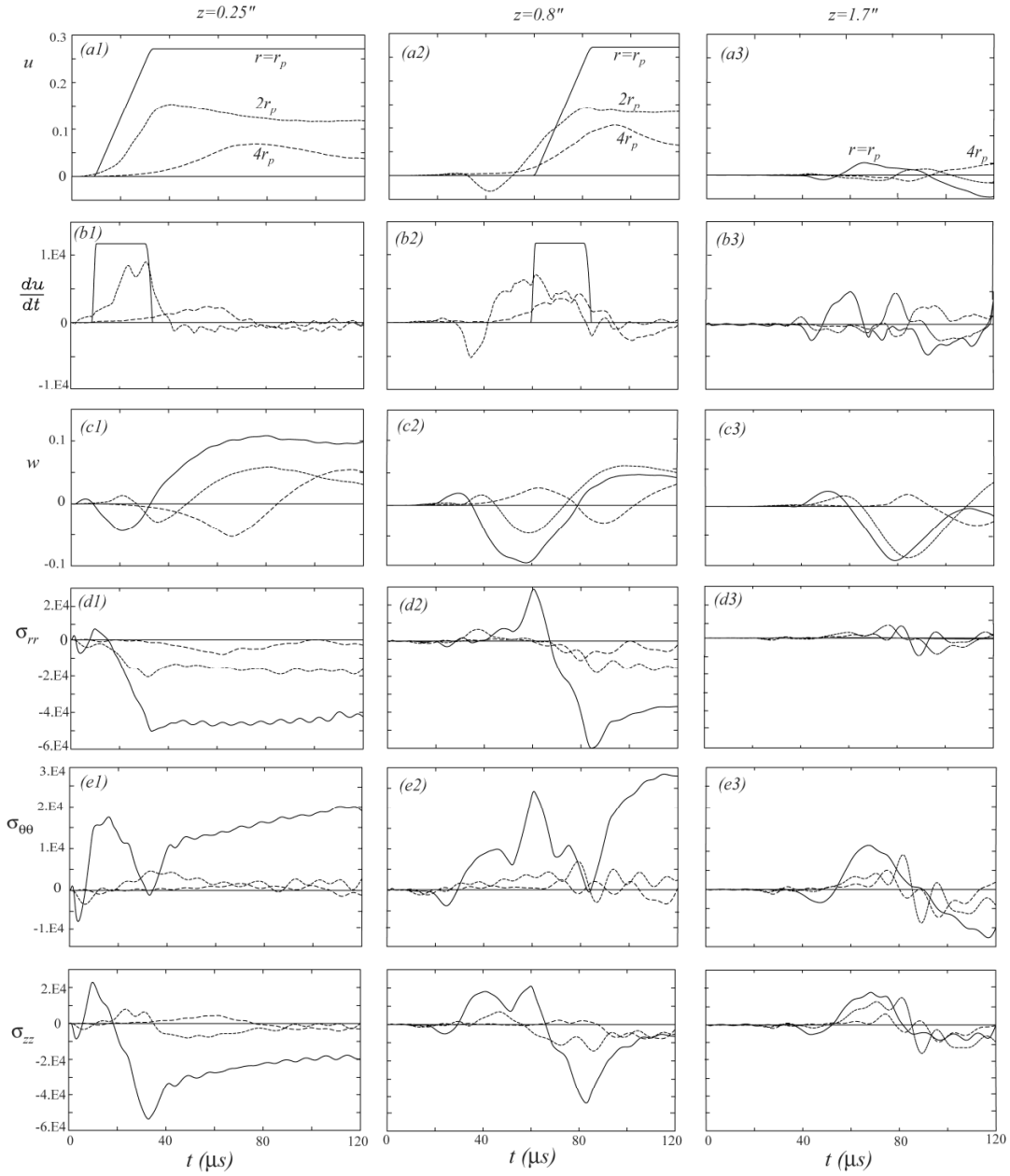

Figure 5. Histories of cylinder with delayed prescribed displacement

(a1) u , (b1) w, (c1) du/dt , (d1) σ_{rr}, (e1) $\sigma_{\theta\theta}$, (f1) σ_{zz} : z=0.25",

(a2) u , (b2) w, (c2) du/dt , (d2) σ_{rr}, (e2) $\sigma_{\theta\theta}$, (f2) σ_{zz} : z=0.8",

(a3) u , (b3) w, (c3) du/dt , (d3) σ_{rr}, (e3) $\sigma_{\theta\theta}$, (f3) σ_{zz} : z=1.7"

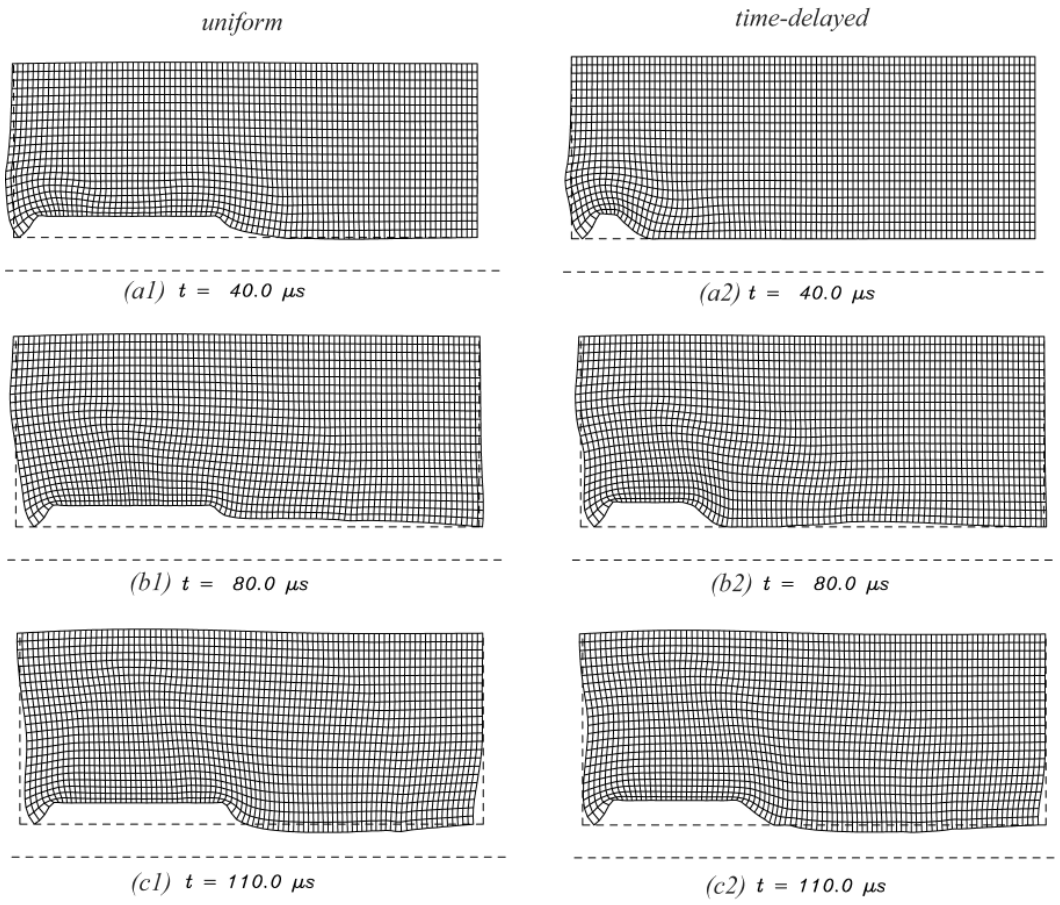

Figure 6. Time snap-shots of cylinder with prescribed displacement
(a1) t=40 μs , (b1) t=80 μs , (c1) t=110 μs : uniform ,
(a2) t=40 μs , (b2) t=80 μs , (c2) t=110 μs : time-delayed

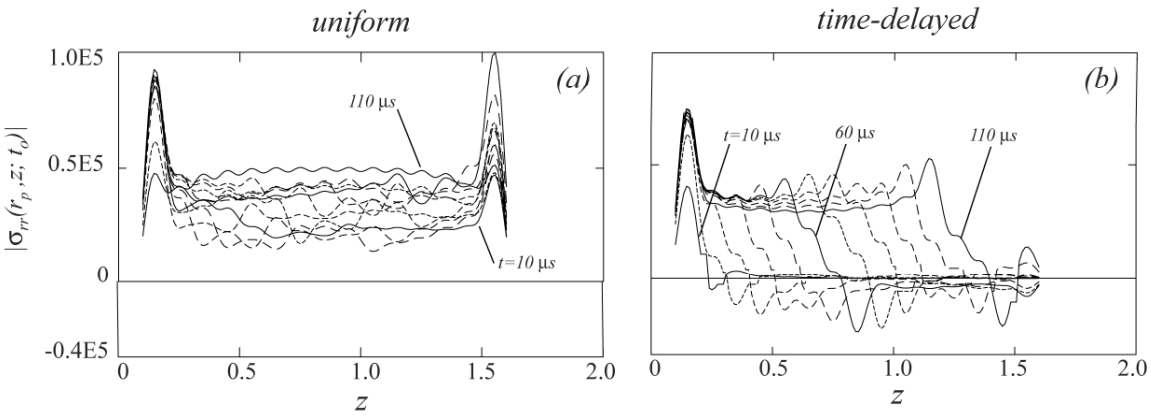

Figure 7. Snap-shots of $|\sigma_{rr}(r_p, z; t_o)|$ distribution in cylinder with prescribed displacement at 10μs <= t_o <= 110μs

(a) uniform : —— top t=10μs, bottom t=110μs

(b) time-delayed : —— far left t=10μs, far right t=110μs

APPENDIX M

Accepted for Publication in the *International Journal of Solids and Structures*

"Transient waves in an inhomogeneous hollow infinite cylinder"

Michael El-Raheb

ATK Mission Research, Laguna Hills, CA

Summary

Effects on transient waves of circumferential and radial inhomogeneity are studied in a plane-strain hollow cylinder. A periodic circumferential inhomogeneity modulating a constant value is analyzed adopting the Galerkin method where trial functions are chosen as the axisymmetric and asymmetric modes of the homogeneous cylinder. A periodic radial inhomogeneity is analyzed by dividing the cylinder into annular segments of constant width. A step-wise variation in modulus is assumed where modulus is constant over each segment. Adopting transfer matrices, continuity of state variables at interfaces of segments establishes the global dynamic equilibrium of the segmented cylinder. The static-dynamic superposition method is employed to solve for transient response.

1. Introduction

Propagation of transient stress waves in human tissue during projectile penetration concerns medical researchers as overpressure from these waves may cause indirect trauma in human organs. As the projectile penetrates into tissue, it moves material by replacing it with its own volume. When tissue fails, it acts more like a fluid, lessening the amount of material being compressed by the moving projectile. In the radial direction, tissue is compressed by an expanding cross-section of the projectile's smoothly curved nose. This rapid expansion generates compressive waves symmetric about the projectile's axis that attenuate with distance. El-Raheb (2004) develops a model that approximates penetrated tissue as a homogeneous hollow finite cylinder with inner radius that of the projectile and a sufficiently large outer radius to avoid interference from reflections at the outer boundary during the simulation time. A radial velocity is prescribed at the cylinder's inner boundary over the finite projectile length accounting for radial expansion from projectile axial motion.

This work evaluates the effect on propagation of material inhomogeneity that may result either from spatial variation in modulus or asymmetric radial tearing. Since real tissue inhomogeneity is complicated to model, the analysis to follow treats two uncoupled types of material inhomogeneity; circumferential or θ-inhomogeneity and radial or r-inhomogeneity. θ-inhomogeneity is asymmetric as modulus E varies periodically with angular coordinate θ but remains constant along the radial coordinate r. In this case both extensional and shear waves are excited. r-inhomogeneity is

axisymmetric as E varies only along r but remains constant along θ. In this case only extensional waves are excited. In practice both θ and r inhomogeneities exist in tissue, nevertheless the two types are presently addressed separately for parametric evaluation of each type's effect avoiding the cross-coupling that may result if both were acting together. Since histories from the homogeneous finite cylinder model (El-Raheb 2004) compared favorably with those from the homogeneous plane-strain model, the latter model is adopted for studying material inhomogeneity.

Whittier and Jones (1967) studied the propagation of longitudinal and torsional waves in a bi-material solid cylinder composed of an inner homogeneous core bonded to an outer homogeneous annular cylinder of different properties. Armenakas (1967), Reuter (1969), Armenakas (1970), studied flexural waves in bi-material cylinders. Keck and Armenakas (1971) presented an exact solution for longitudinal waves in an infinitely long composite hollow cylinder made of three different transversely isotropic layers. Vibrations of homogeneous hollow plane-strain cylinders was analyzed by Gasis (1958), Bird et al (1960), and Baltrukonis et al (1960). The references above were restricted to three concentric axisymmetric layers. Yin and Yue (2002) analyzed the plain-strain axisymmetric problem with multiple annular layers using Laplace transforms to integrate time dependence. Heyliger and Jilania (1992) adopted a variational method and a Ritz approximation to study frequency response of inhomogeneous cylinders and spheres. Steinberg (1995) formulated the inverse spectral problem to determine properties of a cylinder with inhomogeneous materials. Inertial θ-inhomogeneity from

point masses attached to the wall of a thin cylinder was analyzed by El-Raheb and Wagner (1989).

In section 2, θ-inhomogeneity is treated adopting the Galerkin method. Eigenfunctions of the asymmetric homogeneous dynamic equations are utilized as trial functions in the inhomogeneous dynamic equations. Orthogonality of radial and circumferential dependence produces an eigenvalue problem with coupling coefficients as the eigenvector. The static-dynamic superposition method is adopted to solve the transient response. In section 3, a step-wise r-inhomogeneity is treated adopting transfer matrices of annular segments with varying properties. Continuity of stress and displacement at interfaces of segments yields a global transfer matrix producing eigenstates of the multi-layered cylinder. Once more, transient response is found adopting the static-dynamic superposition method. Section 4 discusses transient histories in hollow cylinders with the two types of inhomogeneity.

2. Circumferential inhomogeneity

Consider the plane-strain dynamic equilibrium equations in cylindrical coordinates

$$\begin{aligned} &\partial_r \sigma_{rr} + \left(\sigma_{rr} - \sigma_{\theta\theta}\right)/r + 1/r\ \partial_\theta \tau_{r\theta} = \rho\, \partial_{tt}\, u \\ &\partial_r \tau_{r\theta} + 2\tau_{r\theta}/r + 1/r\ \partial_\theta \sigma_{\theta\theta} = \rho\, \partial_{tt}\, \upsilon \\ &r_p \le r \le r_o\ ,\ \ 0 \le \theta \le 2\pi \end{aligned} \tag{1a}$$

with boundary conditions

$$\begin{aligned} &\sigma_{rr}(r_p,\theta;t) = p_0\ f_p(t)\ , \quad \tau_{r\theta}(r_p,\theta;t) = 0 \\ &\sigma_{rr}(r_o,\theta;t) = 0 \qquad , \quad \tau_{r\theta}(r_o,\theta;t) = 0 \end{aligned} \tag{1b}$$

r_p and r_o are cylinder inner and outer radii, $\sigma_{rr},\sigma_{\theta\theta},\tau_{r\theta}$ are normal and shear stresses, (r,θ) are radial and circumferential coordinates, (u,υ) are corresponding displacements, ρ is density, t is time, p_0 is magnitude of uniform pressure applied at $r = r_p$ and $f_p(t)$ is its time dependence. The constitutive relations are

$$\sigma_{ii} = \lambda\,\Delta + 2\,\mu\,\varepsilon_{ii}\ , \quad ii \equiv rr,\ \theta\theta,\ zz$$
$$\Delta = \varepsilon_{rr} + \varepsilon_{\theta\theta}\ , \quad \varepsilon_{zz} = 0 \qquad (2a)$$
$$\sigma_{ij} = \mu\,\varepsilon_{ij}\ , \quad ij \equiv r\theta,\ \theta z,\ zr$$

$$\varepsilon_{rr} = \partial_r u\ ,\ \varepsilon_{\theta\theta} = u/r + 1/r\ \partial_\theta \upsilon\ ,\ \varepsilon_{zz} = 0$$
$$\varepsilon_{r\theta} = 1/r\ \partial_\theta u\ +\ \partial_r \upsilon\ -\upsilon/r \qquad (2b)$$

(λ, μ) are the $Lame'$ constants. For the homogeneous medium, substituting (2b) in (2a) then in (1a) yields the dynamic displacement equations

$$\mu\left(D_{11}\ u + D_{12}\ \upsilon\right) = \rho\,\partial_{tt} u$$
$$\mu\left(D_{21}\ u + D_{22}\ \upsilon\right) = \rho\,\partial_{tt}\upsilon \qquad (3)$$

$$D_{11} \equiv \left[(\beta+2)\hat{\nabla}_1^2 + 1/r^2\partial_{\theta\theta}\right], \qquad D_{12} \equiv 1/r\ \partial_\theta\left[(\beta+1)\partial_r - (\beta+3)/r\right]$$
$$D_{21} \equiv 1/r\ \partial_\theta\left[(\beta+1)\partial_r + (\beta+3)/r\right], \quad D_{22} \equiv \left[\hat{\nabla}_1^2 + (\beta+2)/r^2\partial_{\theta\theta}\right]$$
$$\hat{\nabla}_1^2 \equiv \partial_{rr} + 1/r\,\partial_r - 1/r^2\ , \quad \beta = \lambda/\mu = 2\nu/(1-2\nu)$$

ν is Poisson ratio. Eq. (3) is the limiting case of Eq. (A1) in Appendix A when the z dependence vanishes.

Assume a circumferentially inhomogeneous modulus $\mu(\theta)$ symmetric about $\theta = 0$ with a Fourier expansion

$$\mu(\theta) = \mu_0 \sum_{l=0}^{N_E} e_l\, C_l(\theta)\ , \qquad S_l(\theta) = \sin(l\theta),\ C_l(\theta) = \cos(l\theta) \qquad (4)$$

Substituting (4) in (2a,b) then in (1a) produces the equations

$$\sum_{l=0} e_l\, C_l(\theta)\ \mu_0\left(D_{11}\ u + D_{12}\ \upsilon\right) + \sum_{l=1} e_l\, l\ S_l(\theta)\ \mu_0\left(\tilde{D}_{11} u + \tilde{D}_{12}\upsilon\right) = \rho\,\partial_{tt} u \qquad (5a)$$

$$\sum_{l=0} e_l\, C_l(\theta)\ \mu_0\left(D_{21}\ u + D_{22}\ \upsilon\right) + \sum_{l=1} e_l\, l\ S_l(\theta)\ \mu_0\left(\tilde{D}_{21} u + \tilde{D}_{22}\upsilon\right) = \rho\,\partial_{tt}\upsilon \qquad (5b)$$

$$\tilde{D}_{11} \equiv -1/r^2\,\partial_\theta \qquad , \quad \tilde{D}_{12} \equiv -1/r\,\partial_r + 1/r^2$$
$$\tilde{D}_{21} \equiv -\beta/r\,\partial_r\ - (\beta+2)/r^2 \quad , \quad \tilde{D}_{22} \equiv -(\beta+2)/r^2\ \partial_\theta$$

To solve (5), the Galerkin method is adopted. u and υ are expanded in terms of orthogonal trial functions satisfying the boundary conditions at the inner and outer walls of the cylinder $r = r_p$ and $r = r_o$. One admissible set is the eigenfunctions of the homogeneous problem in Eq.(3) with $\mu = \mu_0$ the axisymmetric term in the $\mu(\theta)$ expansion (4). For harmonic motions in time with radian frequency ω and periodicity along θ, the solution to (1a) is

$$\begin{aligned} u(r,\theta,t) &= \left(u_1(r,\theta) + u_2(r,\theta)\right)e^{i\omega t} \\ \upsilon(r,\theta,t) &= \left(\upsilon_1(r,\theta) + \upsilon_2(r,\theta)\right)e^{i\omega t} \end{aligned} \tag{6a}$$

$$\begin{aligned} u_1 &= \sum_{n=0}\left\{c_{11n}\,k_{re}\left(n\,J_n(k_{re}r)/(k_{re}r) - J_{n+1}(k_{re}r)\right) + c_{12n}\,n\,J_n(k_{rs}r)/r\right\} C_n(\theta) \\ \upsilon_1 &= \sum_{n=0}\left\{-c_{11n}\,n\,J_n(k_{re}r)/r - c_{12n}\,k_{rs}\left(n\,J_n(k_{rs}r)/(k_{rs}r) - J_{n+1}(k_{rs}r)\right)\right\} S_n(\theta) \\ S_n(\theta) &= \sin(n\theta),\ C_n(\theta) = \cos(n\theta) \end{aligned} \tag{6b}$$

(u_1, υ_1) are derived in Eq. (B1) of Appendix B, and (u_2, υ_2) have the same form as (u_1, υ_1) with $J_n(kr)$ replaced by $Y_n(kr)$ and (c_{21n}, c_{22n}) replacing (c_{11n}, c_{12n}). Expressions for $\sigma_{rr}, \tau_{r\theta}$ similar to those for displacement in (6a) and (6b) can be expressed as

$$\begin{aligned} \sigma_{rr}(r,\theta,t) &= \left(\sigma_{rr1}(r,\theta) + \sigma_{rr2}(r,\theta)\right)e^{i\omega t} \\ \tau_{r\theta}(r,\theta,t) &= \left(\tau_{r\theta1}(r,\theta) + \tau_{r\theta2}(r,\theta)\right)e^{i\omega t} \end{aligned} \tag{7a}$$

$$\begin{aligned} \sigma_{rr1} = \mu\sum_{n=0}\Big\{ & c_{11n}\left(\left(-(\beta+2)(k_{re}r)^2 + 2(n^2-n)\right)J_n(k_{re}r)/r^2 + 2k_{re}\,J_{n+1}(k_{re}r)/r\right) \\ & + 2\,c_{12n}\left((n^2-n)J_n(k_{rs}r)/r^2 - n\,k_{rs}\,J_{n+1}(k_{rs}r)/r\right)\Big\}\ C_n(\theta) \end{aligned} \tag{7b}$$

$$\begin{aligned} \tau_{r\theta1} = \mu\sum_{n=0}\Big\{ & 2c_{11n}\left(-(n^2-n)J_n(k_{re}r)/r^2 + n\,k_{re}\,J_{n+1}(k_{re}r)/r\right) \\ & - 2c_{12n}\left(\left(n^2 - n - (k_{rs}r)^2/2\right)J_n(k_{rs}r)/r^2 + k_{rs}\,J_{n+1}(k_{rs}r)/r\right)\Big\}\ S_n(\theta) \end{aligned} \tag{7c}$$

($\sigma_{rr1}, \tau_{r\theta 1}$) are derived in Eq. (B2) of Appendix B, (k_{re}, k_{rs}) are radial wave numbers defined in Eq. (B1) of Appendix B. ($\sigma_{rr2}, \tau_{r\theta 2}$) have the same form as ($\sigma_{rr1}, \tau_{r\theta 1}$) with $J_n(kr)$ replaced by $Y_n(kr)$ and (c_{11n} , c_{12n}) replaced by (c_{21n} , c_{22n}). Re-write (7a) in the form

$$\mathbf{S}(r,\theta,t) \equiv \left\{\sigma_{rr}\,,\,\tau_{r\theta}\right\}^T = \sum_{n=0} \mathfrak{Y}_n(\theta)\;\bar{\mathbf{B}}_n(r)\;\mathbf{c}_n\;e^{i\omega t}$$
$$\mathfrak{Y}_n(\theta) = \begin{vmatrix} C_n(\theta) & 0 \\ 0 & S_n(\theta) \end{vmatrix} \qquad (8)$$

$\bar{\mathbf{B}}_n(r)$ is a 2×4 matrix of the radial functions in (σ_{rr} , $\tau_{r\theta}$) multiplying $\mathbf{c}_n = \left\{c_{11n}, c_{12n}, c_{21n}, c_{22n}\right\}^T$ in (7b,c). The homogeneous boundary conditions (1a) are

$$\sigma_{rr}(r_p) = 0\,, \quad \sigma_{rr}(r_o) = 0 \qquad (9a)$$

$$\tau_{r\theta}(r_p) = 0\,, \quad \tau_{r\theta}(r_o) = 0 \qquad (9b)$$

Substituting (8) in (9a,b) and enforcing orthogonality of the θ dependence yields a set of uncoupled eigenvalue problems for each circumferential wave number n

$$\mathbf{B}_n\,\mathbf{c}_n = \mathbf{0} \quad , \quad \mathbf{B}_n = \begin{bmatrix} \bar{\mathbf{B}}_n(r_p) \\ \bar{\mathbf{B}}_n(r_o) \end{bmatrix}$$
$$\Rightarrow \det|\mathbf{B}_n| = 0 \;\Rightarrow\; \left\{\varphi(r)\,,\,\psi(r)\,;\,\omega\right\}_{mn} \qquad (10)$$

$\mathbf{B}_n$ is a 4×4 matrix, $\left\{\varphi(r), \psi(r)\right\}_{mn}$ are the displacement eigenfunctions, ω_{mn} are the eigenvalues, and m is radial wave number. In what follows $\varphi_{mn}(r)$ and $\psi_{mn}(r)$ will be written as φ_{mn} and ψ_{mn} for shortness since it is known that they are functions of r only. Expand (u , v) in the eigenfunctions (9)

$$u(r,\theta,t) = \sum_{n=0}\sum_{m=1} a_{mn}(t)\ \varphi_{mn}\ C_n(\theta)$$
$$\upsilon(r,\theta,t) = \sum_{n=1}\sum_{m=1} a_{mn}(t)\ \psi_{mn}\ S_n(\theta) \qquad (11)$$

Substituting (11) in (5a,b) yields

$$\mu_0 \sum_{l=0} e_l C_l(\theta)\ \sum_{k=0}\sum_{j=1} a_{jk}(t)\left(D_{11}^{(r)}\ \varphi + D_{12}^{(r)}\ \psi\right)_{jk} C_k(\theta)$$
$$+\mu_0 \sum_{l=1} e_l\ l\ S_l(\theta) \sum_{k=1}\sum_{j=1} a_{jk}(t)\left(\tilde{D}_{11}^{(r)}\ \varphi + \tilde{D}_{12}^{(r)}\ \psi\right)_{jk} S_k(\theta) \qquad (12a)$$
$$= \rho \sum_{n=0}\sum_{m=1} \ddot{a}_{mn}(t)\varphi_{mn}\ C_n(\theta)$$
$$S_k(\theta) = \sin(k\theta),\ \ C_k(\theta) = \cos(k\theta)$$

$$\mu_0 \sum_{l=0} e_l\ C_l(\theta)\ \ \sum_{k=1}\sum_{j=1} a_{jk}(t)\left(D_{21}^{(r)}\ \varphi + D_{22}^{(r)}\ \psi\right)_{jk} S_k(\theta)$$
$$+\mu_0 \sum_{l=1} e_l\ l\ S_l(\theta) \sum_{k=0}\sum_{j=1} a_{jk}(t)\left(\tilde{D}_{21}^{(r)}\ \varphi + \tilde{D}_{22}^{(r)}\ \psi\right)_{jk} C_k(\theta) \qquad (12b)$$
$$= \rho \sum_{n=1}\sum_{m=1} \ddot{a}_{mn}(t)\psi_{mn}\ S_n(\theta)$$

In (12a,b) the operators $D_{ij}^{(r)}$ are the same as D_{ij} in (5) with the θ dependence eliminated, and $(\dot{\ })$ is derivative with respect to t. From Eq.(3), noting that

$$\left(D_{11}^{(r)}\ \varphi + D_{12}^{(r)}\ \psi\right)_{jk} = -\rho / \mu_0\ \omega_{jk}^2\ \varphi_{jk}$$
$$\left(D_{21}^{(r)}\ \varphi + D_{22}^{(r)}\ \psi\right)_{jk} = -\rho / \mu_0\ \omega_{jk}^2\ \psi_{jk} \qquad (13)$$

reduces (12) to

$$-\sum_{l=0} e_l\ C_l(\theta) \sum_{k=0}\sum_{j=1} \omega_{jk}^2\ a_{jk}(t)\ \varphi_{jk} C_k(\theta)$$
$$-\mu_0 / \rho \sum_{l=1} e_l\ l\ S_l(\theta) \sum_{k=1}\sum_{j=1} a_{jk}(t)\ \left(-n\varphi_{jk} / r^2\ -\ \psi_{jk} / r^2\ + \psi'_{jk} / r\right) S_k(\theta) \qquad (14a)$$
$$= \sum_{n=0}\sum_{m=1} \ddot{a}_{mn}(t)\varphi_{mn} C_n(\theta)$$

$$-\sum_{l=0} e_l C_l(\theta) \sum_{k=1}\sum_{j=1} \omega_{jk}^2\, a_{jk}(t)\, \psi_{jk} S_k(\theta)$$

$$-\mu_0/\rho \sum_{l=1} e_l\, l\, S_l(\theta) \sum_{k=0}\sum_{j=1} a_{jk}(t) \left(\beta\, \varphi'_{jk}/r + (\beta+2)\varphi_{jk}/r^2 + n(\beta+2)\,\psi_{jk}/r^2\right) C_k(\theta) \qquad \text{(14b)}$$

$$= \sum_{n=1}\sum_{m=1} \ddot{a}_{mn}(t)\psi_{mn} S_n(\theta)$$

For each (m,n) dyad, multiplying both sides of Eq. (14a) by $\varphi_{mn}\cos(n\theta)$ and both sides of (14b) by $\psi_{mn}\sin(n\theta)$, integrating over the domain $r_p \le r \le r_o$, $0 \le \theta \le 2\pi$ then adding the two resulting equations produces

$$(1+\delta_{n0})\,\pi\, N_{mn}\; \ddot{a}_{mn}(t) + \sum_{k=0}\sum_{j=1}\left[\Theta^{(1)}_{nk}\, R^{(1)}_{mn,\,jk} + \Theta^{(2)}_{nk}\, R^{(2)}_{mn,\,jk}\right] \omega_{jk}^2\; a_{jk}(t)$$
$$+\; \mu_0/\rho \sum_{k=0}\sum_{j=1}\left[\Theta^{(3)}_{nk}\, R^{(3)}_{mn,\,jk} + \Theta^{(4)}_{nk}\, R^{(4)}_{mn,\,jk}\right] a_{jk}(t) \;=\; 0 \qquad \text{(15a)}$$

$$N_{mn} = \int_{r_p}^{r_o} \left(\varphi_{mn}^2 + \psi_{mn}^2\right) r\, dr, \quad n = 0,1,..,N_\theta \;\;,\;\; m = 1,2,..,N_r$$

$$\Theta^{(1)}_{nk} = \sum_{l=0} e_l \int_0^{2\pi} C_l(\theta)\, C_k(\theta)\, C_n(\theta)\, d\theta \;,\quad \Theta^{(2)}_{nk} = \sum_{l=0} e_l \int_0^{2\pi} C_l(\theta)\, S_k(\theta)\, S_n(\theta)\, d\theta$$
$$\Theta^{(3)}_{nk} = \sum_{l=1} e_l\; l \int_0^{2\pi} S_l(\theta)\, S_k(\theta)\, C_n(\theta)\, d\theta \;,\quad \Theta^{(4)}_{nk} = \sum_{l=1} e_l\; l \int_0^{2\pi} S_l(\theta)\, C_k(\theta)\, S_n(\theta)\, d\theta \qquad \text{(15b)}$$

$$R^{(1)}_{mn,\,jk} = \int_{r_p}^{r_o} \varphi_{mn}\; \varphi_{jk}\; r\; dr \;,\quad R^{(2)}_{mn,\,jk} = \int_{r_p}^{r_o} \psi_{mn}\; \psi_{jk}\; r\; dr$$
$$R^{(3)}_{mn,\,jk} = \int_{r_p}^{r_o} \varphi_{mn} \left(-k\,\varphi_{jk}/r^2 - \psi_{jk}/r^2 + \psi'_{jk}/r\right) r\; dr \qquad \text{(15c)}$$
$$R^{(4)}_{mn,\,jk} = \int_{r_p}^{r_o} \psi_{mn} \left(\beta\; \varphi'_{jk}/r + (\beta+2)\; \varphi_{jk}/r^2 + k\,(\beta+2)\; \psi_{jk}/r^2\right) r\; dr$$

δ_{n0} is the Kronecker delta and $(\,)'$ is derivative w.r.t. r. In arriving at (14a) the orthogonality of $(\varphi_{mn}\,, \psi_{mn})$ was utilized. For a homogeneous

material, $\Theta^{(3)}_{nk} = \Theta^{(4)}_{nk} = 0$, $\Theta^{(1)}_{nk} = \Theta^{(2)}_{nk} = (1+\delta_{n0})\,\pi$ and $R^{(1)}_{mn,jk} + R^{(2)}_{mn,jk} = N_{mn}\,\delta_{mj}\,\delta_{nk}$ reducing (11a) to the simple form

$$\ddot{a}_{mn}(t) + \omega^2_{mn}\,a_{mn}(t) = 0 \tag{16}$$

To diagonalize (14a), form the coupled eigenproblem

$$\begin{aligned} &\left[\mathbf{K}_c - \mathbf{M}_c\omega_c^2\right]\mathbf{a} = \mathbf{0} \quad , \quad \mathbf{a} = \left\{a_{mn}\right\}^T \\ &K_{c\,mn,jk} = \omega^2_{jk}\left[\Theta^{(1)}_{nk}\,R^{(1)}_{mn,jk} + \Theta^{(2)}_{nk}\,R^{(2)}_{mn,jk}\right] + \mu_0/\rho\left[\Theta^{(3)}_{nk}\,R^{(3)}_{mn,jk} + \Theta^{(4)}_{nk}\,R^{(4)}_{mn,jk}\right] \\ &M_{c\,mn,jk} = (1+\delta_{n0})\,\pi\,N_{mn}\,\delta_{mj}\,\delta_{nk} \end{aligned} \tag{17}$$

$\mathbf{K}_c$ is a stiffness matrix of order $(N_r\,N_\theta)\times(N_r\,N_\theta)$, $\mathbf{M}_c$ is a diagonal mass matrix of the same order. The eigenproblem (13) yields the orthogonal eigenset $\left\{\mathbf{\Phi}_{ci}(r,\theta)\,;\,\omega_{ci}\right\}$ where $\mathbf{\Phi}_{ci}(r,\theta)$ is the i^{th} eigenvector coupling the constituent modes $\left\{\varphi_{mn}\,,\,\psi_{mn}\right\}$ by the coupling coefficients $\left\{a_{mn,i}\right\}^T$, and ω_{ci} are the corresponding eigen-frequencies. The coupled state vector $\mathbf{S}_c = \left\{u_c,\,v_c,\,\sigma_{rrc},\,\sigma_{\theta\theta c},\,\sigma_{zzc},\,\tau_{r\theta c}\right\}^T$ can be expanded in terms of $\mathbf{\Phi}_{ci}(r,\theta)$ as

$$\mathbf{S}_c(r,\theta;t) = \sum_i c_i(t)\;\mathbf{\Phi}_{ci}(r,\theta) \tag{18a}$$

$$\begin{aligned} &\mathbf{\Phi}_{cl}(r,\theta) = \sum_n\sum_m a_{mn,l}\,\mathbf{S}_{mn}(r,\theta) \\ &\mathbf{\Phi}_{ci}(r,\theta) = \left\{\bar{u}_c,\,\bar{v}_c,\,\bar{\sigma}_{rrc},\,\bar{\sigma}_{\theta\theta c},\,\bar{\sigma}_{zzc},\,\bar{\tau}_{r\theta c}\right\}^T_i \end{aligned} \tag{18b}$$

$\mathbf{S}_{mn}$ is the state eigenvector of the $(m,n)^{th}$ constituent mode and $\bar{u}_{ci}\,,\,\bar{v}_{ci}\,,...,\,\bar{\tau}_{r\theta ci}$ are components of the i^{th} coupled eigenvector $\mathbf{\Phi}_{ci}(r,\theta)$.

Express displacement $\mathbf{u}(r,\theta;t)$ as a superposition of two terms

$$\mathbf{u}(r,\theta;t) = \mathbf{u}_s(r,\theta)\;f_p(t) \;+\; \mathbf{u}_d\,(r,\theta;t) \tag{19}$$

$\mathbf{u}_s(r,\theta)$ is static displacement vector satisfying (5) with vanishing time dependence and boundary conditions (1b) with $f_p(t)=1$ (see Appendix C), $\mathbf{u}_d(r,\theta;t)$ is dynamic displacement vector satisfying (5) and boundary conditions (1b) with $f_p(t)=0$

$$u_s(r,\theta)=u_{s0}(r)+\sum_{n=0}U_{sn}C_n(\theta)\,,\quad \upsilon_s(r,\theta)=\sum_{n=0}V_{sn}S_n(\theta)$$
$$U_{sn}=\sum_{m=1}b_{mn}\,\varphi_{mn}\quad,\ V_{sn}=\sum_{m=1}b_{mn}\,\psi_{mn} \tag{20}$$

$u_{s0}(r)$ is the axisymmetric radial displacement satisfying the inhomogeneous boundary condition (1b) with $f_p(t)=1$ (see Appendix C). Expand $\mathbf{u}_d(r,\theta;t)$ in the eigenfunctions $(\bar{u}_{ci},\bar{\upsilon}_{ci})$

$$u_d(r,\theta;t)=\sum_i c_i(t)\;\bar{u}_{ci}(r,\theta)\;,\quad \bar{u}_{ci}(r,\theta)=\sum_{n=0}\sum_{m=1}a_{mn,i}\;\varphi_{mn}\;C_n(\theta)$$
$$\upsilon_d(r,\theta;t)=\sum_i c_i(t)\;\bar{\upsilon}_{ci}(r,\theta)\,,\quad \bar{\upsilon}_{ci}(r,\theta)=\sum_{n=1}\sum_{m=1}a_{mn,i}\;\psi_{mn}\;S_n(\theta) \tag{21}$$

$c_i(t)$ is generalized coordinate of the i^{th} coupled eigenfunction. Substituting (19),(20) and (21) in (5) and enforcing orthogonality of the $\{\bar{u}_{ci},\bar{\upsilon}_{ci}\}$ set yields uncoupled equations in $c_i(t)$

$$\ddot{c}_i(t)+\omega_{ci}^2\,c_i(t)=\bar{f}_i(t) \tag{22a}$$

$$\bar{f}_i(t) = N_{si}\ \ddot{f}_p(t) / N_{ii}$$

$$N_{ii} = \int_0^{2\pi}\int_{r_p}^{r_o}\left(\bar{u}_{ci}^2 + \bar{\upsilon}_{ci}^2\right)\ r\ dr\, d\theta\ = \pi\sum_{n=0}(1+\delta_{n0})\int_{r_p}^{r_o}\left(U_{n,i}^2 + V_{n,i}^2\right)\ r\ dr$$

$$N_{si} = \int_0^{2\pi}\int_{r_p}^{r_o}\left(\bar{u}_{ci}\ u_s\ +\ \bar{\upsilon}_{ci}\ \upsilon_s\right) r\ dr\, d\theta \qquad (22b)$$

$$= 2\pi\int_{r_p}^{r_o}\left(U_{s0} + u_{s0}\right)\ U_{0,i}\, r\ dr\ + \pi\sum_{n=1}\int_{r_p}^{r_o}\left(U_{n,i}\ U_{sn} + V_{n,i}\ V_{sn}\right)\ r\ dr$$

$$U_{n,i} = \sum_{m=1} a_{mn,i}\,\varphi_{mn}\quad ,\ V_{n,i} = \sum_{m=1} a_{mn,i}\,\psi_{mn}$$

b_{mn} are coupling coefficients of the coupled static solution. Eq. (22a) admits the solution

$$c_i(t) = -\frac{1}{\omega_{ci}}\int_0^t \sin\omega_{ci}(t-\tau)\ \bar{f}_i(\tau)\ d\tau \qquad (23a)$$

If $f_p(t)$ is piecewise linear with n_s conjoined segments

$$f_p(t) = \sum_{j=1}^{n_s}\left(\alpha_j + \beta_j\,(t-t_j)\right)\left[H(t-t_j) - H(t-t_{j+1})\right]$$

$$\beta_j = \left(f_p(t_{j+1}) - f_p(t_j)\right)/\left(t_{j+1} - t_j\right),\quad \alpha_j = f_p(t_j)\ ,\ \ t_1 = f_p(t_1) = 0 \qquad (23b)$$

$$\ddot{f}_p(t) = \beta_1\delta(t) - \beta_{n_s}\delta(t - t_{n_s+1}) + \sum_{j=1}^{n_s-1}\left(\beta_{j+1} - \beta_j\right)\delta(t - t_{j+1})$$

then (23a) can be integrated analytically with an accuracy independent of the time interval.

3. Radial inhomogeneity

Consider a step-wise radial variation in modulus as follows. Divide the region $r_p \le r \le r_o$ into N_r equidistant annular segments

$$r_j \le r \le r_{j+1}\quad ,\quad j = 1,\ldots, N_r$$
$$\Delta r = \Delta r_j = r_{j+1} - r_j\ = (r_o - r_p)/N_r \qquad (24)$$

Assume that $\mathbf{c}_j = \{c_{1j}, c_{2j}\}^T$ is constant over each segment but varies from segment to segment. Since axial symmetry holds, the following equation applies to the j^{th} segment

$$(\lambda + 2\mu)_j \left(\partial_{rr} + 1/r\,\partial_r - 1/r^2\right) u_j = \rho\,\partial_{tt} u_j \tag{25}$$

For harmonic motions in time with radian frequency ω, Eq. (25) admits the solution for the j^{th} segment

$$\begin{aligned} &u_j(r,t) = \bar{u}_j(r) e^{i\omega t}, \quad \bar{u}_j(r) = c_{1j}\ J_1(k_{ej}\, r) + c_{2j}\ Y_1(k_{ej}\, r) \\ &k_{ej} = \omega / c_{ej} \quad , \quad c_{ej}^2 = (\lambda + 2\mu)_j / \rho \end{aligned} \tag{26}$$

Substituting (26) in the constitutive relations (2a,b) yields

$$\begin{aligned} \bar{\sigma}_{rrj} = {} & \mu_j c_{1j} \left(-(\beta+2)\ k_{ej}\ J_0(k_{ej}\, r) + \ 2\, J_1(k_{ej}\, r)/r\right) \\ & + \mu_j c_{2j} \left(-(\beta+2)\ k_{ej}\ Y_0(k_{ej}\, r) + \ 2\, Y_1(k_{ej}\, r)/r\right) \end{aligned} \tag{27}$$

For each annular segment, express the state vector $\mathbf{S}_j = \{\bar{\sigma}_{rrj}, \bar{u}_j\}^T$ in terms of the constant vector $\mathbf{c}_j = \{c_{1j}, c_{2j}\}^T$

$$\mathbf{S}_j(r) = \mathbf{B}_j(r)\ \mathbf{c}_j \tag{28}$$

$\mathbf{B}_j(r)$ is a matrix with coefficients the functions multiplying (c_{1j}, c_{2j}) in (26) and (27). Evaluating (28) at the two ends of the j^{th} segment then eliminating $\mathbf{c}_j$ determines the (2x2) transfer matrix $\mathbf{T}_j$ relating state vectors at the ends of a segment

$$\mathbf{S}_j(r_{j+1}) = \mathbf{T}_j\, \mathbf{S}_j(r_j) \quad , \quad \mathbf{T}_j \equiv \left[t_{kl}^j\right] = \mathbf{B}_j^{-1}(r_j)\ \mathbf{B}_j(r_{j+1}) \tag{29a}$$

$$\mathbf{c}_j = \mathbf{B}_j^{-1}(r_j)\mathbf{S}_j(r_j) \tag{29b}$$

Enforcing continuity of $\mathbf{S}_j$ at interfaces of segments and homogeneous boundary conditions (8a) at $r = r_p$ and $r = r_o$ yields the global transfer matrix $\mathbf{T}_G$ in tri-diagonal block form and the corresponding global $\mathbf{S}_G$ which is the ensemble of all $\mathbf{S}_j$

$$\begin{aligned} &\mathbf{T}_G \cdot \mathbf{S}_G = \mathbf{0} \quad \Rightarrow \quad \det|\mathbf{T}_G| = 0 \\ &\mathbf{S}_G = \left\{\mathbf{S}_1(r_1), \mathbf{S}_2(r_2), .., \mathbf{S}_j(r_j), .., \mathbf{S}_{N_r}(r_{N_r})\right\}^T \end{aligned} \tag{30}$$

$$\mathbf{T}_G = \begin{bmatrix} -1 & 0 & & & & & & & \\ t_{11}^1 & t_{12}^1 & -1 & 0 & & & & & \\ t_{21}^1 & t_{22}^1 & 0 & -1 & & & & & \\ & & t_{11}^2 & t_{12}^2 & -1 & 0 & & & \\ & & t_{21}^2 & t_{22}^2 & 0 & -1 & & & \\ & & & & . & . & & & \\ & & & & . & . & t_{11}^{N_r} & t_{12}^{N_r} & -1 & 0 \\ & & & & & & t_{21}^{N_r} & t_{22}^{N_r} & 0 & -1 \\ & & & & & & & & -1 & 0 \end{bmatrix}$$

Eq. (30) determines the eigenset $\{\mathbf{S}_G; \omega\}$ and in turn $\mathbf{C}_j = \left\{\mathbf{c}_1, \mathbf{c}_2, .., \mathbf{c}_j, .., \mathbf{c}_{N_r}\right\}^T$ from (29b).

To solve the transient response problem, decompose the displacement $u(r;t)$ as a superposition of two terms in the manner as was done for the circumferential inhomogeneity

$$u(r,t) = u_s(r)\ f_p(t) + u_d(r,t) \tag{31}$$

$u_s(r)$ is static displacement satisfying (25) with vanishing time dependence and boundary conditions (1b) with $f_p(t) = 1$, and $u_d(r;t)$ is dynamic displacement

satisfying (25) and boundary conditions (1b) with $f_p(t) = 0$. The static state vector $\mathbf{S}_{sj} = \{\sigma_{rrs}, u_s\}_j^T$ of the j^{th} segment takes the form

$$\sigma_{rrsj}(r) = 2(\lambda+\mu)_j\, c_{1sj} + 2\mu_j\, c_{2sj}/r^2 \tag{32a}$$

$$u_{sj}(r) = c_{1sj}\, r + c_{2sj}/r \tag{32b}$$

The global static transfer matrix is determined following the steps that led to Eq. (28) and (29)

$$\begin{aligned} &\mathbf{T}_{Gs}\cdot\mathbf{S}_{Gs} = \mathbf{p}_0 \quad , \quad \mathbf{p}_0 = \{p_0, 0, 0, ..., 0\}^T \\ &\mathbf{S}_{Gs} = \left\{\mathbf{S}_{s1}(r_1),\, \mathbf{S}_{s2}(r_2), .., \mathbf{S}_{sj}(r_j), .., \mathbf{S}_{sN_r}(r_{N_r})\right\}^T \end{aligned} \tag{33}$$

Expand u_d in its eigenfunctions $\varphi_m(r)$

$$\begin{aligned} &u_d(r,t) = \sum_m a_m(t)\, \varphi_m(r) \\ &\varphi_m(r) = \sum_{j=1}^{N_r} k_{ejm}\left(c_{1jm}\, J_1(k_{ejm}\, r) + c_{2jm}\, Y_1(k_{ejm}\, r)\right)\Big(H(r-r_j) - H(r-r_{j+1})\Big) \end{aligned} \tag{34}$$

$H(r)$ is the Heaviside function, $k_{ejm} = \omega_m / c_{ej}$ and ω_m is the m^{th} eigenvalue. Substituting (32a,b) in (31) then in (25) and enforcing orthogonality of the $\{\varphi_m\}$ set yields uncoupled equations in $a_m(t)$

$$\begin{aligned} &\ddot{a}_m(t) + \omega_m^2\, a_m(t) = \overline{f}_m(t) \\ &\overline{f}_m(t) = N_{sm}\, \ddot{f}_p(t)/N_m \quad , \quad N_m = \int_{r_p}^{r_o} \varphi_m^2\, r\, dr \, , \quad N_{sm} = \int_{r_p}^{r_o} \varphi_m\, u_s\, r\, dr \end{aligned} \tag{35}$$

Eq. (35) admits the solution

$$a_m(t) = -\frac{1}{\omega_m}\int_0^t \sin\omega_m(t-\tau)\, \overline{f}_m(\tau)\, d\tau \tag{36}$$

4. Results

Consider a plane-strain cylinder with properties

$$E_0 = 3.1\times10^9\ dyn/cm^2,\ \rho = 0.93\ g/cm^3,\ \nu = 0.48$$
$$r_p = 0.635\ cm,\ r_o = 7.62\,cm \qquad (37)$$

This yields extensional and shear wave speeds c_e and c_s 1.71 and 0.34 km/s and the ratio $c_e/c_s \simeq 5$. Fig. 1 plots the resonant frequency spectrum Ω versus discrete n with radial wave number m as parameter. Although each frequency corresponds to a discrete integer n value, the points are joined to facilitate discerning constant m lines in the explanation to follow. Lines of constant m are almost parallel with slope proportional to c_s. A constant m-line L_m changes slope and coalesces with the next constant m-line L_{m+1} without crossing it. Coalescence without crossing is necessary for uniqueness of the eigen-states. Near coalescence, L_m reverts to its original slope while L_{m+1} proceeds through similar steps to coalesce with L_{m+2} and so on. Remote from coalescence, these lines have a slope proportional to c_s and correspond to shear modes. Near coalescence, envelopes are also straight lines with slope proportional to c_e and correspond to extensional modes. Shear modes are denser than extensional modes when c_e/c_s is large as in the present case. Coupling of shear and extensional modes for $n \geq 1$ is what distinguishes asymmetric from axisymmetric motions.

Since the static solution is prerequisite to solving transient response, understanding the effect of θ-inhomogeneity on the static problem will help understanding its effect on transient response. The first step starts with the simple case of the static axisymmetric homogeneous cylinder with unit

prescribed pressure at its inner boundary $r = r_p$. Fig. 2 plots radial distribution of displacement u_0 and stresses σ_{rr0} and $\sigma_{\theta\theta 0}$. Remote from $r = r_p$, $u_0 \propto 1/r$ and $(\sigma_{rr0},\ \sigma_{\theta\theta 0}) \propto 1/r^2$, with magnitude equal to applied pressure p_0. As expected, σ_{rr0} is compressive and $\sigma_{\theta\theta 0}$ is tensile since internal pressure expands the cylinder along the radius.

Consider the plane-strain cylinder with θ-inhomogeneity in the form of Eq. (4) including only 2 terms

$$\mu(\theta) = \mu_0 \left(1 + 0.5\cos(2\theta)\right) \tag{38}$$

$\mu(\theta)$ in (38) is symmetric about $\theta = 0$ and $\theta = \pi/2$ requiring that only even n's be included in the expansion (C8) of Appendix C. Convergence of the static solution was achieved with $m = 60$ and $n = 0, 2, 4$. Fig. 3(a1-e1) plots dependent variable along r with θ as parameter and Fig. 3(a2-e2) plots these variables along θ with r as parameter. At $\theta = 0$ where E is largest (Fig. 3(a1)), u_c decreases along r like u_0 in Fig. 2(a) with peak $u_{cmx}(r_p, 0)$ at $r = r_p$ slightly less than that of u_0. As θ increases, $u_{cmx}(r_p, \pi/4)$ diminishes to almost 1/2 $u_{cmx}(r_p, 0)$. Along θ (Fig. 3(a2)), u_c is periodic following approximately the $\cos(2\theta)$ distribution of $\mu(\theta)$. This means that along a constant r-line, the cross-section is squashed with larger curvature at $\theta = 0$ and smallest curvature at $\theta = \pi/2$. This results in flexure of the cross-section adding to $\sigma_{\theta\theta c}$ a periodic stress component that changes from compressive at $\theta = 0$ to tensile at $\theta = \pi/2$. Indeed Fig. 3(d1,d2) shows a compressive over-stress at $\theta = 0$ with magnitude $6\,p_0$ and a tensile over-stress

with magnitude $2p_0$. The same argument applies to σ_{zzc} in Fig. 3(e1,e2). Note that in Fig. 2 σ_{zz0} is not plotted since it is small since $\sigma_{zz0} = \beta_0/(1+\beta_0)\, r_p^2/(r_o^2 - r_p^2) \approx r_p^2/r_o^2 \ll 1$. It appears then that in the static case, θ-inhomogeneity magnifies compressive and tensile stresses because of flexure at and near the inner boundary, and raises axial stress substantially from the homogeneous case.

Consider transient response of a homogeneous plane-strain cylinder forced by a $10\mu s$ trapezoidal pulse of unit intensity, with $1\,\mu s$ rise and fall times and a $8\mu s$ plateau. Fig. 4 plots histories of dependent variables within a $60\mu s$ time range. Fig. 4(a) shows u histories at 3 different radial stations. u increases almost linearly while the forcing pulse is nonzero then drops smoothly until waves reflect from the free boundary $r = r_o$. Note the time delay in response for $r = 2r_p$ and $r = 4r_p$ equal to travel time of extensional waves to reach these stations from $r = r_p$. Fig. 4(b) plots velocity history. Velocity increases steeply with rise time that of the forcing pulse, then continues to increase at a reduced rate until the forcing pulse elapses consistent with the shape of the u history in Fig. 4(a). The smooth rise during the plateau portion of the pulse is characteristic of cylindrical symmetry as it is flat in 1-D and 2-D. σ_{rr} follows the shape of the forcing pulse closely since it must satisfy the boundary condition at $r = r_p$ (see Fig. 4(c)). However, $\sigma_{\theta\theta}$ while being tensile for all r in the static case (Fig. 2(b)), is compressive throughout the duration of the pulse then changes to tensile after the pulse elapses. An explanation is that shortly after the pulse is applied, a narrow annular region bounded by the extensional wave-

front undergoes stress while the wave-front acts as a solid but moving boundary. During this time, the state of stress in this instantaneously confined annular region is almost hydrostatic where all three normal stress components are approximately equal. Release of pressure at the end of the pulse and radial motion of the wave-front reverts to the free motion when $\sigma_{\theta\theta}$ changes to tensile.

Consider transient response of the plane-strain cylinder with the θ-inhomogeneity given by (38). Fig. 5 plots histories of each dependent variable along a column for a specific θ. Three values of θ are chosen: $0, \pi/4, \pi/2$. Unless specified on the ordinate of some variable, labels along a row are the same for all θ. Exceptions to this rule are when the variable at $\theta = 0$ is substantially larger than that for other values of θ. At $\theta = 0$ (Fig. 5(a1)), magnitudes of the u histories are approximately half those for the other θ's. This may seem counter intuitive as it is the opposite of the static case (Fig. 3(a1,a2)). Yet, the explanation is the same as that for the sign of $\sigma_{\theta\theta}$ in the homogeneous cylinder (Fig. 4(d)). Shortly after the pulse is applied, the wave-front confines a narrow annular region near $r = r_p$ where the state of stress is hydrostatic. Since at $\theta = 0$, modulus is 3 times larger than at $\theta = \pi/2$, and since hydrostatic displacement is inversely proportional to modulus, the result in Fig. 5(a1) is obtained. Histories of circumferential displacement υ are plotted only for $\theta = \pi/4$ (Fig. 5(b2)) since $\upsilon \propto \sin(n\theta)$ vanishes at $\theta = 0$ and $\theta = \pi/2$ for n=2 and n=4. Magnitude of υ is approximately 1/5 that of u for the θ shown. Also, travel time is approximately 5 times that for u in Fig. 5(a2). This implies that υ propagates at the speed of shear waves c_s. Histories of σ_{rr} (Fig. 5(c1-c3))

qualitatively resemble the corresponding ones of the homogeneous cylinder (Fig. 4(c)). The difference is that magnitude of σ_{rr} reduces with modulus as evidenced by comparing Fig. 5(c1) to Fig. 5(c2,c3). Histories of $\sigma_{\theta\theta}$ at $\theta = 0$ (Fig. 5(d1)) are particularly interesting. Throughout the duration of the pulse, response is comparable to the homogeneous cylinder. After the pulse elapses, $\sigma_{\theta\theta}$ becomes tensile reaching a peak $3.5\, p_0$ at $t = 90\mu s$. The first peak of $\sigma_{\theta\theta}$ occurs at the 1/4 period of the coupled fundamental resonance with a frequency of 2.6 KHz compared to the fundamental axisymmetric resonance of the homogeneous cylinder at 6.1 KHz. For an impulsive pressure, setting $\overline{f}_i(\tau) = \delta(\tau)$ in (23a) yields $a_i(t) \propto \sin(\omega_i t)/\omega_i$ implying that the largest amplitude of free oscillation is inversely proportional to the fundamental resonance. This explains the larger $\sigma_{\theta\theta}$ amplitude of the inhomogeneous cylinder compared the homogeneous one. Histories of σ_{zz} (Fig. 5(e1-e3)) resemble those of σ_{rr} (Fig. 5(c1-c3)) except that magnitude at $\theta = 0$ is approximately double that at $\theta = \pi/4$. Finally, velocity histories (Fig. 5(f1-f3)) follow the u histories (Fig. 5(a1-a3)) in that magnitude of velocity at $\theta = 0$ is lower than that at $\theta = \pi/4$ and at $\theta = \pi/2$.

In the case of r-inhomogeneity assume the following distribution of modulus $E(r)$

$$E(r) = E_0\left(1 + 0.5\sin\left(4\pi(r - r_p)/(r_o - r_p)\right)\right) \qquad (39)$$

where E_0 and all other properties are given in (37). In this way, the highest to lowest $E(r)$ ratio is 3 similar to the θ-inhomogeneity. The cylinder is divided into 45 annular constant width segments each assigned a constant $E(r_i)$

following (39) with r_i being the mean radius of the i^{th} segment. The corresponding stepwise c_e distribution is shown in Fig. 6. The cylinder is forced by the same $10\mu s$ trapezoidal pulse used in the case of the θ-inhomogeneity. Fig. 7(a-e) plots histories of the cylinder in the interval $0 \le t \le 80\mu s$. Throughout the duration of the pulse, histories of the cylinder with r-inhomogeneity are almost the same as those of the homogeneous case (see Fig. 4). During this time, response is confined to a narrow ring close to $r = r_p$, where magnitude depends only on properties in this region. After the pulse elapses and the wave-front moves outward, response then differs from the homogeneous case especially after reflection from the outer boundary $r = r_o$.

It is evident from the examples above that for the same level of inhomogeneity, θ-inhomogeneity has a more pronounced effect on transient response both in shape and magnitude. The fundamental reason is that with a θ-inhomogeneity, asymmetric waves are excited that include both extensional and shear components adding to the spectrum modes with lower frequency. These modes magnify amplitude of free motion for all dependent variables.

5. Conclusion

Transient response of a plane-strain hollow cylinder was analyzed for both θ and r inhomogeneity. For a θ-inhomogeneity with periodic modulation noteworthy results are

1. Dependent variables acquire a periodicity along the circumference
2. Static $\sigma_{\theta\theta}$ and σ_{zz} are magnified at $\theta = 0$ and $r = r_p$ compared to the homogeneous case

3. Static $\sigma_{\theta\theta}$ is modulated by a flexural components that is compressive along the axis of highest modulus and tensile along the axis of weakest modulus
4. Asymmetric waves are induced that include extensional and shear components adding modes with lower frequencies to the spectrum. This in turn magnifies amplitude of $\sigma_{\theta\theta}$ and σ_{zz} after the forcing pulse elapses and free harmonic motion starts.

For a periodic r-inhomogeneity the principal results are

1. When the forcing pulse is acting, response resembles the homogeneous case
2. Differences in response appear after the pulse elapse especially after reflection from the outer boundary
3. Fixing the level of inhomogeneity, θ-inhomogeneity has a more pronounced effect on response than r-inhomogeneity because of the absence of shear waves in the latter.

Asymmetric dynamic solution of homogeneous finite cylinder

For periodic motions in time, The Navier equations of elastodynamics can be written in vector form as

$$(\lambda+\mu)\nabla(\nabla\bullet\mathbf{u})+\mu\nabla\bullet(\nabla\mathbf{u})+\rho\omega^2\mathbf{u}=\mathbf{0} \qquad \text{(A1)}$$

where λ and μ are $Lame'$'s constants, ρ is density, $\mathbf{u}$ is displacement vector, and ω is radian frequency. For cylindrical coordinates (r,θ,z) where z is along the axis of revolution, $\mathbf{u}$ can be expressed in terms of three scalar potentials φ,ξ,η as follows

$$\begin{aligned}&\mathbf{u}=\nabla\varphi+\nabla\times(\xi\mathbf{e}_z)+\nabla\times\nabla\times(\eta\mathbf{e}_z)\\&\mathbf{u}\equiv u\,\mathbf{e}_r+\upsilon\,\mathbf{e}_\theta+w\mathbf{e}_z\end{aligned} \qquad \text{(A2)}$$

where $\mathbf{e}_r, \mathbf{e}_\theta, \mathbf{e}_z$ are a unit vectors along r, θ, z. Substituting (A2) in (A1) then taking the divergence yields

$$\nabla^2\varphi + k_e^2\varphi = 0 \quad , \quad \nabla^2 \equiv \partial_{rr} + 1/r\,\partial_r + 1/r^2\,\partial_{\theta\theta} + \partial_{zz}$$
$$k_e = \omega / c_e \quad , \quad c_e^2 = (\lambda + 2\mu)/\rho \tag{A3}$$

Substituting (A2) in (A1) and taking the curl yields

$$\nabla^2\xi + k_s^2\xi = 0$$
$$\nabla^2\eta + k_s^2\eta = 0 \tag{A4}$$
$$k_s = \omega / c_s \quad , \quad c_s^2 = \mu/\rho$$

For simply-supported boundary conditions at $z = 0, l$ and periodicity along θ, φ, ξ, η can be expressed in terms of Bessel functions in r and harmonic functions in θ and z

$$\varphi(r,\theta,z) = \left(c_{11}\,J_n(k_{re}r) + c_{21}\,Y_n(k_{re}r)\right)\,S_m(z)\,C_n(\theta)$$
$$\xi(r,\theta,z) = \left(c_{12}\,J_n(k_{rs}r) + c_{22}\,Y_n(k_{rs}r)\right)\,S_m(z)\,S_n(\theta) \tag{A5a}$$
$$\varphi(r,\theta,z) = \left(c_{13}\,J_n(k_{rs}r) + c_{23}\,Y_n(k_{rs}r)\right)\,C_m(z)\,C_n(\theta)$$

$$S_n(\theta) = \sin(n\theta) \quad , \quad C_n(\theta) = \cos(n\theta)$$
$$S_m(z) = \sin(k_{zm}z), \quad C_m(z) = \cos(k_{zm}z)$$
$$k_{re}^2 = k_e^2 - k_{zm}^2 \quad , \quad k_{rs}^2 = k_s^2 - k_{zm}^2 \quad , \quad k_{zm} = m\pi/l \tag{A5b}$$
$$m = 1, 2, \ldots, M \quad , \quad n = 0, 1, \ldots, N$$

m is an integer axial wave number that follows from the exact solution of the separated axial dependence satisfying simply supported boundary conditions at $z = 0, l$ which require that $u(r,\theta,z) = \upsilon(r,\theta,z) = \sigma_{zz}(r,\theta,z) = 0$ at $z = 0, l$. Similarly, n is an integer circumferential wave number that follows from the exact solution of the separated circumferential dependence satisfying continuity of dependent variable along the cylinder's circumference. Subscript

m in k_{zm} will be dropped hereafter for shortness. If D is a dependent variable, then

$$D\left(J_n, J_{n+1}; Y_n, Y_{n+1}\right) = D_1\left(J_n, J_{n+1}\right) + D_2\left(Y_n, Y_{n+1}\right) \tag{A6}$$

Since D_2 has the same form as D_1 except that the primitives J_n, J_{n+1} in D_1 are replaced by Y_n, Y_{n+1} in D_2, only expressions for D_1 will be listed below for shortness. Substituting (A5) in (A2) produces expressions for displacements

$$\begin{aligned} u_1 = \sum_n \sum_m \Big\{ & c_{11mn}\, k_{re}\left(n\, J_n(k_{re}r)/(k_{re}r) - J_{n+1}(k_{re}r)\right) + c_{12mn}\, n\, J_n(k_{rs}r)/r \\ & - c_{13mn}\, k_{rs}k_z\left(n\, J_n(k_{rs}r)/(k_{rs}r) - J_{n+1}(k_{rs}r)\right)\Big\} S_m(z) C_n(\theta) \end{aligned} \tag{A7a}$$

$$\begin{aligned} \upsilon_1 = \sum_n \sum_m \Big\{ & -c_{11mn}\, n\, J_n(k_{re}r)/r - c_{12mn}\, k_{rs}\left(n\, J_n(k_{rs}r)/(k_{rs}r) - J_{n+1}(k_{rs}r)\right) \\ & + c_{13mn}\, n k_z\, J_n(k_{rs}r)/r\Big\} S_m(z) S_n(\theta) \end{aligned} \tag{A7b}$$

$$w_1 = \sum_n \sum_m \left\{ c_{11mn}\, k_z\, J_n(k_{re}r) + c_{13mn}\, k_{rs}^2\, J_n(k_{rs}r)\right\} C_m(z) C_n(\theta) \tag{A7c}$$

The constitutive relations are

$$\begin{aligned} & \sigma_{ii} = \lambda \Delta + 2\mu \varepsilon_{ii}\ , \quad ii \equiv rr, \theta\theta, zz \\ & \Delta = \varepsilon_{rr} + \varepsilon_{\theta\theta} + \varepsilon_{zz} \\ & \sigma_{ij} = \mu \varepsilon_{ij}\ , \quad ij \equiv r\theta, \theta z, zr \end{aligned} \tag{A8}$$

$$\begin{aligned} & \varepsilon_{rr} = \partial_r u\ ,\ \varepsilon_{\theta\theta} = u/r + 1/r\ \partial_\theta \upsilon\ ,\ \varepsilon_{zz}\partial_z w \\ & \varepsilon_{r\theta} = 1/r\ \partial_\theta u\ +\ \partial_r \upsilon\ - \upsilon/r \\ & \varepsilon_{\theta z} = \partial_z \upsilon + 1/r\ \partial_\theta w\ ,\ \varepsilon_{zr} = \partial_r w + \partial_z u \end{aligned} \tag{A9}$$

Substituting (A7) in (A9) then in (A8) produces

$$\begin{aligned} \sigma_{rr1} = \mu \sum_n \sum_m \Big\{ & c_{11mn}\left(\left(-(\beta+2)(k_{re}r)^2 + 2(n^2-n) - \beta(k_z r)^2\right) J_n(k_{re}r)/r^2 + 2k_{re}\, J_{n+1}(k_{re}r)/r\right) \\ & + 2c_{12mn}\left((n^2-n) J_n(k_{rs}r)/r^2 - n k_{rs}\, J_{n+1}(k_{rs}r)/r\right) \\ & - 2c_{13mn}\, k_z\left(\left(n^2 - n - (k_{rs}r)^2\right) J_n(k_{rs}r)/r^2 + k_{rs} J_{n+1}(k_{rs}r)/r\right)\Big\}\ S_m(z)\ C_n(\theta) \end{aligned} \tag{A10a}$$

$$\sigma_{\theta\theta 1} = \mu \sum_n \sum_m \Big\{ c_{11mn} \Big(-\big(2(n^2-n) + \beta (k_e r)^2\big) J_n(k_{re} r)/r^2 - 2k_{re}\, J_{n+1}(k_{re} r)/r \Big)$$
$$+ 2c_{12mn} \Big(-(n^2-n) J_n(k_{rs} r)/r^2 + n\, k_{rs}\, J_{n+1}(k_{rs} r)/r \Big) \qquad \text{(A10b)}$$
$$+ 2\, c_{13mn}\, k_z \Big(\big(n^2-n\big) J_n(k_{rs} r)/r^2 + k_{rs} J_{n+1}(k_{rs} r)/r \Big) \Big\}\, S_m(z)\, C_n(\theta)$$

$$\sigma_{zz1} = \mu \sum_n \sum_m \Big\{ -c_{11mn} \big((\beta+2)\, k_z^2 + \beta\, k_{re}{}^2 \big) J_n(k_{re} r) - 2c_{13mn}\, k_z\, k_{rs}^2\, J_n(k_{rs} r) \Big\}\, S_m(z)\, C_n(\theta) \qquad \text{(A10c)}$$

$$\tau_{r\theta 1} = \mu \sum_n \sum_m \Big\{ 2c_{11mn} \Big(-(n^2-n) J_n(k_{re} r)/r^2 + n\, k_{re}\, J_{n+1}(k_{re} r)/r \Big)$$
$$- 2c_{12mn} \Big((n^2 - n - (k_{rs} r)^2/2) J_n(k_{rs} r)/r^2 + k_{rs}\, J_{n+1}(k_{rs} r)/r \Big) \qquad \text{(A10d)}$$
$$+ 2c_{13mn}\, k_z \Big(\big(n^2-n\big) J_n(k_{rs} r)/r^2 - n\, k_{rs} J_{n+1}(k_{rs} r)/r \Big) \Big\}\, S_m(z)\, S_n(\theta)$$

$$\tau_{\theta z 1} = \mu \sum_n \sum_m \Big\{ -2c_{11mn}\, n\, k_z\, J_n(k_{re} r)/r - c_{12mn}\, k_z \big(n\, J_n(k_{rs} r)/r - k_{rs}\, J_{n+1}(k_{rs} r) \big)$$
$$+ c_{13mn}\, n \big(k_z^2 - k_{rs}^2 \big) J_n(k_{rs} r)/r \Big\}\, C_m(z)\, S_n(\theta) \qquad \text{(A10e)}$$

$$\tau_{rz 1} = \mu \sum_n \sum_m \Big\{ 2c_{11mn} k_z \big(n J_n(k_{re} r)/r - k_{re}\, J_{n+1}(k_{re} r) \big) + c_{12mn}\, n k_z J_n(k_{rs} r)/r$$
$$+ c_{13mn} (k_z^2 - k_{rs}^2) \big(-n J_n(k_{rs} r)/r + k_{rs}\, J_{n+1}(k_{rs} r) \big) \Big\}\, C_m(z)\, C_n(\theta) \qquad \text{(A10f)}$$

$$S_n(\theta) = \sin(n\theta)\,, \quad C_n(\theta) = \cos(n\theta)\,, \quad n = 0, 1, \ldots, N$$
$$k_{re} = k_e = \omega / c_e\,, \quad k_{rs} = k_s = \omega / c_s\,, \quad \beta = \lambda / \mu$$

The Bessel functions in (A5a) through (A10) are real when ω is greater than both shear and extensional cut-off frequencies of the m^{th} axial mode

$$\omega \geq \omega_{co,e}^{(m)} = k_z\, c_e \;\Rightarrow k_e \geq k_z \quad , \quad \omega \geq \omega_{co,s}^{(m)} = k_z\, c_s \;\Rightarrow k_s \geq k_z \qquad \text{(A11)}$$

Since $c_e > c_s$ then (A5a) through (A10) are valid when $\omega \geq k_z c_e$. However, if $k_z c_s < \omega < k_z c_e$ then $J_n(k_{re} r)$, $Y_n(k_{re} r)$ are replaced by $I_n(k_{re} r)$, $K_n(k_{re} r)$. Similarly, if $\omega < k_z c_s$ then $J_n(k_{rs} r)$, $Y_n(k_{rs} r)$ are replaced by $I_n(k_{rs} r)$, $K_n(k_{rs} r)$. Expressions for displacement and stress similar in form to (A7) and (A10) follow with appropriate changes in sign but will not be listed here for shortness.

Appendix B: Asymmetric dynamic solution of plane-strain cylinder

For the plane-strain problem, displacements and stresses are found from Appendix A when the z dependence and axial displacement w vanish. Expressions for u and υ are

$$
\begin{aligned}
u_1 &= \sum_n \left\{ c_{11n}\, k_{re} \left(n\, J_n(k_{re}r)/(k_{re}r) - J_{n+1}(k_{re}r) \right) + c_{12n}\, n\, J_n(k_{rs}r)/r \right\} C_n(\theta) \\
\upsilon_1 &= \sum_n \left\{ -c_{11n}\, n\, J_n(k_{re}r)/r - c_{12n}\, k_{rs} \left(n\, J_n(k_{rs}r)/(k_{rs}r) - J_{n+1}(k_{rs}r) \right) \right\} S_n(\theta) \\
S_n(\theta) &= \sin(n\theta)\,, \quad C_n(\theta) = \cos(n\theta)\,, \qquad n = 0,1,\ldots,N \\
k_{re} &= k_e = \omega / c_e\,, \quad k_{rs} = k_s = \omega / c_s
\end{aligned}
\tag{B1}
$$

Expressions for stresses $\sigma_{rr}, \sigma_{\theta\theta}, \sigma_{zz}, \tau_{r\theta}$ are

$$
\begin{aligned}
\sigma_{rr1} = \mu \sum_n \Big\{ & c_{11n} \Big(\left(-(\beta+2)(k_{re}r)^2 + 2(n^2-n) \right) J_n(k_{re}r)/r^2 + 2k_{re}\, J_{n+1}(k_{re}r)/r \Big) \\
& + 2\, c_{12n} \Big((n^2-n) J_n(k_{rs}r)/r^2 - n k_{rs}\, J_{n+1}(k_{rs}r)/r \Big) \Big\} C_n(\theta)
\end{aligned}
\tag{B2a}
$$

$$
\begin{aligned}
\sigma_{\theta\theta 1} = \mu \sum_n \Big\{ & c_{11n} \Big(-\left(2(n^2-n) + \beta\, (k_e r)^2 \right) J_n(k_{re}r)/r^2 - 2k_{re}\, J_{n+1}(k_{re}r)/r \Big) \\
& + 2 c_{12n} \Big(-(n^2-n) J_n(k_{rs}r)/r^2 + n k_{rs}\, J_{n+1}(k_{rs}r)/r \Big) \Big\} C_n(\theta)
\end{aligned}
\tag{B2b}
$$

$$
\sigma_{zz1} = \mu \sum_n \left\{ -2 c_{11n}\, \beta\, k_{re}{}^2\, J_n(k_{re}r) \right\} C_n(\theta)
\tag{B2c}
$$

$$
\begin{aligned}
\tau_{r\theta 1} = \mu \sum_n \Big\{ & 2 c_{11n} \Big(-(n^2-n) J_n(k_{re}r)/r^2 + n k_{re}\, J_{n+1}(k_{re}r)/r \Big) \\
& - 2 c_{12n} \Big(\left(n^2 - n - (k_{rs}r)^2/2 \right) J_n(k_{rs}r)/r^2 + k_{rs}\, J_{n+1}(k_{rs}r)/r \Big) \Big\} S_n(\theta)
\end{aligned}
\tag{B2d}
$$

Appendix C. Asymmetric static solution of plane-strain cylinder

For the homogeneous cylinder with material properties (λ_0, μ_0), the static solution is obtained by solving Eq. (1a) with vanishing time dependence. The solution takes the form

$$
u_s(r,\theta) = c_u\, r^{\alpha} C_n(\theta)\,, \quad \upsilon(r,\theta) = c_\upsilon\, r^{\alpha}\, S_n(\theta)
\tag{C1}
$$

where c_u and c_υ are constant coefficients. Substituting (C1) in (1a) yields the equations

$$\begin{aligned}\left((\lambda_0+2\mu_0)(\alpha^2-1)-\mu_0 n^2\right)c_u + n\left((\lambda_0+\mu_0)\alpha-(\lambda_0+3\mu_0)\right)c_\upsilon = 0\\ n\left((\lambda_0+\mu_0)\alpha+(\lambda_0+3\mu_0)\right)c_u - \left((\lambda_0+2\mu_0)n^2-\mu_0(\alpha^2-1)\right)c_\upsilon = 0\end{aligned} \quad \text{(C2)}$$

A non-trivial solution requires that the determinant of the coefficients of c_u and c_υ vanish. This yields a fourth order polynomial in α with 4 roots

$$\alpha = \pm(n\pm 1) \quad \text{(C3)}$$

The solution (C1) then takes the form

$$u_s(r,\theta) = \sum_{n=0}\sum_{i=1}^{4} c_{u,ni}\, r^{\alpha_{ni}}\, C_n(\theta) \quad \text{(C4a)}$$

$$\upsilon_s(r,\theta) = \sum_{n=0}\sum_{i=1}^{4} c_{\upsilon,ni}\, r^{\alpha_{ni}}\, S_n(\theta) \quad \text{(C4b)}$$

Substituting each of the roots of (C3) in (C2) determines a relation between $c_{u,ni}$ and $c_{\upsilon,ni}$

$$c_{\upsilon,ni} = -\frac{\left((\lambda_0+2\mu_0)(\alpha_{ni}^2-1)-\mu_0 n^2\right)}{n\left((\lambda_0+\mu_0)\alpha_{ni}-(\lambda_0+3\mu_0)\right)}c_{u,ni} \quad \text{(C5)}$$

Substituting (C4) into the constitutive relations (2) gives

$$\sigma_{rrs}(r,\theta) = \sum_{n=0}\sum_{i=1}^{4}\left\{c_{u,ni}\left(\lambda_0\left(\alpha_{ni}+1\right)+2\mu_0\alpha_{ni}\right)+c_{\upsilon,ni}\, n\,\lambda_0\right\} r^{\alpha_{ni}-1} C_n(\theta)$$

$$\sigma_{\theta\theta s}(r,\theta) = \sum_{n=0}\sum_{i=1}^{4}\left\{c_{u,ni}\left(\lambda_0\left(\alpha_{ni}+1\right)+2\mu_0\right)+c_{\upsilon,ni}\, n(\lambda_0+2\mu_0)\right\} r^{\alpha_{ni}-1} C_n(\theta)$$

$$\sigma_{zzs}(r,\theta) = \lambda_0\sum_{n=0}\sum_{i=1}^{4}\left\{c_{u,ni}\left(\alpha_{ni}+1\right)+c_{\upsilon,ni}\, n\right\} r^{\alpha_{ni}-1} C_n(\theta)$$

$$\tau_{r\theta s}(r,\theta) = -\mu_0\sum_{n=0}\sum_{i=1}^{4}\left\{c_{u,ni}\, n - c_{\upsilon,ni}\left(\alpha_{ni}-1\right)\right\} r^{\alpha_{ni}-1} S_n(\theta) \quad \text{(C6)}$$

Substituting (C5) in the boundary conditions

$$\sigma_{rrs}(r_p) = \sum_{n=0}^{N_\theta} p_n C_n(\theta)\,, \quad \sigma_{rrs}(r_o) = 0 \tag{C7a}$$

$$\tau_{r\theta s}(r_p) = 0 \quad , \quad \tau_{r\theta s}(r_o) = 0 \tag{C7b}$$

yields N_θ uncoupled linear equations in each set of coefficients $c_{u,ni}$ and $c_{\upsilon,ni}$.

For the cylinder with θ-inhomogeneity in E given by (4), the static equations (5a,b) with vanishing time derivative are solved by the Galerkin method. A set of orthogonal trial functions is assumed each satisfying the homogeneous differential equations (3) and boundary conditions (9). Candidate functions are the eigenfunctions of the homogeneous cylinder with $n \geq 0$. Since the total static solution is made of the axisymmetric static solution modified by an asymmetric part accounting for material inhomogeneity, that static solution is added to the set of trial functions. In this way, the displacement expansion takes the form

$$\begin{aligned} u_s(r,\theta) &= \sum_{n=0}\sum_{m=1} b_{mn}\ \varphi_{mn}\ C_n(\theta)\ +\ u_{s0}(r) \\ \upsilon_s(r,\theta) &= \sum_{n=1}\sum_{m=1} b_{mn}\ \psi_{mn}\ S_n(\theta) \end{aligned} \tag{C8}$$

$\{\varphi(r),\psi(r)\}_{nm}$ are the eigenfunctions of the homogeneous problem determined by (10) satisfying the homogeneous boundary conditions (9), and $u_{s0}(r)$ is static axisymmetric radial displacement defined by (C4a) with $n = 0$, satisfying the inhomogeneous boundary conditions (C7a)

$$u_{s0}(r) = -p_0\ r_p^2\ \left(r/(\beta_0+1) + r_o^2/r\right)/\left(2\mu_0(r_o^2 - r_p^2)\right)\,, \quad \beta_0 = \lambda_0/\mu_0 \tag{C9}$$

Substituting (C8) in the static equivalent of (5a,b), then multiplying (5a) by $\varphi_{mn}\cos(n\theta)$ and (5b) by $\psi_{mn}\sin(n\theta)$, integrating over the domain $r_p \le r \le r_o$, $0 \le \theta \le 2\pi$ then adding the two equations produces

$$\rho \sum_{k=0} \sum_{j=1} \left[\Theta^{(1)}_{nk} R^{(1)}_{mn,\,jk} + \Theta^{(2)}_{nk} R^{(2)}_{mn,\,jk} \right] \omega^2_{jk}\ b_{jk}$$
$$+ \mu_0 \sum_{k=0} \sum_{j=1} \left[\Theta^{(3)}_{nk} R^{(3)}_{mn,\,jk} + \Theta^{(4)}_{nk} R^{(4)}_{mn,\,jk} \right] b_{jk} \ = \ - p_0\, \delta_{n0}\, \Theta^{(4)}_{n0}\, R^{(0)}_{mn} \qquad \text{(C10)}$$
$$R^{(0)}_{mn} = -r_p^2 / \left(r_o^2 - r_p^2 \right) \int_{r_p}^{r_o} \psi_{mn} \left(1 + \left(r_o / r \right)^2 \right)\ dr$$

All other quantities in (C10) are defined in (15b,c). The linear simultaneous equations (C10) determine the coefficients b_{jk}.

Since the functions $\{\varphi(r), \psi(r)\}_{nm}$ are only trial functions and not solutions of the static equations, not all functions are physically admissible. In fact, the lowest mode $m = 1$ for $n \ge 2$ is dropped for reasons to follow. Fig. C1(a1) plots normalized $u_{s0}(r)$ which varies exponentially with r. Fig. C1(b1) and C1(c1) plot $\varphi_{01}(r)$ and $\varphi_{11}(r)$ which follow the same qualitative behavior. For modes $\varphi_{21}(r)$, $\varphi_{31}(r)$, $\varphi_{41}(r)$ etc., this trend changes as shown in Fig. C1(a2,b2,c2) as these functions increase with r. These shapes although consistent with extensional dynamic resonances, are inconsistent with static deformation from pressure at the inner boundary as shown in Fig. C1(a1). Functions with higher wave number as $\varphi_{22}(r)$, $\varphi_{32}(r)$, $\varphi_{42}(r)$ etc. (Fig. C1(a3,b3,c3)) are all admissible. It then follows that for $n \ge 2$ extensional modes with $m = 1$ are inadmissible trial functions excluded in the expansion (C8).

References

Armenakas, A., 1967. Propagation of harmonic waves in composite circular cylindrical shells I: Theoretical investigation. American Institute of Aeronautics and Astronautics Journal 5, 740-744.

Armenakas, A., Keck, H., 1970. Harmonic non-axisymmetric waves with short wave lengths propagating in composite rods. Journal of the Acoustical Society of America 48, 1160-1169.

Baltrukonis, J., 1960. Free transverse vibrations of a solid mass in an infinitely long rigid circular cylindrical tank. ASME Journal of Applied Mechanics 27, 663-668.

Bird, J., Hart, R., McClure, F., 1960. Vibration of thick-walled hollow cylinders: Exact numerical solutions. Journal of the Acoustical Society of America 32, 1403-1412.

El-Raheb, M., Wagner, P., 1989. Wave propagation in a thin cylinder that includes point masses. Journal of the Acoustical Society of America 85, 759-767.

El-Raheb, M., 2004. Wave propagation in a hollow cylinder due to prescribed velocity at the boundary. International Journal of Solids & Structures, 41/18-19, pp 5051-5069.

Gazis, D., 1958. Exact analysis of the plane-strain vibration of thick-walled hollow cylinders. Journal of the Acoustical Society of America 30, 786-794.

Heyliger, P., Jilania, A., 1992. The free vibration of inhomogeneous elastic cylinders and spheres. International Journal of Solids and Structures 29, 2689-2708.

Keck, H., Armenakas, A., 1971. Wave propagation in transversely isotropic layered cylinders. Journal of Engineering Mechanics 97, 541-558.

Reuter, R., 1969. Dispersion of flexural waves in circular bimaterial cylinders – Theoretical treatment. Journal of the Acoustical Society of America 46, 643-648.

Steinberg, L., 1995. Inverse spectral problems for inhomogeneous elastic cylinders. Journal of Elasticity 38, 133-151.

Whittier, J., Jones, J., 1967. Axially symmetric wave propagation in a two-layered cylinder. International Journal of Solids and Structures 3, 657-675.

Yin, X., Yue, Z., 2002. Transient plane-strain response of multilayered elastic cylinders to axisymmetric impulse. ASME Journal of Applied Mechanics 69, 825-835.

Acknowlegment:

This work was supported by a grant from DARPA, executed by the U.S. Army Medical Research and Materiel Command/TATRC Contract # W81XWH-04-C-0084. The views, opinions and/or findings contained in this paper are those of the author and should not be construed as an official Department of the Army position, policy or decision unless so designated by other documentation.

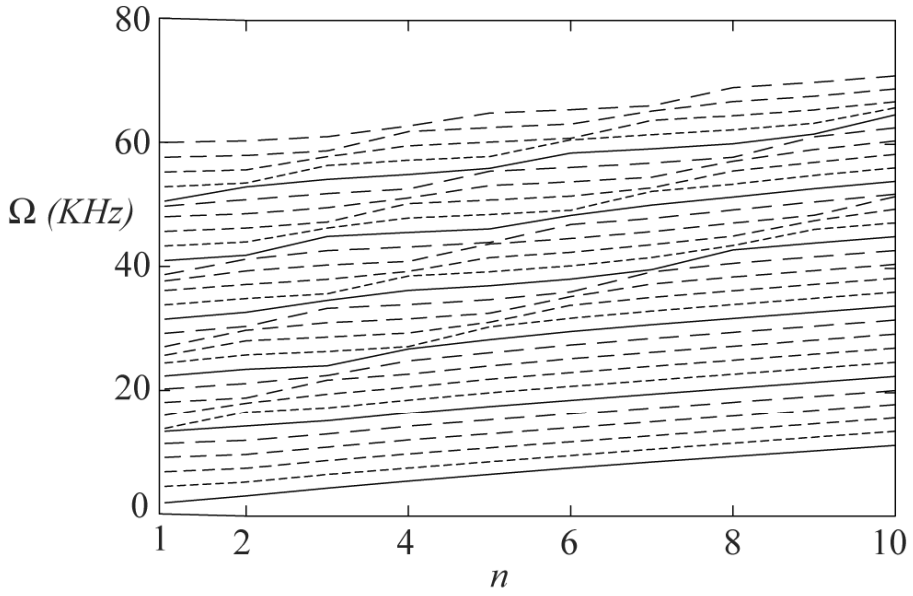

Figure 1. Asymmetric mode frequency spectrum of homogeneous plane-strain cylinder

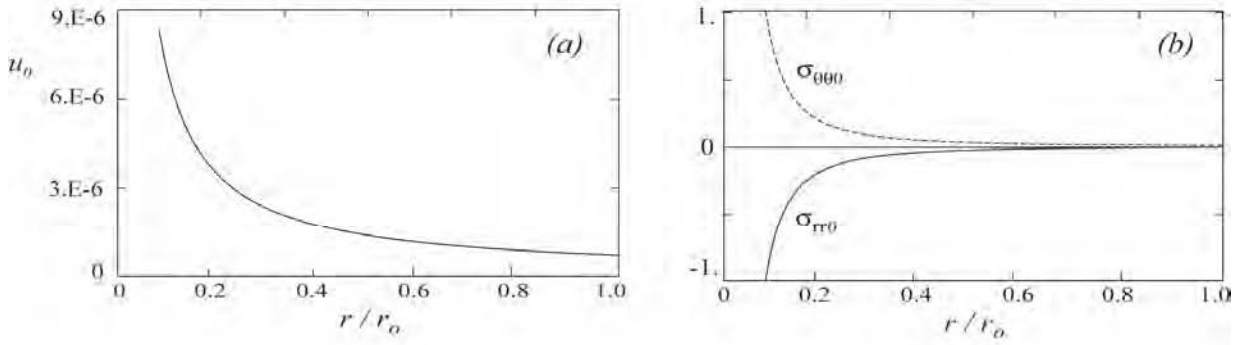

Figure 2. Axisymmetric static variables of homogeneous plane strain cylinder

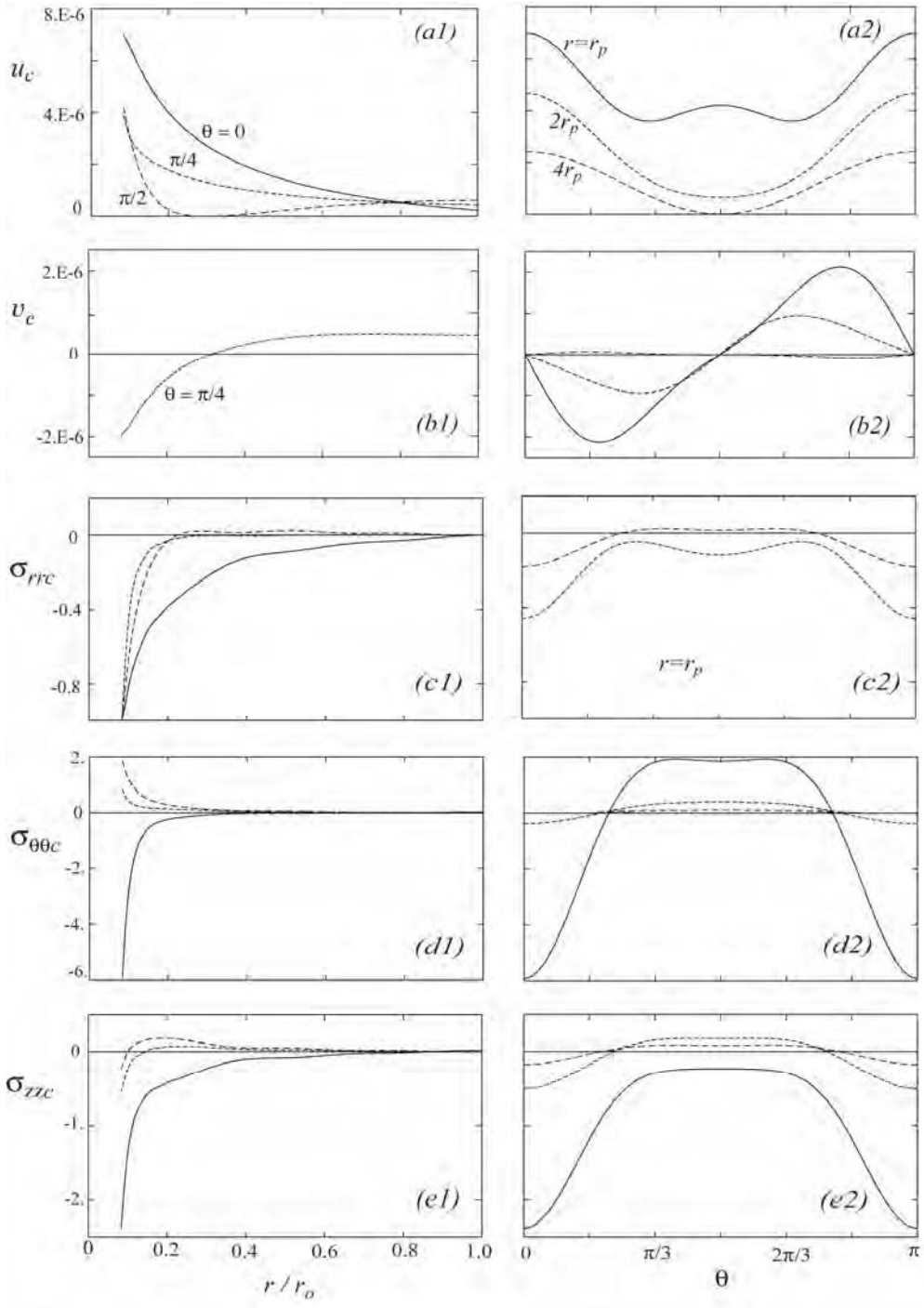

Figure 3. Static variables of plane-strain cylinder with θ–inhomogeneity

(a1) - (e1) along r , (a2) - (e2) along θ

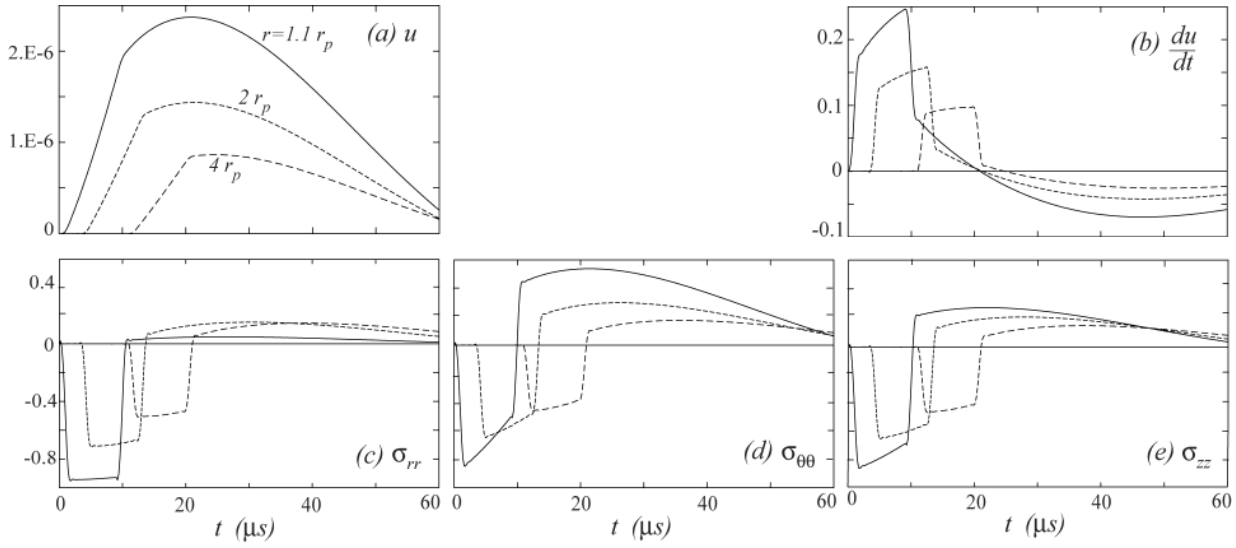

Figure 4. Histories of homogeneous plane-strain cylinder

(a) u , (b) du/dt , (c) σ_{rr} *, (d)* $\sigma_{\theta\theta}$ *, (e)* σ_{zz}

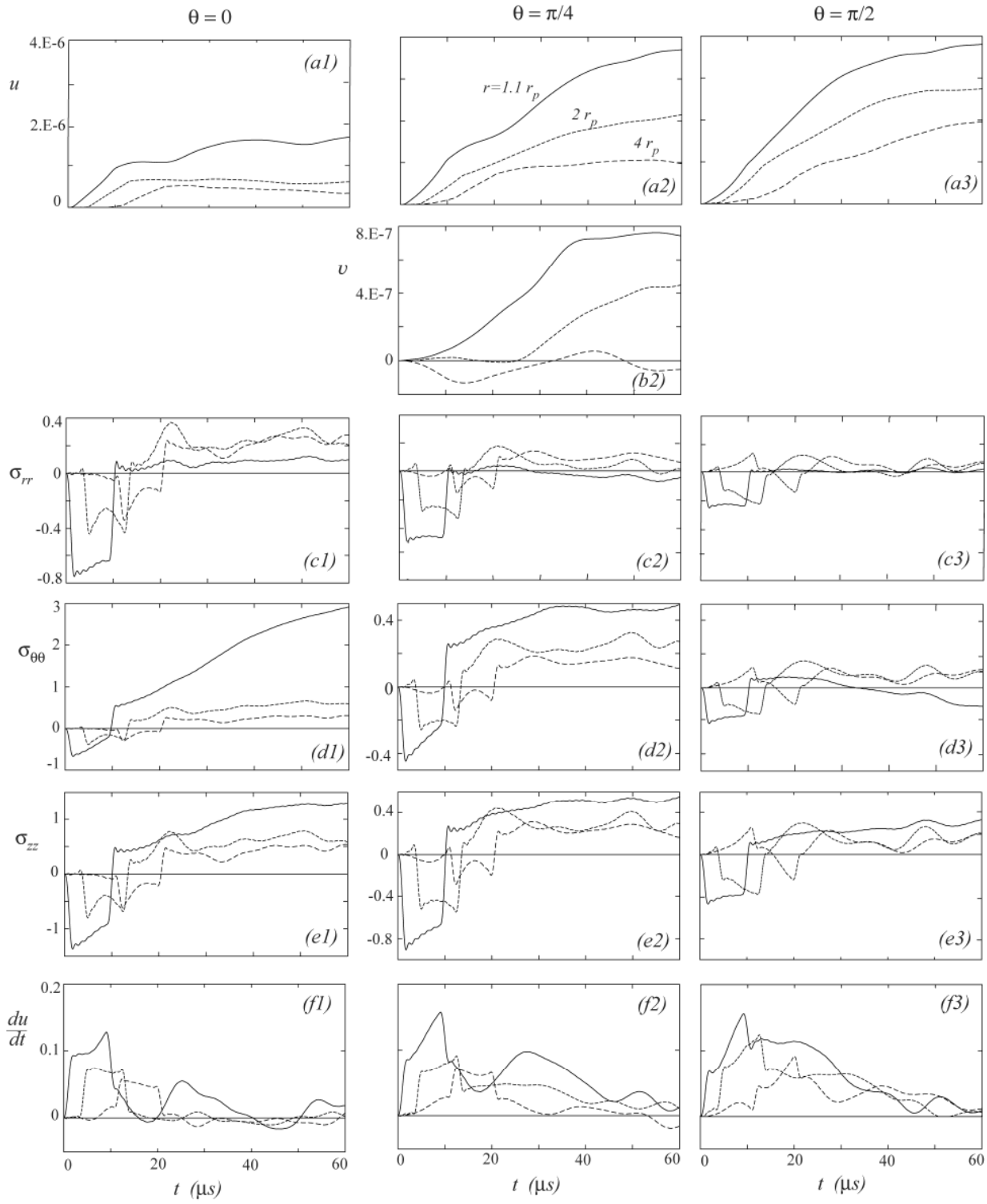

Figure 5. Histories of plane-strain cylinder with θ *– inhomogeneity*

(a1) - (f1) $\theta = 0$, *(a2) - (f2)* $\theta = \pi/4$, *(a3) - (f3)* $\theta = \pi/4$

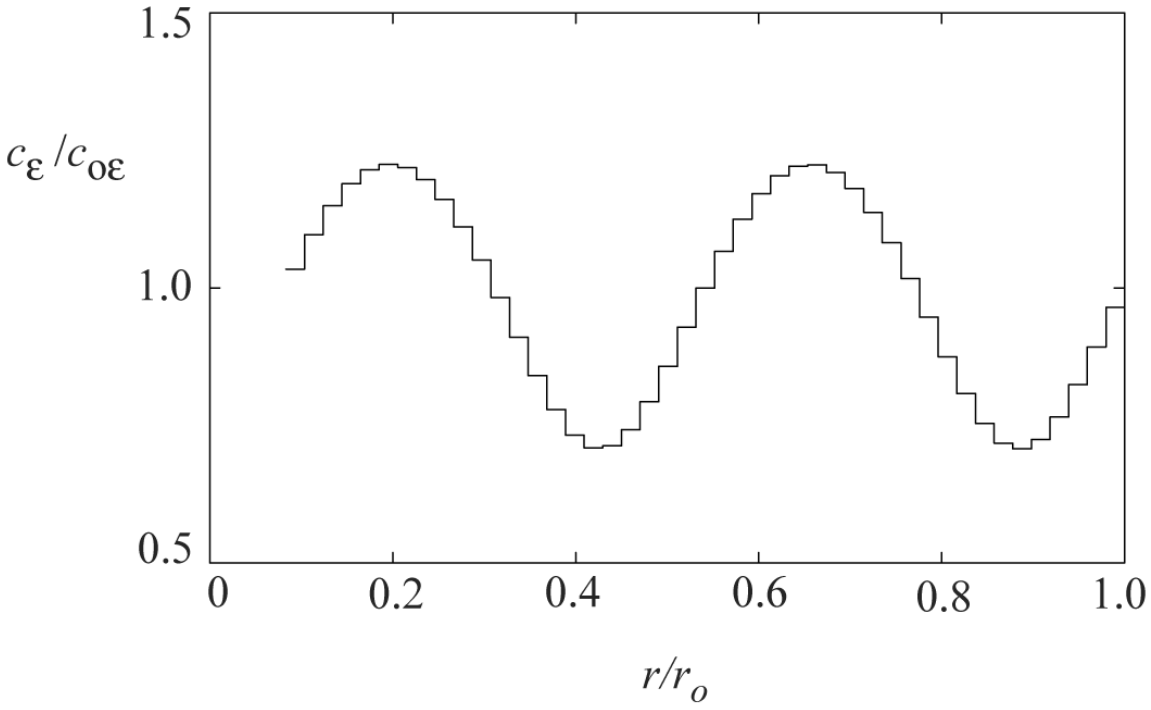

Figure 6. Radial step-wise distribution of normalized c_ε

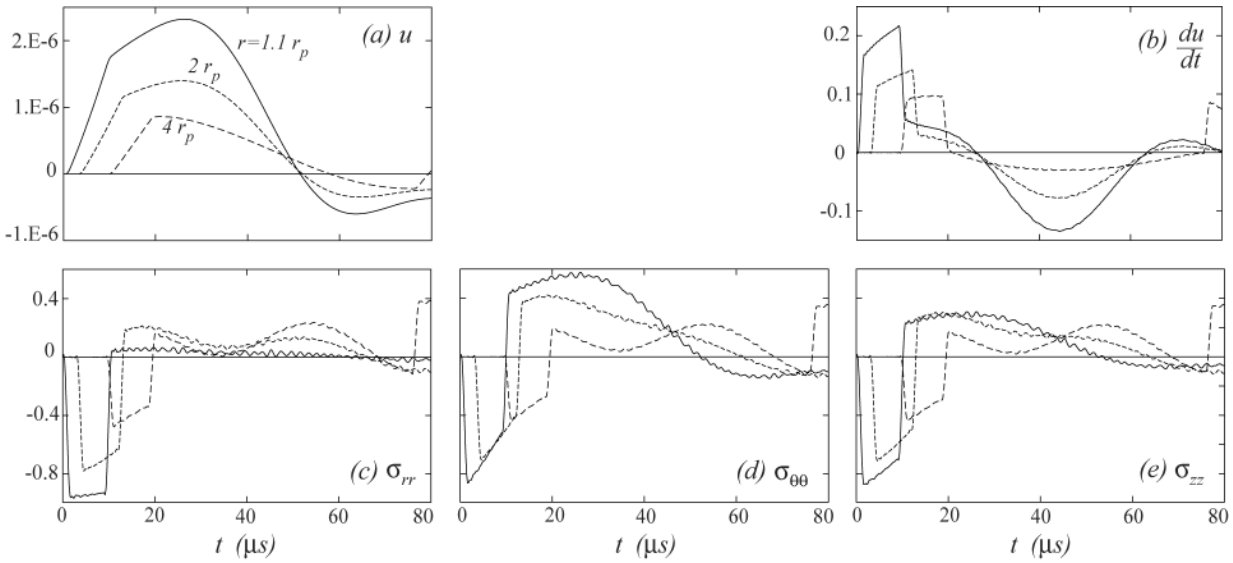

Figure 7. Histories of plane-strain cylinder with r-inhomogeneity

(a) u , (b) du/dt , (c) σ_{rr} *, (d)* $\sigma_{\theta\theta}$ *, (e)* σ_{zz}

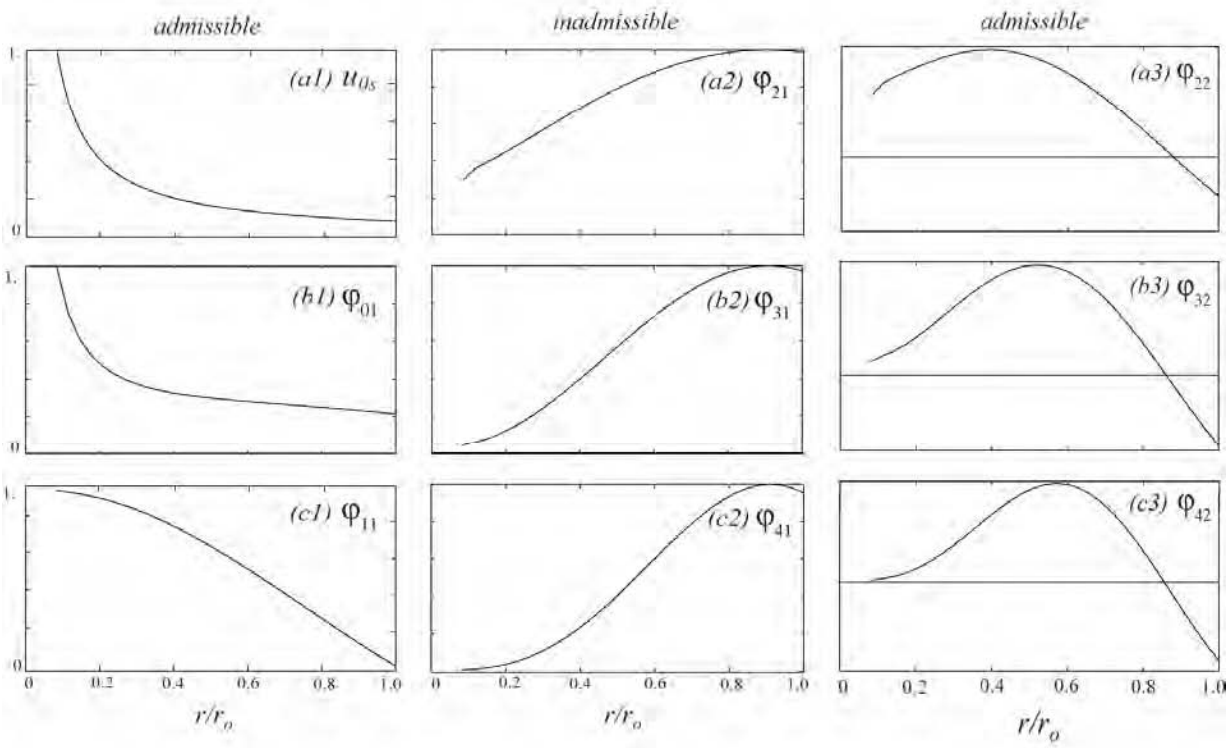

Figure C1. Sample of low wave number admissible and inadmissible trial functions in static response

(a1) u_{0s} *static n=0 ,* *(a2)* φ_{21} *n=2, m=1,* *(a3)* φ_{22} *n=2, m=2*

(b1) φ_{01} *n=0, m=1,* *(b2)* φ_{31} *n=3, m=1,* *(b3)* φ_{32} *n=3, m=2*

(c1) φ_{11} *n=1, m=1,* *(c2)* φ_{41} *n=4, m=1,* *(c3)* φ_{42} *n=4, m=2*

APPENDIX N

Slides Presented at MMVR 13

ANALYTIC SIMULATION OF TISSUE DAMAGE FROM PENETRATING WOUNDS TO THE HEART (PART 1)

Bob Eisler
ATK Mission Research
Applied Mechanics and Material Sciences Group
Laguna Hills, California

Presented at: *Medicine Meets Virtual Reality 12*
Long Beach, California
January 2004

This work is supported by the U.S. Army Medical Research and Materiel Command under Contract No. W81XWH-04-C-0084. The views, opinions and/or findings contained in this report are those of the author(s) and should not be construed as an official Department of the Army position, policy or decision unless so designated by other documentation.

PHASE I OBJECTIVE

Develop analytic models describing tissue damage from ballistic impact by low velocity fragments (categories of fragments shown at bottom) penetrating heart. Tissue damage includes descriptions of projectile trajectory through heart and tissue damage lateral to projectile trajectory (*wound tract*).

SCOPE

- **TASK 1 – ANALYTICAL SIMULATION OF PROJECTILE TRAJECTORY**
  - *Tissue Mechanical Properties*
  - *Projectile Retardation*
  - *Simulation of Arbitrary Projectile*
- **TASK 2 – ANALYTIC SIMULATION OF WOUND TRACT**
  - *Analytic Simulation of Tissue Transient Response*
  - *Analytic Simulation of Wound Tract Geometry*
- **TASK 3 – BALLISTIC EXPERIMENTS ON TISSUE SURROGATES**

Platelet $\frac{L}{D} \to \varepsilon$

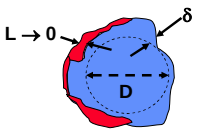

"Chunky" Equivalent Sphere $\frac{L}{D} \approx 1$

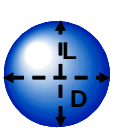

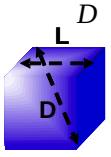

Slender High Aspect Ratio Fragment

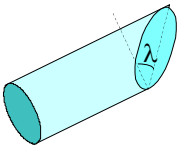

$\frac{L}{D} \succ 1$

PROBLEMS/ISSUES

- **GENERAL PURPOSE NUMERICAL DISCRETIZATION TOOLS SUCH AS FINITE ELEMENT CODES CANNOT PROPERLY ADDRESS PROJECTILE-TISSUE INTERACTION**
  - Require high strain rate material properties for human tissue as input which do not exist and cannot be acquired
    - High penetration velocities - tissue interaction with projectile fluid-like
    - Low penetration velocities - target response is like hyperelastic and viscoplastic solid
    - Most of wound tract established at intermediate velocities where multiphase material interacts with projectile at high strain rates
  - Require detailed material models of failure which is local process
    - Relevant material properties do not exist and probably cannot be acquired
    - Analysis requires highly refined mesh (frequency content > MHz) not consistent with late-time structural response (frequency content Hz → kHz)
- **HYBRID APPROACH WITH ANALYTIC MODEL THAT DESCRIBES RESPONSE LOCAL TO WOUND TRACT AND PROVIDES INITIAL/BOUNDARY CONDITIONS TO NUMERICAL DISCRETIZATION SCHEME FOR GLOBAL RESPONSE**
  - Require feedback loops between global and local models

CLAIMS/ASSUMPTIONS

- ***Observation***. Empirically observed that penetration depth, $\delta(v)$, as a function of striking velocity, v, of a spherical projectile into soft materials like gelatin (and presumably soft tissue as well) have sigmoidally shaped curves bounded by low velocity and high velocity asymptotes
- **Retarding force on spherical projectile can be derived from the $\delta=\delta(v)$**
  - More complicated projectile geometries can be represented as ensemble of spherical projectiles where retarding forces can be derived by integrating resultant forces from constituent spheres about projectile geometry.
- **For Unknown Material (e.g., Human Tissue)**. The Taylor series expansion of the asymptotes for the curves can be rigorously derived.*
  - Limits of these asymptotes as $v\rightarrow 0$ and $v\rightarrow\infty$ have dominate leading terms
  - Coefficients of terms can be expressed in terms of independently measured material properties which can be used to construct $\delta=\delta(v)$ for unknown materials
  - $\delta=\delta(v)$ *for* intermediate velocities can be established by matching slopes of high and low velocity asymptotes.
  - Allows determination of projectile retarding forces in unknown materials where quasistatic properties are available
- Projectile rotational kinematics and trajectory can be determined by continuum techniques once retarding forces specified
- Testing methodology by measuring quasistatic material properties and reconstructing $\delta=\delta(v)$ for unknown materials which is then correlated with experimental $\delta=\delta(v)$ *from* ballistic testing

* A.K. Chatterjee and R. D. Eisler, et al. *Ballistic Penetration into Gelatin*, IMPACT, WAVES, AND FRACTURE, Proceedings Of The Werner Goldsmith Symposium, sponsored by the Applied Mechanics Division of the American Society of Mechanical Engineers and the University of California at Los Angeles, Los Angeles, 28 - 30 June 1995, ASME Applied Mechanics Division, Volume 205, pp. 9-20, 1995

METHODOLOGY

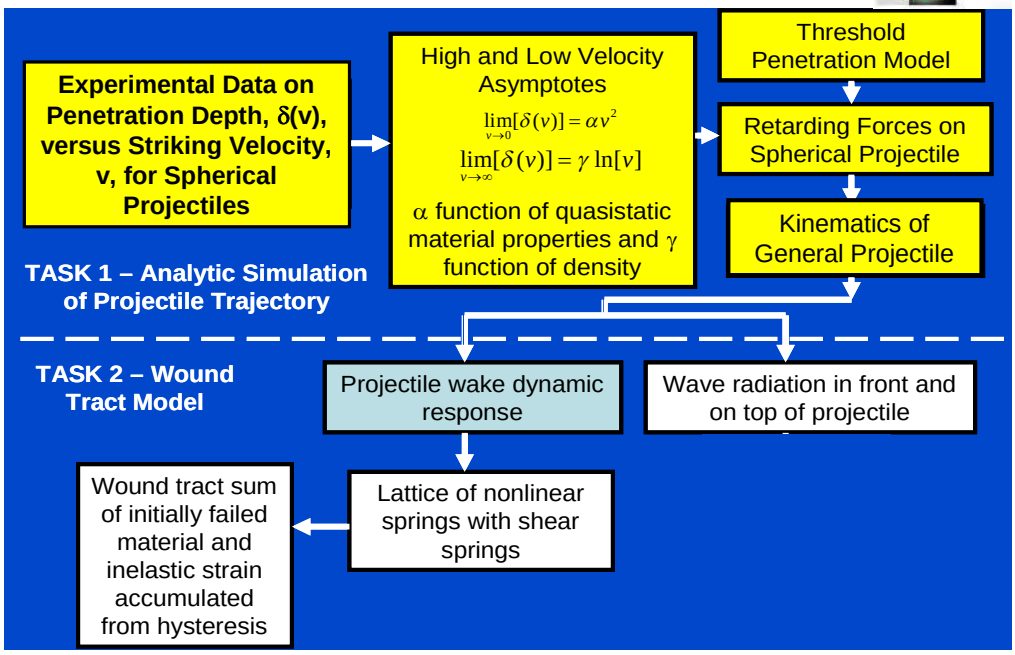

MODEL PARAMETERS EXPRESSED IN TERMS OF CURRENTLY AVAILABLE HUMAN TISSUE PROPERTIES

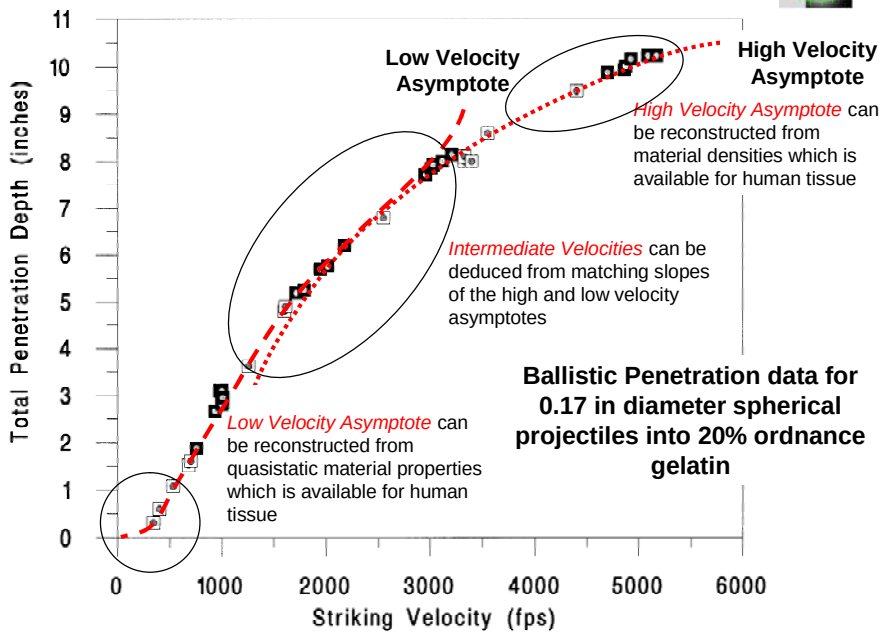

SIMULATED RESULTS FROM ANALYTICAL CODE

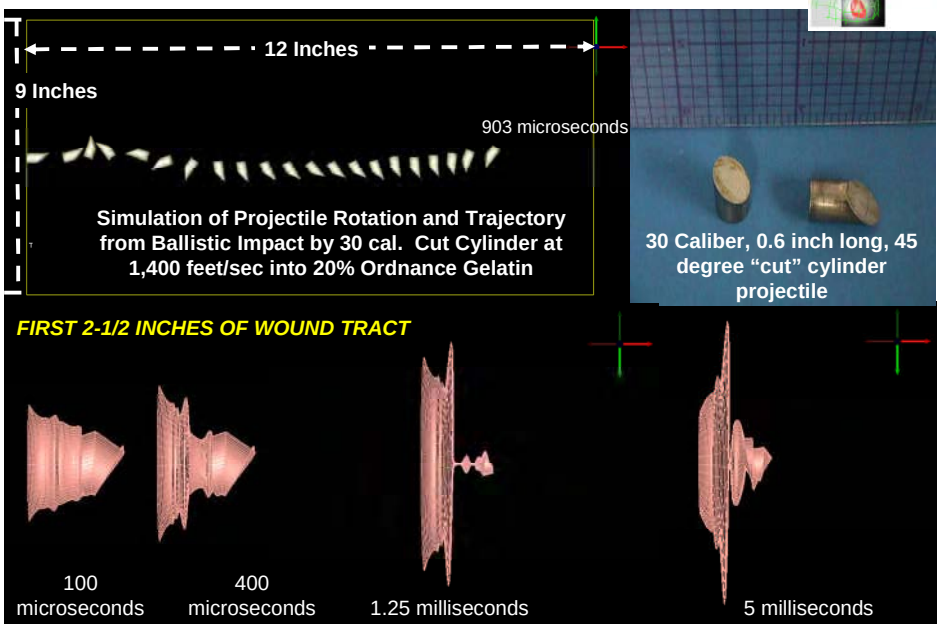

COMPARISON BETWEEN ANALYTICAL RESULTS AND BALLISTIC EXPERIMENTS

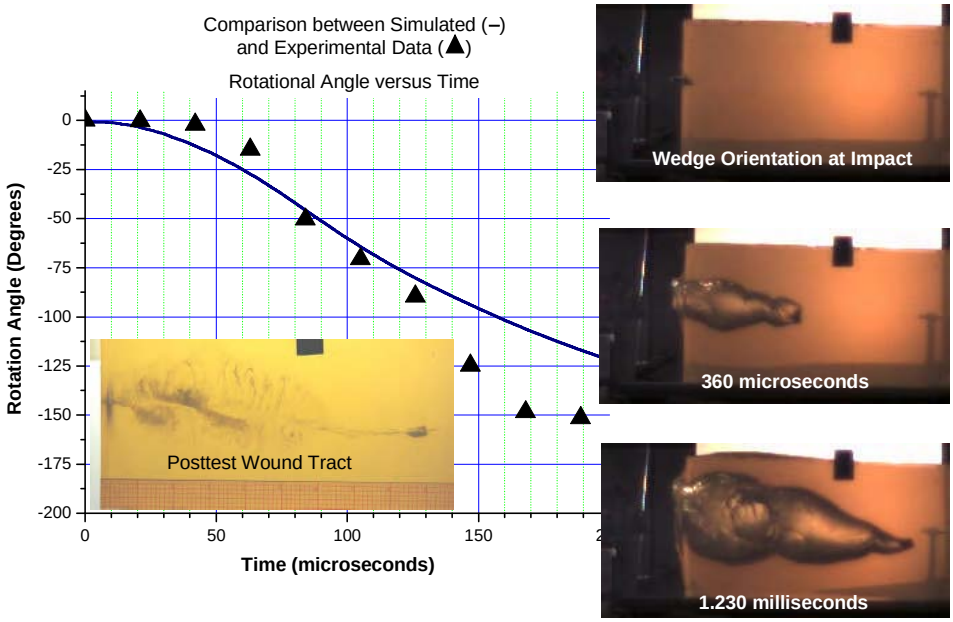

NEXT STEP: FRAGMENT IMPACT INTO HUMAN LEFT VENTRICLE

Fragment Ballistic Impact

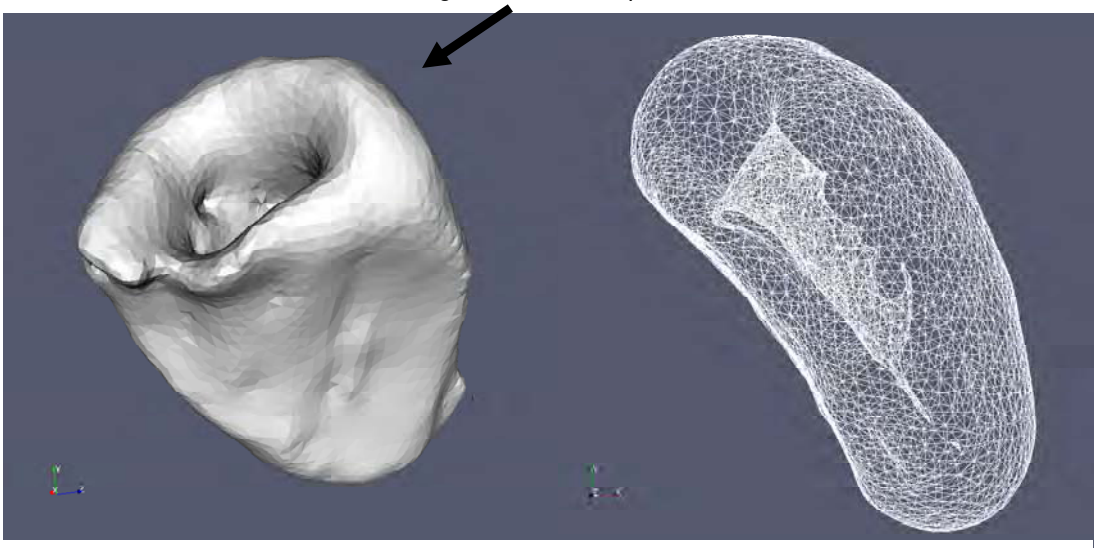

Pressure Contours on Impact Surface of Left Ventricle (LV) Myocardium from Impact by Wedge

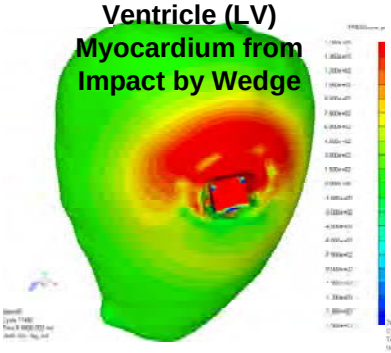

Pressure Contours Through Thickness of LV Myocardium from Impact by Wedge

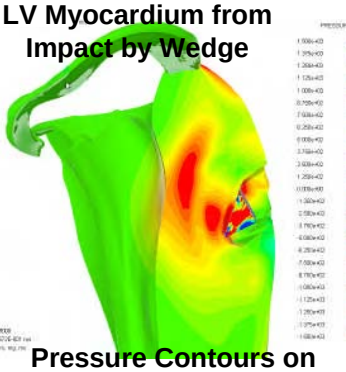

Strain Contours Through Thickness of LV Myocardium from Impact by Wedge

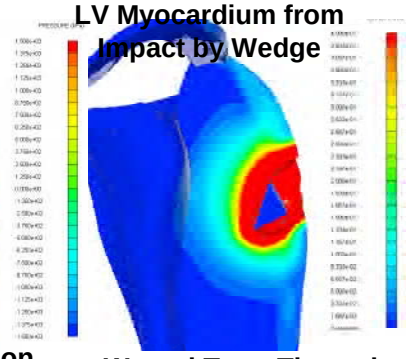

Impact of Cylindrical Projectile on LV Pericardium

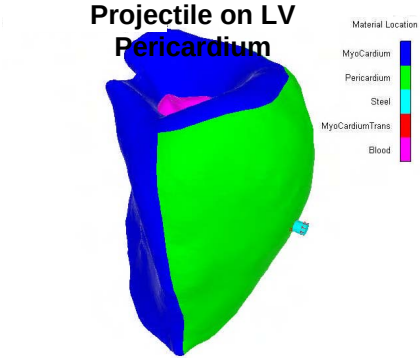

Pressure Contours on Impact Surface of LV Myocardium from Impact by Cylinder

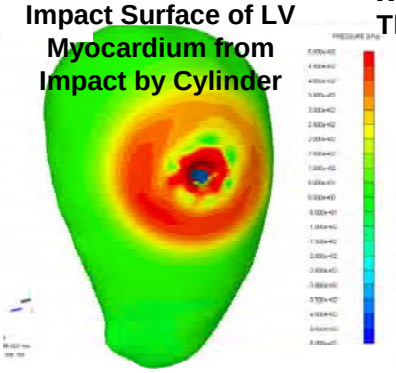

Wound Tract Through Thickness of LV from Cylinder

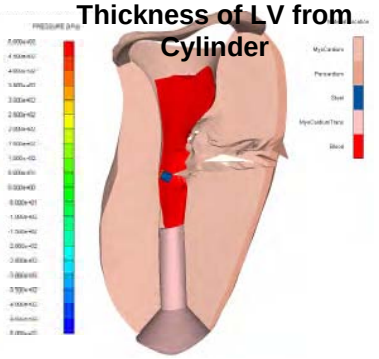

APPENDIX O

BRIDGE EFFORT

BEHIND ARMOR RESPONSE TO NON-PENETRATING PROJECTILES AND BLAST

A series of 2D Hydro code calculations was conducted to address various mechanical response modes of ceramic breast plates used in current body armor. Of particular interest were stresses promoted at the interface between the 'catcher' portion of the vest and human tissue behind the plate for an incident threat (blast or projectile) that is defeated by the armor. Moreover, future upgrades entail increasing the performance (ballistic limit) of the plate so this in turn will also increase the stresses transmitted to the tissue.

The initial analysis yielded good correlation with published ballistic limits for the baseline 4.8 Pounds per Square Foot (psf) protective vest design. This plate is designed to defeat a 7.62 M80 ball round at muzzle velocity. The baseline plate consists of a 0.27-inch thick Boron Carbide Plate fixed to 0.29-inch (45 layer) Spectra Shield. Subsequent analysis included and enhanced design with an areal density of 5.9 psf which was designed to defeat a 7.62 APM2 threat. At a nominal striking velocity of 2900 fps (muzzle velocity) normal to the plate impact surface, the stresses at the interface between the Spectra Shield backer-plate and human tissue were significantly reduced compared to the impact surface stresses. However, these stresses were still significant. The high mechanical impedance of the ceramic plate which is designed to cause high impact stresses that fragment the incident projectile also result in high stresses promoted in underlying tissue.

The 2D hydrocode model that was developed for this effort is shown in Figure 0-1.

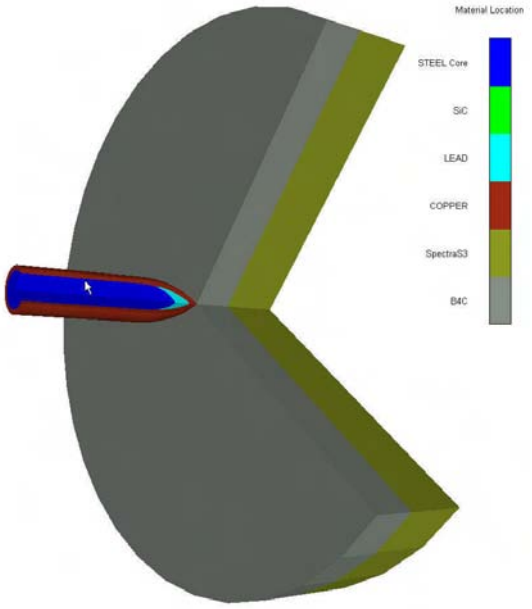

FIGURE 0-1. Hydro code Model for Baseline SAPI Configuration

Snapshots of the early time (3.6 µsecs.) and late time (73 µsecs.) material response of the projectile and target are shown in Figures O-2a and b. At early time it is seen that the nose of the projectile has failed as well as the front surface of the ceramic. At late time it is seen that the projectile has been defeated and is fragmented. A cone of the ceramic material has failed and there is significant deformation and initial failure near the centerline of the Spectra Shield back-plate.

The velocity versus time in the center potion of the projectile for the cases of a nominal 2900 fps (no penetration) and a 3000 fps (penetration) are shown in Figure O-3. It is predicted that ceramic and projectile failure occur around 30 µsec leading to the 'blip' in the velocity shown in the associated figures

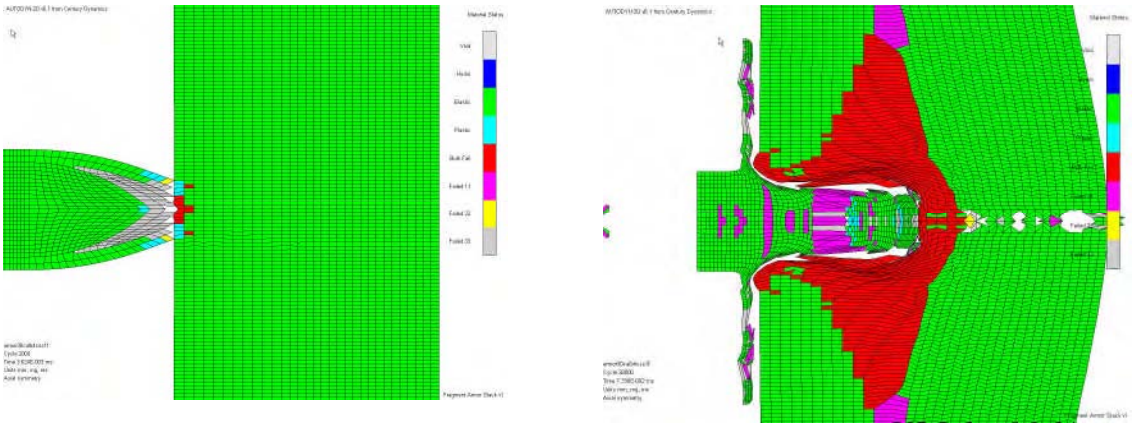

FIGURE O-2a, b. Early/Late Time Material Response of Projectile/Target at Nominal Striking Velocity

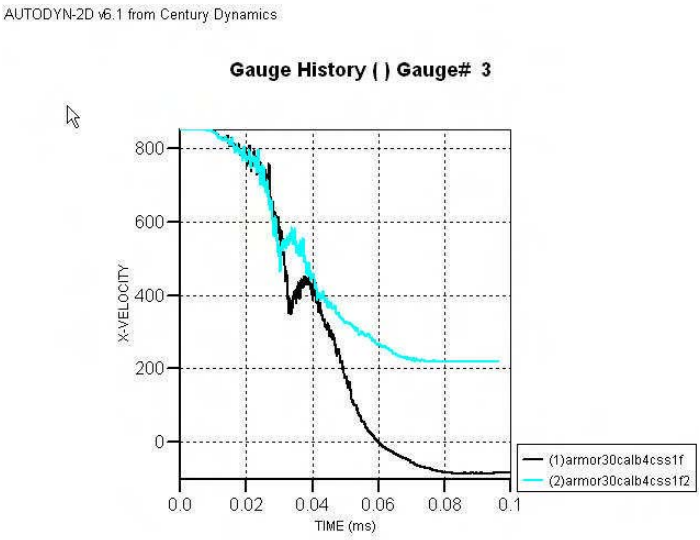

FIGURE O-3. Velocity versus Time for 2900 and 3000 fps Striking Velocities (2900 fps event is defeated and 3000 fps event fully Penetrates armor).

The resulting projectile/target response for the 3000 fps impact case at late time (72 µsecs.) is shown in Figure O-4. Note that the projectile has failed but **penetrated** the Spectra Shield.

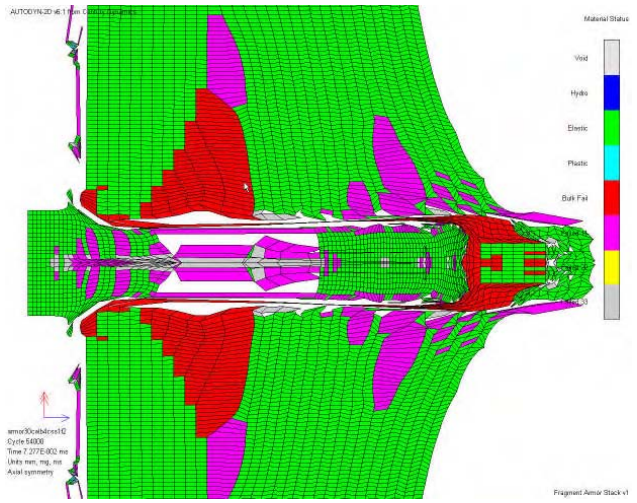

FIGURE O-4. Late Time Material Response of Projectile/Target at 3000 fps Striking Velocity

Once correlation was achieved with published data for the ceramic breast plate in isolation, the analysis was repeated using the configuration above backed by 0.2-inches of ordnance gelatin simulating human tissue. Of interest in this case was the stresses developed in the gelatin given that the Spectra Shield was not penetrated. The geometry is shown in Figure O-5

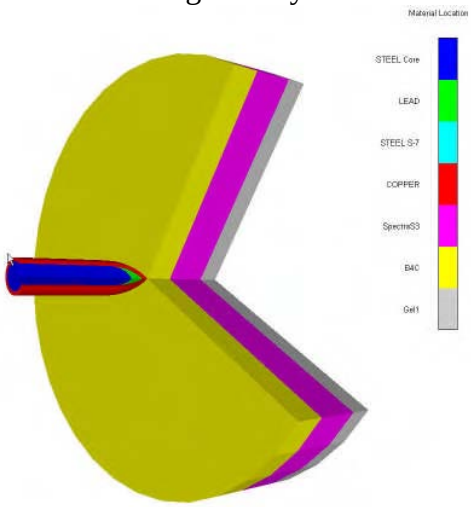

Figure O-5. Hydrocode Model for Ceramic Breast Plate and Gelatin Backing

The state of the materials at late elapsed times following impact assuming Gelatin is bonded to the Spectra Shield (SS) is shown in Figures O-6a and b. The location of the corresponding materials is shown in Figure O-7.

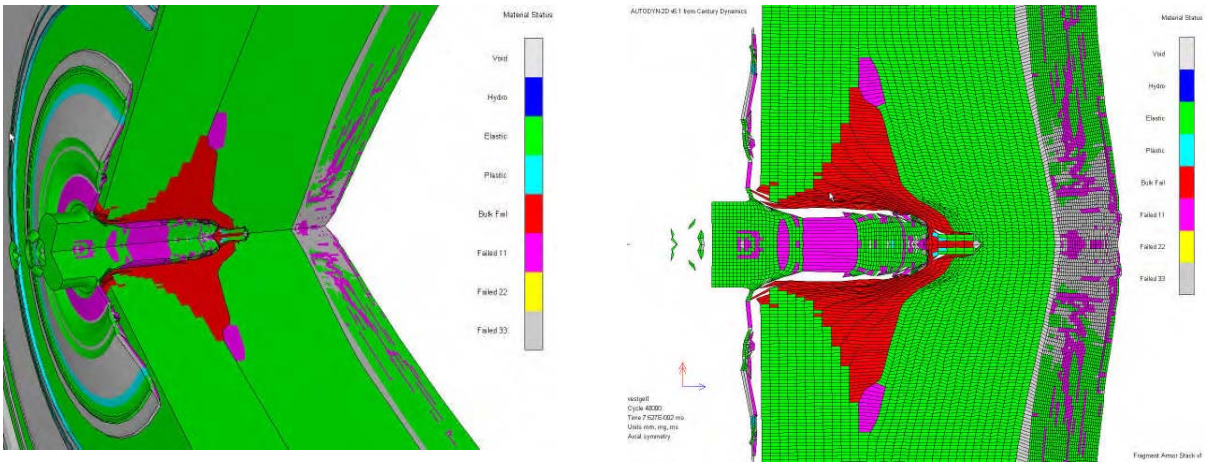

FIGURE 6 a,b. Late-Time Material Failure of Ceramic Breast Plate and Gelatin Configuration

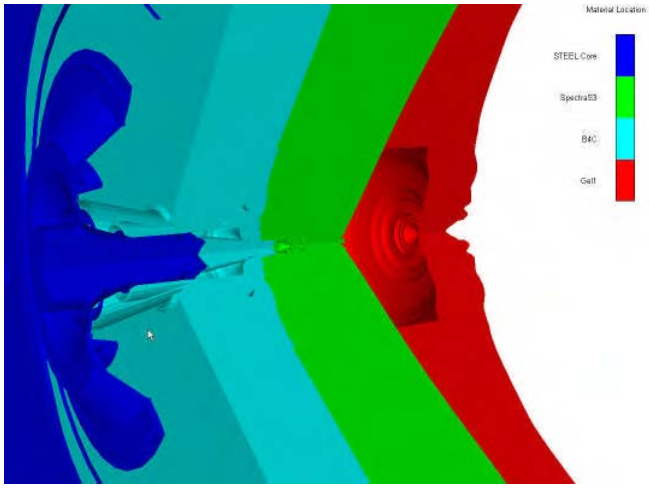

FIGURE O-7. Late-Time Material Location for Ceramic Breast Plate and Gelatin Configuration

The thru the thickness stress versus time histories for the ceramic/SS interface (Gauge 23), rear of SS (Gauge 27), near front surface of gelatin (Gauge 28) and middle of gelatin (Gauge 30) are shown in Figure O-8a. The near impact surface stress is compared with the ceramic/SS interface stress in Figure O-8b.

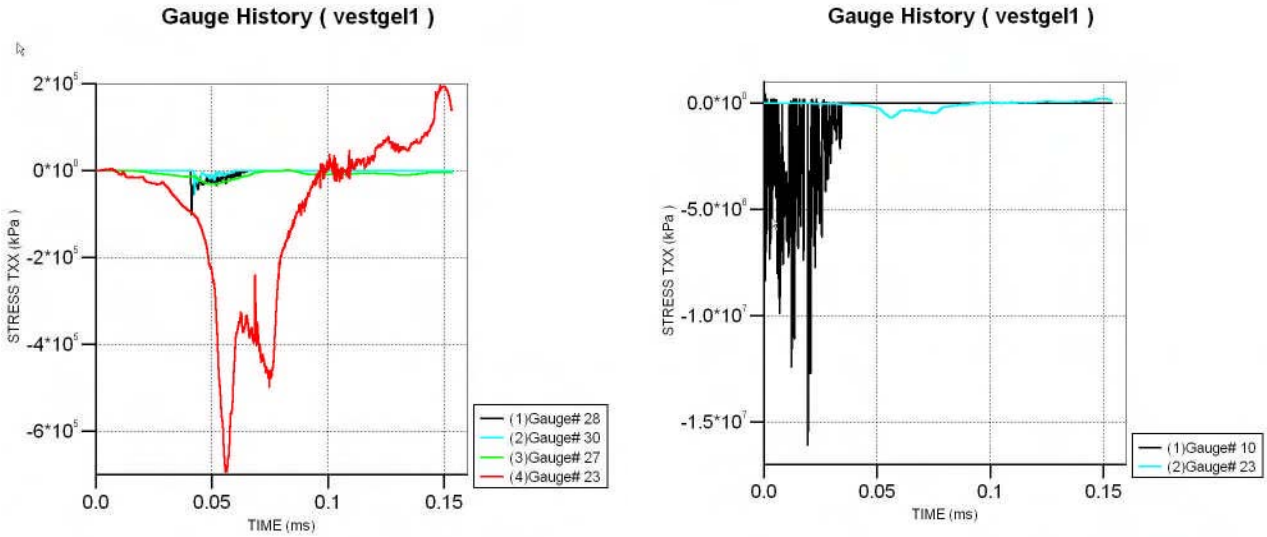

FIGURE O-8a ,b. Stress versus Time for Various Locations in Ceramic Breast Plate and Gelatin Configuration

A comparison of the peak stresses at various locations is given in Table O-1. It is seen that a substantial amount of attenuation occurs as the impact induced pulse propagates thru the various layers but the stresses created in the gelatin are still sufficient to cause tissue damage.

TABLE O-1. Summary of Peak Stresses in Materials

Location	Peak Stress (ksi)	% of Peak Stress	Failure Stress (ksi)
Near Impact Site	1700	100	
Ceramic/SS Interface	100	6	
Back of SS	5	0.3	
Near Front Surface of Gelatin	15	0.6	0.4
Middle of Gelatin	7	0.4	0.4

The late time state of the various materials is shown in Figure O-9.

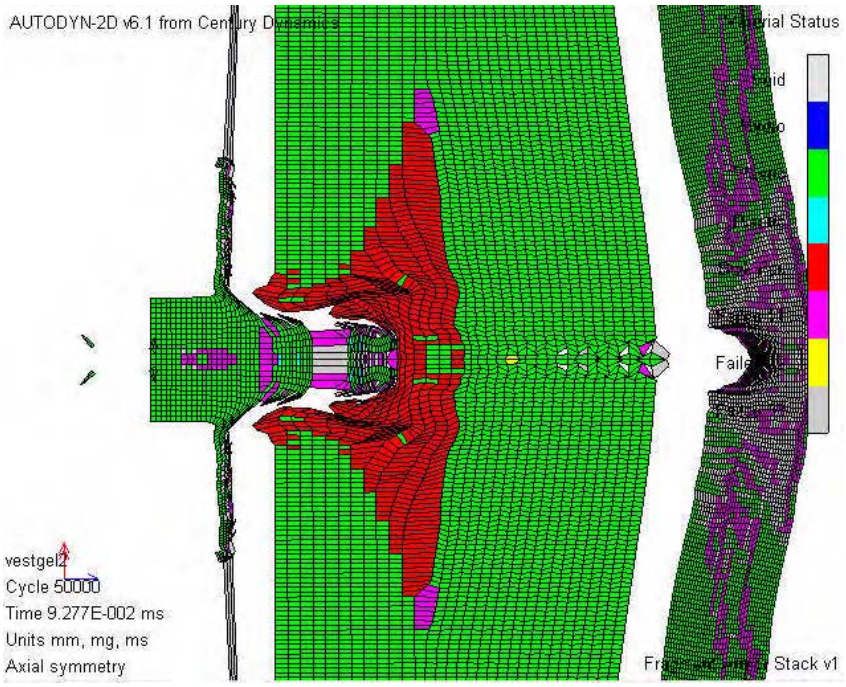

FIGURE O-9. Late-Time Material State for Ceramic Breast Plate and Gelatin Configuration

An additional set of hydrocode calculations were conducted to address the response of behind armor tissue to non-penetrating APM2 and blast wave loading. Of interest are the character of the stress pulse and the deformation of the tissue stimulant behind the armor. An APM2 projectile traveling at 2900 fps and a blast wave of several hundred µsec and 1 Bar peak stress and a rapidly rising blast pulse of several msec and a 6.8 Bar rapidly rising blast pulse were modeled.

The projectile which did not penetrate the vest transferred much of its momentum to the vest which then impacted the tissue simulant. Damage in the Spectra Shield resulted in damage to the gelatin. The projectile then rebounded resulting in enhanced momentum transfer to the target. The lower peak pressure blast pulse cased significant deformation in the gelatin and ceramic breast plate enhanced which also promoted significant induced stresses. The higher magnitude pressure blast pulse caused significant damage to the tissue simulant.

A 2D hydro code model was constructed as shown in Figure O-10. In this case the tissue stimulant was ‘stood’ off from the Spectra Shield by approximately 1.6 mm which just allows the Spectra Shield to impact the gelatin. The rear of the gelatin is assumed to be a transmitting boundary thus allowing the stress pulse to be transmitted without and reflection at the boundary. The first simulation was run using the APM2 projectile. The tissue simulant is restrained from moving in the direction of the projectile impact.

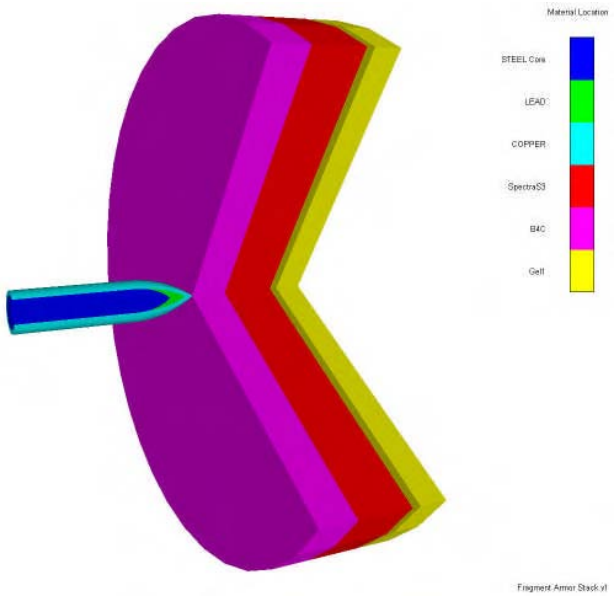

Figure O-10. Hydrocode Model for Ceramic Breast Plate and Gelatin Configuration

Snapshots of the stress contours in the materials just after contact of the Spectra Shield on the gelatin (57 µsecs.) and late time (210 µsecs.) when significant deformation of the gelatin occurs are shown in Figure O-11a and b.

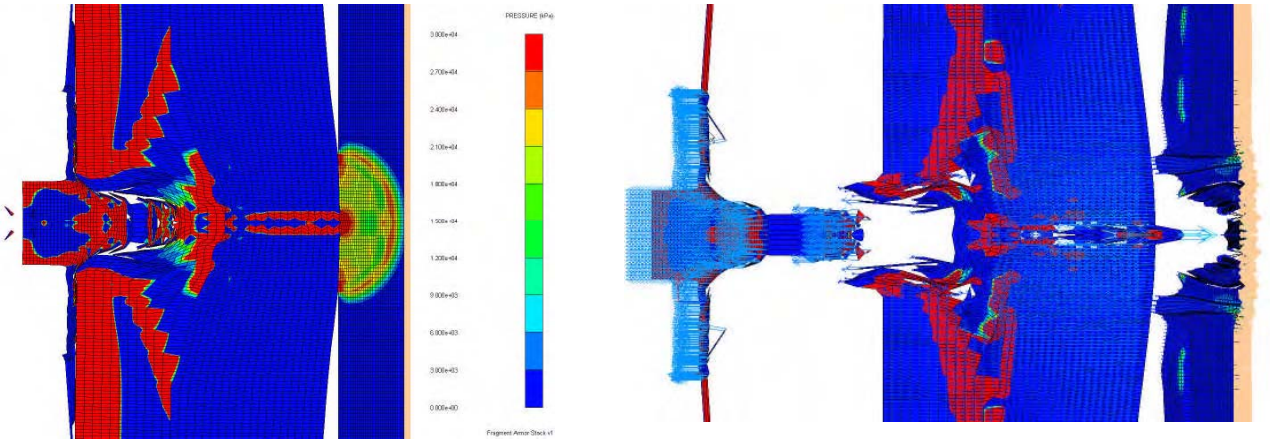

FIGURE O-11a ,b. Early/Late Time Material Response of Projectile/Tissue

A plot of stress versus time in the tissue simulant along the centerline is shown in Figure O-12. Note that the stress pulse with any significant duration (5 µsecs) and has an average magnitude of about 300 bars. The gelatin displaces about 1.6 mm in the 210 msecs time-interval in which the problem was run

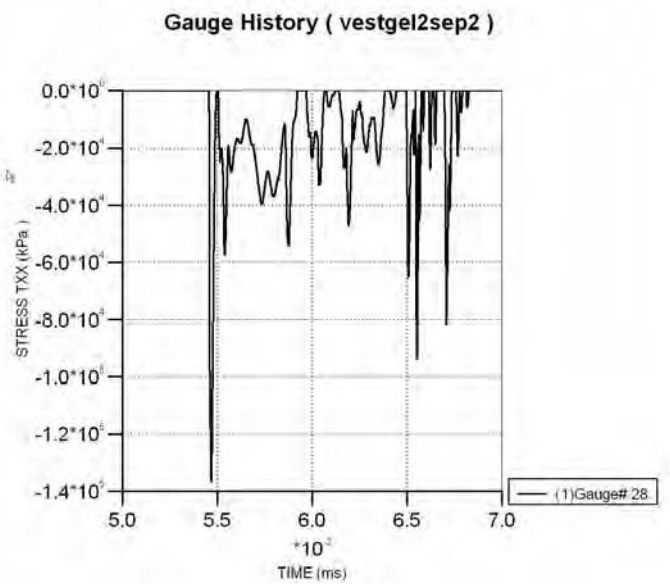

FIGURE O-12. Stress vs. Time Near Front of Gelatin

The second set of analysis was conducted assuming a prescribed blast wave loading on the ceramic front surface of the target. In this case the pulse was assumed to rise rapidly over 20 µsecs to a peak pressure of 1 bar (100 KPa) and decay linearly to zero in 230 µsecs. The model is shown in Figure O-13.

.

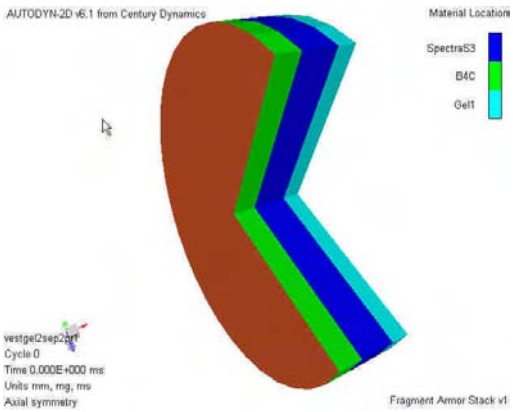

FIGURE O-13. Model of Ceramic Breast Plate and Gelatin Configuration

The thru the thickness stress versus time for a point near the front of the gelatin is shown in Figure O-14. Note that at about 0.41 msec the rear of the Spectra Shield impacts the gelatin causing a very short duration pressure spike. The stress contours at this impact time are shown in figure O-15. Recall that the peak impact stress is 100kPa. The peak stress in the gelatin is more than twice this value.

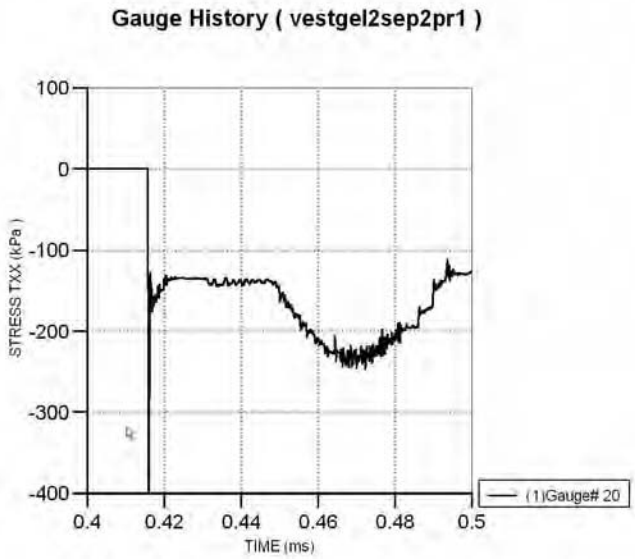

Figure O-14. Stress vs. Time Near Front of Gelatin

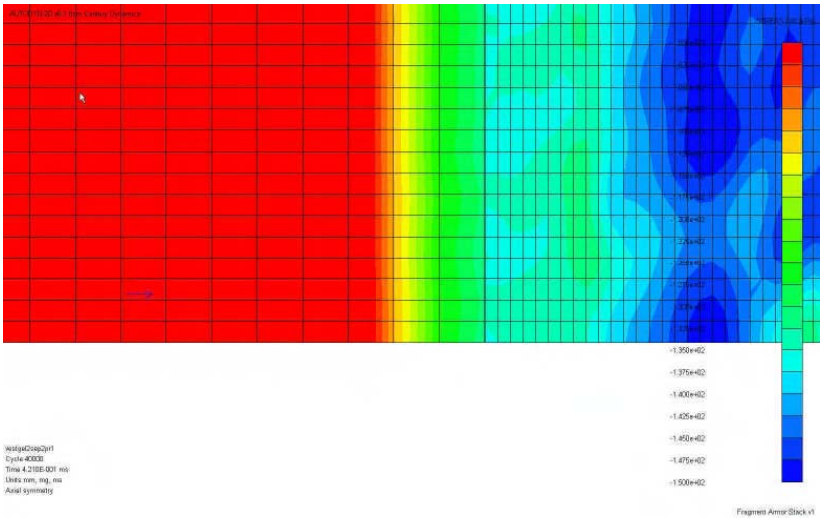

FIGURE O-15. Stress vs. Time Near Front of Gelatin

The impulse delivered by the surface loading pulse results in momentum generation in the targets. The time history of the momentum in the various layers is shown in Figure O-16. Note that the tissue simulant ultimately contains about 10% of the momentum of the target.

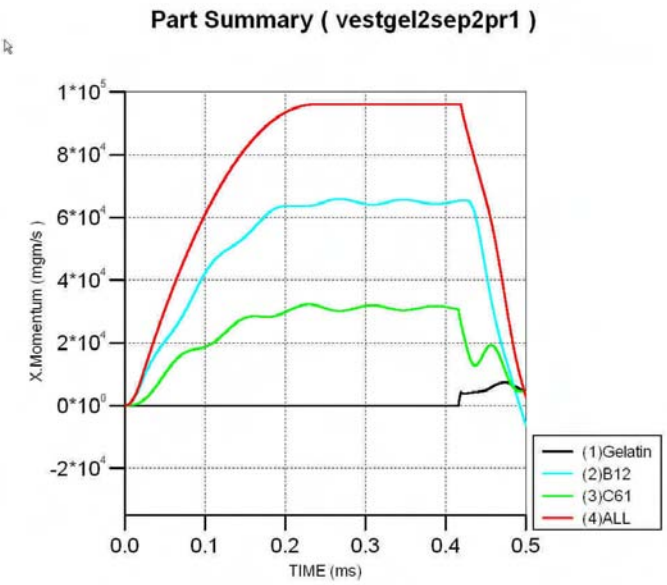

Figure O-16. Momentum versus Time in the Various Layers

The final set of analysis was conducted assuming a more severe blast wave loading on the front surface of the target. In this case the pulse was assumed to rise rapidly over 20 μsecs to a peak pressure of 6.8 bar (680 KPa) and decay linearly to zero in 5 msecs. The thru the thickness stresses versus time near the ceramic, Spectra Shield and tissue front surfaces are shown in Figure O-17. It is noted that at about 0.12 msec the rear of the Spectra Shield impacts the gelatin causing a very short duration pressure spike. Recall the peak impact stress is 680 KPa. The peak stress in the gelatin is ~ 3 times this value. In this loading case, the gelatin is predicted to undergo significant failure as shown in Figure O-18.

The impulse delivered by the surface loading pulse results in momentum generation in the targets. The time history of the momentum in the various layers is shown in Figure O-19 and is significantly different in character than that shown for the previous loading case. Note that the gelatin again ultimately contains about 10% of the momentum of the target.

Both the projectile and the blast pulses will cause the vest to impact the gelatin causing significant deformation and stress. The peak stresses transmitted to the gelatin could in theory be mitigated by designing ‘poorer’ mechanical coupling of the vest via clothing or a larger standoff.

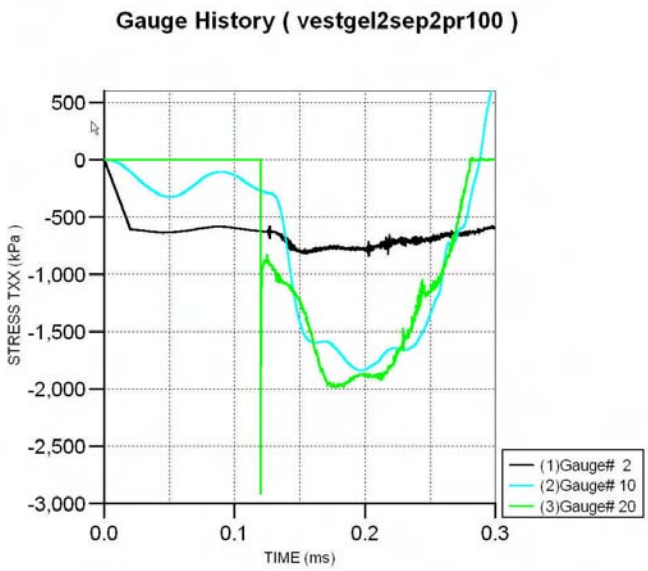

FIGURE O-17. Stress versus Time in the Various Layers

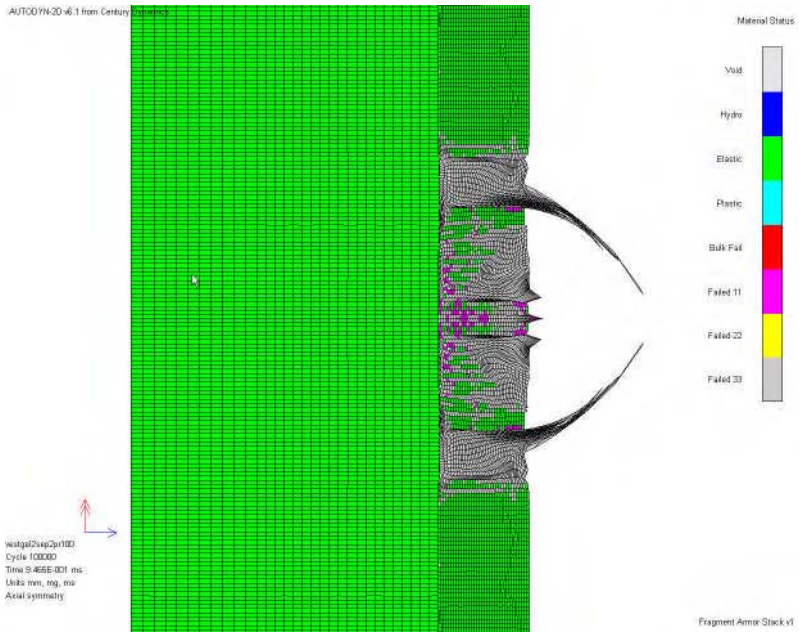

FIGURE O-18. Material State at 1 msec.

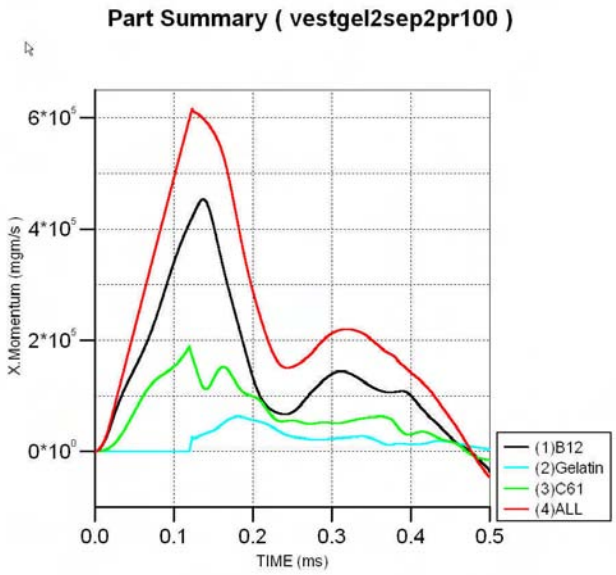

FIGURE O-19. Momentum versus Time in the Various Layers

A comparison of the peak stresses at various locations is given in Table O-2. It is seen that a substantial amount of attenuation occurs as the impact induced pulse propagates through the various layers but the stresses created in the tissue are still significant.

TABLE O-2. Summary of Peak Stresses in Materials

Location	Peak Stress (ksi)	% of Peak Stress	Failure Stress (ksi)
Near Impact Site	1700	100	
Ceramic/SS Interface	100	6	
Back of SS	5	0.3	
Near Front Surface of Gelatin	15	0.6	0.4
Middle of Gelatin	7	0.4	0.4